

Thiophene-Based Organic Thermoelectric Materials: Exploring Molecular Design, Doping Techniques and Nanocomposite Formations

by

NEETHI RAVEENDRAN

10CC19A39015

A thesis submitted to the
Academy of Scientific & Innovative Research
for the award of the degree of

DOCTOR OF PHILOSOPHY

in
SCIENCE

Under the supervision of
Dr. Vijayakumar C.



**CSIR-National Institute for Interdisciplinary
Science and Technology (CSIR-NIIST),
Thiruvananthapuram - 695 019**



Academy of Scientific and Innovative Research
AcSIR Headquarters, CSIR-HRDC campus
Sector 19, Kamla Nehru Nagar,
Ghaziabad, U. P. - 201 002, India

JANUARY 2024

This thesis is dedicated to the two most important men in my life; my dearest papa Raveendran, who gave me the desire and determination to aim high, and my other half Preeth, who gave me the will and wings to get there through his incredible support!



Dr. Vijayakumar Chakkooth, PhD

Principal Scientist, Chemical Sciences and Technology Division

Associate Professor, Academy of Scientific and Innovative Research (AcSIR)

Tel: +91-471-2515-484 (O) +91-9447-835-815 (M); E-mail: cvijayakumar@niist.res.in

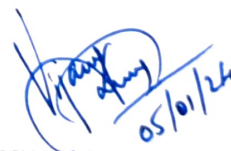
January 05, 2024

CERTIFICATE

This is to certify that the work incorporated in this Ph.D. thesis entitled, "***Thiophene-Based Organic Thermoelectric Materials: Exploring Molecular Design, Doping Techniques and Nanocomposite Formations***", submitted by ***Ms. Neethi Raveendran*** to the Academy of Scientific and Innovative Research (AcSIR) in fulfillment of the requirements for the award of the Degree of ***Doctor of Philosophy in Science***, embodies original research work carried out by the student. We further certify that this work has not been submitted to any other University or Institution in part or full for the award of any degree or diploma. Research materials obtained from other sources and used in this research work have been duly acknowledged in the thesis. Images, illustrations, figures, tables etc., used in the thesis from other sources, have also been duly cited and acknowledged.


5/1/24

Neethi Raveendran


05/01/24

Dr. Vijayakumar C.

(Supervisor)

STATEMENTS OF ACADEMIC INTEGRITY

I, Neethi Raveendran, a Ph.D. student of the Academy of Scientific and Innovative Research (AcSIR) with Registration No. 10CC19A39015 hereby undertake that, the thesis entitled "*Thiophene-Based Organic Thermoelectric Materials: Exploring Molecular Design, Doping Techniques and Nanocomposite Formations*" has been prepared by me and that the document reports original work carried out by me and is free of any plagiarism in compliance with the UGC Regulations on "*Promotion of Academic Integrity and Prevention of Plagiarism in Higher Educational Institutions (2018)*" and the CSIR Guidelines for "*Ethics in Research and in Governance (2020)*".

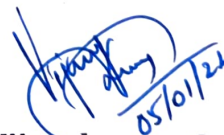


Neethi Raveendran

January 05, 2024

Thiruvananthapuram

It is hereby certified that the work done by the student, under my supervision, is plagiarism-free in accordance with the UGC Regulations on "*Promotion of Academic Integrity and Prevention of Plagiarism in Higher Educational Institutions (2018)*" and the CSIR Guidelines for "*Ethics in Research and in Governance (2020)*".



Dr. Vijayakumar C.

January 05, 2024

Thiruvananthapuram

DECLARATION

I, Neethi Raveendran, AcSIR Registration No. 10CC19A39015 declare that my thesis entitled, "***Thiophene-Based Organic Thermoelectric Materials: Exploring Molecular Design, Doping Techniques and Nanocomposite Formations***" is plagiarism-free in accordance with the UGC Regulations on "*Promotion of Academic Integrity and Prevention of Plagiarism in Higher Educational Institutions (2018)*" and the CSIR Guidelines for "*Ethics in Research and in Governance (2020)*".

I would be solely held responsible if any plagiarised content in my thesis is detected, which is violative of the UGC regulations 2018.

Handwritten signature in blue ink, consisting of a stylized 'N' followed by 'R' and the date '5/1/24' written below it.

Neethi Raveendran

January 05, 2024

Thiruvananthapuram

ACKNOWLEDGEMENTS

I express profound gratitude and high regard to Dr. Vijayakumar C., my thesis supervisor, for proposing the research topic and providing inspirational guidance, concern, support, and encouragement, ultimately contributing to the successful completion of this thesis work.

I extend my gratitude to Dr. C. Anandharamakrishnan, the Director, and Dr. A. Ajayaghosh, the former Director of the CSIR-National Institute for Interdisciplinary Science and Technology, for providing the essential facilities required to conduct this research.

I sincerely acknowledge Dr. C. H. Suresh, Dr. V. Karunakaran, and Dr. Jayamurthy P., former and present AcSIR coordinators, CSIR-NIIST for the timely help and advice for the academic procedures of AcSIR.

I am very much thankful to Dr. Narayanan Unni K. N. and Dr. Joshy Joseph, my Doctoral Advisory Committee (DAC) members, for their help, suggestions and encouragement throughout my PhD period. I extend my special thanks to Dr. Biswapriya Deb, my DAC member, for assisting me in grasping the fundamental concepts related to my research topic.

I would like to express my gratitude to Dr. K. V. Radhakrishnan, Dr. P. Sujatha Devi, and Dr. R. Luxmi Varma present and former Heads, Chemical Sciences and Technology Division for their unwavering support.

I express my gratitude to all the faculty members of AcSIR at CSIR-NIIST for their assistance and support throughout the duration of the coursework.

I would like to thank Dr. Mangalam S. Nair, Dr. K. R. Gopidas, Dr. V. K. Praveen, Dr. Suraj Soman, Dr. Sreejith Sankar, Dr. Ishita Neogi, Dr. Jubi John, Dr. Adersh Asok, Dr. Sunil Varughese, Dr. Bhoje Gowd E., Dr. Saju Pillai, Dr. K. Yoosaf, and Dr. Bijitha Balan, present and former, and all other scientists of the NIIST, for all the help and support extended to me.

I would like to acknowledge Prof. Akinori Saeki (Osaka University) for the PYS measurement, Dr. Pongsakorn Kanjanaboos (Mahidol University) for the conducting AFM analysis, Dr. C. P. Vinod and Mr. Deo Shrinivas (CSIR- NCL) for the UPS measurement, Dr. S. N. Potty and Mr. Pravin Kadhane (C-MET) for the Hall-effect

measurement studies, Mr. Gajender Saini (IITB) for the GIXRD measurement, and Mr. Vishnu P. (CLIF, Kerala University) for the UV-Vis-NIR measurement.

I would also like to thank Mr. Robert Philip, Mr. Nithin and Ms. Viji for the general help, Mr. Peer Mohammed for XPS analysis, Mr. Harish Raj for SEM analysis, Mr. Amal Raj for XRD analysis, Mr. Kiran Mohan for TEM analysis, Mr. Merin Santhosh and Ms. Aswathy C. S. for AcSIR related formalities.

I am grateful to my present and former labmates Susanna Poulouse, Dr. Dheepika R., Amarjith V. Dev, Avija A. V., Navin Jacob, Riya Martin, Nishana K., Dr. Suresh Kumar G. S., Dr. Naeem K. C., Dr. Tanwistha Ghosh, Dr. Jayanthi S Panicker, Dr. Chinnadurai M., Dr. John Paul K. P., Christy Prasad, Nayana Krishna, Manesh Mohan, Abhijith S., Neethu M., Devika S., and Inayathullah for their love, care and support throughout my research period. I also thank M. Sc. project students Sruthi M. K., Shafvan Basheer Ahamed, Raghi K. S. for all the help and love.

Words are inadequate to express my gratitude to Dr. Vijitha I., Dr. Indulekha M., Dr. Shibna B., Sheba, Nishna, Vibhu Darshan, Vijayakumar S., Anagha Thomas, Pavithra V. Prabhu, Anjali Sajeev, Dr. Anjali B. R., my dear friends of CSTD for their care, love, support, and encouragement, which made my life in NIIST memorable. I also thank all the present and former members of the CSTD and friends at other Divisions of CSIR-NIIST for their help and cooperation.

I owe an eternal debt of gratitude to my Papa, Amma, my sister Neetu and brother Pradeep, my nephew Dhruv, my in-laws and other family members for their enduring energy, unconditional love, and constant support that have been invaluable throughout my life. I am forever indebted to my other half Preeth and my little one Jaanvi for their patience, understanding, constant motivation, love, and incredible support. I also wish to express my gratitude and extend my appreciation to all my teachers for their invaluable assistance and blessings.

Finally, I sincerely thank Council of Scientific & Industrial Research (CSIR) SRF and Gas Authority of India Ltd. (GAIL) for financial assistance.

Above all, I express gratitude to the omnipotent force for providing me with strength during challenging moments.

Neethi Raveendran

TABLE OF CONTENTS

Certificate		i
Statements of Academic Integrity		ii
Declaration		iii
Acknowledgments		iv
Table of Contents		vi
List of Abbreviations		ix
Preface		xii
CHAPTER 1	An Overview of Organic Thermoelectrics: Materials, Devices and Applications	1-54
1.1	Abstract	1
1.2	Introduction	2
1.2.1	Thermoelectric effect	3
1.2.2	Thermoelectric parameters and efficiency	4
1.2.3	Design of a thermoelectric generator	7
1.3	Organic thermoelectric materials	9
1.3.1	Molecular structure engineering	10
1.3.1.1	Backbone engineering	12
1.3.1.2	Heteroatom effect	14
1.3.1.3	Side-chain effect	15
1.3.1.4	Energy level regulation	17
1.3.1.5	Molecular packing	19
1.3.2	Doping	20
1.3.2.1	Acid-base doping	22
1.3.2.2	Redox doping	25
1.3.2.3	Doping-induced structural modifications	29
1.3.2.4	Dopant: semiconductor processing approaches	30
1.3.3	Composite formation with nanostructured carbon nanomaterials	34
1.3.3.1	Compositing methods	35
1.3.3.2	Interfacial energy filtering effect	39
1.3.3.3	Reducing thermal conductivity	41
1.3.3.4	Interfacial phonon scattering	43
1.4	Organic thermoelectric generators	44

1.5	Objective of the present investigation	47
1.6	References	48
CHAPTER 2	Influence of Molecular Structure on Doping Efficiency and Fermi Level Alignment in Self-Assembled Thiophene Derivatives	55-98
2.1	Abstract	55
2.2	Introduction	56
2.3	Results and discussion	65
2.3.1	Optical and electronic properties	66
2.3.2	Doping of the organic small molecules	67
2.3.3	Doping-related charge transfer states	71
2.3.4	Thermoelectric properties	73
2.3.5	Charge carrier mobility	77
2.3.6	Surface morphology	78
2.3.7	XPS valence band spectra	81
2.3.8	Thermal stability	85
2.4	Conclusions	88
2.5	Experimental section	89
2.5.1	Materials and methods	89
2.6	References	92
CHAPTER 3	Enhancing Thermoelectric Efficiency in Benzodithiophene-Thienothiophene Copolymers: The Role of Doping-Induced Charge Transfer	99-140
3.1	Abstract	99
3.2	Introduction	100
3.3	Results and discussion	110
3.3.1	Doping of the polymers	111
3.3.2	Doping signatures through UPS spectroscopy	113
3.3.3	Thermoelectric properties	115
3.3.4	Degree of charge transfer	118
3.3.5	X-ray photoelectron spectroscopy	120
3.3.6	Molecular ordering of the polymer thin films	124
3.3.7	Aggregation of the polymers	128
3.3.8	Current mapping	131
3.4	Conclusions	132
3.5	Experimental section	133
3.5.1	Materials and methods	133
3.6	References	136

CHAPTER 4	Enhanced Thermoelectric Properties of Thiophene Based Small Molecule/SWCNT Composites Through Supramolecular Functionalization	141-182
4.1	Abstract	141
4.2	Introduction	142
4.3	Results and discussion	150
4.3.1	Photophysical properties	151
4.3.2	Thermal stability	153
4.3.3	Wide angle X-ray scattering	154
4.3.4	Raman spectroscopy	155
4.3.5	Microstructural analysis	156
4.3.6	Thermoelectric properties	161
4.3.7	Temperature dependent thermoelectric properties	164
4.3.8	Energy level estimation	167
4.3.9	Fabrication of thermoelectric generator	169
4.3.10	Performance of the TEG	170
4.3.11	Flexibility of the TEG	171
4.4	Conclusions	172
4.5	Experimental section	173
4.5.1	Materials and methods	173
4.5.2	Synthesis and characterization	176
4.6	References	180
	Abstract of the Thesis	183
	List of Publications	185
	List of Patents	186
	List of Posters Presented in Conference	187

LIST OF ABBREVIATIONS

Å	Angstrom
α	Seebeck coefficient
κ	Thermal conductivity
σ	Electrical conductivity
μ	Carrier mobility
n	Charge carrier density
q	Elementary charge
ΔS	Entropy
AFM	Atomic force microscopy
Sb ₂ Te ₃	Antimony telluride
Bi ₂ Te ₃	Bismuth telluride
BDT	Benzo-[1,2-b:4,5-b']dithiophene
BDD	Benzodithiophene-dione
BTBT	Benzothienobenzothiophene
BE	Binding energy
CNT	Carbon nanotube
CaH ₂	Calcium hydride
CPD	Contact potential difference
CTC	Charge transfer complex
C-AFM	Conductive atomic force microscopy
CuPc	Copper phthalocyanine
CN6-CP	Hexacyano-trimethylene-cyclopropane
C ₆₀	Fullerene
CsCO ₃	Cesium carbonate
CDT-BTZ	Poly[2,1,3-benzothiadiazole-4,7-diyl(4,4-dihexadecyl-4H-cyclopenta[2,1-b:3,4-b']dithiophene-2,6-diyl)]
DOS	Density of states
DETA	Diethylenetriamine
DOVS	Density of valence state
DPP	Diketopyrrolopyrrole
DC	Direct current
EA	Electron affinity
EDX	Energy dispersive X-ray spectroscopy
EBSA	4-ethylbenzenesulfonic acid
EDOT	3,4-ethylenedioxythiophene
E_F	Fermi energy level
eV	Electron volt
FET	Field-effect transistor
FTS	Tridecafluoro-1,1,2,2-tetrahydrooctyl)trichlorosilane

FeCl ₃	Ferric chloride
F4TCNQ	2,3,5,6-Tetrafluoro-7,7,8,8-tetracyanoquinodimethane
FFT	Fast Fourier transform
GIXRD	Grazing incidence X-ray diffraction
<i>h</i>	Planck's constant
HRTEM	High-resolution transmission electron microscopy
HOMO	Highest occupied molecular orbit
HAT6	2,3,6,7,10,11-hexakis(hexyloxy)triphenylene
ICT	Integer charge transfer
IoT	Internet of things
IE	Ionization energy
<i>k_B</i>	Boltzmann constant
KE	Kinetic energy
KP	Kelvin probe
<i>L</i>	Lorenz factor
LUMO	Lowest occupied molecular orbit
ME	Mobility edge
MWCNT	Multi-walled carbon nanotube
MSeNPs	Metal selenide nanoparticles
NIR	Near infra-red
N-DMBI	4-(2,3-Dihydro-1,3-dimethyl-1H-benzimidazol-2-yl)-N,N-dimethylbenzenamine
NOPF ₆	Nitrosonium hexafluorophosphate
OTE	Organic thermoelectrics
OFET	Organic field-effect transistors
OSC	Organic semiconductors
PCT	Partial charge transfer
PA	Polyaniline
PBTTT	Poly(2,5-bis(3-alkylthiophen-2-yl)-thieno-[3,2-b]thiophene)
PBDTTT-C	poly[[4,8-bis-(2-ethylhexyloxy)-benzo(1,2-b:4,5-b')dithiophene]-2,6-diyl-alt-(4-(2-ethylhexanoyl)-thieno[3,4-b]thiophene)-2,6-diyl]
PBDTTT-C-T	Poly[[4,8-bis[5-(2-ethylhexyl)-2-thienyl]benzo[1,2-b:4,5-b']dithiophene-2,6-diyl][2-(2-ethyl-1-oxohexyl)thieno[3,4-b]thiophenediyl]]
PBDTTT-FTTE	Poly[4,8-bis(5-(2-ethylhexyl)thiophen-2-yl)benzo[1,2-b:4,5-b']dithiophene-2,6-diyl-alt-(4-(2-ethylhexyl)-3-fluorothieno[3,4-b]thiophene)-2-carboxylate-2,6-diyl]
PPy	Polypyrrole
PANI	Polyaniline
PEDOT	Poly 3,4-ethylenedioxythiophene
PSS	Poly(4-styrenesulfonate)
PTh	Polythiophene

PF	Power factor
PDI	Perylene diimide
QE	Quenching efficiency
SEM	Scanning electron microscopy
SWCNT	Single-walled carbon nanotube
SPS	Spark plasma sintering
TE	Thermoelectrics
TEG	Thermoelectric generator
TEC	Thermoelectric cooler
TEM	Transmission electron microscopy
TGA	Thermogravimetric analysis
TTE	Thienothiophene
TFSI	Tri[bis(trifluoromethane)sulfonimide
UPS	Ultra-violet photoelectron spectroscopy
UV	Ultra-violet
VB	Valence band
VBM	Valence band maxima
VRH	Variable range hopping
WAXS	Wide-angle X-ray scattering
WF	Work function
XPS	X-ray photoelectron spectroscopy
ZnPc	Zinc phthalocyanine
ZT	Figure of merit

PREFACE

The rising prominence of renewable energy sources, compelled by dwindling fossil fuel reserves, climate change, and pervasive energy waste, has necessitated innovative methods of energy capture. An estimated 67% of primary energy is currently lost as heat, underscoring the importance of technologies that can harness this waste heat for electricity production. Thermoelectric generators (TEGs) are increasingly seen as viable solutions to energy wastage, given their sustainability. As solid-state devices, TEGs convert heat into electricity utilizing the Seebeck effect, thereby promoting efficient waste heat harvesting from a plethora of sources. These sources range from thermal and nuclear power plants to automotive exhausts, incinerators, and industrial wastewater. Further, electricity can also be generated from unconventional sources like solar and geothermal energy, and even the human body. TEGs offer significant advantages, including noise-free operation, extended lifespan, the absence of moving parts, and impressive scalability. However, despite their potential, the current reliance on traditional, costly materials for the construction of TEGs poses a significant challenge to their economic feasibility. The material cost forms a sizable barrier to widespread adoption and usage. This challenge emphasizes the necessity of developing new, cost-effective materials as a crucial part of ongoing thermoelectric (TE) research.

Organic small molecules and polymers are well-suited candidates in converting low-grade heat (less than 232°C) into electricity due to their flexibility, low thermal conductivity, and the ability to tune their electronic properties through chemical modification, making them ideal for efficient waste heat harvesting. Organic TE materials also have the potential for scalability and compatibility with printed flexible devices, thereby increasing their utility. These advantages streamline the creation of personal, portable, and flexible TE modules. Nevertheless, a significant drawback of organic semiconductors is their modest electrical conductivity, curtailing their practical applicability. The performance of organic TE materials can be significantly enhanced through a variety of methods. This thesis aims to explore strategies focused on improving the performance of organic TE materials, specifically through molecular engineering, chemical doping, and the formation of organic/inorganic nanocomposites. All these modifications can meaningfully increase the charge carrier mobility, and consequently, the TE performance.

The thesis is divided into four chapters. The first chapter introduces the fundamental concepts of thermoelectrics and deeply elucidates the factors impacting charge transport properties. It also provides a comprehensive overview of organic thermoelectrics, discussing the current state-of-the-art materials. Additionally, it delves into various strategies to enhance the TE efficiency of selected organic-based TE systems in detail.

Chapter 2 details our investigation into the impact of slight molecular structure modifications on the TE characteristics of two thiophene-based small molecules (OT1 and OT2). The molecules only differ in their end substitutions with varying acceptor strengths, leading to distinct self-assembled morphologies. OT2, when doped with FeCl₃, demonstrated high electrical conductivity and a power factor of 52.0 $\mu\text{Wm}^{-1}\text{K}^{-2}$. In contrast, OT1 under identical conditions, presented significantly lower conductivity and a power factor of 1.6 $\mu\text{Wm}^{-1}\text{K}^{-2}$. The higher doping efficiency in OT2 can be attributed to the weaker acceptor strength of its end group. Enhanced charge carrier transport in OT2 was facilitated by a low-lying highest occupied molecular orbital (HOMO) energy level and an increased density of states around the HOMO post-doping. The maintenance of self-assembly after doping also proved crucial for improved electrical properties. These findings underscore the significance of molecular engineering in the development of high-performance TE materials.

Chapter 3 delves into our examination of the TE properties of two donor-acceptor polymers, PBDTTT:C (P1) and PBDTTT:EFT (P2), doped with F4TCNQ. These polymers, comprised of benzodithiophene (BDT) as the donor and thienothiophene (TT) as the acceptor, differ in their alkyl side chains. Our investigations revealed diverse charge transfer states arising from variations in polymer aggregation upon the addition of F4TCNQ. This variation prompted further exploration of the polymers' aggregation behavior. In P2, aggregation in the solution state encouraged the formation of ion pairs with F4TCNQ through integer charge transfer (ICT), enhancing the doping efficiency. Conversely, in P1, the formation of P1-F4TCNQ charge transfer complexes via partial charge transfer resulted in a non-aggregated state, leading to lower doping efficiency. The presence of ICT states in P2-F4TCNQ culminated in superior TE performance, reaching 73.10 $\mu\text{Wm}^{-1}\text{K}^{-2}$. These findings suggest that the rational molecular design of polymers can be employed to develop high-performing organic TE materials.

The last chapter focuses on the synthesis of a semiconducting thiophene-based organic small molecule (OTF) and its interaction with SWCNT. We introduced an effective solution-based method to disperse and debundle the SWCNT by incorporating OTF, resulting in a nanocomposite material. This process of efficient debundling, paired with the charge transfer between the two components, resulted in improved TE performance. The interfacial energy filtering effect between OTF and SWCNT boosted the power factor, achieving $124 \mu\text{Wm}^{-1}\text{K}^{-2}$ at room temperature and $215 \mu\text{Wm}^{-1}\text{K}^{-2}$ at $100 \text{ }^\circ\text{C}$. A flexible TEG was constructed, with seven legs of the composite serving as the active material and silver electrodes as the interconnects. These devices demonstrated exceptional flexibility, producing a power output of 150 nW (@ $\Delta T=100 \text{ K}$). The composite material displayed a Fermi energy level closer to that of the electrode, which significantly reduced the Schottky energy barrier, enabling free flow of charge carriers.

Chapter 1

An Overview of Organic Thermoelectrics: Materials, Devices and Applications

1.1. Abstract

Organic thermoelectrics is emerging as a significant area in energy conversion, offering unique benefits over traditional inorganic thermoelectrics. Organic thermoelectric materials are known for their cost-effectiveness, easy processing, and high flexibility. They exhibit molecular diversity and flexible mechanical properties, often outperforming inorganic counterparts. Their lightweight nature and ease of processing make them ideal for various applications. Notably, organic thermoelectrics are effective in waste heat harvesting for electricity, portable power generation, and in creating energy-efficient electronic devices. Their low thermal conductivity, coupled with the capacity to form large, flexible, and lightweight modules, results in enhanced thermoelectric performance. Additionally, their non-toxic and environmentally friendly characteristics position them as a promising direction for sustainable energy conversion technologies. This chapter provides an overview of the fundamentals of thermoelectrics, strategies to improve material efficiency, and the latest progress in organic thermoelectric technology.

1.2. Introduction

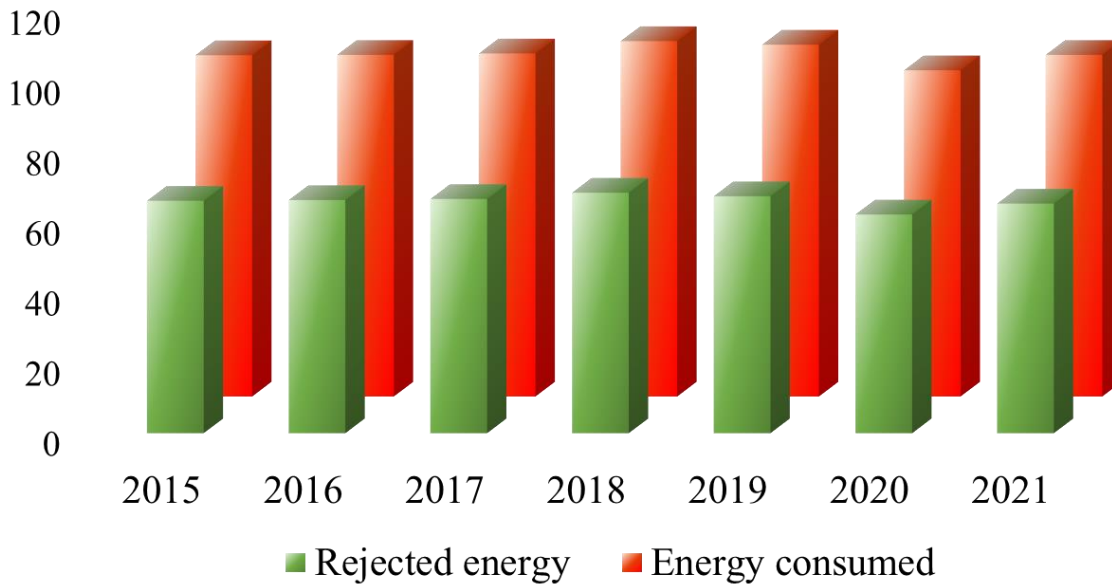


Figure 1.1. Energy consumption reported by Lawrence Livermore National Laboratory. (Adapted from reference 2)

Global energy demand has been steadily increasing and is projected to remain a critical issue in the coming decade.^[1] This rise is driven by factors such as growing world population, economic development, urbanization, industrialization, and the widespread use of electronic devices. Addressing this surging demand is crucial, especially considering environmental concerns like fossil fuel depletion and global climate change. The Lawrence Livermore National Laboratory in the United States reports that both renewable and non-renewable energy sources contribute to total energy consumption, with approximately 60% being lost as rejected energy, as shown in **Figure 1.1.**^[2] A significant portion of this wasted energy is in form of heat. Although some heat loss in certain sectors is inevitable, it can be mitigated through improved

equipment efficiency or by employing technology that recover waste heat. In this context, thermoelectric generators (TEGs) present a viable solution for reducing energy waste.^[3] TEGs are designed to deliver silent, long-lasting conversion without the need of moving parts.^[3-4] The major advantages of TEGs include harvesting thermal energy from various sources like thermal and nuclear power plants, automotive exhausts, incinerators, hot water released from industries, motor vehicles and other industrial sectors. Additionally, TEGs can generate energy from sources like solar, geothermal and human body.^[3,5]

1.2.1. Thermoelectric effect

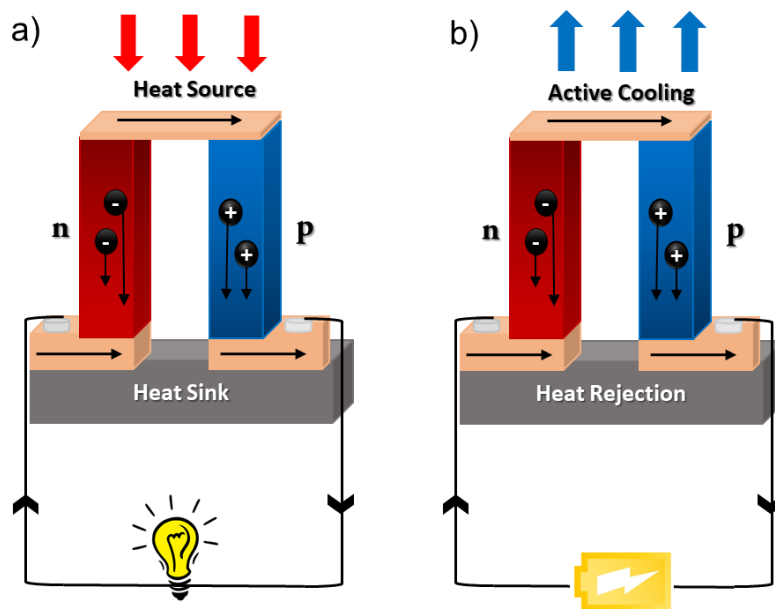


Figure 1.2. Schematic illustration of a) Seebeck effect, b) Peltier effect. (Adapted from reference 6)

TEGs directly convert heat into electrical energy through the Seebeck effect. This phenomenon occurs when a temperature gradient across thermoelectric (TE) materials

creates a potential difference, causing charge carriers to move from the hotter to the cooler area.^[6] Complementing TEGs are thermoelectric coolers (TECs), which operate based on the Peltier effect. This is essentially the reverse of the Seebeck effect, where passing an electrical current through a junction of two different materials results in the absorption or release of heat at the junction, depending on the direction of the current.^[7] A typical TEG is composed of two TE materials, the n-type and p-type semiconductors (also known as legs), arranged both electrically in series and thermally in parallel as shown in **Figure 1.2**. In other words, the n-type and p-type materials are connected end to end, forming thermocouples. This forms a series electrical connection which is necessary to maintain a continuous path for the flow of charge carriers (electrons and holes) when a temperature gradient is applied. On the other hand, these thermocouples are aligned side by side between a hot and a cold plate, creating a parallel thermal connection. This arrangement ensures that each thermocouple experiences the same temperature difference between its hot and cold junctions, allowing for the efficient generation of electrical power from the temperature gradient.

1.2.2. Thermoelectric parameters and efficiency

The energy conversion efficiency of TEGs depends on the material properties and its performance can be determined by a dimensionless quantity named as Figure-of-Merit, ZT .^[8] It is expressed as;

$$ZT = \frac{\alpha^2 \sigma T}{k} \quad (1.1)$$

where α is the Seebeck coefficient, σ is the electrical conductivity, T is the absolute temperature and κ , the thermal conductivity. The performance can also be denoted in terms of power factor (PF);

$$PF = \alpha^2 \sigma \quad (1.2)$$

The product of α^2 and σ is denoted as thermoelectric power factor. An ideal TE material should possess excellent σ to reduce Joule heating, minimal κ to prevent thermal loss, and a high α for efficient heat-to-electricity conversion or electricity-to-cooling conversion.^[4,9]

Electrical conductivity is often related to the carrier concentration by the Drude's relationship as follows;

$$\sigma = nq\mu \quad (1.3)$$

where q is the carrier charge, n gives the charge carrier density, and μ is the carrier mobility.

To assure a significant α value, it is vital to have a single type of charge carrier. Due to their intrinsically low carrier concentration, insulators and semiconductors have large α . In the case of metals and degenerate semiconductors, the Seebeck coefficient is dependent on n through Mott's relation;

$$\alpha = \frac{8\pi^2 k_B^2}{3eh^2} m^* T \left(\frac{\pi}{3n} \right)^{2/3} \quad (1.4)$$

where k_B is the Boltzmann constant, h is the Planck's constant and m^* is the effective mass of the carriers.^[10] When the sign of α is positive, holes are the most prevalent

carriers of the TE material, and the TE material is p-type. When the α value of the TE material is negative, it indicates that the principal charge transport is through electrons and that the material exhibits n-type behaviour. Since Seebeck coefficient has an inverse relationship with n , increasing n value increases the σ and hence decreases the α . Due to this trade-off relationship, which is being considered as a major limitation, there should be an optimal n where proper balancing on σ and α occurs and therefore resulting in an increased PF. Decoupling the σ - α relationship is therefore considered challenging to obtain high performing TE materials.^[9-10]

In order to maximize the ZT , a low κ is required. κ of a material can be separated into electronic (κ_e) and lattice (κ_L) contributions.

$$\kappa = \kappa_e + \kappa_L \quad (1.5)$$

κ_e arises from the movement of charge carriers, such as electrons, in the material. In conductive materials like metals, electrons can easily move through the lattice, resulting in high κ_e .^[11] However, in insulators or semiconductors, the movement of charge carriers is restricted, leading to a lower κ_e .

κ_e can be defined using Wiedemann–Franz law as;

$$\kappa_e = L\sigma T \quad (1.6)$$

where L corresponds to the Lorenz factor.

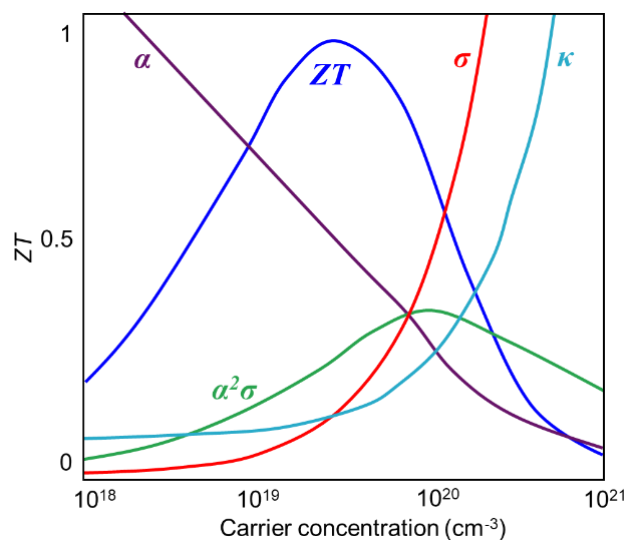


Figure 1.3. Enhancing ZT through tuning of carrier concentration. (Adapted from reference 12)

The energy conversion efficiency associated with any TE material is strongly determined by the electronic as well as thermal properties. In order to maximize σ and minimize κ , the material should exhibit a ‘phonon glass-electron crystal’ like behavior. The peak performance in TE materials is observed within a range of carrier concentrations spanning from 10^{19} to 10^{21} cm^{-3} as highlighted in **Figure 1.3**.^[12] Thus, heavily doped semiconductors are the favoured category of materials for TE, given their ability to operate optimally within this specified carrier concentration range.

1.2.3. Design of a thermoelectric generator

A typical TEG comprises of thermoelectric couples (legs) having p-type legs (free holes) and n-type legs (electrons) connected electrically in series connection and thermally in parallel arrangement. In order to power an electric load through the circuit,

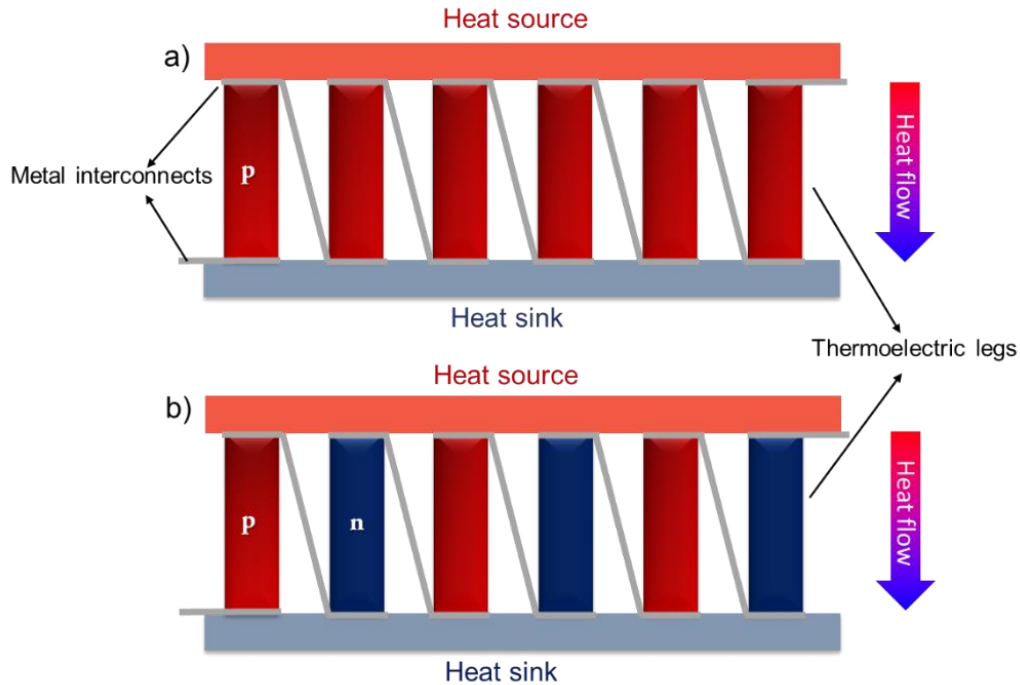


Figure 1.4. Schematic representation of planar a) p-only and b) p-n junction TEG. (Adapted from reference 12)

a TEG uses heat flow across a temperature gradient. In a TEG, the power output is determined by the electrical current, which is driven by the voltage generated through the Seebeck effect due to the temperature difference across the thermoelectric material.

Figure 1.4 shows the representation of a typical TEG with a) p legs and b) p-n legs connected in series *via* metallic interconnects. In a Peltier cooler, an external DC power supply provides the electric current that flows through the device. This current utilizes the Peltier effect to absorb heat from the top surface of the cooler, thereby chilling it. The absorbed heat is then released at the opposite surface of the device. Both devices require a heat sink to remove the heat that is rejected.

1.3. Organic thermoelectric materials

Initially, research in TE primarily focused on inorganic materials but has since expanded to include both hybrid and fully organic materials. Conventional TE materials largely depend on tellurides and selenides, such as Bi_2Te_3 , Sb_2Te_3 , SnSe , along with similar alloys.^[6] Notably, SnSe has attracted great scientific attention due to its low κ and achieved a remarkable ZT of 2.6 at 923 K, as reported by Kanatzidis *et al.*^[13] Moreover, heavily doped $\text{PbTe}_{1-x}\text{Se}_x$ reported by Snyder *et al.* achieved a ZT as high as 1.8 at 850 K through careful tuning of doping levels and composition adjustments.^[14] While these materials have found widespread application in TEGs, they often face challenges such as potential toxicity, limited availability, complex fabrication processes, and scalability issues. Additionally, majority of these inorganic TE materials reach peak performance only at high temperatures (>500 K). This characteristic limits their suitability for harvesting low-grade waste heat (<500 K), which constitutes over 50% of the total available waste heat. Moreover, materials like Bi_2Te_3 , which are currently utilized for room temperature applications, are being outperformed by some of the OSCs that have surpassed its ZT through tailored molecular design and optimized charge transport properties. This advancement has led to the emergence of organic thermoelectric (OTE) materials as a specialized area within TE research, offering promising alternatives for efficiently utilizing low-grade waste heat.^[15]

In contrast to their inorganic counterparts, OTE materials offer advantages such as lower κ , facile solution-based processing, scalability, and adaptability to printed

flexible devices.^[10,16-17] The literature reports on OTE primarily constitutes highly conductive doped polyacetylenes (PA), first generation of conjugated polymers like PPy, PANI, PEDOT, and PTh. Coordination polymers and small organic molecules represent another category of OTE materials.^[18] Small organic molecules offer distinct advantages compared to polymers. They are relatively easy to synthesize and provides better reproducibility when generating multiple batches of the material, possess low κ , maximizes ZT .

Several approaches are employed in the design, synthesis, and analysis of structure-property relationships in both polymers and small molecules to develop high-performance TE materials. Significant advancements have been made through molecular design, doping techniques, variations in alkyl chains, hybridization with carbon-based materials like carbon nanotubes and graphene, as well as the incorporation of inorganic materials into organic matrices. These developments have led to improvements in σ and the precise control of n . This section will focus on recent research progress in OTE materials, particularly polymers and small molecules, exploring strategies to enhance the TE efficiency. This discussion aims to offer new insights into elucidating the structure-property relationships crucial for the development of high-performance OTE materials.

1.3.1. Molecular structure engineering

The optimization of the host molecular structure is crucial for enhancing the TE properties of a material. π -conjugated systems are characterized by a series of alternate

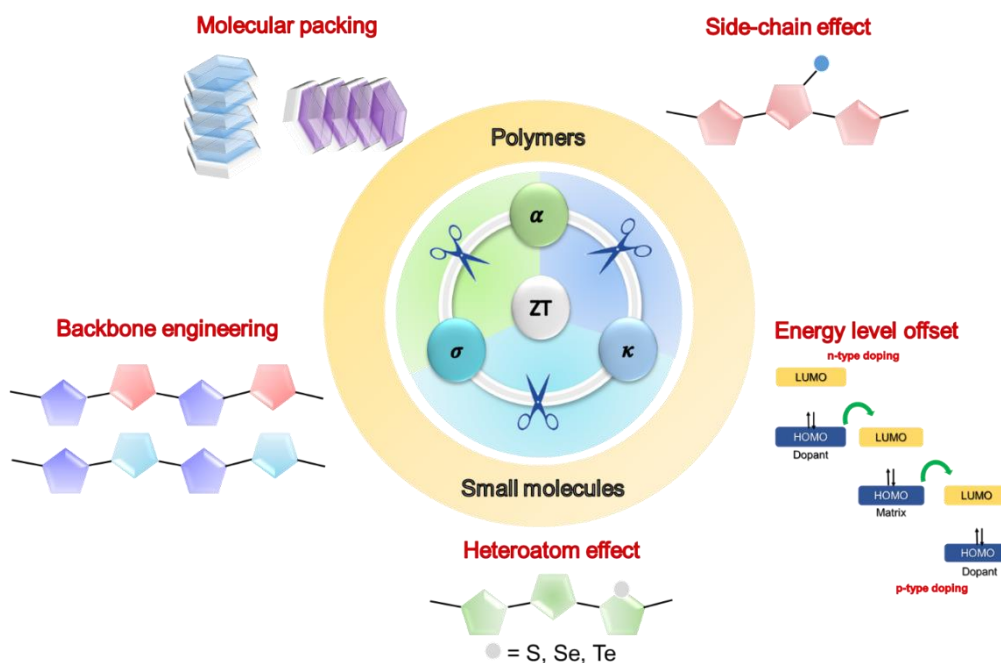


Figure 1.5. Optimization strategies involved in maximizing TE efficiency.

single and multiple bonds between carbon atoms, creating a pathway for delocalized π electrons to move freely along the conjugated structure. The presence of a large π -conjugated structure is therefore essential for providing electrical conductivity to these materials.^[19] Electrical conductivity can be further tailored by modifying the morphology, stacking, and defect sites of the materials.^[20] Optimization strategies often involve designing and synthesizing materials at the molecular level or introducing dopants to modify the electronic and phononic properties of the host material.^[4,21] In this section, we discuss some of the aspects aligned with the structural modifications which include backbone engineering, heteroatom effect, side-chain alteration, achieving favorable energy level offset, and appropriate molecular packing for optimization of the TE properties of organic materials (**Figure 1.5**).

1.3.1.1. Backbone engineering

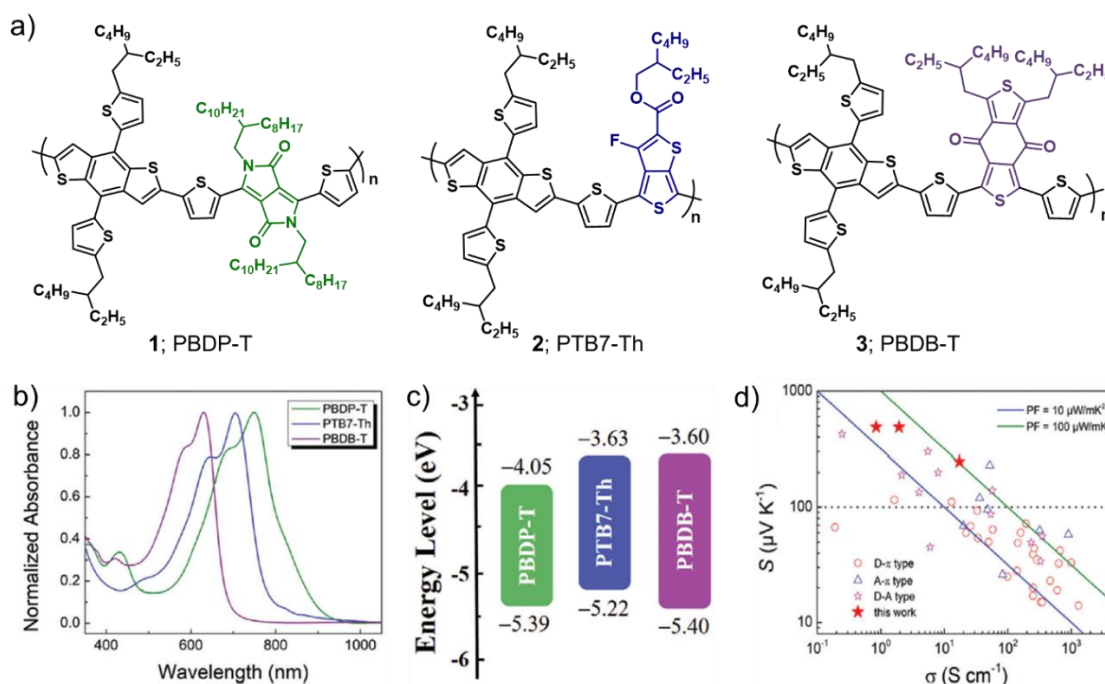


Figure 1.6. a) Molecular structures of D-A copolymers **1**, **2** and **3**, b) UV-Vis-NIR absorption spectra, c) Corresponding energy levels, d) TE performance comparison with different p-type polymers. (Adapted from reference 22)

The backbone of a polymer or small molecule, essentially its central structure, greatly influences its electronic characteristics. By manipulating this backbone structure, scientists can precisely control aspects like energy band gaps, electron affinity, and electrical conductivity, which are critical for the material's performance in specific applications. In the area of electronic and optoelectronic applications, such modifications can lead to materials that exhibit enhanced charge transport, better light absorption, or improved energy transfer efficiency. In energy-related applications, particularly thermoelectrics, the backbone design is instrumental in defining the

Seebeck coefficient and electrical conductivity of the material.^[21] By carefully designing the molecular backbone, researchers can create materials that efficiently convert temperature differences into electrical energy, which is central to the functioning of TEGs. This ability to tailor-make materials with specific electronic properties opens up avenues for more efficient, flexible, and lightweight thermoelectric devices, which can be utilized in a variety of settings, ranging from industrial waste heat recovery to powering wearable electronics.

Tang *et al.* reported a few donor–acceptor (D–A) copolymers with benzodithiophene (BDT) as the donor core and varying acceptor units like diketopyrrolopyrrole (DPP), thieno[3,4-*b*]thiophene (TT), and benzodithiophene-dione (BDD) (**1**; PBDP-T, **2**; PTB7-Th, **3**; PBDB-T, **Figure 1.6**).^[22] They studied the structure-property relationship between the TE properties of the copolymers with the electron-withdrawing ability of the acceptor units. The relatively shallower Lowest unoccupied molecular orbital (LUMO) energy level of **3** compared to **1** and **2** may be attributed to the absence of π -unit thiophenes in the backbone. Thiophenes can also act as donors despite having less effective electron donors, therefore this would somewhat increase the average electron-donating capacity of D units. Due to the significantly better charge transfer and higher carrier density after p-doping with FeCl₃, σ was improved with a decrease in the electron-withdrawing ability of the A units. The copolymer **3** displays a peak PF of 105.5 $\mu\text{Wm}^{-1}\text{K}^{-2}$ at room temperature and a highest carrier mobility of 0.046 $\text{cm}^2\text{V}^{-1}\text{s}^{-1}$.

1.3.1.2. Heteroatom effect

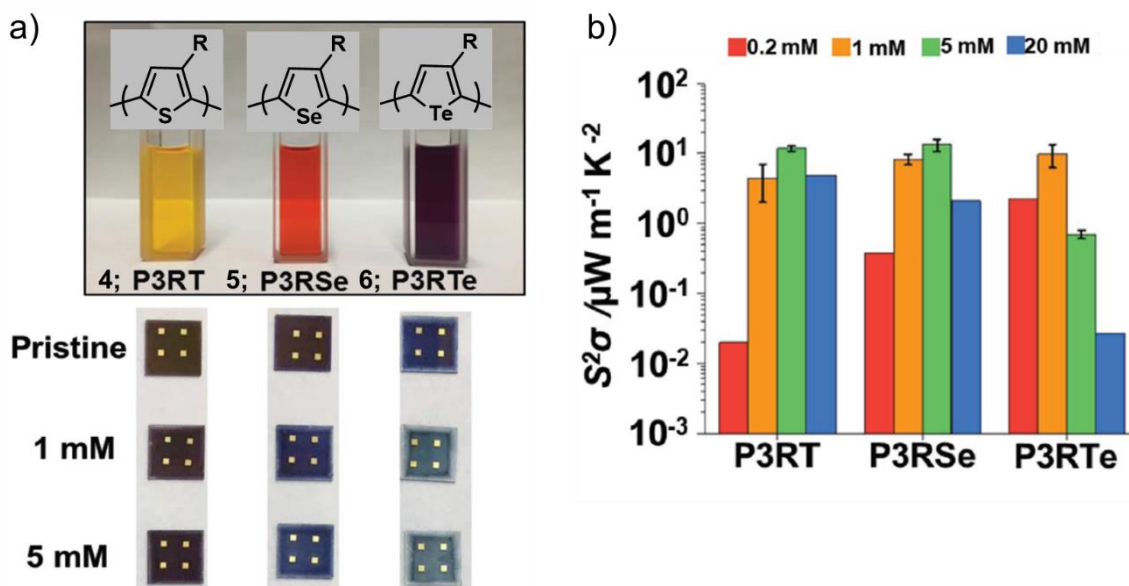


Figure 1.7. a) Chemical structures of poly(3-alkylchalcogenophenes) **4**, **5** and **6**, b) Power factors on doping with different concentration of FeCl_3 . (Adapted from reference 26)

Although early molecular design research seemed to concentrate on finding new molecular backbones or changing functional groups, studies that maintain the fundamental molecular structure framework but altering the chemical properties by changing the heteroatoms have recently received attention. Heteroatom substitutions in organic semiconductors (OSCs) are often expected to result in denser chain packing, stronger molecular interactions, and more appropriate energy levels, all of which will alter the carrier mobility of the organic semiconductors.^[25] Gregory *et al.* reported the TE properties of poly(3-alkylchalcogenophene) thin films with varying the heteroatoms like sulphur (**4**; P3RT), selenium (**5**; P3RSe), and tellurium (**6**; P3RTe) as shown in **Figure 1.7a**.^[26] The TE properties were tuned by doping with FeCl_3 . On changing the

atom from S to Te, the bandgap reduces and energy states moves closer to the chemical potential. This results in an overall decrease in α with a substantial increase in σ . Therefore, **5** and **6** may attain PF of over $10 \mu\text{Wm}^{-1}\text{K}^{-2}$ at low dopant concentrations (**Figure 1.7b**), which is equivalent to heavily doped polythiophenes.

1.3.1.3. Side-chain effect

The π -conjugated backbones of OTE materials are fundamental to their functionality, as they directly influence charge transfer efficiency. These backbones provide a pathway for delocalized electrons, facilitating efficient charge transport which is critical for the material's TE performance. On the other hand, alkyl side chains, typically attached to the π -conjugated backbone, play multiple roles beyond merely solubilizing the material.^[27] These side chains significantly impact the molecular packing within the material, influencing the overall crystallinity and thereby affecting charge transport properties. The length, shape, and polarity of these side chains are vital factors that determine the solubility and overall charge transport efficiency of the polymer. Longer alkyl chains might increase solubility but can also lead to a more amorphous material, which might reduce charge mobility. Conversely, shorter chains might enhance packing but reduce solubility, demonstrating the balance needed in designing these materials.^[28]

Side-chain engineering is critical in controlling the interaction with dopants. Properly designed side chains can facilitate better dispersion of dopants within the semiconductor matrix, leading to more uniform doping and enhanced electrical conductivity. However, in some cases, the presence of bulky or inappropriate side

chains can hinder this dispersion, leading to inhomogeneities and reduced performance. Researchers are continuously exploring different side-chain architectures to optimize this aspect, considering factors like branching, length, and functional groups to achieve a balance between solubility, dopant dispersion, and efficient charge transport. The interaction between alkyl side chains and the π -conjugated backbone also affects the overall morphology and thermoelectric properties of the material. The torsional angle between the backbone and side chains, for instance, can influence the planarity of the molecule, thus affecting the π - π stacking and, subsequently, the electronic properties. Researchers are leveraging advanced synthesis techniques and computational modeling to understand and optimize these interactions, leading to a new generation of OTE materials with improved performance and application potential.

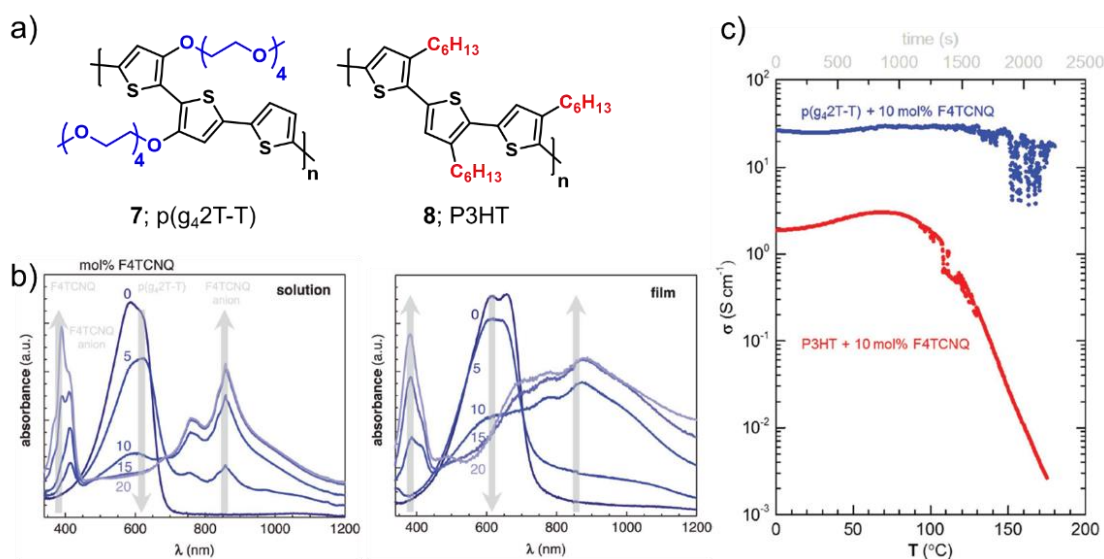


Figure 1.8. a) Molecular structures of 7 and 8, b) UV-Vis-NIR absorption spectra on varying F4TCNQ concentration in solution and film state, c) σ plot at 10 mol% F4TCNQ. (Adapted from reference 27)

Kroon *et al.* conducted an in-depth analysis of the TE properties of **7**; p(g42T-T) and **8**; P3HT (**Figure 1.8**) where **7** has oligoethylene glycol and **8** has hexylthiophene as the alkyl side-chain.^[27] The glycolic side chains assists the molecular doping of polythiophene. The essential role played by polar side chains is that they facilitates the coprocessing of the polymer with the dopants from a solution without the risk of precipitation. This allows for improved solubility and that leads to a homogeneous distribution of the dopant throughout the polymer matrix when the solution is cast as a thin film. High σ of 100 Scm^{-1} could be achieved for **7** on doping with 10 mol% F4TCNQ.

1.3.1.4. Energy level regulation

Regulating energy levels is a crucial aspect in improving the TE performance of materials. By precisely engineering the energy levels, we can enhance α and reduce κ at the same time.^[28] To enhance σ , OSC materials require doping, which involves the transportation of electrons between dopants and semiconductor molecules. The main factor that affects the TE characteristics is the position of the Fermi level (E_F) with respect to the highest occupied molecular orbital (HOMO) and LUMO.^[29] When α is positive, the transport is primarily done by holes that go through the HOMO level. When α is negative, transport is done by electrons that passes through the LUMO level. In OSC materials, α is related to the energy difference between the transmission energy level (E_T) and the Fermi level (E_F);

$$\alpha = \frac{k}{q} \left(\frac{E_T - E_F}{kT} + A \right) \quad (1.7)$$

where k is the Boltzmann constant, T is the absolute temperature, q is the unit charge, and A denotes a dimensionless numerical factor.

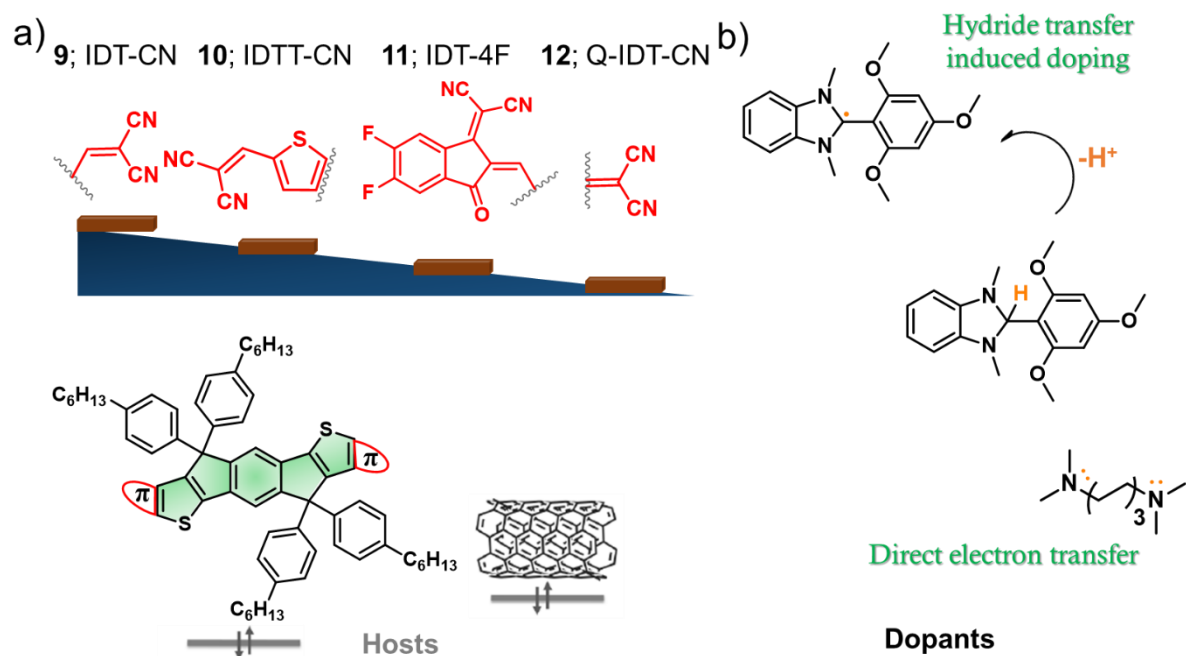


Figure 1.9. a) Molecular structures and energy level offsets of **9**, **10**, **11** and **12** with respect to SWCNT. b) Hydride and direct electron transfer mechanism. (Adapted from reference 30)

Yin *et al.* reported few indaceno dithiophene (IDT) cored OSCs (**9**; IDT-CN, **10**; IDTT-CN, **11**; IDT-4F, **12**; Q-IDT-CN) as shown in **Figure 1.9**.^[30] The OSCs have slight changes in the LUMO levels and that results in synchronously lowered energy bandgaps. The n-doping process was easier with progressive lowering of the bandgaps. Here, the doping levels can be controlled by host-dopant synergism, hence delivering varied TE performances for IDT-single walled carbon nanotube (SWCNT) hybrids ranging from PF of $1.3 \mu\text{Wm}^{-1}\text{K}^{-2}$ to $159.6 \pm 1.4 \mu\text{Wm}^{-1}\text{K}^{-2}$.

1.3.1.5. Molecular packing

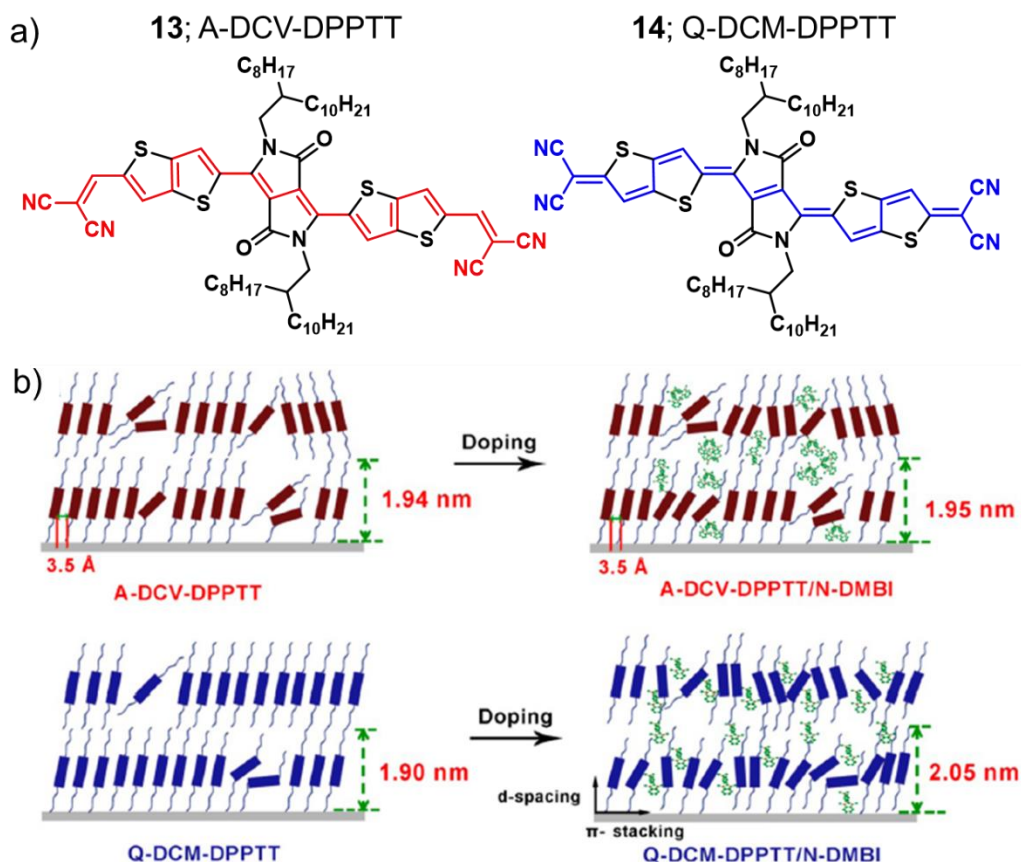


Figure 1.10. a) Molecular structures of **13** and **14**, b) Schematic representation of the molecular packing before and after doping with N-DMBI. (Adapted from reference 33)

The morphology and microstructure created by conjugated molecules have a direct impact on the efficiency of carrier transport between those molecules. In the context of OSCs, the transfer of charges between molecules is greatly affected by the thin film microstructure. When the molecules are packed in an orderly manner, it leads to higher carrier mobility and electrical conductivity.^[31] The presence of a disordered microstructure can lead to electron localization and trapping, which can reduce the

efficiency of carrier transport. Therefore, efficient carrier transport can often be achieved through a molecular packing structure that is highly organized.^[32]

Huang *et al.* developed two pyrrolo appended thieno-[3,2-b]thiophene derivatives (**13**; A-DCV-DPPTT, **14**; Q-DCM-DPPTT, **Figure 1.10**) with different conjugated structures.^[33] Owing to their different conjugated structures, they possess different morphology. The film formed by derivative **13** displays a polycrystalline nature with larger grain sizes and derivative **14** terraced surface with smaller grains were formed. The introduction of dopant N-DMBI on derivative **13** has restricted effect on the molecular packing as both the π - π stacking (3.50 Å) and the d-spacing distance (1.94 nm) remains unaltered on doping. Contrary to this, in case of derivative **14**, the d-spacing increases from 1.90 nm to 2.05 nm. Chemical doping of **14** led to a less ordered molecular packing and changed intermolecular stacking and this may result negatively in the charge transport property.

1.3.2. Doping

The charge carrier concentration (n) of a semiconductor material can be modulated or controlled through the addition of a dopant. This process is known as doping, and it is a fundamental technique used in semiconductor device fabrication to alter the electrical properties of the material.^[34-35] Doping in organic semiconductors can be achieved through two primary mechanisms: acid-base doping and redox doping.

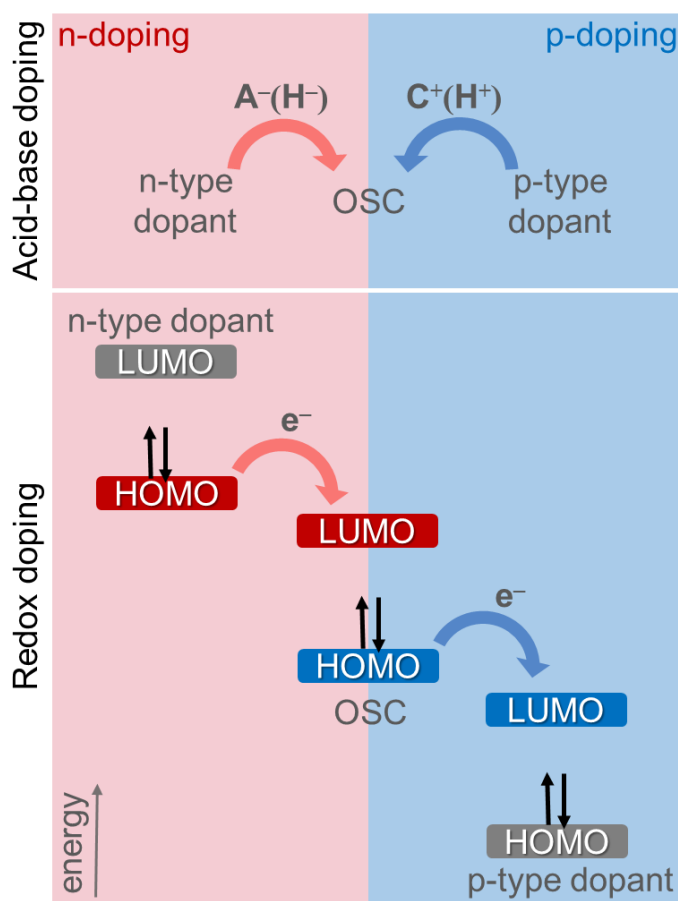


Figure 1.11. Illustration of the charge transfer process in acid-base and redox doping mechanisms. (Adapted from reference 34)

Acid-base doping involves the transfer of cations (positively charged ions) or anions (negatively charged ions) to the semiconductor backbone. This process modifies the charge density within the organic semiconductor.^[4,21] Redox doping, on the other hand, involves the transfer of electrons between the dopant and the semiconductor. This process results in a charge-transfer complex or ion pair between the semiconductor and the dopant. In redox doping, the dopant can either be an electron donor (reducing agent) or an electron acceptor (oxidizing agent).^[36,37] This choice of the dopant determines

whether the semiconductor becomes p-type (electron acceptor) or n-type (electron donor) doped.^[4,14] In the former context, the presence of a counterion ensures charge neutrality. Positive (radical cation) or negative (radical anion) polarons are produced when one electron is added or removed, or when an anion or cation is added. At higher doping levels, these polarons combine to generate bipolarons. The delocalization of polarons and bipolarons exists over a number of repeating units. The basic mechanism of acid-base doping and redox doping is represented schematically in **Figure 1.11**.

1.3.2.1. Acid-base doping

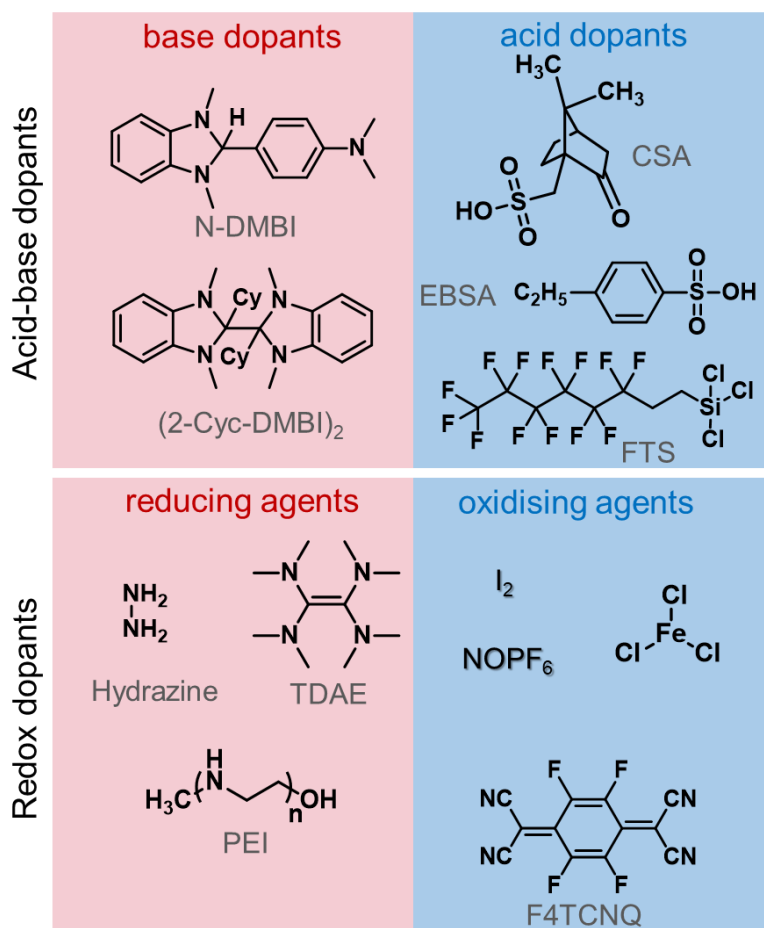


Figure 1.12. Acid-base and redox dopants in literature.

The transfer of a proton (H^+) to the conjugated backbone of an organic semiconductor is commonly referred to as acid doping and it results in a p-type material.^[38-39] Acid doping introduces positive charge carriers (holes) into the conjugated backbone, leading to an increase in positive charge density within the polymer and thereby enhancing its electrical conductivity. Some of the molecules that act as acid-base dopants are shown in **Figure 1.12**.

Patel *et al.* reported the acid doping of poly(2,5-bis(3-tetradecylthiophen-2-yl)thieno[3,2-b]thiophene) (**15**; PBTTT-C₁₄) by distinctly different dopants (EBSA, 4-ethylbenzenesulfonic acid, and (FTS, tridecafluoro-1,1,2,2-tetrahydrooctyl)trichlorosilane (**Figure 1.13**)).^[38] The differential TE properties of **15** on treatment with the dopants by two different methods like immersion in solvent (EBSA) and vapour doping (FTS) were examined. Thin films of **15** doped by EBSA are obtained conductive through protonation. EBSA anion acts as the counterion for maintaining the charge neutrality. FTS doping, on the other hand forms a thin layer over the layer of the OSC. Charge carriers are produced by the FTS layer on the polymer film's surface electrostatically doping from the permanent dipole or through protonic doping where partially cross-linked siloxane polymer is formed the acidic silanol groups from the self-polymerized FTS units. An overall PF of $110 \pm 34 \mu W m^{-1} K^{-2}$ is obtained for vapour FTS doped **15**.

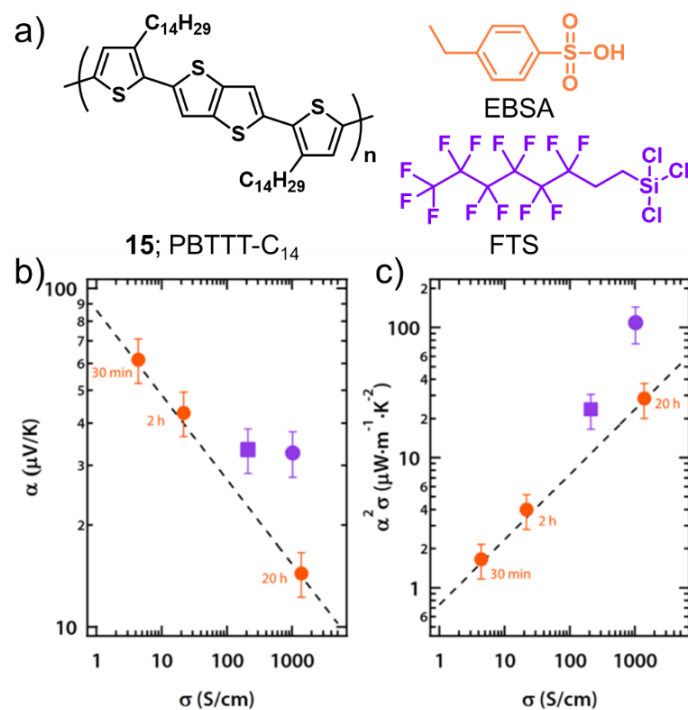


Figure 1.13. a) Chemical structures of **15**, dopants EBSA and FTS, b) Seebeck coefficient, c) Power factor v/s electrical conductivity on log scale (EBSA doping denoted by orange circles, FTS doping by purple). (Adapted from reference 38)

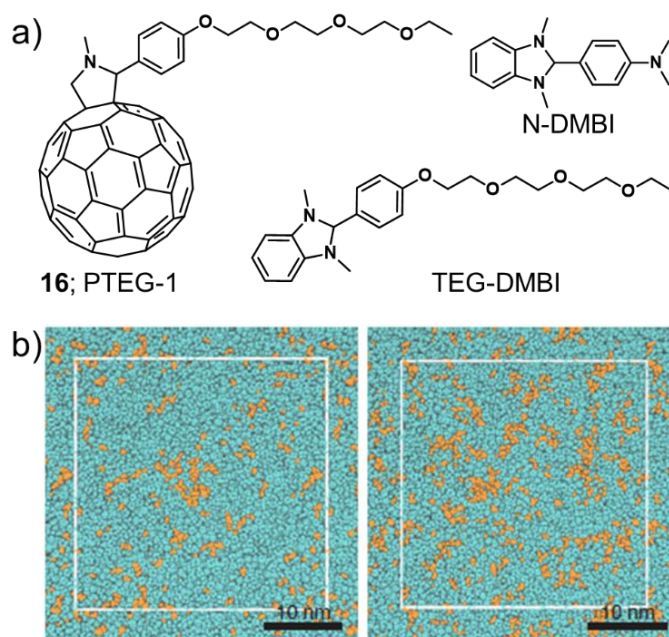


Figure 1.14. a) Chemical structures of **16**, dopants N-DMBI and TEG-DMBI, b) Coarse grain molecular dynamics simulation for N-DMBI doped and TEG-DMBI doped **16**. (Adapted from reference 42)

The n-doping of organic semiconductors occurs through hydride transfer (H^-). This is often called as base doping and results in an n-type material.^[40-41] Qui *et al.* introduced polar triethylene glycol (TEG) side chain into fullerene host (**16**) as well as the dopant molecule DMBI (**Figure 1.14**).^[42] Solution-processed films of **16** doped with TEG-DMBI offer a higher miscibility than films doped with commercially available N-DMBI. The surface of the doped films of **16** exhibits clear phase islands after mixing with dopants, but to varying degrees for N-DMBI and TEG-DMBI, respectively. As a result, achieving a doping efficiency of up to 18% at dopant concentrations of 20 mol% is realized, leading to elevated carrier density and μ , which is crucial for higher σ .

1.3.2.2. Redox doping

When an electron is transferred (fully or partially) from a donor to an acceptor molecule, an ion pair (integer charge transfer/ICT) or charge-transfer complex (partial charge transfer/PCT) is created. This process is known as redox doping.^[43] P-type doping occurs through the process of electron transfer from the HOMO of an organic semiconductor to the LUMO of the acceptor, while n-type doping involves the electron transfer from the HOMO of a donor to the LUMO of a semiconductor. Effective redox doping requires a slight offset in the energy levels of the HOMO and LUMO involved. The first known example of strong p-type redox doping is polyacetylene with iodine doping. Due to its poor environmental stability, other redox dopants like F4TCNQ, NOPF₆, FeCl₃ were explored later.^[24-25,44-45] Some of the molecules that act as redox dopants are shown earlier in **Figure 1.12**.

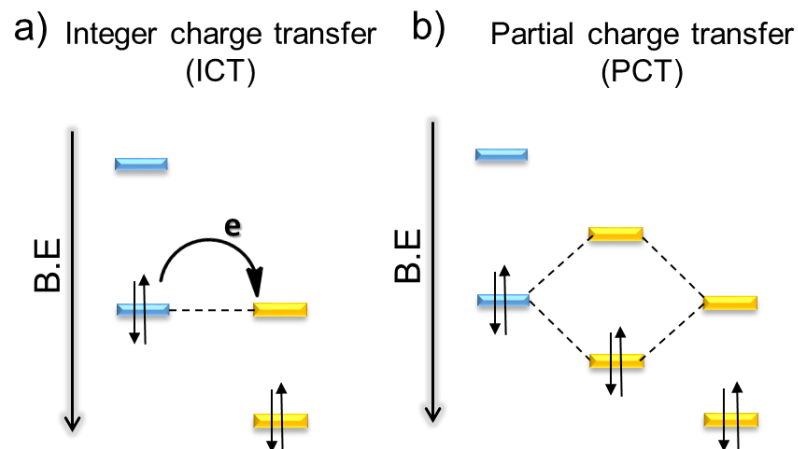


Figure 1.15. Integer charge transfer and partial charge transfer mechanism. (Adapted from reference 43)

Ion-pair formation (IPA) or Integer charge transfer (ICT):

The core assumption of ICT for the case of p-type doping is that one electron will be transferred if the acceptor's EA is higher than the OSC's IE or equal to it. This transfer of one electron will be facilitated from HOMO of OSC to LUMO of dopant which results in the formation of dopant anion and OSC cation which is called as the ion pair.^[46] For several OSCs, this has been demonstrated spectroscopically, primarily through the observation of the absorption features in the visible (electronic transitions) and infrared (vibrations).^[34,47] The schematic representation of mechanism of integer charge transfer is shown in **Figure 1.15a**.

Mendez *et al.* observed ICT as the fundamental charge transfer mechanism in case of a polythiophene polymer (**8**; P3HT) on doping with F4TCNQ (**Figure 1.16**).^[48] Formation of ICT is evidenced by the characteristic shift in the cyano vibrations of F4TCNQ in the Fourier transform infrared (FTIR) spectroscopy that indicates its fully

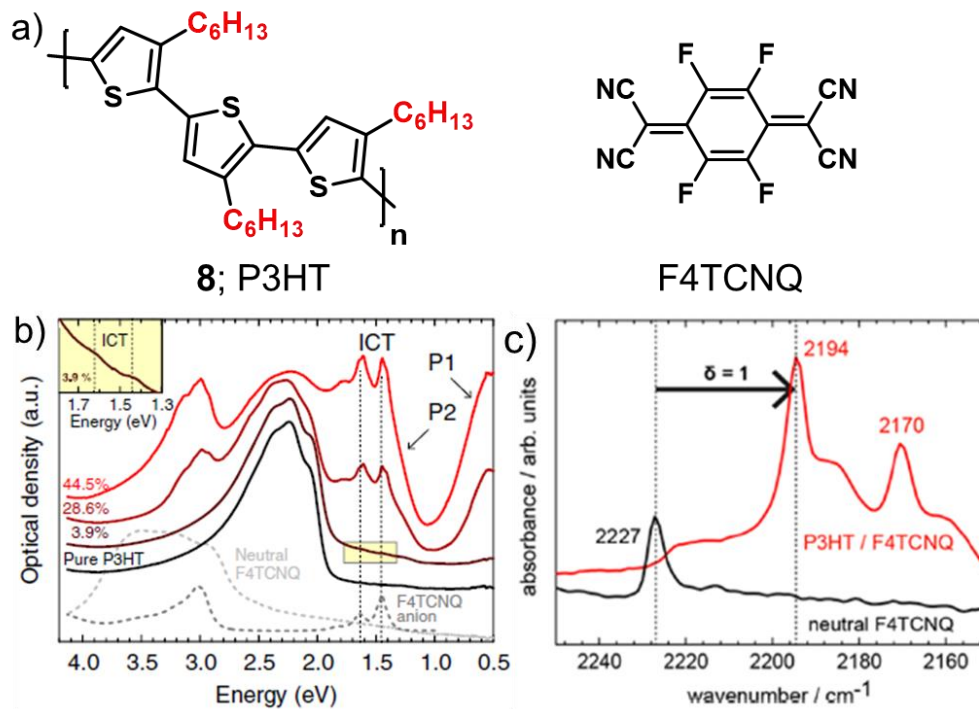


Figure 1.16. a) Chemical structure of **8** and F4TCNQ, Spectral signatures of Integer charge transfer b) UV-Vis-NIR absorption, c) FTIR absorption spectra of the cyano vibration. (Adapted from reference 48)

ionized state. The fully ionized species are also visible from the optical transitions which can be observed from the Ultraviolet-Visible-Near infrared (UV-Vis-NIR) absorption spectra. The presence of a mobile charge carrier or hole in the OSC matrix and a localized charge on the ionized dopant, such as a positive polaron (in case of p-type doping), are assumed to result through ground-state ICT. These results seem to indicate that quaterthiophenes (**17**; **Figure 1.16**) should display phenomenology that is quite similar to the parent polymer **8** after molecular doping with F4TCNQ. Unlike the parent polymer **8** where charge transfer occurs through ground-state ICT, **17** exhibited an alternate charge transfer mechanism.

Charge transfer complex (CPX) or Partial charge transfer (PCT):

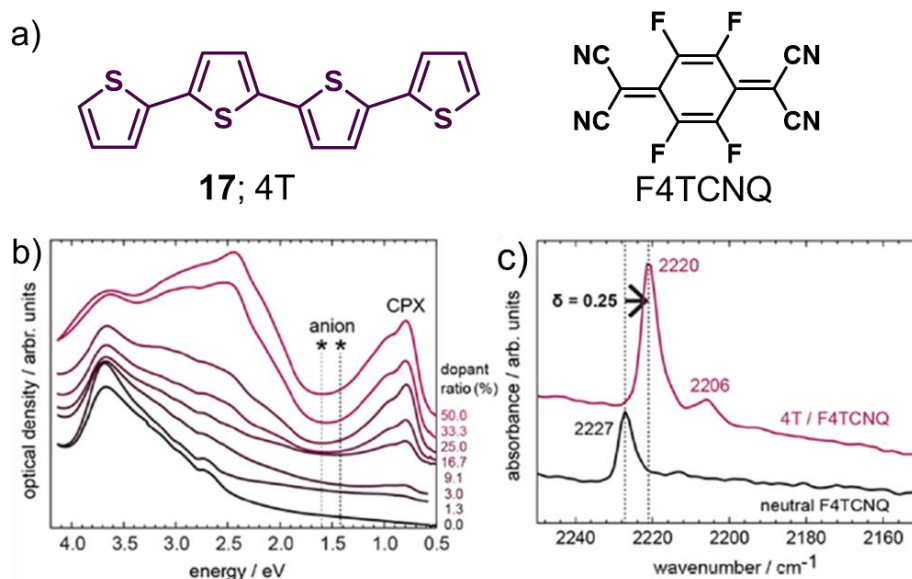


Figure 1.17. a) Chemical structure of **17** and F4TCNQ, Spectral signatures of partial charge transfer b) UV-Vis-NIR absorption, c) FTIR absorption spectra of the cyano vibration. (Adapted from reference 48)

The alternate mechanism of charge transfer between OSC and dopant is the formation of ground state charge transfer complex or partial charge transfer. This involves the hybridization of frontier molecular orbitals of the OSC and the dopant to form new set of occupied bonding and unoccupied antibonding orbitals.^[34,49-50] The amount of charge transfer can have non-integer values which can be determined by the relative amplitude of CPX's HOMO and LUMO with the parent molecules. The overall charge of the state is neutral. The schematic representation of mechanism of partial charge transfer is shown in **Figure 1.15b**.

Unlike the parent molecule which exhibited the formation of ionized species of F4TCNQ in the NIR region in UV-Vis-NIR absorption spectra, **17** (**Figure 1.17**) on

doping with F4TCNQ did not exhibit features of any ionized species of the dopant (**Figure 1.17**).^[48] The characteristic cyano vibrations exhibits only small shifts which corresponds to a partial charge transfer. When a dopant molecule like F4TCNQ is introduced into the OSC, its frontier molecular orbitals interact with that of the OSC. This interaction leads to mixing or hybridization of the orbitals and these new orbitals can be occupied (bonding) or empty (antibonding).

The energy of CTC's frontier levels are given by;

$$E_{CTC,H/L} = \frac{H_{OSC} + L_{dop}}{2} \pm \sqrt{(H_{OSC} - L_{dop})^2 + 4\beta^2} \quad (1.8)$$

and it depends on the HOMO energy level of OSC (H_{OSC}), the dopant LUMO energy level (L_{dop}), and the resonance integral β .^[34] Here, the H_{OSC} and L_{dop} do not necessarily need to be in resonance and that hybridization occurs when the EA of the dopant is higher or lower than the IE of the OSC in the case of p-type doping and *vice versa* in the case of n-type doping. Hence, it makes CTC formation unique and potentially important in cases where other types of molecular interactions, like ICT formation are not observed.

1.3.2.3. Doping-induced structural modifications

In doping organic semiconductors like polymers and small molecules, the dopant molecules can reach concentrations of up to several tens of mole percent.^[51] In contrast, when it comes to inorganic semiconductors, doping typically involves adding only a minute quantity of the dopant material. Due to the incorporation of such large amount

of dopant, there is a concomitant change occurring in the nanostructure of the OSC. Here, intercalation of the dopant molecules into the semiconductor chain is often caused.^[52] These structural changes can have a profound impact on the material's TE performance. Hence, doping has a substantial impact on the micro and nanostructure of the OSC, leading to significant changes in its electronic properties, including the density of states (DOS).^[26] These states can act as traps or recombination centers for charge carriers, hence influencing charge transport. The introduction of dopants can also shift the energy levels of the OSC's HOMO and LUMO, affecting the bandgap and overall electronic structure.^[31] Glaudell *et al.* studied the structural changes associated with P3HT and PBTTT-C₁₄.^[53] Solution doping with the small molecule tetrafluorotetracyanoquinodimethane (F4TCNQ) results in insertion of dopant molecules to the ordered regions of the polymer that results in disruption of the molecular packing. However, vapour deposition of the dopant alkyl silane (tridecafluoro-1,1,2,2,-tetrahydrooctyl)-trichlorosilane (FTS) results in the formation of a self-assembled monolayer over the polymer creating a surface dipole. Hence, FTS does not incorporate into the ordered crystalline domains as was seen with F4TCNQ doping, but it does produce a slight disruption of the crystallite size.

1.3.2.4. Dopant: Semiconductor processing approaches

Dopants play a crucial role in semiconductor processing, as they are used to modify the electrical properties of semiconductor materials by introducing foreign materials into the crystal lattice. These foreign materials can either add or remove electrons from

the semiconductor, creating n-type or p-type materials, respectively. Due to charge delocalization effects, space-filling, or planarization of the conjugated backbone, the amount of dopant, and its size might affect the host semiconductor's nanostructure.^[54] The doping technique determines the amount of dopant incorporated and how much control over the nanostructure may be achieved. The two major doping methods are co-processing and sequential processing.

Co-processing:

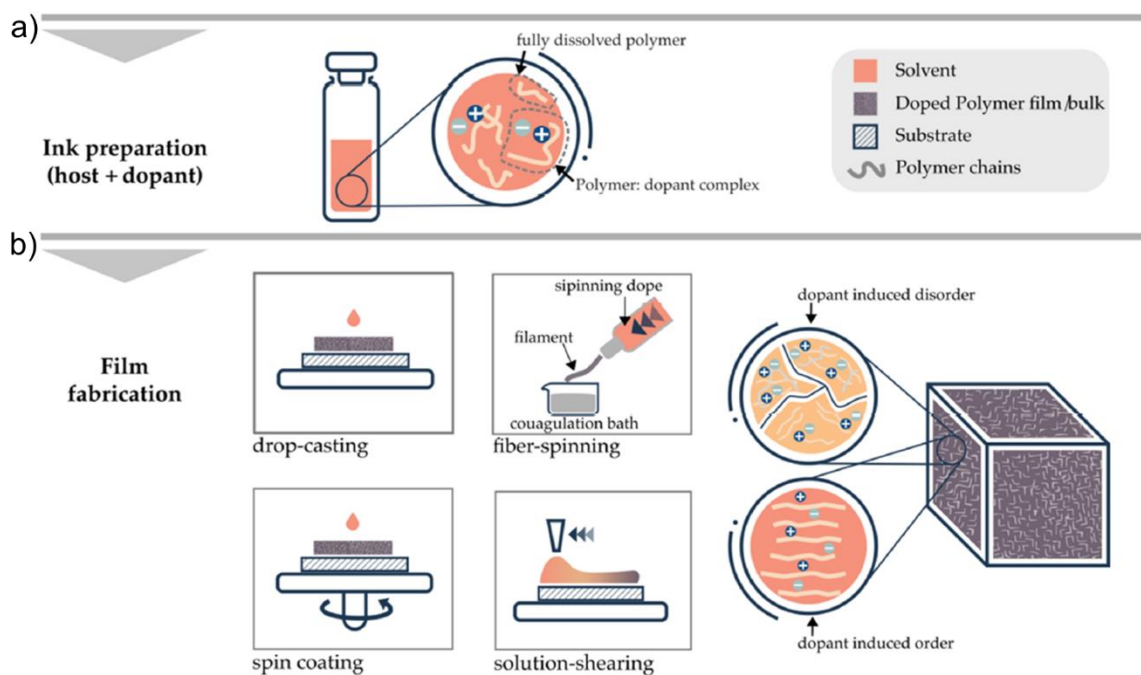


Figure 1.18. Schematic representation of a) co-processing of OSC host and dopant solution, b) film fabrication techniques. (Adapted from reference 54)

The simultaneous deposition of the semiconductor host and the dopant is referred to as co-processing, also known as codeposition. By dissolving both compounds in a

specific solvent system, this can be performed from solution by solution processing the resultant mixture (by, for example, spin coating, solution shearing, fiber spinning, or dropcasting) (**Figure 1.18**).^[54] This approach is used to incorporate dopant atoms directly into the semiconductor material while it is being formed, allowing for precise control over doping levels and uniformity. It often offers better control over the doping profile, reduces the number of post-processing techniques and gives an uniform dopant distribution. The energy levels of both host and dopant are in such a way that it interacts electronically and that it may lead to PCT states. As a result, aggregates, bimolecular crystals, and gels frequently occur.^[34] For instance, in the solid state, F4TCNQ and **17**; **17** create bimolecular crystals that have an effect on the degree of intermolecular hybridization between the host and dopant and only cause charge-transfer complexes or PCT.^[48] Codeposition can also result in phase separated domains when there is lack of miscibility in the binodal or spinodal decomposition. For example, co-processed films of **8** and F4TCNQ revealed strongly phase separated domains in atomic force microscopy (AFM), even at extremely low levels of dopant.^[34]

Sequential processing:

In the sequential processing method, the dopant is incorporated onto a host semiconductor film which is already present (**Figure 1.19**). The host material is either casted from a solution or vapour deposited onto a substrate or casted as a free standing film.^[54] In certain cases, additional efforts are made to enhance the microstructure of the OSC's in order to maximize charge transport. Among these procedures are either

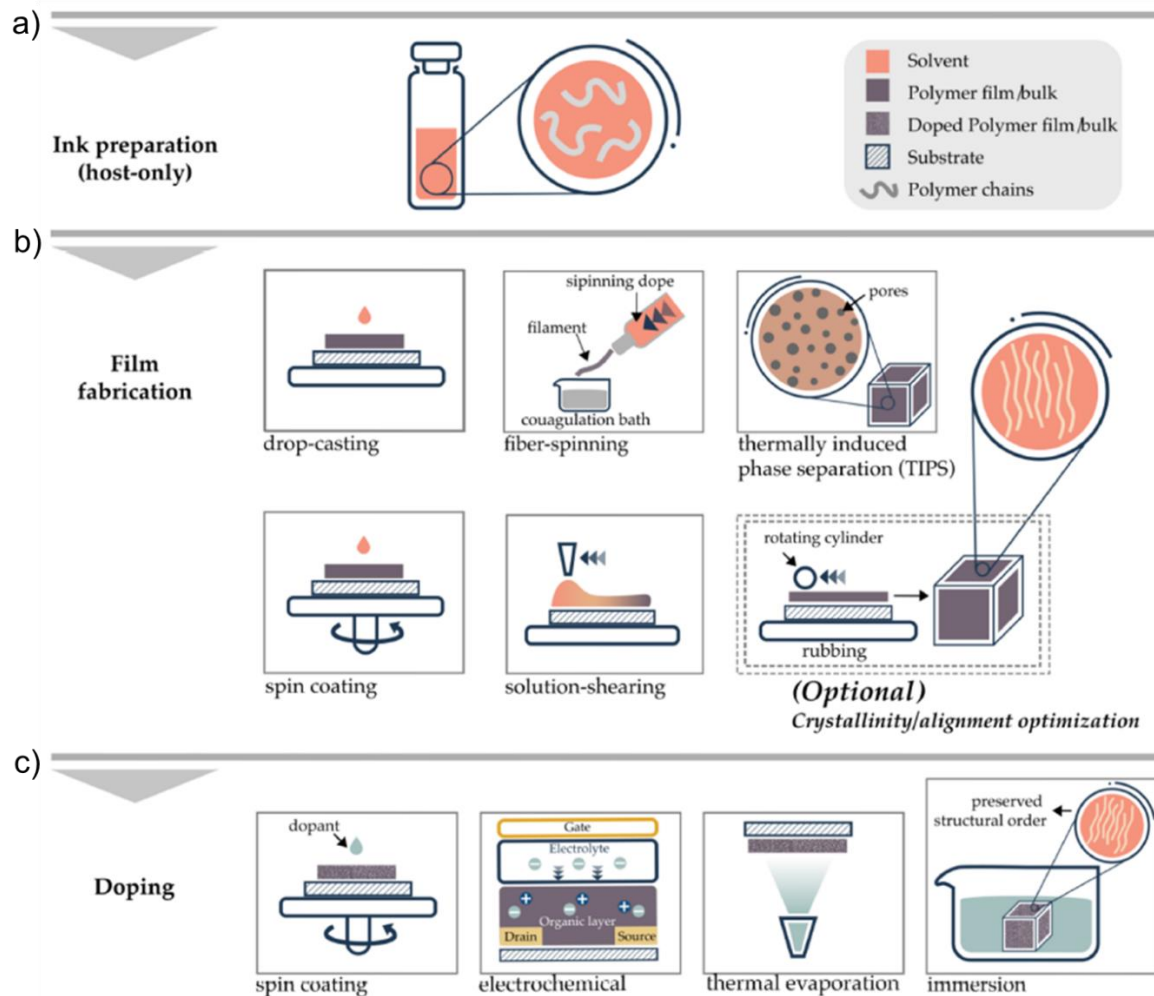


Figure 1.19. Schematic representation of a) sequential processing of OSC host and dopant solution, b) film fabrication techniques, c) doping techniques. (Adapted from reference 54)

enhancing crystallinity through thermal or vapour annealing, as well as increasing molecular alignment through processes like stretching or rubbing, among others.^[55] The subsequent phase involves the process of doping, which is a commonly employed technique accomplished through electrochemical means or the deposition of molecular dopants from solution, such as *via* spin coating, immersion, or thermal evaporation

methods. Reversing the order of the deposition technique is also possible in case of thermal evaporation methods.

The electrochemical oxidation of semicrystalline **8** leads to an initial localization of holes within the crystalline segments of the polymer. A comparable distribution of charge and counterions is observed during the sequential p-doping of conjugated polymers. When the dopant F4TCNQ is selectively introduced into the amorphous sections of regioregular **8**, it results in an augmentation of the conjugation within these amorphous polymer chains.^[56] However, processes involving doping through solution or vapour are not without their associated difficulties and complexities.^[57] The diffusion of dopants is constrained by the thickness of the material, and the uniformity of doping throughout the entire material is dependent upon factors such as the thickness and porosity of the host film, along with the diffusion coefficient of the dopant. Hence, vapour-based doping presents a substantial limitation for applications like TE, where the necessity for materials with thicknesses ranging from micrometers to millimeters that is capable of sustaining substantial thermal gradients becomes a critical factor.

1.3.3. Composite formation with nanostructured carbon nanomaterials

Nanostructured carbon allotropes are inexpensive and environmentally benign materials that come in a variety of shapes and sizes, including fullerene, carbon nanotubes (CNTs), graphene, and graphite.^[58] Incorporating carbon allotropes with organic thermoelectric materials can successfully improve the σ of the organic material and hence an improved TE performance.^[59] The probable decoupling between the

electronic transport properties, σ and α , has been shown by the nanocarbon-based thermoelectric composites.^[60] The thermal conductivity of the composites of carbon allotropes is low which is a result of significant phonon scattering at the interfaces.^[61] But, careful control over the compositing level of carbon allotrope-organic semiconductor is also necessary. Also, achieving a balance between the electrical and thermal properties, as well as ensuring good dispersion of these carbon allotropes within the composite matrix are critical considerations.^[59,62]

1.3.3.1. Compositing methods

The compositing methods between carbon allotropes (such as graphene or carbon nanotubes) and other semiconductor materials (such as polymers or small molecules) can be categorized into two: ex situ and in situ compositing.

Ex situ compositing:

Ex situ compositing techniques use external forces to directly and uniformly combine organic semiconductors with carbon allotropes. These methods typically rely on mechanical mixing or other physical techniques to ensure a uniform dispersion of carbon allotropes within the TE matrix. Ex situ compositing methods can be further classified into two subcategories based on the nature of the processes involved: solid-state-based methods and solution-based methods.^[63] Solid-state-based methods include mechanical mixing which involves physically blending carbon allotropes and the semiconductor material in a solid-state form. External forces are applied to ensure a

uniform dispersion. Common techniques include ball milling and attrition milling.^[64] The next method is hot pressing where the mixture is pressed under high temperature and pressure conditions. This process can lead to the sintering of the composite, creating strong bonds between the components. Spark plasma sintering (SPS) is also carried out to create dense and well-bonded composites. It involves the application of pulsed DC currents and external pressure to sinter the composite materials at high temperatures.

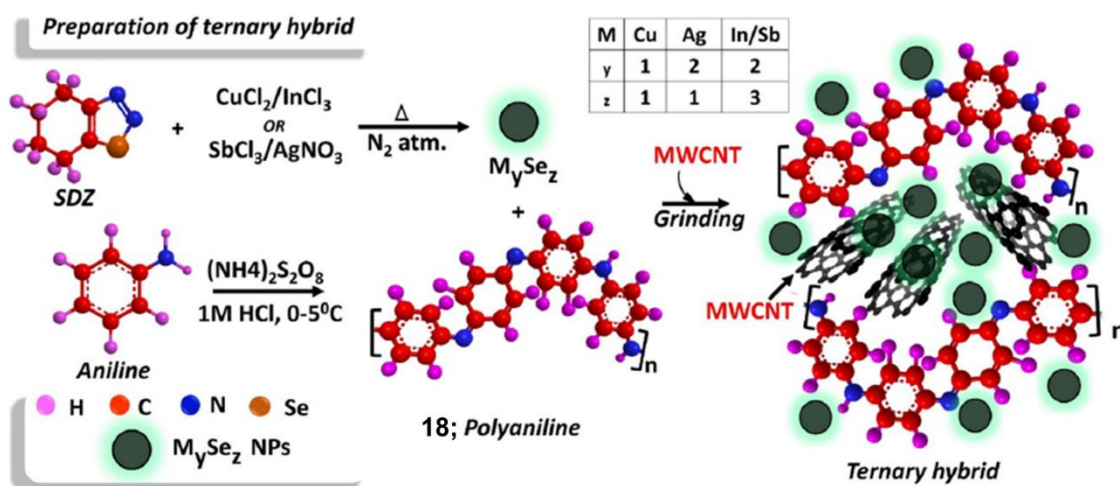


Figure 1.20. Schematic representation of ex situ compositing of **18**, MWCNT, and metal selenide nanoparticles (MSeNPs). (Adapted from reference 65)

Khanna and co-workers reported ex situ synthesis of a ternary composite which includes multiwalled carbon nanotubes (MWCNT) as the carbon allotrope, OSC (**18**; PANI) along with metal selenide nanoparticles (MSeNPs) like selenides of Cu, Ag, In, and Sb (**Figure 1.20**).^[65] The as-synthesized MSeNPs which were used as fillers are incorporated with MWCNT and **18** for the ternary hybrid synthesis. They are homogeneously mixed by mechanically grinding using a mortar and pestle. The

inorganic fillers acts like energy filters and further enhances the TE performance of the ternary composites when compared to the binary composites.

Solution-based methods includes solution mixing and deposition. In this method, the mixture is dispersed in a solution, often with the help of solvents or surfactants. This solution is then deposited or coated onto a substrate or matrix to create the composite. The techniques used for the deposition or coating include spin coating, dip coating, and inkjet printing. Another process called chemical precipitation is also used for composite preparation where nanoscale particles or precursors are formed in a solution containing the mixture and which is further processed for preparing the composite. Alternate mechanisms like electrodeposition techniques are used to deposit both the OSC material and carbon allotropes onto a substrate. This method is commonly used for thin-film composites.

In situ compositing:

In in situ composite processes, the achievement of uniform composites during crystal growth or polymerization frequently relies on exploiting relatively weak chemical bonding or interactions between carbon allotropes and other atoms or molecules.^[66] This approach allows for the simultaneous formation of the composite material with intimate mixing at the atomic or molecular level. Chemical vapour deposition (CVD) is a commonly employed in situ technique where a carbon source gas is introduced into a reactor along with other precursor gases that contain the atoms or molecules of the TE material.^[67] With appropriate temperature and pressure conditions, simultaneous

growth of the composite material takes place. In some cases, epitaxial growth occurs where the allotropes of carbon align their crystal lattice with that of the semiconductor due to van der Waals forces or other interactions. Surface functionalization of carbon allotropes is the most commonly adopted in situ method wherein the functional groups or molecules that have affinity for both carbon and the semiconductor can be introduced, facilitating better adhesion and interaction between the components.^[68]

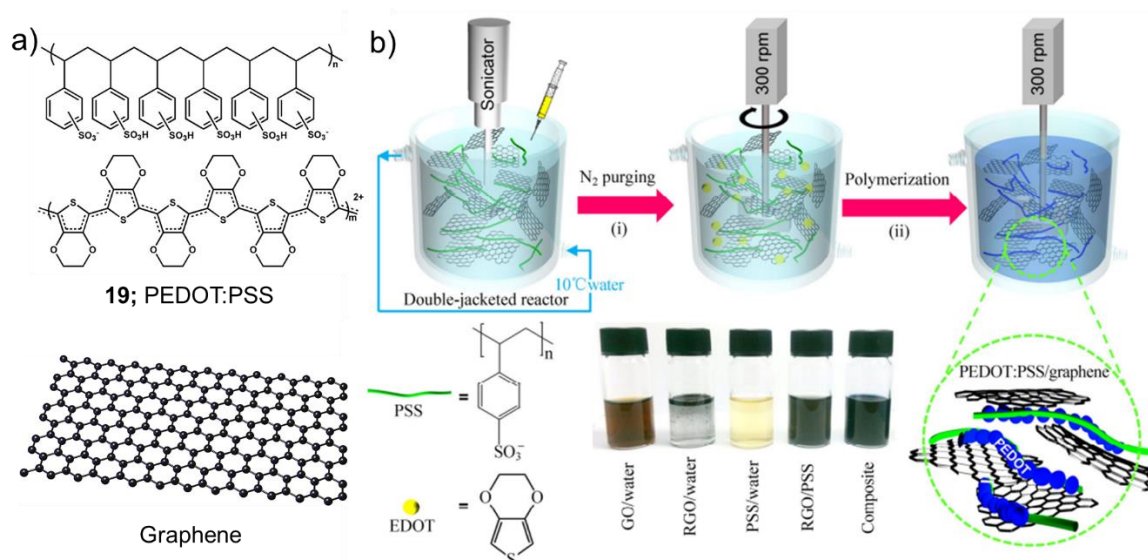


Figure 1.21. a) Chemical structures of **19** and graphene, b) Schematic representation of the in situ compositing of **19**/graphene nanocomposites and the photographs of dispersions after sonication of GO, RGO, PSS, RGO/PSS, and **19**/graphene composites in water. (Adapted from reference 69)

Yoo *et al.* reported compositing of organic semiconductor (**19**; PEDOT:PSS) and graphene which is a carbon allotrope by in situ polymerization technique (**Figure 1.21**).^[69] Polymerization was initiated by the addition of 3,4-ethylenedioxythiophene (EDOT) monomer to a dispersion containing graphene and poly(4-styrenesulfonate) (PSS). The key benefit of this synthetic technique is the ability to produce highly

conductive **19**/graphene composite without the need for additional reduction procedures that involves hazardous chemicals or unfavorable high temperatures.

Hence, ex situ method allows for better control over the individual synthesis of the semiconductor material and the carbon allotropes. It is often used when the semiconductor and the carbon allotropes have significantly different synthetic requirements. On the other hand, in situ compositing can lead to stronger interfaces between the carbon allotropes and the semiconductor, potentially improving the overall performance of the composite. However, it may be more challenging to control the growth conditions and achieve uniform dispersion.

1.3.3.2. Interfacial energy filtering effect

Introducing carbon allotropes into the other semiconductor materials like OSCs can modify their electrical properties by utilizing the interfacial energy filtering effect. Owing to the variance in band structures between carbon allotropes and the OSC matrix, there exists an energy offset at the interface of carbon allotropes and the matrix.^[70] This energy offset acts as a selective barrier that screens out low-energy carriers, resulting in a raised average carrier energy, ultimately leading to an increase in the α .^[71] In order to attain an optimal energy filtering effect, it is vital to fine-tune the height (ΔE_g) of the energy offset to remain below 0.2 eV, while simultaneously managing the width (the separation between adjacent barriers) of the energy offset to be approximately 3 nm.

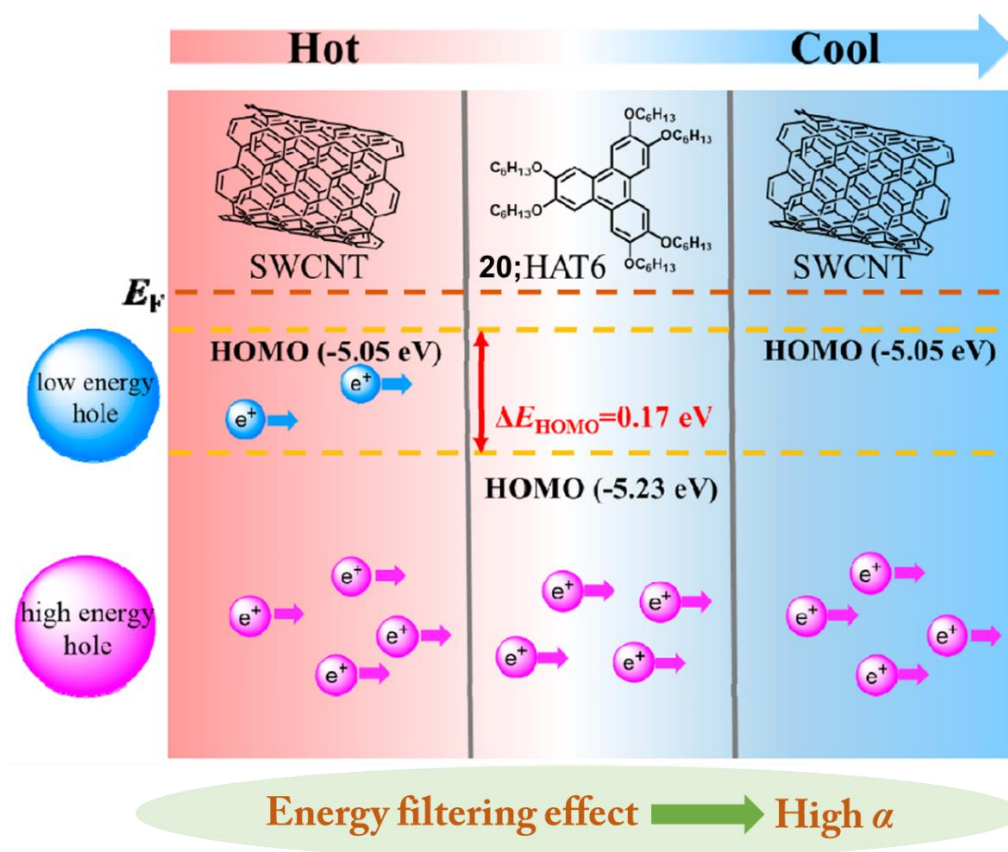


Figure 1.22. Schematic representation of the energy filtering effect between the interface of **20** and SWCNT. (Adapted from reference 72)

Experimentally, Li *et al.* found that the interfacial energy filtering effect between SWCNTs and discotic liquid-crystal 2,3,6,7,10,11-hexakis(hexyloxy)triphenylene (**20**; HAT6) has induced an increase in α (**Figure 1.22**).^[72] Consequently, the composite films comprising exhibited notably enhanced α , surpassing those of the pristine SWCNT film by more than two-fold. This enhancement was also reflected in the PF, which escalated from 102.98 ± 19.45 to 408.23 ± 48.96 $\mu\text{Wm}^{-1}\text{K}^{-2}$ at room temperature. Choi *et al.* fabricated a ternary composite film consisting of graphene, **19**, and tellurium nanowires. Since the film consists of two heterojunctions, each of them contributed to

the energy filtering effect. The experimentally determined α for both binary (**19**/Te nanowire: DTe) and ternary (graphene/**19**/Te nanowire: GDTe) composites were significantly higher than the theoretical values (without considering the interfacial energy filtering effect).

1.3.3.3. Reducing thermal conductivity

Apart from achieving high electrical performance, it is also essential to decrease κ_L in order to minimize overall κ and enhance the ZT . When carbon allotropes are combined with other OSCs, the introduction of additional elements, such as interfaces and chemical interactions, can lead to further disruption of phonons and result in a reduction of κ_L .^[58] The thermal conductivity of carbon allotropes can vary greatly based on their structure, form, and synthesis method, ranging from exceptionally high values like $6600 \text{ Wm}^{-1}\text{K}^{-1}$ for individual SWCNTs to values suggesting they can act as thermal insulators for bundled MWCNT systems with a thermal conductivity below $0.1 \text{ Wm}^{-1}\text{K}^{-1}$.^[60]

Phonon conduction is commonly regarded as the primary mechanism for thermal energy transport within carbon nanotubes. Despite the metallic character of certain carbon nanotubes, which might suggest the possibility of thermal energy conduction through electrons, phonon conduction is still a prominent mechanism in many cases. Thermal transport remains predominantly governed by the coherent phonon lattice vibrations. Even with the use of the most precise reaction control systems, carbon nanotubes inevitably exhibit defects upon formation, including topological defects and

vacancies, which induce scattering events and subsequently reduce the phonon mean free path. The nanotube-nanotube coupling often lowers the thermal conductivity by one order of magnitude.^[60]

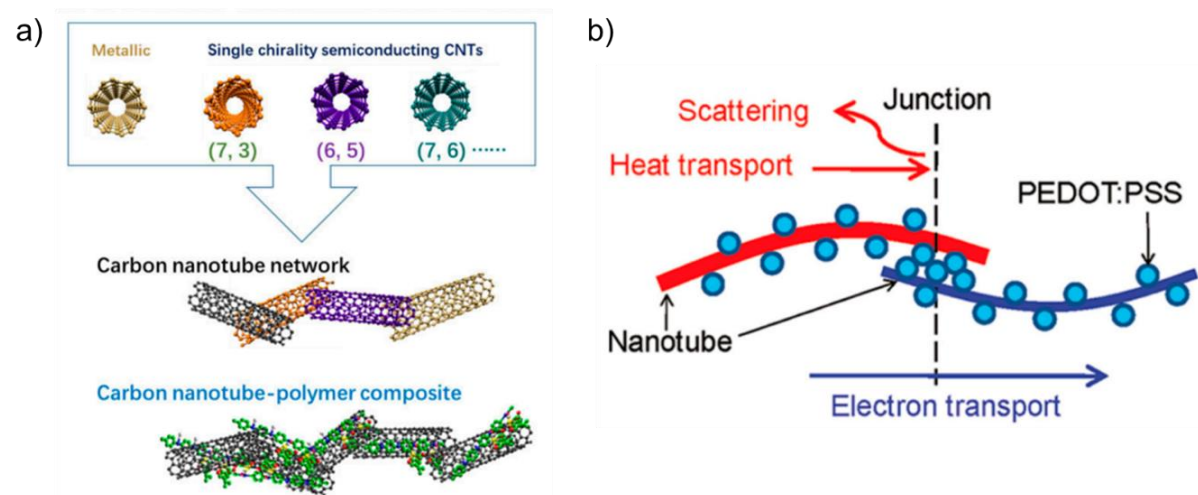


Figure 1.23. a) Representation of carbon nanotube based materials, carbon nanotube-polymer composite, b) Depiction of heat and electron transport in **19**/carbon nanotube composite. (Adapted from reference 73)

Due to the lowered κ , composites based on carbon nanotube exhibits enhanced ZT . Hence, preparation of carbon nanotube based composites is one of the widely used strategy to design high performance TE materials. Due to the rapid advancement in conducting polymers, **19** has emerged as one of the most extensively utilized polymers for composite formation. A junction configuration, as depicted in **Figure 1.23**, is thought to be responsible for the exceptional TE transport properties observed, particularly the formation of a network of interconnected electron channels at the interfaces.^[73] Furthermore, owing to the disparity in the molecular vibrational spectra between CNTs and **19**, the transmission of phonons at the junction points is hindered,

thereby inhibiting the enhancement of κ and the reduction of the α . Ultimately, the ZT value was optimized and achieved a value of 0.02 at room temperature.

1.3.3.4. Interfacial phonon scattering

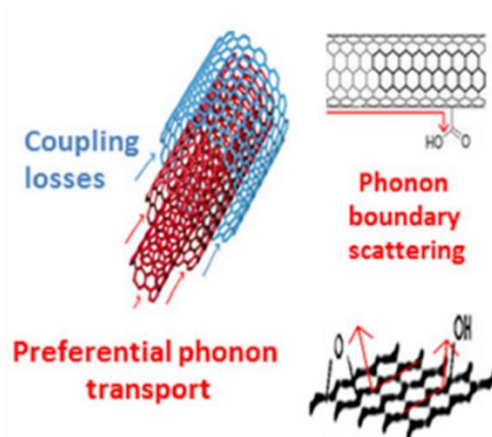


Figure 1.24. Schematic representation of the interfacial phonon scattering in carbon nanotubes. (Adapted from reference 75)

The interactions taking place at the boundaries between carbon allotropes and the matrix materials effectively scatter mid-to long-wavelength phonons, resulting in a decrease in κ_L .^[73] However, it's essential to exercise precise control over the level of carbon allotrope compositing, as it induces interfacial phonon scattering, which can concurrently lower κ_L and improve the ZT .^[61] Apart from the carbon allotropes themselves, the amorphous interlayer positioned between the carbon allotropes and the matrix material can also efficiently reduce κ_L .^[11] When CNTs or graphene are grown in situ, they typically acquire carbonyl groups with surface-bound oxygen-containing functional moieties. During the process of combining them with other materials, an amorphous layer can develop as a result of these surface functionalization as shown in

Figure 1.24, leading to the scattering of phonons and an additional reduction in κ_L .^[61,74,75]

1.4. Organic thermoelectric generators

The practical implementation of OTE materials can be achieved through the designing of devices that utilize these materials as their core components. The ease of solution processability of these materials presents a significant advantage for fabricating devices through printing technology, making them highly suitable for practical use. Additionally, innovative device designs are crucial to fully harness the potential of such systems.

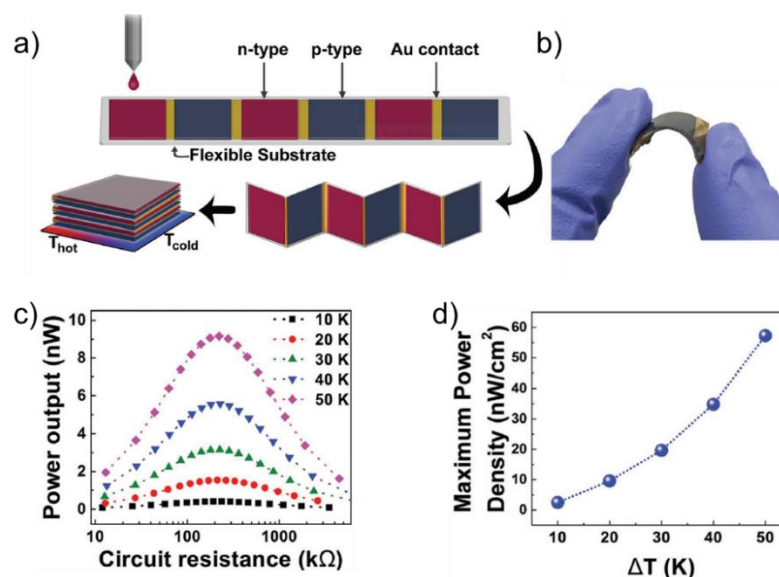


Figure 1.25. a) Design of a flexible thermoelectric module, b) Photograph of the prototype TEG module, c) Output power as a function of circuit resistance, d) Power density as a function of the temperature gradient. (Adapted from reference 76)

A 10-leg flexible device was fabricated using a facile solution-based technique and novel geometric design (**Figure 1.25**).^[76] The "stacked" configuration necessitates

bending each leg at both of its contact points. Perylene diimide (PDI) based derivatives coated over Te nanowire formulated as TE inks was employed as the active semiconducting material. The maximum power density obtained was 57 nWcm^{-2} at $\Delta T=50 \text{ K}$. From a mechanical standpoint, these devices exhibited robust stability when subjected to bending. Furthermore, this design exhibits modularity, facilitating facile adjustments in the number of legs interconnected in a series configuration. This methodology offers opportunities for the creation of novel device architectures beneficial for flexible power generation while maintaining cost-efficiency in processing.

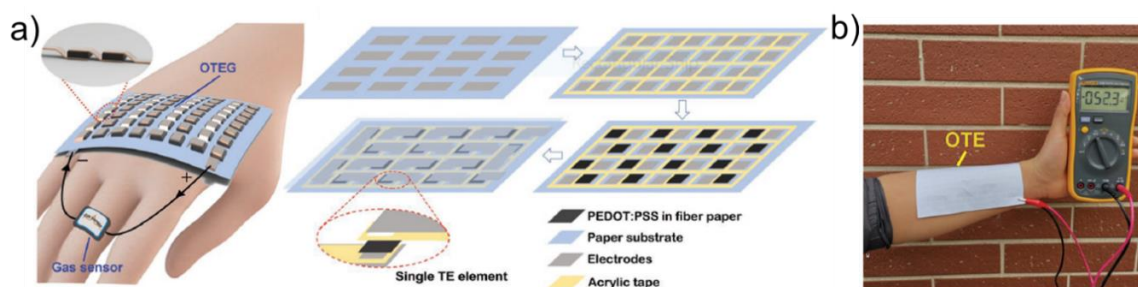


Figure 1.26. a) Schematic representation of the flexible OTEG and the fabrication process of PEDOT:PSS legs on the paper substrate, b) TEG demonstration by attaching on human arm. (Adapted from reference 77)

By incorporating organic self-powered sensing components, Di *et al.* have developed a system that seamlessly integrates a flexible organic TEG with PEDOT:PSS legs onto paper substrates as shown in **Figure 1.26**.^[77] TEG fabrication was carried out using base treated **19** (TE element) and silver (electrode). The device configuration comprises of 162 TE legs integrated onto a flexible paper substrate, demonstrating an output

performance with a peak voltage and power output reaching 0.52 V and 0.32 μW , respectively at a $\Delta T=85.5$ K.

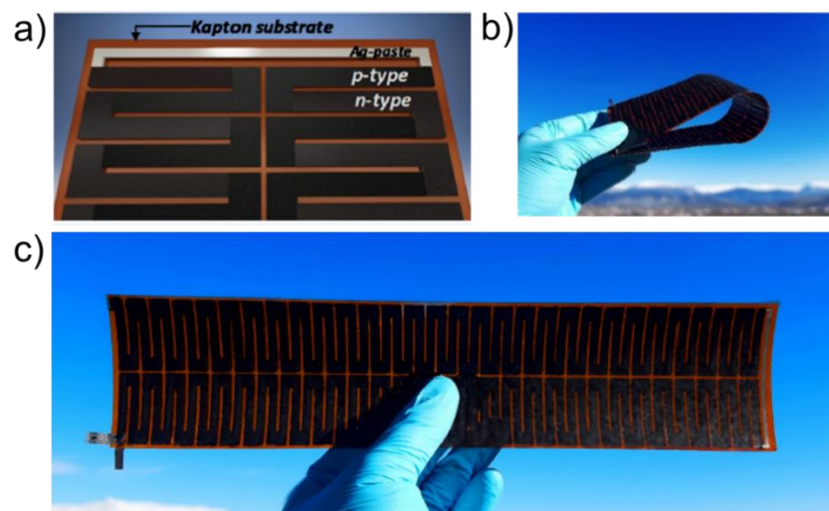


Figure 1.27. a) Fully printed TEG, b) Flexibility of the OTEG, c) SWCNT based OTEG. (Adapted from reference 78)

The construction of metal-free, flexible module exclusively utilizing all-organic TE materials was demonstrated by Mytafides *et al.* in 2021 (**Figure 1.27**).^[78] This TEG is fabricated with cost-effective CNT inks dispersed in an aqueous medium, further enhanced by a mask-assisted approach to define a precise circuit architecture. It achieves an open-circuit voltage (V_{OC}) of 1.05 V and a short-circuit current (I_{SC}) of 1.30 mA under a $\Delta T=150$ K, consequently yielding a power output of 342 μW . The fabricated OTEG exhibits high scalability, opening avenues for the large-scale and printable manufacturing of highly efficient flexible OTEGs within the realm of industrial production.

1.5. Objective of the present investigation

The capacity of TE devices to transform thermal energy into electrical power is anticipated to play a pivotal role in addressing global energy challenges, particularly in the context of the energy crisis. The conversion of waste heat from primary sources such as industrial hot water discharges, automotive exhaust, and high-temperature industrial processes is increasingly recognized for its potential societal benefits. However, the current reliance on conventional, costly materials for TEGs impedes their wider adoption and economic feasibility. Therefore, developing cost-effective, high-performance materials is a crucial aspect of TE research. Organic semiconductors, particularly thiophene-based small molecules and polymers, are chosen due to their exceptional electrical conductivity, tunable energy levels, excellent thermal stability, and facile synthesis, holding the promise of developing efficient and versatile TE materials.

Our first objective is to explore the impact of minor variations in the molecular structure of thiophene-based small molecules, particularly focusing on different end substitutions that vary in acceptor strength. We aim to understand how these modifications affect self-assembled morphologies, energy level offsets, and, consequently, their TE properties. The second objective involves investigating charge transfer states in semiconducting copolymers based on benzodithiophene when doped with strong electron acceptors like F4TCNQ. We seek to determine how this doping influences the TE performance of these copolymers. The third objective is to create

nanocomposites by integrating thiophene-based small molecules with SWCNTs to enhance the electrical conductivity and overall TE performance of the resulting materials. We also aim to fabricate proof-of-concept TE devices using the best-performing materials to demonstrate their potential in power generation.

1.6. References

- [1] W. Shi, T. Deng, Z. M. Wong, G. Wu, S. W. Yang, *npj Comput. Mater.* **2021**, 7, 107.
- [2] Lawrence Livermore National Laboratory, *Energy 2021 United States* **2021**.
- [3] D. Champier, *Energy Convers. Manag.* **2017**, 140, 167.
- [4] R. Kroon, D. A. Mengistie, D. Kiefer, J. Hynynen, J. D. Ryan, L. Yu, C. Müller, *Chem. Soc. Rev.* **2016**, 45, 6147.
- [5] R. Freer, A. V. Powell, *J. Mater. Chem. C* **2020**, 8, 441.
- [6] S. B. Riffat, X. Ma, *Appl. Therm. Eng.* **2003**, 23, 913.
- [7] N. Jaziri, A. Boughamoura, J. Müller, B. Mezghani, F. Tounsi, M. Ismail, *Energy Reports* **2020**, 6, 264.
- [8] T. M. Tritt, M. A. Subramanian, *MRS Bulletin* **2006**, 31, 188.
- [9] M. He, F. Qiu, Z. Lin, *Energy Environ. Sci.* **2013**, 6, 1352.
- [10] B. T. McGrail, A. Sehirlioglu, E. Pentzer, *Angew. Chemie- Int. Ed.* **2015**, 54, 1710.
- [11] M. F. Sanad, A. E. Shalan, S. O. Abdellatif, E. S. A. Serea, M. S. Adly, M. A. Ahsan, *Top Curr Chem.* **2020**, 6, 378.
- [12] G. J. Snyder, E. S. Toberer, *Mater. Sustain. Energy A* **2010**, 7, 101.
- [13] L. D. Zhao, S. H. Lo, Y. Zhang, H. Sun, G. Tan, C. Uher, C. Wolverton, V. P. Dravid, M. G. Kanatzidis, *Nature*, **2014**, 7, 373.
- [14] Y. Pei, X. Shi, A. LaLonde, H. Wang, L. Chen, G. J. Snyder, *Nature*, **2011**, 473, 66.

-
- [15] Y. Zhang, W. Wang, F. Zhang, K. Dai, C. Li, Y. Fan, G. Chen, Q. Zheng, *Small* **2022**, *18*, 2104922.
- [16] Y. Bao, Y. Sun, F. Jiao, W. Hu, *Adv. Electron. Mater.* **2023**, *9*, 2201310.
- [17] L. Deng, Y. Liu, Y. Zhang, S. Wang, P. Gao, *Adv. Funct. Mater.* **2023**, *33*, 2210770.
- [18] D. Zhou, H. Zhang, H. Zheng, Z. Xu, H. Xu, H. Guo, P. Li, Y. Tong, B. Hu, L. Chen, *Small* **2022**, *18*, 2200679.
- [19] W. Shi, J. Chen, J. Xi, D. Wang, Z. Shuai, *Chem. Mater* **2014**, *26*, 2669.
- [20] S. N. Patel, A. M. Glaudell, K. A. Peterson, E. M. Thomas, K. A. O'Hara, E. Lim, M. L. Chabinyc, *Sci. Adv.* **2017**, *3*, e1700434.
- [21] J. Li, A. B. Huckleby, M. Zhang, *J. Materiomics* **2022**, *8*, 204.
- [22] J. Tang, J. Ji, R. Chen, Y. Yan, Y. Zhao, Z. Liang, *Adv. Sci.* **2022**, *9*, 2103646.
- [23] J. Ding, Z. Liu, W. Zhao, W. Jin, L. Xiang, Z. Wang, Y. Zeng, Y. Zou, F. Zhang, Y. Yi, Y. Diao, C. R. McNeill, C. Di, D. Zhang, D. Zhu, *Angew. Chemie- Int. Ed.* **2019**, *58*, 18994.
- [24] S. A. Gregory, A. K. Menon, S. Ye, D. S. Seferos, J. R. Reynolds, S. K. Yee, *Adv. Energy Mater.* **2018**, *8*, 1802419.
- [25] V. Vijayakumar, E. Zaborova, L. Biniek, H. Zeng, L. Herrmann, A. Carvalho, O. Boyron, N. Leclerc, M. Brinkmann, *ACS Appl. Mater. Interfaces* **2019**, *11*, 4942.
- [26] V. Untilova, T. Biskup, L. Biniek, V. Vijayakumar, M. Brinkmann, *Macromolecules* **2020**, *53*, 2441.
- [27] R. Kroon, D. Kiefer, D. Stegerer, L. Yu, M. Sommer, C. Müller, *Adv. Mater.* **2017**, *29*, 1700930.
- [28] D. Kiefer, R. Kroon, A. I. Hofmann, H. Sun, X. Liu, A. Giovannitti, D. Stegerer, A. Cano, J. Hynynen, L. Yu, Y. Zhang, D. Nai, T. F. Harrelson, M. Sommer, A. J. Moulé, M. Kemerink, S. R. Marder, I. McCulloch, M. Fahlman, S. Fabiano, C. Müller, *Nat. Mater.* **2019**, *18*, 149.
- [29] J. Emmy, T. Biskup, Y. Zhang, R. Kroon, S. Barlow, S. R. Marder, C. Mu, *Chem.*

-
- Mater.* **2022**, *34*, 5673.
- [30] X. Yin, F. Zhong, Z. Chen, C. Gao, G. Xie, L. Wang, C. Yang, *Chem. Eng. J.* **2020**, *382*, 122817.
- [31] A. H. Sakr, L. Biniek, J. L. Bantignies, D. Maurin, L. Herrmann, N. Leclerc, P. Lévêque, V. Vijayakumar, N. Zimmermann, M. Brinkmann, *Adv. Funct. Mater.* **2017**, *27*, 1700173.
- [32] J. E. Cochran, M. J. N. Junk, A. M. Glauddell, P. L. Miller, J. S. Cowart, M. F. Toney, C. J. Hawker, B. F. Chmelka, M. L. Chabinyc, *Macromolecules* **2014**, *47*, 6836.
- [33] D. Huang, H. Yao, Y. Cui, Y. Zou, F. Zhang, C. Wang, H. Shen, W. Jin, J. Zhu, Y. Diao, W. Xu, C. A. Di, D. Zhu, *J. Am. Chem. Soc.* **2017**, *139*, 13013.
- [34] I. Salzmann, G. Heimel, M. Oehzelt, S. Winkler, N. Koch, *Acc. Chem. Res.* **2016**, *49*, 370.
- [35] B. Lüsse, M. Riede, K. Leo, *Phys. Status Solidi A* **2013**, *210*, 9.
- [36] Z. Liang, Y. Zhang, M. Souri, X. Luo, A. M. Boehm, R. Li, Y. Zhang, T. Wang, D. Y. Kim, J. Mei, S. R. Marder, K. R. Graham, *J. Mater. Chem. A* **2018**, *6*, 16495.
- [37] H. Li, J. Song, J. Xiao, L. L. Wu, H. E. Katz, L. Chen, *Adv. Funct. Mater.* **2020**, *30*, 2004378.
- [38] S. N. Patel, A. M. Glauddell, D. Kiefer, M. L. Chabinyc, *ACS Macro Lett.* **2016**, *5*, 268.
- [39] S. Wu, X. Wu, W. Xing, Y. Sun, Y. Zou, W. Xu, D. Zhu, *Macromol. Rapid Commun.* **2020**, *41*, 1900322.
- [40] D. Yuan, D. Huang, C. Zhang, Y. Zou, C. A. Di, X. Zhu, D. Zhu, *ACS Appl. Mater. Interfaces* **2017**, *9*, 28795.
- [41] Y. Lu, Z. Di Yu, H. I. Un, Z. F. Yao, H. Y. You, W. Jin, L. Li, Z. Y. Wang, B. W. Dong, S. Barlow, E. Longhi, C. Di, D. Zhu, J. Y. Wang, C. Silva, S. R. Marder, J. Pei, *Adv. Mater.* **2021**, *33*, 2005946.

-
- [42] L. Qiu, J. Liu, R. Alessandri, X. Qiu, R. M. Koopmans, W. A. Havenith, S. J. Marrink, R. C. Chiechi, L. J. Koster, J. C. A. Hummelen, *J. Mater. Chem. A* **2017**, *5*, 21234.
- [43] B. Li, X. Li, F. Yang, Y. Chen, X. Mao, S. Wan, H. Xin, S. Yan, M. Wang, C. Gao, L. Wang, *ACS Appl. Energy Mater.* **2021**, *4*, 4662.
- [44] J. Li, C. W. Rochester, I. E. Jacobs, S. Friedrich, P. Stroeve, M. Riede, A. J. Moulé, *ACS Appl. Mater. Interfaces* **2015**, *7*, 28420.
- [45] V. Ignatious, N. Raveendran, A. Prabhakaran, Y. Tanjore Puli, V. Chakkooth, B. Deb, *Chem. Eng. J.* **2021**, *409*, 128294.
- [46] O. Z. Arteaga, B. Dörling, A. Perevedentsev, J. Martín, J. S. Reparaz, M. C. Quiles, *Macromolecules* **2020**, *53*, 609.
- [47] D. A. Stanfield, Y. Wu, S. H. Tolbert, B. J. Schwartz, *Chem. Mater.* **2021**, *33*, 2343.
- [48] H. Méndez, G. Heimel, S. Winkler, J. Frisch, A. Opitz, K. Sauer, B. Wegner, M. Oehzelt, C. Röthel, S. Duhm, D. Többens, N. Koch, I. Salzmann, *Nat. Commun.* **2015**, *6*, 8560.
- [49] H. Li, Z. Xu, J. Song, H. Chai, L. Wu, L. Chen, *Adv. Funct. Mater.* **2022**, *32*, 2110047.
- [50] C. P. Theurer, M. Richter, D. Rana, G. Duva, D. Lepple, A. Hinderhofer, F. Schreiber, P. Tegeder, K. Broch, *J. Phys. Chem. C* **2021**, *125*, 23952.
- [51] P. Y. Yee, D. T. Scholes, B. J. Schwartz, S. H. Tolbert, *J. Phys. Chem. Lett.* **2019**, *10*, 4929.
- [52] A. R. Chew, R. Ghosh, Z. Shang, F. C. Spano, A. Salleo, *J. Phys. Chem. Lett.* **2017**, *8*, 4974.
- [53] A. M. Glaudell, J. E. Cochran, S. N. Patel, M. L. Chabinyc, *Adv. Energy Mater.* **2014**, *5*, 1401072.
- [54] A. D. Scaccabarozzi, A. Basu, F. Aniés, J. Liu, O. Z. Arteaga, R. Warren, Y. Firdaus, M. I. Nugraha, Y. Lin, M. C. Quiles, N. Koch, C. Müller, L. Tsetseris,

-
- M. Heeney, T. D. Anthopoulos, *Chem. Rev.* **2022**, *122*, 4420.
- [55] V. Vijayakumar, P. Durand, H. Zeng, V. Untilova, L. Herrmann, P. Algayer, N. Leclerc, M. Brinkmann, *J. Mater. Chem. C* **2020**, *8*, 16470.
- [56] I. E. Jacobs, E. W. Aasen, J. L. Oliveira, T. N. Fonseca, J. D. Roehling, J. Li, G. Zhang, M. P. Augustine, M. Mascal, A. J. Moulé, *J. Mater. Chem. C* **2016**, *4*, 3454.
- [57] D. T. Scholes, S. A. Hawks, P. Y. Yee, H. Wu, J. R. Lindemuth, S. H. Tolbert, B. J. Schwartz, *J. Phys. Chem. Lett.* **2015**, *6*, 4786.
- [58] B. Kumanek, D. Janas, *J. Mater. Sci.* **2019**, *54*, 7397.
- [59] E. Muchuweni, E. T. Mombeshora, *Appl. Surf. Sci. Adv.* **2023**, *13*, 100379.
- [60] X. Wang, H. Wang, B. Liu, *Polymers* **2018**, *10*, 1196.
- [61] M. Ohnishi, J. Shiomi, *APL Mater* **2019**, *7*, 013102.
- [62] L. Zhang, J. Jin, S. Huang, B. Tan, J. Luo, D. Wang, D. Liu, L. Wang, *Chem. Eng. J.* **2021**, *426*, 131859.
- [63] Y. Wang, J. Yang, L. Wang, K. Du, Q. Yin, Q. Yin, *ACS Appl. Mater. Interfaces* **2017**, *9*, 20124.
- [64] B. Abad, I. Alda, P. Díaz-Chao, H. Kawakami, A. Almarza, D. Amantia, D. Gutierrez, L. Aubouy, M. M. González, *J. Mater. Chem. A* **2013**, *1*, 10450.
- [65] A. S. Kshirsagar, C. Hiragond, A. Dey, P. V. More, P. K. Khanna, *ACS Appl. Energy Mater.* **2019**, *2*, 2680.
- [66] Q. Yao, Q. Wang, L. Wang, L. Chen, *Energy Environ. Sci.* **2014**, *7*, 3801.
- [67] Q. Y. Li, T. Feng, W. Okita, Y. Komori, H. Suzuki, T. Kato, T. Kaneko, T. Ikuta, X. Ruan, K. Takahashi, *ACS Nano* **2019**, *13*, 9182.
- [68] C. Cho, K. L. Wallace, P. Tzeng, J. H. Hsu, C. Yu, J. C. Grunlan, *Adv. Energy Mater.* **2016**, *6*, 1502168.
- [69] D. Yoo, J. Kim, J. H. Kim, *Nano Res.* **2014**, *7*, 717.
- [70] S. Wei, Y. Zhang, H. Lv, L. Deng, G. Chen, *Chem. Eng. J.* **2022**, *428*, 131137.
- [71] J. Choi, J. Y. Lee, S. S. Lee, C. R. Park, H. Kim, *Adv. Energy Mater.* **2016**, *6*,

1502181.

- [72] X. Li, Z. Yu, H. Zhou, F. Yang, F. Zhong, X. Mao, B. Li, H. Xin, C. Gao, L. Wang, *ACS Sustain. Chem. Eng.* **2021**, *9*, 1891.
- [73] B. A. Macleod, N. J. Stanton, I. E. Gould, D. Wesenberg, R. Ihly, Z. R. Owczarczyk, K. E. Hurst, C. S. Fewox, C. N. Folmar, K. H. Hughes, B. L. Zink, J. L. Blackburn, A. J. Ferguson, *Energy Environ. Sci.* **2017**, *10*, 2168.
- [74] S. Cho, K. Kikuchi, A. Kawasaki, *Acta Mater.* **2012**, *60*, 726.
- [75] M. M. Gallego, R. Verdejo, M. Khayet, J. M. O. de Zarate, M. Essalhi, M. A. L. Manchado, *Nanoscale Res. Lett.* **2011**, *6*, 610.
- [76] E. W. Zaia, M. P. Gordon, V. Niemann, J. Choi, R. Chatterjee, C. Hsu, J. Yano, B. Russ, A. Sahu, J. J. Urban, *Adv. Energy Mater.* **2019**, *9*, 1803469.
- [77] C. Zheng, L. Xiang, W. Jin, H. Shen, W. Zhao, F. Zhang, C. Di, D. Zhu, *Adv. Mater. Technol.* **2019**, *4*, 1900247.
- [78] C. K. Mytafides, L. Tzounis, G. Karalis, P. Formanek, A. S. Paipetis, *ACS Appl. Mater. Interfaces* **2021**, *13*, 11151.

Chapter 2

Influence of Molecular Structure on Doping Efficiency and Fermi Level Alignment in Self-Assembled Thiophene Derivatives

2.1. Abstract

*This study delves into the TE characteristics of thiophene-based small molecules, specifically examining how variations in molecular structure influence TE performance. We focus on two thiophene-based small molecules (**OT1** and **OT2**), which differ only in their end substitution with varying acceptor strengths. This difference led to distinct morphologies when self-assembled. **OT2** doped with FeCl_3 displayed high electrical conductivity and power factor ($52.0 \mu\text{Wm}^{-1}\text{K}^{-2}$), while **OT1** exhibited significantly lower conductivity and power factor ($1.6 \mu\text{Wm}^{-1}\text{K}^{-2}$) under identical conditions. The weaker acceptor strength of the end group in **OT2** resulted in higher doping efficiency. Improved charge carrier transport in **OT2** was due to a low-lying highest occupied molecular orbital (HOMO) energy level and enhanced density of states around the HOMO after doping. Maintaining its self-assembly after doping was also crucial for better electrical properties. These findings emphasize the importance of molecular engineering in developing high-performance TE materials.*

2.2. Introduction

An ideal TE material should possess high electrical conductivity and low thermal conductivity, which is referred to as the "electron-crystal, phonon-glass" combination.^[1,2] Organic semiconductors, due to their low thermal conductivity, fall into the latter category.^[3-7] However, it is challenging to obtain high performance materials due to the mutually restricted TE transport coefficients, *i.e.*, an increase in σ results in a decrease in α , while the electronic contribution to the thermal conductivity (κ_e) increases.^[8,9] As a result, significant efforts have been dedicated to enhancing the σ of organic TE materials through chemical doping, which introduces mobile charge carriers by incorporating molecules that oxidizes or reduces the organic semiconductor by sustaining the α .^[10-13] Examples of this include oxidative doping of thiophene polymers and small molecules with ferric chloride, iodine, silver perchlorate, and tetrafluoro tetracyanoquinodimethane.^[14-21]

Among various organic semiconductors (OSCs), conducting polymers have exhibited good TE properties.^[22,23] A distinctive feature of the OSCs is their amenability to solution-based processing techniques, such as spin-coating, printing, or dip-coating, which are conducive to scalable and cost-effective manufacturing. This makes them particularly attractive for large-scale production of flexible and lightweight TE devices. Moreover, the inherent flexibility and mechanical robustness of these materials allow for the fabrication of devices that can withstand bending and stretching, expanding their applicability to wearable technology and flexible

electronics. The TE performance of the polymers hinges on their structural characteristics, including molecular weight, degree of polymerization, and the nature of side chains, which can significantly affect their electrical conductivity, Seebeck coefficient, and thermal conductivity. For instance, the level of doping and the type of dopant used can modulate the electrical conductivity of these polymers by introducing charge carriers or altering the band structure. Similarly, the alignment and packing of polymer chains influence the charge transport mechanisms and, consequently, the material's overall TE performance. Precise molecular architecture and robust crystallinity of conjugated small molecules offer distinct advantages over polymers in terms of well-defined chemical composition and negligible batch-to-batch variation.

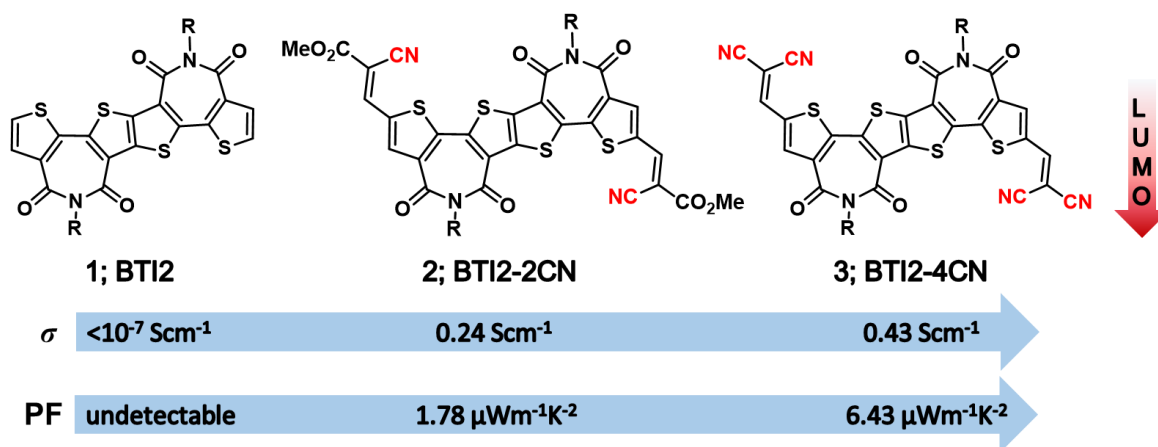


Figure 2.1. Molecular structure of fused bithiophene based derivatives 1, 2 and 3, Corresponding electrical conductivity and power factor with increasing cyano functionalization. (Adapted from reference 24)

Subtle structural changes can have a profound impact on a molecule's energy levels and electrical properties. This intricate interplay opens up a vast playground for researchers to design novel materials with tailored functionalities for diverse

applications. In a study by Wang *et al.*, a new category of small organic thin-film materials has been developed, achieved through terminal cyanation to a ladder-type heteroarenes (**1**, **2** and **3**, **Figure 2.1**). Notably, the cyanation effectively reduced the LUMO energy level from -2.90 eV (for **1**) to -4.14 eV (for **3**), leading to a substantial enhancement in the doping efficiency. Furthermore, the introduction of terminal cyano-functionalization preserves close molecular packing and promotes efficient intermolecular charge transfer among these modified molecules, resulting in notable μ of up to 0.40 $\text{cm}^2\text{V}^{-1}\text{s}^{-1}$. Hence, owing to the low-lying LUMO and high μ , a σ of 0.43 Scm^{-1} and a PF of 6.34 Wm^{-1}K^2 could be attained for the tetracyanated derivative **3** which is significantly higher than derivatives **1** and **2**.^[24] These results show that the terminal cyanation effectively increases the σ of doped small molecules, leading to a substantial improvement in their performance.

Molecules possessing a strong crystalline nature tends to aggregate, forming extensive crystalline domains, thereby leading to a notable decline in overall performance. Conversely, molecules with less pronounced crystallinity can accommodate a greater number of dopants, yet they frequently exhibit suboptimal μ . Side chain engineering has emerged as a powerful tool for fine-tuning the crystallinity of organic semiconductors. Duan *et al.* developed three small molecules by utilizing naphthalene bis-isatin building blocks. The molecules possess same structural units but different alkyl chains (**4**, **5** and **6**, **Figure 2.2**). The study demonstrates that crystallinity is a pivotal factor in modulating the doping characteristics of small

molecules.^[25] Through careful control of crystalline characteristics, OTE device utilizing **5** can attain a delicate balance, preserving high μ while simultaneously facilitating effective doping. It was found that on increasing the alkyl chain length, molecular packing is disrupted leading to reduced crystallinity and μ . On the other hand, partial fluorination promotes crystalline domain formation but due to strong aggregation thereby hinders the dopant miscibility. Hence, **5** (having the shorter alkyl chain) with N-DMBI doping exhibited a higher crystallinity and this yields a substantial PF of $1.07 \mu\text{Wm}^{-1}\text{K}^{-2}$ at 100°C .^[25]

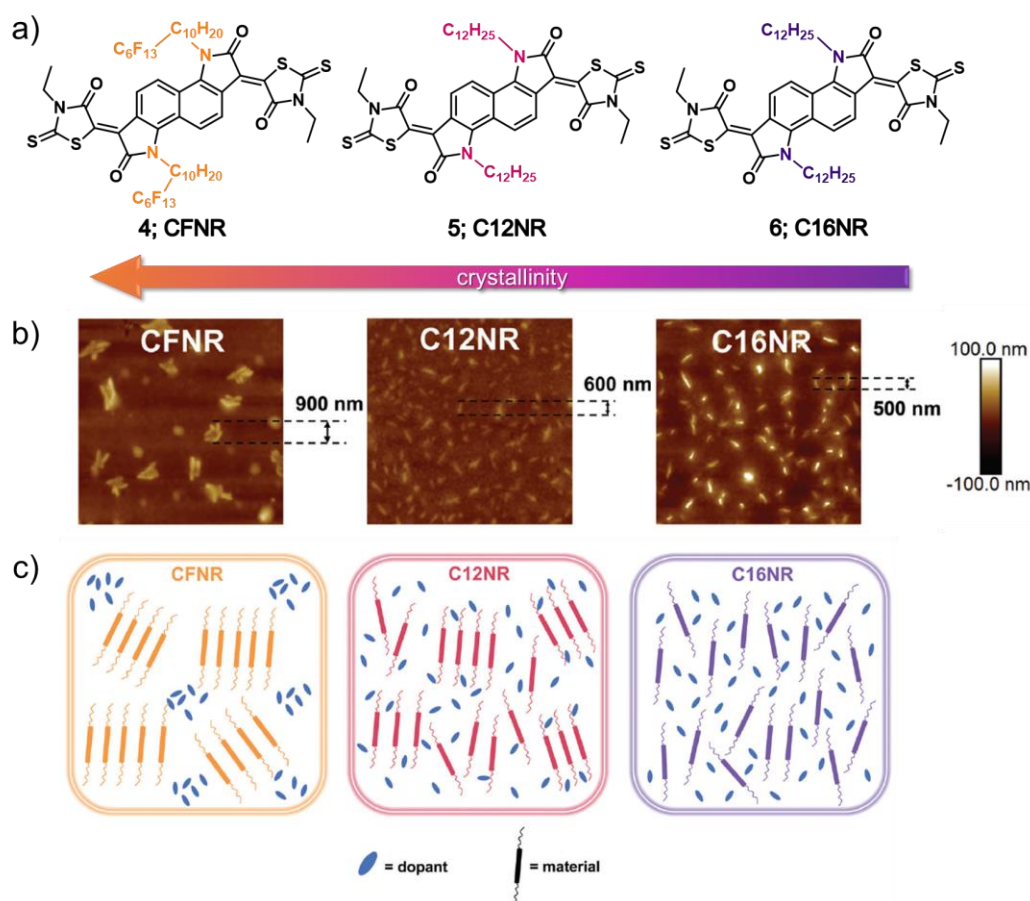


Figure 2.2. a) Molecular structures of **4**, **5** and **6**, b) AFM images of thin films of **4**, **5** and **6** with dopant, c) Representation of dopant interaction within the OSC. (Adapted from reference 25)

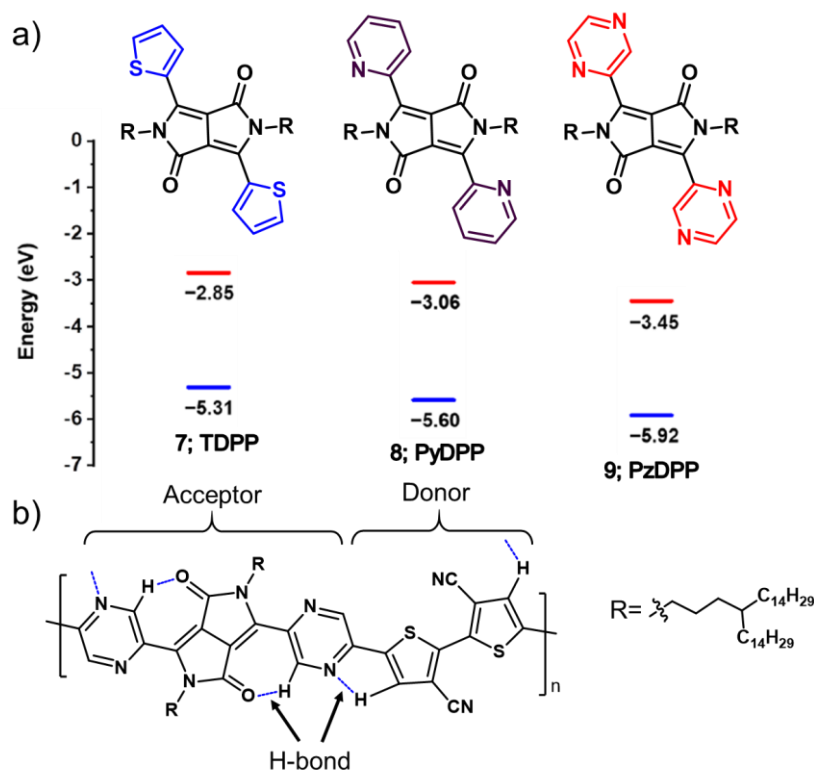


Figure 2.3. a) Molecular structures of DPP derivatives **7**, **8** and **9**, b) Structure of the polymer indicating H-bonds. (Adapted from reference 26)

Yan *et al.* developed DPP-based derivatives (**7**, **8** and **9**, **Figure 2.3**) where **9** displays a structurally rigid and planar backbone configuration that is locked conformationally. Notably, it features a considerably low LUMO of -4.03 eV. From the DFT calculations, molecular structures of **7** and **9** has a small dihedral angle between the pyrazine moiety and the DPP core. However, the optimized trimer structure takes a coplanar conformation. Other strategies like using non-planar donor units or glycolic side chain to increase doping efficiency often leads to low μ and hence lower σ . In this work, polymer **9** achieves a closer π stacking, higher μ , and higher σ simultaneously, indicating that it is capable of n-doping effectively and

exhibiting high TE performance without sacrificing the polymer interchain interactions. Recent studies also suggests that if there is good miscibility between the polymer and the dopant, the charge transfer will be efficient with reduced trap states. This leads to lesser energetic disorder in the film and that gives a more defined energy gradient for the charge transport, again boosting α and PF. Here, polymer **9** exhibited the highest σ of 8.4 S cm^{-1} and PF of up to $57.3 \mu\text{Wm}^{-1}\text{K}^{-2}$.^[26]

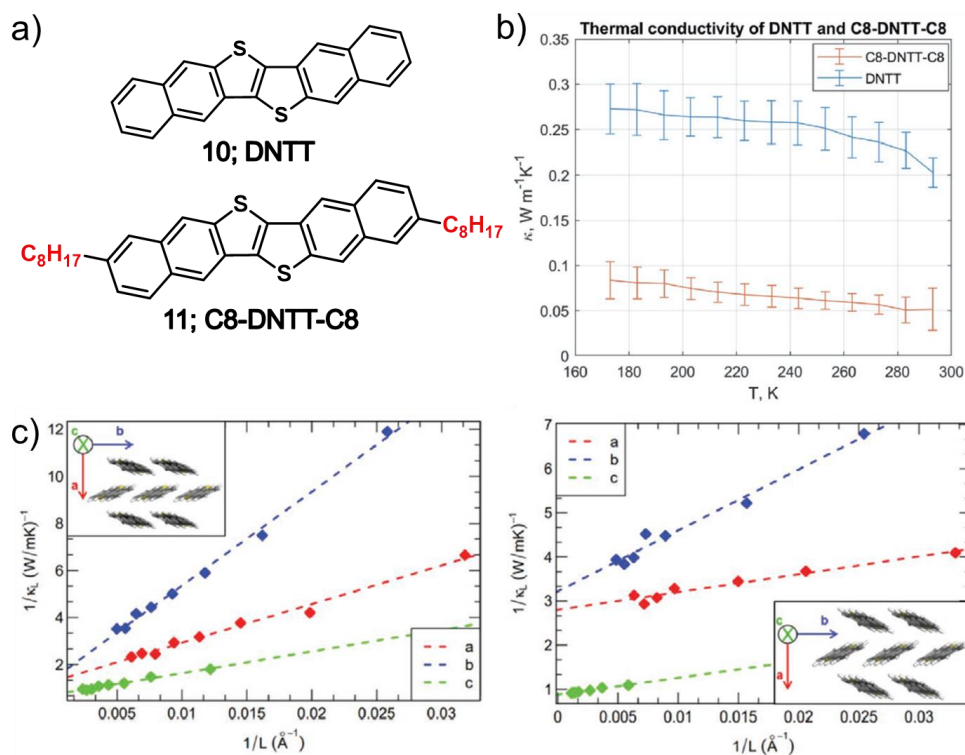


Figure 2.4. a) Molecular structures of **10** and **11**, b) In-plane thermal conductivity of **10** and **11** with respect to temperature, c) $1/\kappa_{\parallel}$ plotted as a function of box length dimensions a, b, c for molecules **10** and **11** (Alkyl chains are removed in **11** for sake of clarity). (Adapted from reference 27)

Herringbone-stacked alkylated molecular materials based on thienoacenes have recently surfaced as top-performing OSCs, showcasing p-type charge carrier mobilities exceeding $10 \text{ cm}^2\text{V}^{-1}\text{s}^{-1}$. Sirringhaus and co-workers developed

dinaphtho[2,3-*b*:2',3'-*f*]thieno[3,2-*b*]thiophene derivatives (**10** and **11**, **Figure 2.4**) which exhibited a similar stacking. The high μ is often associated with the reduced dynamic disorder. On alkylation of **10** to form **11**, the in-plane phonon modes shifts towards higher frequencies thereby suppressing its effect on disorder. It also reduces the out-of-plane sliding motions. **Figure 2.4c** shows the κ_L values of 0.79, 0.73, 1.40 $\text{Wm}^{-1}\text{K}^{-1}$ for molecule **10** and 0.35, 0.31, 1.14 $\text{Wm}^{-1}\text{K}^{-1}$ for molecule **11** along the directions *a*, *b*, *c*. The introduction of extended alkyl side chains to aromatic rings leads to a significant reduction in in-plane κ , attributed to the disruption of coherent phonon transport. This drop results in significantly low experimental κ , approaching approximately $0.05 \text{ W m}^{-1}\text{K}^{-1}$ which is the lowest experimentally obtained κ so far. This provides a possibility to decouple electron and phonon transport in these materials, which offers significant potential for improving the ZT .^[27]

The thermal activation energy of conductivity ($E_{\text{act},\sigma}$) dominates the electrical characteristics of doped OSCs. This can be determined from the Coulomb binding energy ($E_{\text{coul,ICTC}}$) or static energy disorder (σ_{ICTC}) of the integer charge transfer complexes. Zhong *et al.* demonstrated the manipulation of $E_{\text{act},\sigma}$ of two donor-acceptor (D-A) polymers (**12** and **13**, **Figure 2.5**) with varying the donor part from carbazole to dithienopyrrole. According to a density functional theory (DFT) calculation, **13** has substantially larger HOMO distributions than **12** does, and it also has less structural disorder, both of which helps to lower the E_{coul} or σ_{ICTC} of the integer charge transfer complexes at low and high doping concentrations, respectively. At low doping

concentration, it tends to increase the radius of the radical cation of the latter rather than the former. Interestingly, introducing a fine-tuned dithienopyrrole donor to the π -conjugation backbone effectively restrains both the $E_{\text{coul,ICTC}}$ and σ_{ICTC} values linked to distinct charge transfer mechanisms, contributing to a high σ of 70 Scm^{-1} . The optimized PF for the carbazole derivative was $10.8 \mu\text{Wm}^{-1}\text{K}^{-2}$, which was about six times higher than that of the dithienopyrrole derivative ($1.8 \mu\text{Wm}^{-1}\text{K}^{-2}$).^[28]

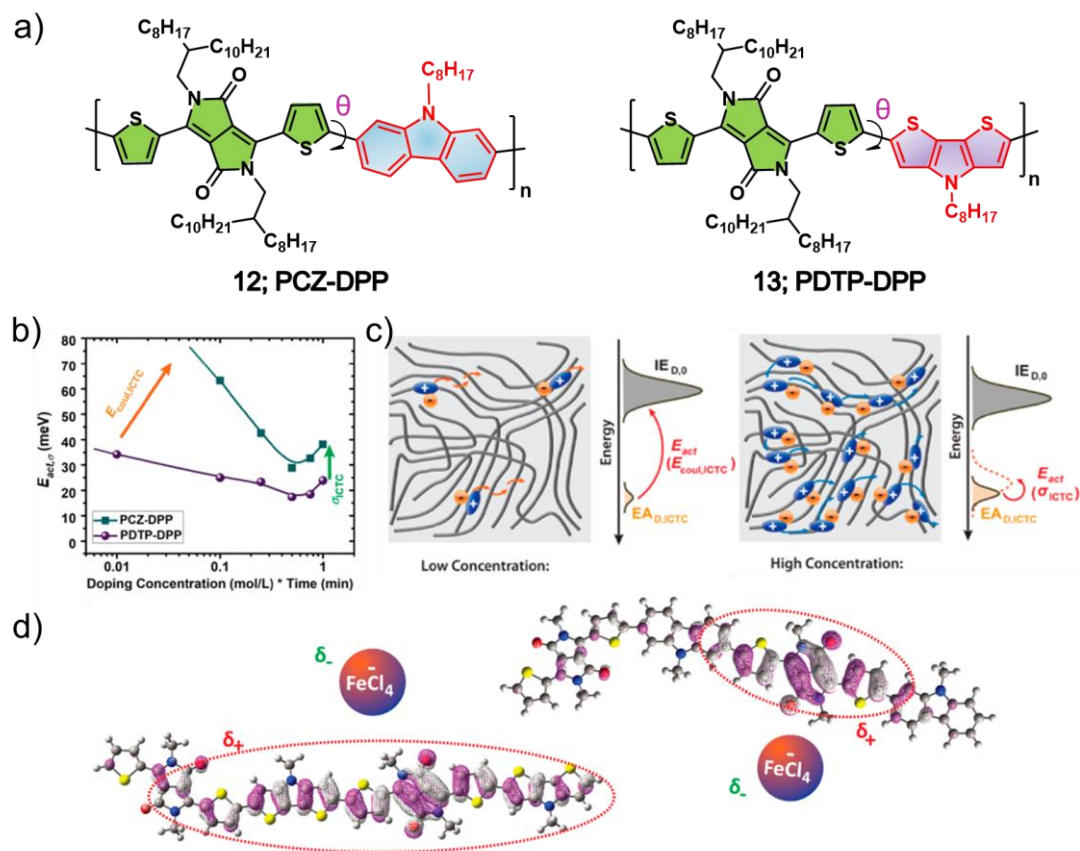


Figure 2.5. a) Molecular structures of **12** and **13**, b) $E_{\text{act},\sigma}$ of **12** and **13** at different FeCl_3 concentration, c) Schematically summarized charge transport of polymers in low and high dopant concentration, d) Diagram showing the formation of ICTC between the radical cation and FeCl_4^- anion. (Adapted from reference 28)

Semiconducting organic small molecules are considered to be favourable choice for TE applications due to their well-defined structures, which can ensure reproducibility and provide a better understanding of structure-property relationships. However, the development and study of small molecule-based TE materials are still in their early stages.^[29-31] It has been suggested that careful molecular design is essential for achieving good TE performance in small molecules, as the available pathways for charge transport are limited to intermolecular routes. These intermolecular interactions can be affected by molecular and supramolecular properties, meaning that even small structural differences can result in significant variations in TE performance. Despite these challenges, it is possible to design small organic semiconductors that are suitable for TE applications through the use of molecular engineering. In this context, we have previously reported on the differential self-assembly of two thiophene-based acceptor-donor-acceptor type semiconducting small molecules (**OT1** and **OT2**) in the film state,^[32] in which the orientation of chromophores during self-assembly was found to be significantly influenced by the presence of alkyl chains on the rhodanine end groups and thiophene backbone. Herein, we analyze the TE properties of these molecules and their dependence on molecular structure and find a significant correlation between TE performance and structural factors.

2.3. Results and discussion

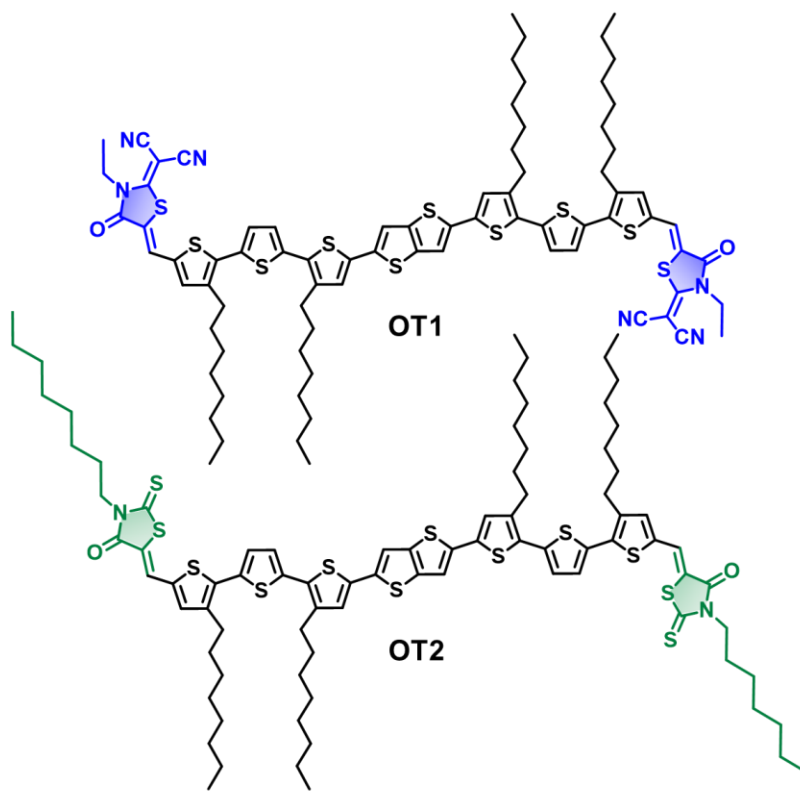


Figure 2.6. Chemical structures of the molecules **OT1** and **OT2** under study.

The chemical structures of the molecules utilized in this chapter are depicted in **Figure 2.6**. These molecules consist of a central thienothiophene unit flanked by dioctyl terthiophenes on both sides. The end groups of **OT1** and **OT2** are 2-(1,1-dicyanomethylene)rhodanine and *N*-octylrhodanine, respectively. The self-assembly of these two small molecules in the film state considerably differed wherein the orientation of chromophores during self-assembly was found to be significantly influenced by the presence of alkyl chains on the rhodanine end groups and thiophene backbone.

2.3.1. Optical and electronic properties

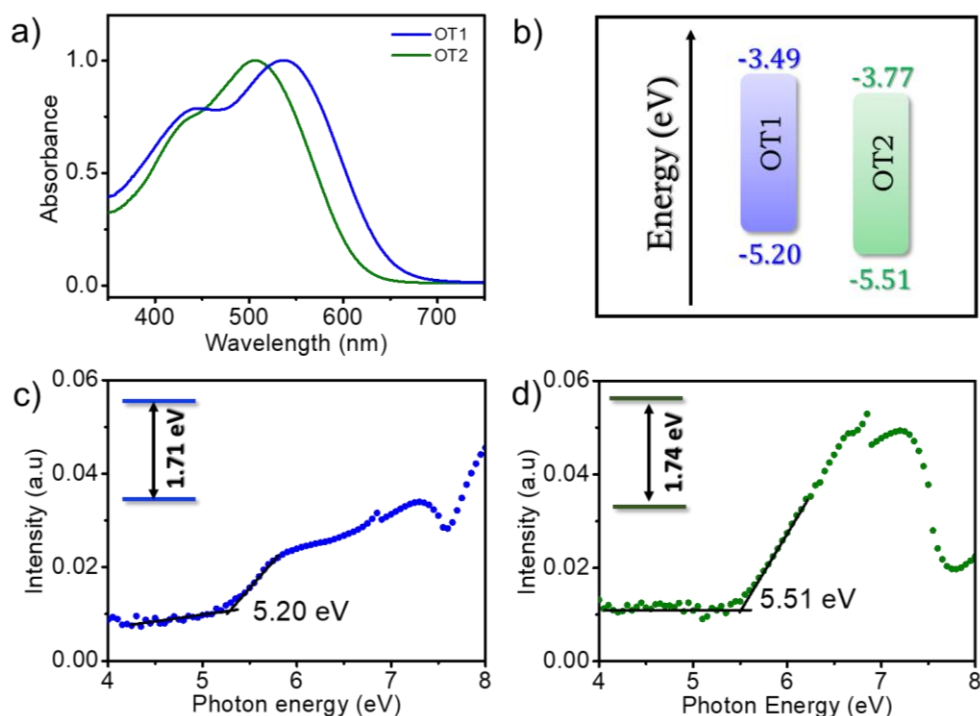


Figure 2.7. a) UV-visible absorption spectra in chloroform, b) Energy level diagram of the molecules under study, HOMO energy levels of c) **OT1** and d) **OT2** were obtained from ultraviolet photoelectron spectroscopy (the inset shows the bandgap of the molecules).

The UV-visible absorption spectra of the small molecules reveals that 2-(1,1-dicyanomethylene)rhodanine in **OT1** is more electron deficient (strong acceptor) than that of *N*-octylrhodanine in case of **OT2** (weak acceptor). This is reflected from the red-shifted absorption maxima of **OT1** at 538 nm, compared to the absorption maximum of **OT2** at 506 nm (**Figure 2.7a**). The bandgaps of **OT1** and **OT2** were calculated from the absorption onsets to be 1.71 and 1.74 eV, respectively (**Figure 2.7b**). The HOMO energy levels were measured in the film state using ultraviolet

photoelectron spectroscopy (UPS) and found to be -5.20 eV for **OT1** and -5.51 eV for **OT2** (Figure 2.7c and d).

2.3.2. Doping of the organic small molecules

Organic semiconducting molecules typically have low electrical conductivity, which hinders their use in TE applications. Doping these molecules, which alter the distribution of electrons through oxidation or reduction, can improve electrical conductivity without increasing thermal conductivity.^[33,34] In this work, the role of doping on the molecules under study was investigated using the p-type dopant FeCl_3 , which has been shown to enhance the electronic conductivity and, therefore, the TE characteristics of organic semiconductors.^[33-35] FeCl_3 exhibits solution compatibility, strong oxidation capabilities, a lower electron affinity (4.62 eV), and effectiveness at high-loading concentrations.^[33,36]

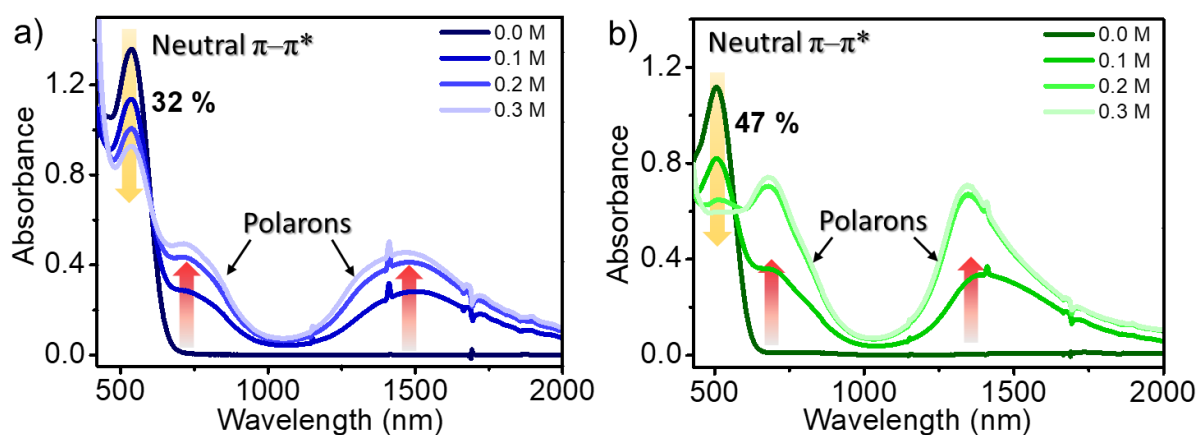


Figure 2.8. UV-Vis-NIR absorption spectral changes of a) **OT1** and b) **OT2** with increased doping of FeCl_3 (concentration of FeCl_3 is shown in the inset). The quenching of the neutral $\pi-\pi^*$ absorption and the enhancement in polaronic absorptions upon doping with FeCl_3 are denoted by yellow and red arrows, respectively.

To analyze the extent of charge transfer between the molecules and the dopant, ultraviolet-visible-near infrared (UV-vis-NIR) spectra of the sample films with various dopant concentrations were collected (**Figure 2.8**). With an increase in the dopant concentration, the emergence of new peaks were observed in both samples; 708 nm and 1459 nm for **OT1**; 683 nm and 1348 nm for **OT2**. This was associated with a lowering in the intensity of the respective π - π^* absorptions. When FeCl_3 was added to the molecules, the conjugated backbones lost an electron, became positively charged, and formed a complex with dopant anions (FeCl_4^-). The generated positive charge delocalizes over the thiophene rings, resulting in a positive polaron with a charge of $+e$ and a spin of $1/2$. This creates localized electronic states in the semiconductor bandgap,^[34] as evidenced by the new peaks in the absorption spectra. The ratio of the polaronic absorption band to the neutral absorption band determines the concentration of polarons.^[33] This ratio was higher in **OT2** (0.66) than in **OT1** (0.36), indicating a higher doping efficiency and, therefore, a higher potential for better electrical conductivity in **OT2** films.

X-ray photoelectron spectroscopy (XPS) was used for analyzing the elemental composition of both the pristine and doped samples (**Figure 2.9**). The presence of Fe2p and Cl2p peaks in the XPS survey spectrum of the doped samples confirms the incorporation of the dopant into the thin films. The concentration of FeCl_3 varied from 0.05 M to 0.30 M, resulting in Fe doping concentrations of 0.5-5.2 wt% in both films. It should be noted that XPS elemental analysis is only valid for the few atomic layers

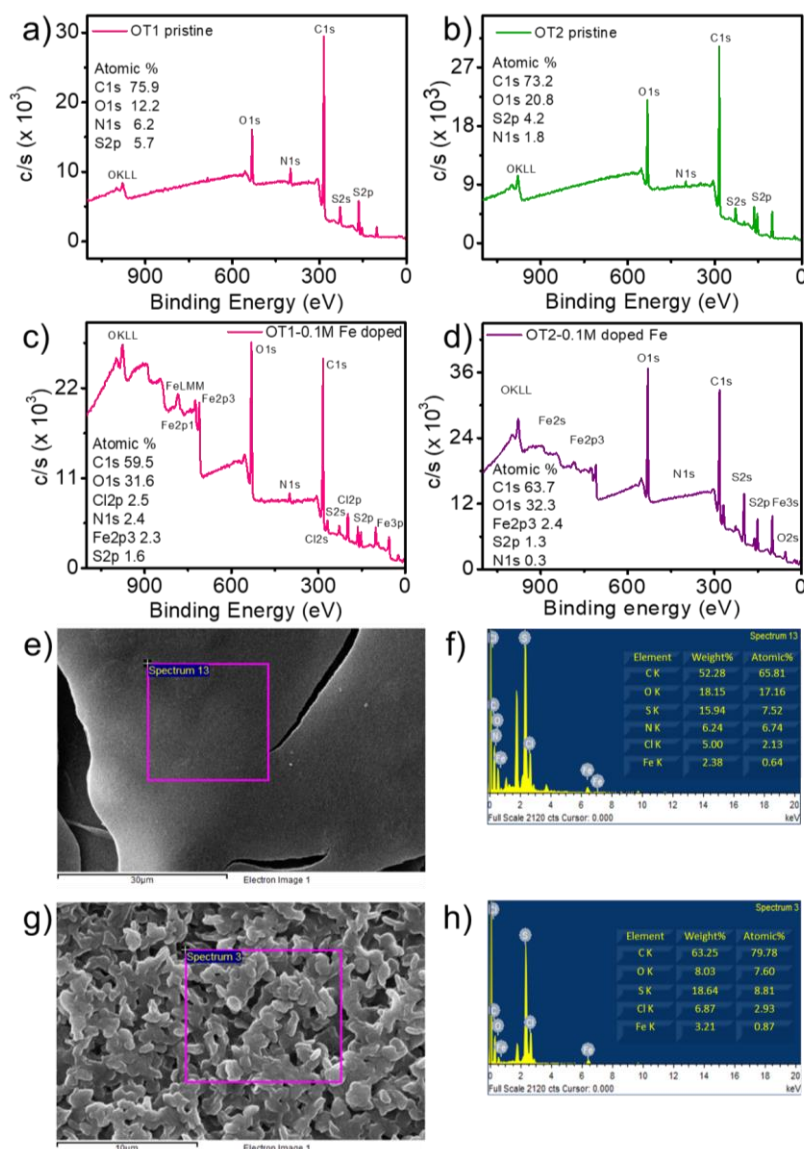


Figure 2.9. XPS survey spectra of a), b) pristine and c), d) 0.10 M FeCl_3 doped films of **OT1** and **OT2** respectively, SEM images of e) **OT1**, g) **OT2** doped with 0.10 M FeCl_3 , The corresponding elemental composition obtained from the SEM-EDX analysis of f) **OT1**, h) **OT2** doped with 0.10 M FeCl_3 .

beneath the surface, so some discrepancy with the full thickness of the films may be expected. More precise doping concentration ranges were obtained using scanning electron microscopy (SEM) equipped with energy dispersive X-ray spectroscopy (EDX) on the doped films (**OT1** and **OT2** with 0.10 M dopants; **Figure 2.9**), which

validated the presence of 2.3-2.4% Fe. Previous research by Liang *et al.* has shown that the efficiency of p-type doping in an organic semiconductor is influenced by the difference in ionization energy (IE) of the semiconductor and the electron affinity (EA) of the dopant.^[33] A larger difference between these two parameters generally results in higher doping efficiency. In this case, the ionization energy (equivalent to HOMO of organic molecules) of **OT1** and **OT2**, as determined by UPS, was 5.20 and 5.51 eV, respectively. According to literature reports, the electron affinity of FeCl₃ is 4.62 eV.^[36] The difference between the ionization energy of the molecule and the electron affinity of the dopant was 0.58 eV for **OT1** and 0.89 eV for **OT2**, indicating a higher doping efficiency possibility for **OT2**. This difference should be responsible for the increased concentration of polarons observed in **OT2**.^[33]

There are several mechanisms possible for the extrinsic doping of organic semiconductors. One of them is the integer charge transfer between semiconductor and the dopant, which requires suitably aligned LUMO of the dopant (or EA) and HOMO of the organic molecule (or IE). This generates negative charge on the dopant and counter charge on the organic molecule.^[15,33] Since organic molecules are having a deep HOMO, it never matches with the electron affinity of common oxidizing agents such as FeCl₃. Such semiconductor/dopant systems follow the charge transfer complex mechanism, through the hybridization of the molecular orbitals of both semiconductor and dopant.^[37] Another mechanism is the formation of Lewis acid-base adduct through the interaction between the electron deficient Fe³⁺ ions from the

dopant and the electron rich heteroatom on the organic semiconductor. The acid-base adduct formation results in positively charged species or radical cations in the organic semiconductor matrix, which enhances the carrier concentration.^[38,39] Matching between the HOMO of the semiconductor and electron affinity of the dopant are not necessary in such systems. In the present case, the formation of Lewis acid-base adduct formation could be the plausible mechanism of doping due to the presence of electron rich and easily oxidizable sulphur atoms on the molecules.

2.3.3. Doping-related charge transfer states

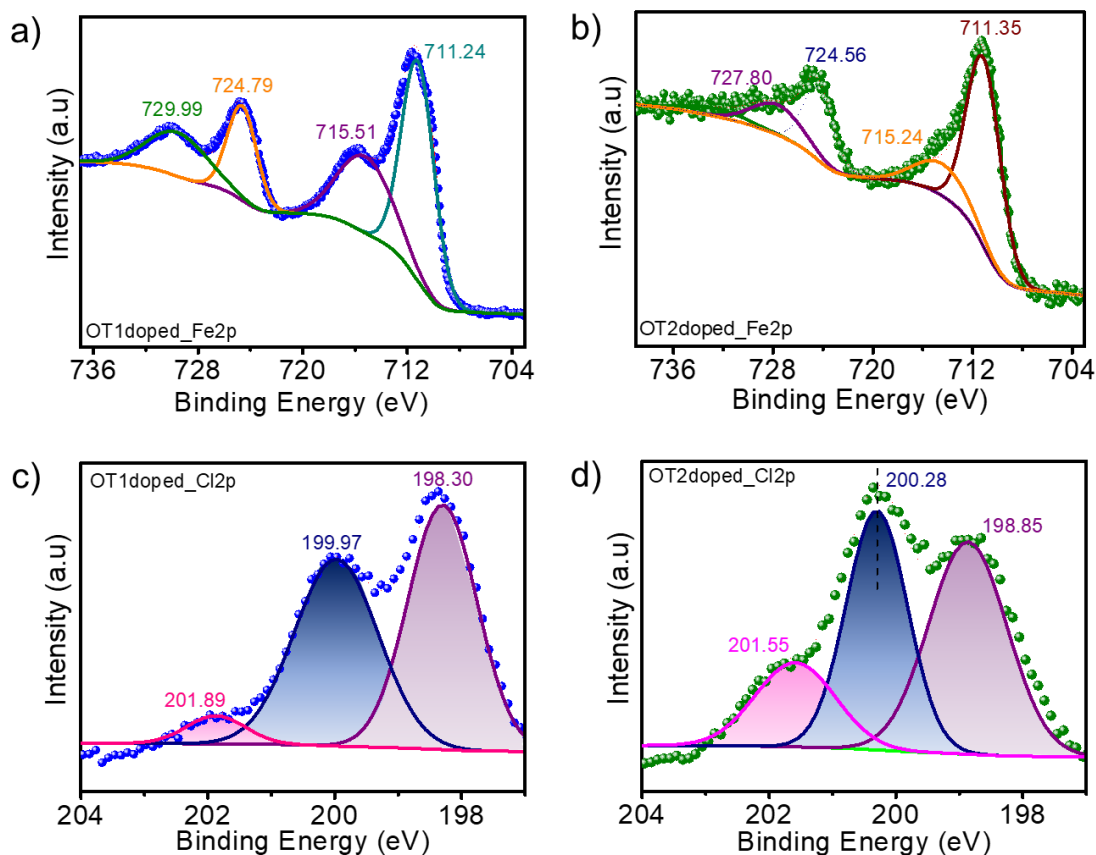


Figure 2.10. High-resolution XPS spectra of Fe2p for a) OT1 and b) OT2, Cl2p for c) OT1 and d) OT2 films doped with 0.10 M FeCl₃.

XPS stands as a valuable tool for delving into the electronic properties of doped organic semiconductors, which includes the identification of charge transfer complexes. **Figure 2.10** presents the high-resolution XPS core-level spectra of Fe2p and Cl2p for doped samples. The deconvolution shows that the Fe2p_{3/2} and Fe2p_{1/2} peaks for **OT1** are found at binding energies ~711.24 and ~724.79 eV, respectively (**Figure 2.10a**). On the other hand, the same peaks were observed at ~711.35 and ~724.56 eV, respectively, for **OT2** (**Figure 2.10b**). This confirms the presence of Fe³⁺ cations in the form of [FeCl₄]⁻.^[40] The presence of characteristic shake-up satellite peaks for both samples at ~715.51, ~729.99 eV for **OT1**, and ~715.24, ~727.80 eV for **OT2**, affirms the existence of Fe³⁺. The Cl2p core level spectra can be resolved into two peaks corresponding to Cl2p_{3/2} at ~198.30 and ~199.97 eV for **OT1** (**Figure 2.10c**) and ~198.85 and ~200.28 eV for **OT2** (**Figure 2.10d**). The peaks at ~198.30 in **OT1** and ~198.85 eV in **OT2** denotes the Fe-Cl bonding in FeCl₄⁻. FeCl₄⁻ formed during the doping acts as a counter ion to the thiophene radical cation. The peak at ~199.97 eV for **OT1** is due to ionic chlorine (Cl⁻).^[40,41] However, the peaks close to ~200.28 eV in **OT2** correspond to C-Cl bonding. The core level spectra showed higher intensity at this binding energy region for **OT2**, which denotes a higher proportion of C-Cl bonding, whereas, in **OT1**, a higher proportion of Fe-Cl bonding is observed. This demonstrates a higher doping level in the case of **OT2**. A similar observation with a higher proportion of C-Cl bonding in PBDB-T was reported by Tang *et al.*^[42,43] The low intense peaks at ~201.89 eV in the former and ~201.55 eV in

the latter correspond to the $Cl_{2p_{1/2}}$. Hence, varying acceptor strength leads to different molecule-dopant energetics and results in the disparity of the molecules towards $FeCl_3$ doping. A weak acceptor in **OT2** would be a less competitor for the p-dopant. In contrast, the strong acceptor in **OT1** can take up the electrons from the donor unit (thiophene backbone), thus hindering the hole transfer process between the $FeCl_3$ and donor unit leading to lower doping efficiency.

2.3.4. Thermoelectric properties

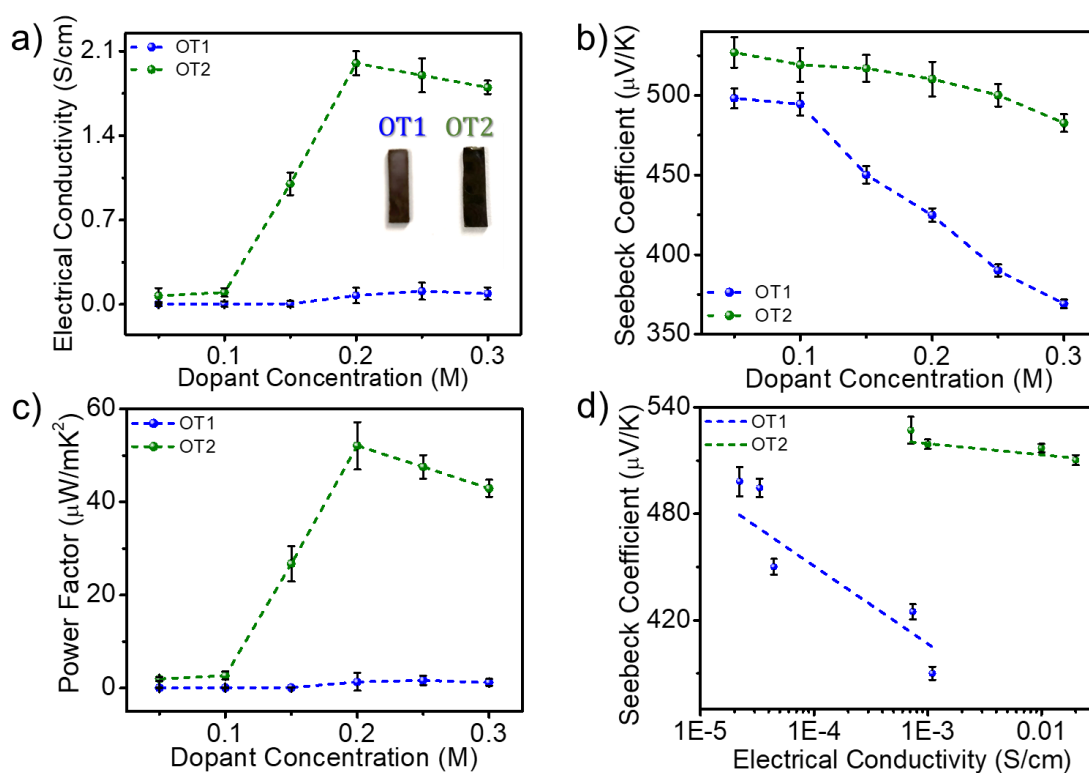


Figure 2.11. a) Electrical conductivity, b) Seebeck coefficient, and c) Power Factor of **OT1** and **OT2** with varying doping concentrations of $FeCl_3$ measured at 303 K, d) Seebeck coefficient plotted as a function of electrical conductivity ($\ln \sigma$) for **OT1** and **OT2**. The error bars represent the standard deviation of data from five samples. Device photos are shown in the inset.

Figure 2.11 shows the σ , α , and PF of pristine and doped samples. The σ of pristine films was low, in the order of 10^{-4} Scm^{-1} ($1.1 \times 10^{-4} \text{ Scm}^{-1}$ for **OT1**; $2.5 \times 10^{-4} \text{ Scm}^{-1}$ for **OT2**). A significant increase in σ was observed for **OT2** with increasing FeCl_3 concentration, whereas only a moderate increase was observed in **OT1**. A peak σ value of $\sim 0.02 \text{ Scm}^{-1}$ was obtained for **OT2** with 0.20 M dopant. On the other hand, a peak value of only $1.1 \times 10^{-3} \text{ Scm}^{-1}$ was obtained for **OT1** with 0.25 M dopant. No further increase in σ was observed by increasing FeCl_3 concentration beyond 0.25 M for **OT1** and 0.20 M for **OT2**. Both films showed positive Seebeck values, which confirm the p-type characteristics of the molecules. They showed a decreasing trend with increasing dopant concentration. Mott's relation can explain this inverse relationship between σ and α (**Equation 1.4**). In this equation, the Seebeck coefficient, Boltzmann constant, absolute temperature, and carrier concentration are represented by α , k_B , T , and n , respectively.^[44,45] According to this relationship, increasing n upon doping would improve σ and reduce α . **Figure 2.11d** shows a well-defined linear relationship with a negative gradient between α and $\ln \sigma$, which indicates the trade-off between them with an increase in doping concentration.^[46] Similar relationships were previously reported in polymers like poly(3-octylthiophene), poly(2,5-bis(3-tetradecylthiophen-2-yl)thieno[3,2-b]thiophene), and polyaniline.^[47-49] As the graph suggests, the trade-off relationship is disproportional for the two derivatives under study, which is highly favourable for **OT2**. In other words, both pristine films possess high α , but the low σ limits their TE performance.

When σ was increased by doping with FeCl_3 , α of **OT1** decreased drastically, whereas α of **OT2** had been reduced only marginally. As a result, **OT2** exhibited a peak PF of $52.0 \mu\text{Wm}^{-1}\text{K}^{-2}$ @ 0.20 M dopant concentration which is about 31 times higher than the peak PF of **OT1** ($1.6 \mu\text{Wm}^{-1}\text{K}^{-2}$ @ 0.25 M dopant concentration).

The disparity in the TE behavior of the molecules can be correlated to the differences in doping efficiency and polaron formation. Recently, Tam *et al.* reported that α could be described as the flow of entropy per unit charge across a junction, which can be obtained from a combination of two distinct contributions.^[50]

$$\alpha = \alpha_{\text{presence}} + \alpha_{\text{transport}} \quad (2.1)$$

where α_{presence} represents the variation in the entropy of the system due to the introduction of a charge carrier, whereas $\alpha_{\text{transport}}$ is calculated as the net energy transferred in moving a single charge carrier divided by the product of the elementary charge (q) and temperature (T). The contribution of $\alpha_{\text{transport}}$ to the Seebeck coefficient depends on the charge transport mechanism. The α_{presence} can be further decomposed into changes in three individual physical phenomena, such as entropy of mixing (ΔS_{mixing}), spin entropy (ΔS_{spin}), and vibrational entropy ($\Delta S_{\text{vibration}}$) by the introduction of a carrier with a charge of q .

$$\alpha_{\text{presence}} = (\Delta S_{\text{mixing}} + \Delta S_{\text{spin}} + \Delta S_{\text{vibration}})/q \quad (2.2)$$

The addition of charge carriers will result in the formation of polarons when the charge carrier is strongly coupled to the lattice vibrations or phonons of the material. Polarons in organic semiconductors can be either localized or delocalized, depending on the strength of the electron-phonon coupling, the size of the polaron, the intrachain/intermolecular distribution of the frontier molecular orbitals, and the temperature of the material. In general, a polaron is considered to be localized when it is confined to a small region of the material, and its wave function has a well-defined shape. On the other hand, a polaron is considered to be delocalized when it is spread out over a large region of the material, and its wave function has a diffuse shape. If a polaron is delocalized, the charge carriers can move more freely through the material without being confined to a small region, making charge transport more effective. If a polaron is delocalized and spans over more atoms, the vibrational modes of the atomic sites that the polaron occupies can become softer, which means that they can vibrate more easily. This can be considered as a "softening" of the lattice; one of the most important consequences of this softening is the increase of total change in vibrational entropy ($\Delta S_{\text{vibration}}$) for the polaron. This increase in $\Delta S_{\text{vibration}}$ enhances the Seebeck coefficient. Additionally, when the polaron moves between various locations in the system due to the thermal motion of the atoms at these locations, the vibrational energy transferred with the polaron also adds to the Seebeck coefficient as part of $\alpha_{\text{transport}}$. In the present work, higher doping efficiency and polaron formation was observed in **OT2**, as is evident from UV-Vis-NIR absorption and XPS analysis. This

translates to an increased α for **OT2** than **OT1**, resulting in an overall increase in PF for the former.

2.3.5. Charge carrier mobility

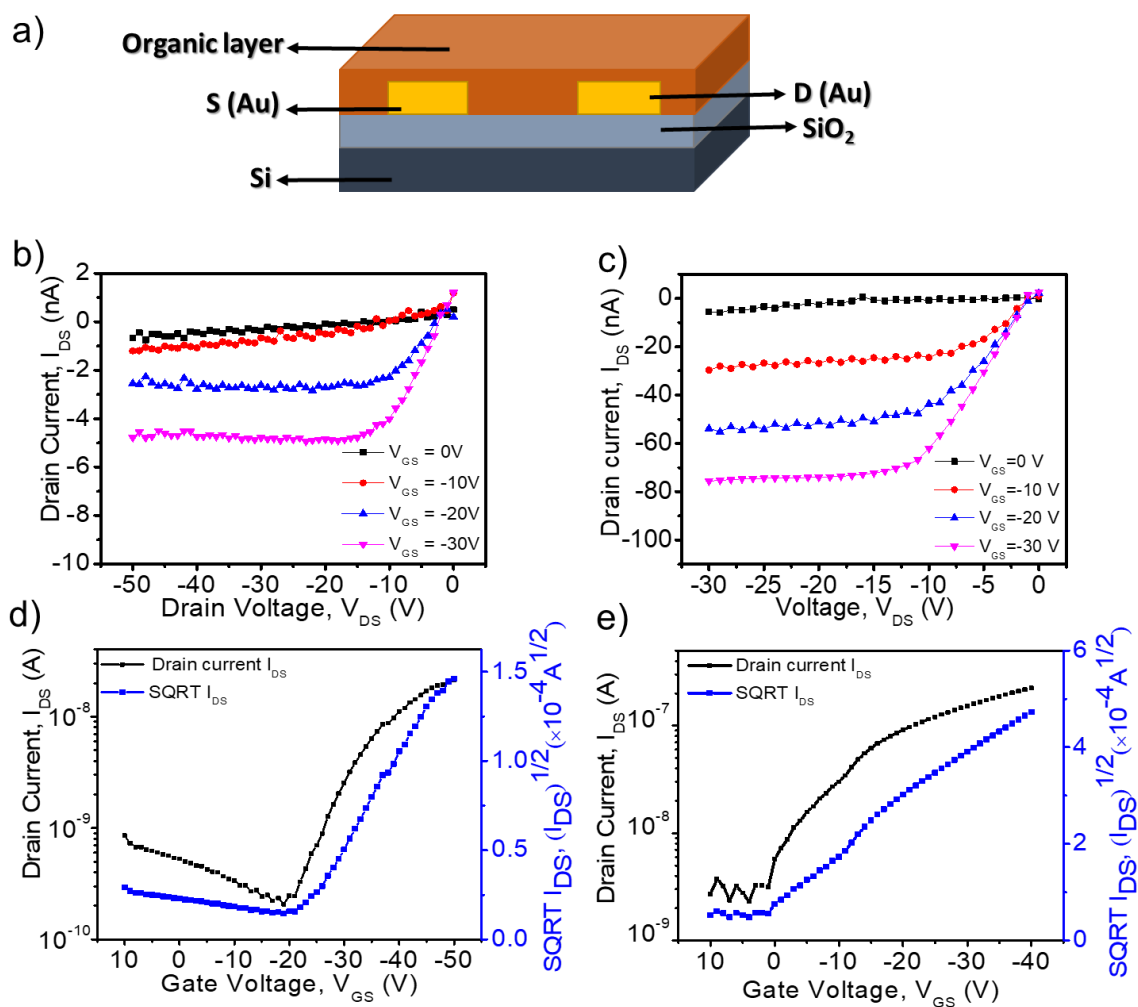


Figure 2.12. a) The schematic structure of the bottom-gate, bottom contact based FET device, FET output characteristics of b) **OT1** c) **OT2**, FET transfer characteristics d) **OT1** e) **OT2**.

Charge carrier mobility was determined using field-effect transistor (FET) measurements. The FET device structure and characteristics are given in the **Figure 2.12**. Mobility (μ) was calculated using the equation,

$$\mu = \frac{2L}{WC_i} \times \left(\frac{\partial \sqrt{I_{DS}}}{\partial V_{GS}} \right)^2 \quad (2.3)$$

where L is the channel length, W is the channel width, C_i is the capacitance per unit area of the insulator, I_{DS} is the output current in the saturation region, and V_{GS} is the gate voltage.^[51] We adopted a bottom gate–bottom contact FET device architecture to acquire hole mobility (μ_h) values. Mobility values were extracted from the saturation region of the transfer curves. **OT1** and **OT2** exhibits a value of $2.28 \times 10^{-4} \text{ cm}^2/\text{Vs}$ ($n= 0.12 \times 10^{19} \text{ cm}^{-3}$) and $5.33 \times 10^{-3} \text{ cm}^2/\text{Vs}$ ($n= 5.2 \times 10^{19} \text{ cm}^{-3}$), respectively. The variance in charge carrier mobility is responsible for the differing TE performance among these derivatives.

2.3.6. Surface morphology

The electrical and TE performance of organic semiconductors can be significantly influenced by the surface morphology and self-assembly of these materials. Surface morphologies of the pristine and doped films obtained using an atomic force microscope (AFM) are displayed in **Figure 2.13**. AFM image of the pristine molecules shows smooth, terraced-like surfaces for **OT1** and leaf-like intercalating networks for **OT2**. The change in morphologies are attributed to the different stacking of the molecules on the substrate.^[32] Upon incorporation of the dopant, charge carriers

generated in the film, leading to enhancement in σ . However, the intercalation of dopant ions can influence the film structure on a micro and macro scale, which in turn can affect its electrical and TE properties. In this study, significant morphological changes were observed in the films upon intercalation of dopants. In the case of **OT1**,

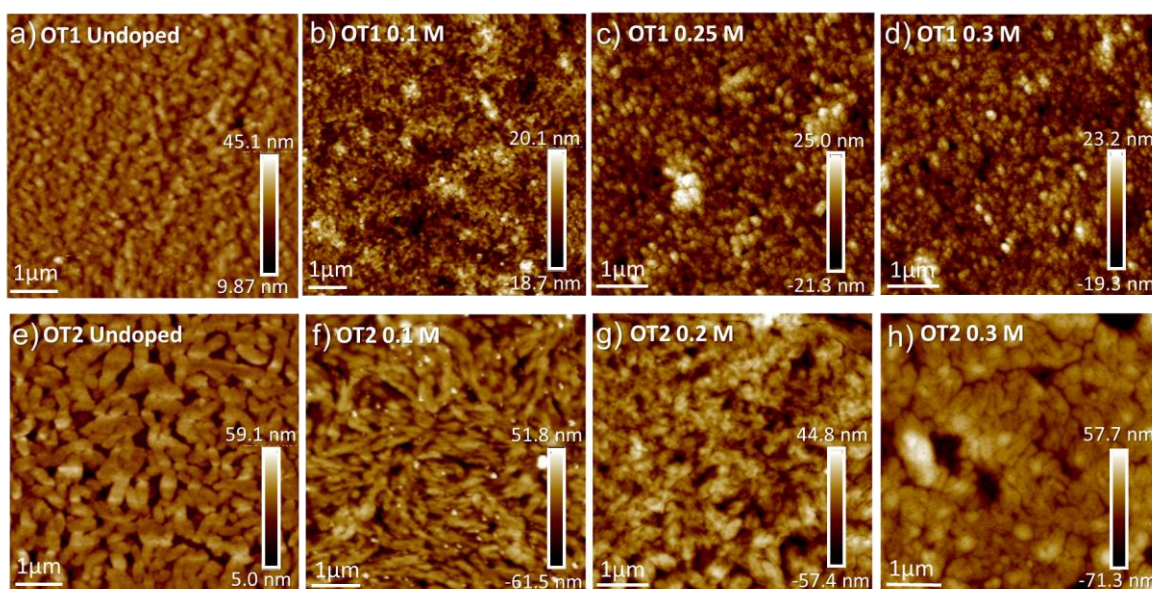


Figure 2.13. AFM images of drop-cast a) - d) **OT1**, e) - h) **OT2** with varying FeCl_3 concentration.

complete destruction of the self-assembled structures and lose of connectivity between the aggregates was observed. However, though there were notable changes in the morphology, the self-assembled structures remained intact and well connected in **OT2** after the addition of the dopant. It should be noted that the size and shape of the self-assembled nanostructures of the molecules have a significant impact on their electrical conductivity and TE performance.

Generally, in a polycrystalline film, the grain boundaries can trap the charge carriers, hindering their effective transport. Grain boundaries often lead to different

energy landscapes for the charge carriers. It includes deep/shallow valley or high/low energy barriers for the charge carriers. In other words, more the grain boundaries present, the lower the electrical conductivity. The grain size of the nanostructures was

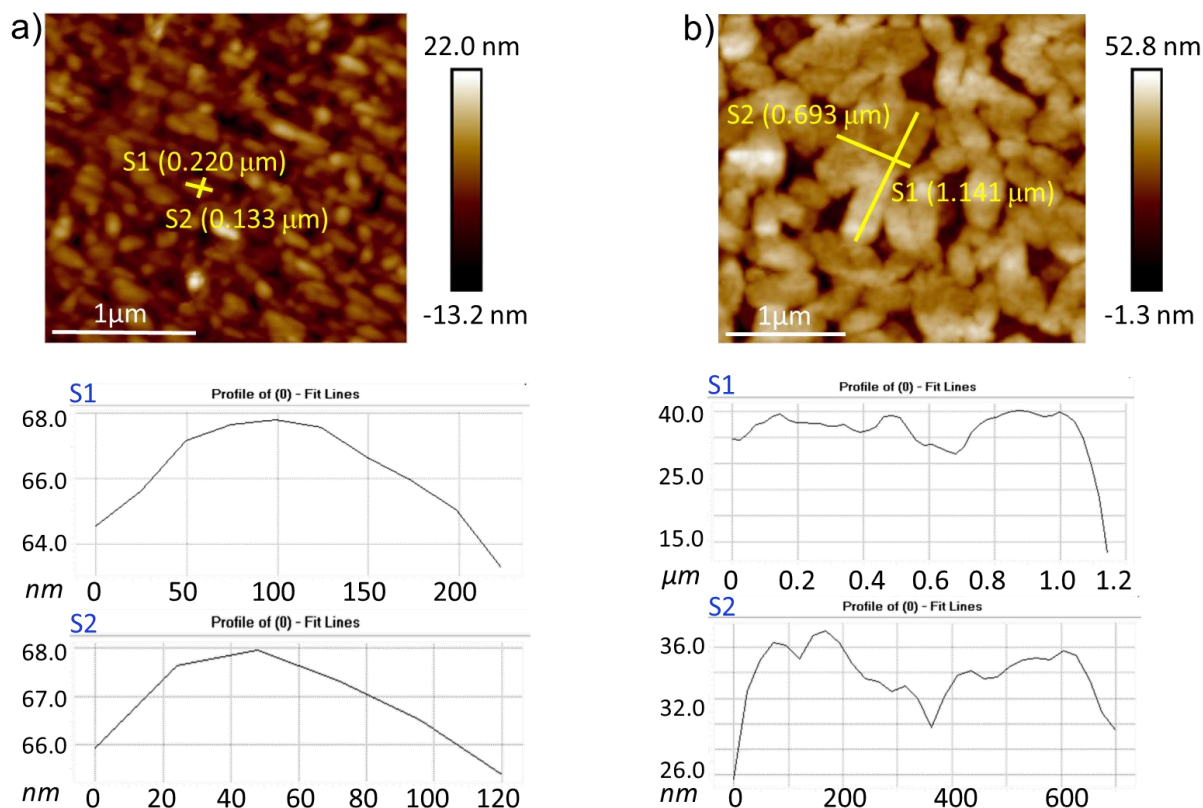


Figure 2.14. AFM morphology of a) OT1 and b) OT2, the grain length and width are indicated by yellow lines. Corresponding line cut profiles are shown in the lower panel. The length and width of the grains are indicated by S1 and S2, respectively.

calculated from the AFM morphology using the corresponding line-cut profiles (Figure 2.14). OT2 consists of larger grains ($\sim 0.791 \mu\text{m}^2$) with fewer grain boundaries, whereas OT1 has smaller grains ($\sim 0.029 \mu\text{m}^2$) and more grain boundaries. The retention of self-assembled structures, even after doping and the presence of

larger grains with fewer grain boundaries in **OT2**, resulted in higher electrical conductivity and better TE performance.

2.3.7. XPS Valence band spectra

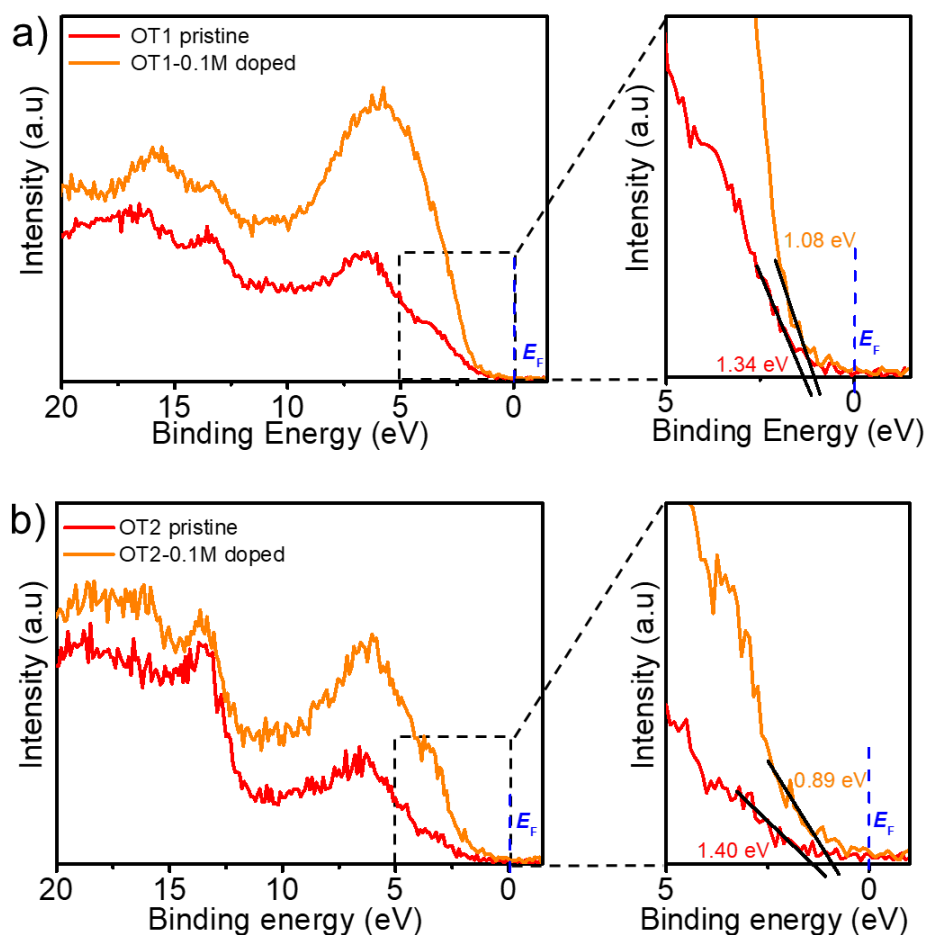


Figure 2.15. XPS Valence band spectra of a) **OT1** and b) **OT2** before and after doping. The corresponding zoomed area near the onset of the spectra and Fermi level is shown on the right side.

The impact of doping on Fermi level alignment of both samples was analyzed using XPS. Fermi level alignment refers to the adjustment of the Fermi energy (the highest energy level occupied by electrons at absolute zero temperature) at the interface of two materials with different work functions. In the context of organic TE

materials, it is important to align the Fermi energy levels of the organic semiconductor with the energy levels of the metal contacts in order to achieve efficient charge transport and maximize the TE performance. When a metal is brought into contact with an organic semiconductor, there is an energy level mismatch between the Fermi levels of the two materials, which can lead to charge carrier injection barriers and reduced electrical conductivity. By adjusting the Fermi energy levels of the organic semiconductors through doping, it is possible to achieve better charge carrier injection and increase the electrical conductivity of the organic semiconductor. This in turn can improve the TE performance of the material by increasing the power factor and reducing the thermal conductivity.

XPS spectra revealed the evolution of the density of states (DOS) distribution near the valence band maximum (VBM) and Fermi level alignment on FeCl₃ doping (**Figure 2.15**). High-purity gold coating on the substrate was used as the energy reference. The VBM position was found by extrapolating the low binding energy edge of the spectrum and its intersection with the internal baseline. The electronic DOS of the semiconductors is related to α and PF through the transport equation,

$$\alpha = \frac{\pi^2 k_B^2 T}{3e} \left(\frac{\partial \ln \mu}{\partial E} + \frac{\partial \ln N}{\partial E} \right)_{E_f} \quad (2.4)$$

In this equation, the Boltzmann constant, absolute temperature, electron charge, and carrier mobility are represented by k_B , T , e , and μ , respectively. Here, $N(E_f)$ is related to the DOS and its slope at the Fermi level (E_F), which is related to α .^[52,53] In the case of the pristine films, the density of states (DOS) is centered on the HOMO

levels, which are responsible for charge transport. However, upon doping with FeCl₃, there is a significant increase in the DOS, which is indicative of a higher carrier density. As a result, there is an overall improvement in the electrical conductivity of the material. The increased carrier density initially fills the deep trap states and then shifts the Fermi level closer to the transport level (*i.e.*, HOMO). This proximity of the Fermi level to the HOMO results in a lower activation barrier for charges in the vicinity of the HOMO. When dopants such as FeCl₃ are added to a semiconductor, the Fermi level is pinned at a crossover point between the donor-like states of the organic molecules and the acceptor-like states of the dopant. The $E_F - E_{\text{HOMO}}$ of **OT1** and **OT2** before doping were ~1.34 and ~1.40 eV, respectively. On doping, the HOMO of both molecules moves closer to the reference E_F .^[19] Here, the HOMO moves closer to the Fermi level in **OT2** (0.89 eV) than in **OT1** (1.08 eV), considerably increasing the σ of the former. Further, the XPS results suggest that the lower the difference in $E_F - E_{\text{HOMO}}$, the more proportionate the α vs. $\ln \sigma$ plot indicating the trade-off relationship between α and σ . **Figure 2.16** show the binding energy changes of C1s and S2p of the pristine and doped samples. Compared to the pristine samples, C1s and S2p peaks are shifted slightly towards the lower binding region after doping with FeCl₃. This binding energy shift towards the lower energy region indicates the overall aligning of E_F towards HOMO,^[28] which is in agreement with the XPS results.

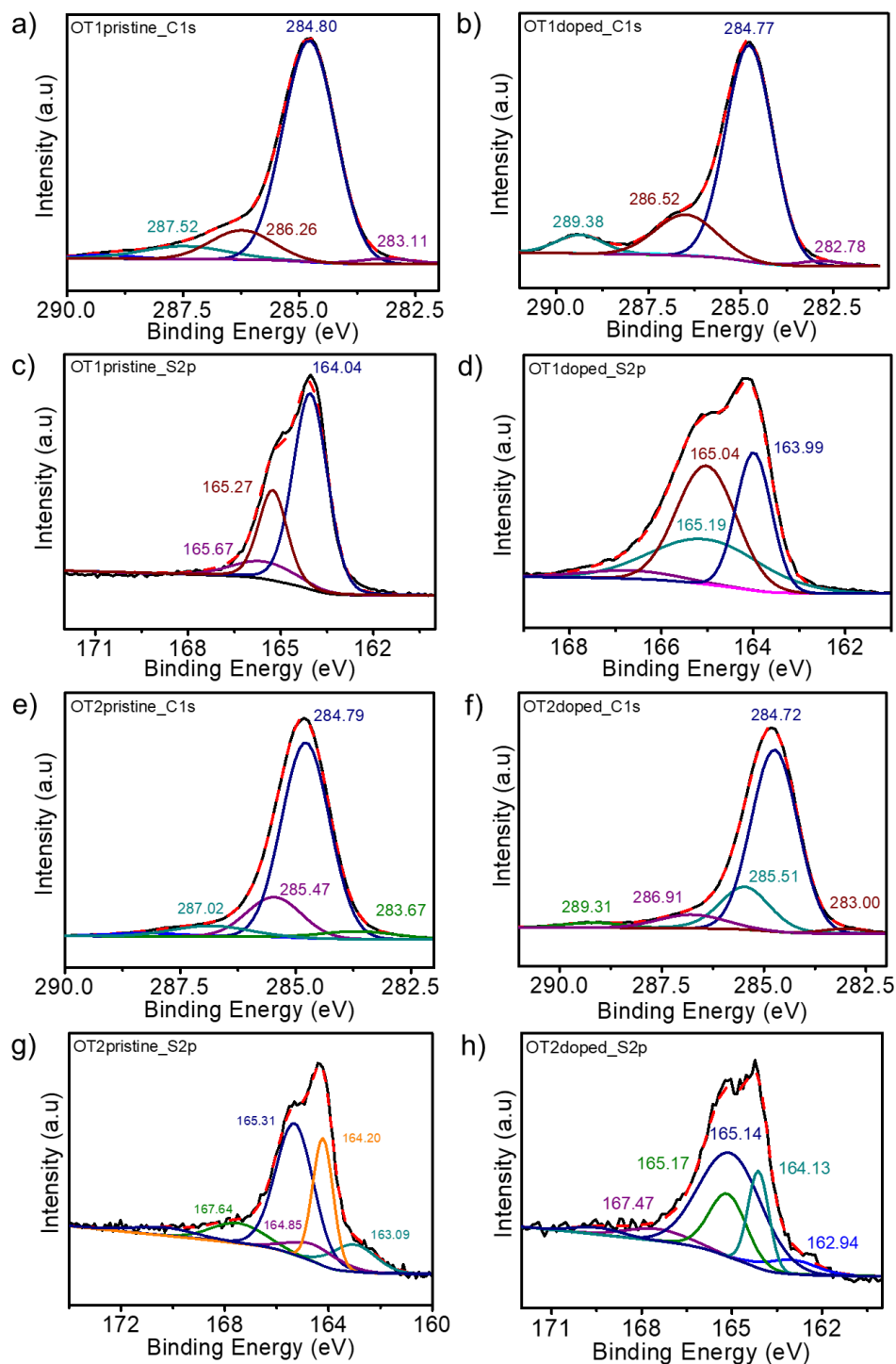


Figure 2.16. High resolution C1s spectra of a) pristine and b) 0.10 M FeCl₃ doped **OT1**, High resolution S2p spectra of c) pristine and d) 0.10 M FeCl₃ doped **OT1**, High resolution C1s spectra of e) pristine and f) 0.10 M FeCl₃ doped **OT2**, High resolution S2p spectra of g) pristine and h) 0.10 M FeCl₃ doped **OT2**.

2.3.8. Thermal stability

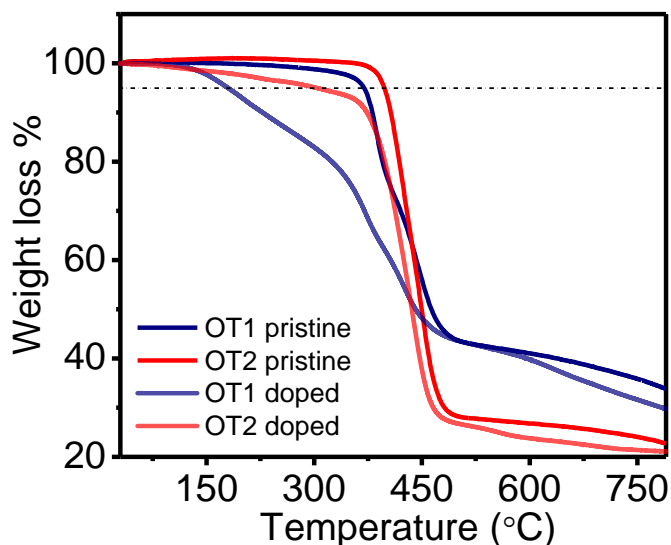


Figure 2.17. Thermogravimetric analysis of pristine and 0.10 M FeCl_3 doped **OT1** and **OT2**.

The thermal stability of the molecules were characterized using Thermogravimetric analysis (TGA). The pristine small molecules displayed good thermal stability up to 350 °C. The T_5 value showing ~5% loss were occurring above 180 °C for doped samples of **OT1** and **OT2** as shown in **Figure 2.17**. The increased thermal stability of **OT2** is attributed to the increase in alkyl chain length, which imparts better intermolecular interactions that contributes to the better thermal stability.

As observed from the UV-Vis-NIR, UPS, and XPS spectra, higher doping efficiency in **OT2** leads to the HOMO shifting closer toward E_F . Hence, it could be inferred that the α depends strongly on the electron-withdrawing capability of the acceptor units. A higher doping efficiency could also be achieved by tuning the acceptor strength, resulting in an increased PF. Morphological analysis through AFM proves that the retention of the self-assembled structures in post-doped **OT2** also

supports the enhancement σ . Such minimum variations in the molecular structure lead to a remarkable difference in the TE performance of organic semiconductors. The achieved power factor for **OT2** is competitive enough with the similar materials reported in literature. Besides, we compared the TE performance of a few p-type organic semiconductors (with or without dopants) to that of **OT2/FeCl₃** system and are summarized in **Table 2.1**.

Table 2.1. Comparative table showing TE performance of a few p-type organic semiconductors reported in literature with that of **OT2/FeCl₃** system in the present study.

Compound	Dopant	σ (S/cm)	α (μ V/K)	PF (μ W/mK ²)	ZT	Ref
Pentacene	F4TCNQ	0.03	280	0.16	–	54
Pentacene	F4TCNQ	0.43	~200	2	–	54
Pentacene	Iodine	60	40-60	13	~8 x10 ⁻³	55
Pentacene	Iodine	56	~60	20	–	56
CuPc	CN6-CP	0.76	130	1.3	–	57
PBTTT	FeCl ₃ , TFSI	691	25	46.4	–	58
(BTBT) ₂ PF ₆	–	2100	15	47	–	59
(TMTSF) ₂ PF ₆	–	540	22	26	–	60
ZnPc	–	~8.1 x10 ⁻⁷	285	~6.6 x10 ⁻⁶	–	61
C ₆₀	CsCO ₃	1715	6.6	28.8	–	62
Pentacene	CN6-CP	10.1		36.4	–	63
PDFD-T	FeCl ₃	363.0	46.8	79.5	–	64
PCPDTSBT	FeCl ₃	11.9	204.6	49.80	–	65
CDT-BTZ	F4TCNQ	4.4	147.37	9.55	–	66
OT2	FeCl ₃	2	510.3	52.08	–	This work

The table summarizes the recent literature reports of a few organic semiconductors with dopants such as FeCl₃, F4TCNQ, iodine, bis(trifluoromethanesulfonyl)imide (TFSI), CsCO₃, hexacyano-trimethylene-cyclopropane (CN6-CP) for TE application.

The study on the TE properties of self-assembled thiophene derivatives reported in this work presents promising opportunities for practical applications and future directions in TE research. The findings demonstrate that small modifications in molecular structure can significantly affect the TE characteristics of organic semiconductors. One potential direction for future research could be the development of new high-performance TE materials based on the findings of this study. By leveraging molecular engineering, researchers could tailor the structure of organic semiconductors to achieve enhanced TE performance. This could lead to the creation of more efficient and cost-effective TE materials for power generation and cooling applications. Another direction could be the optimization of doping strategies for organic semiconductors. The study highlights the importance of achieving high doping efficiency for enhancing electrical conductivity and power factor in TE materials. Researchers could further investigate and develop new doping techniques to improve the performance of organic TE materials. Additionally, the study emphasizes the significance of maintaining the self-assembled structure of organic semiconductors after doping to achieve enhanced electrical properties. Researchers could explore methods for preserving the morphology and connectivity of organic TE materials post-doping, potentially leading to the development of more stable and reliable TE materials.

2.4. Conclusions

In conclusion, the TE characteristics of two thiophene-based molecules, **OT1** and **OT2**, were investigated. Both molecules have different acceptor units as their end groups. By combining UV-Vis-NIR, UPS, XPS, SEM, and AFM techniques, we found that **OT2** exhibits higher doping efficiency and a low-lying HOMO, as well as an increased density of states when doped with FeCl₃. These characteristics enhance the charge transport properties of **OT2** and can be correlated with the presence of a weak acceptor. Our results also suggest that the TE properties of these molecules are highly correlated to their molecular packing. Even though the morphology is changed, the self-assembled structure of **OT2** and their connectivity was preserved after doping, which leads to enhanced electrical conductivity. The density of states and valence band spectra analysis revealed the Fermi energy level is aligned with the valence band maximum/HOMO, resulting in an enhancement in electrical conductivity and a decrease in the Seebeck coefficient after doping. Consequently, **OT2** exhibits a power factor of 52.0 $\mu\text{Wm}^{-1}\text{K}^{-2}$, while **OT1** only shows a power factor of 1.6 $\mu\text{Wm}^{-1}\text{K}^{-2}$. These findings demonstrate that small structural modifications in organic semiconductors can tune their TE properties to achieve improved performance.

2.5. Experimental section

2.5.1. Materials and methods

Materials: All the reagents and chemicals used were purchased from Sigma Aldrich, TCI, Alfa Aesar, or SD Fine Chemicals. **OT1** and **OT2** were synthesized according to the procedures previously reported by our group.^[32]

Measurements: The thickness of the films was measured using a stylus profilometer (Veeco Dektak 6M). The radius of the stylus tip is 2 μm . Bruker Vision64 software is used as the visual user interface.

Absorption spectroscopy: Electronic absorption spectra were recorded on Lambda 950 UV-Vis-NIR spectrophotometer. The spectra in the wavelength ranging from 250 to 2000 nm was recorded. The instrument control and data manipulation software used is UV WinLab. The molecules were dissolved in chloroform and spin-coated on quartz substrate to form a thin film. For doped samples, the pristine thin-films were immersed in FeCl_3 /nitromethane solution for 30 minutes and rinsed with the same solvent to remove any excess dopant present.

Atomic Force Microscopy: The tapping mode AFM images were recorded in Bruker Multimode-8HR AFM. The tip used for the measurement is NSG10/Pt and the images were processed using NanoScope analysis 1.5 software. The sample solutions were drop-cast on 1×1 cm glass substrate. The samples were air-dried and solvent was removed to form a thin film.

Thermogravimetric Analysis: The thermal stability of the samples was measured by thermogravimetric analysis (TGA; Q50 TGA from TA Instruments). The samples were heated from room temperature to 800 °C at a heating rate of 10 °C/min in nitrogen atmosphere.

Scanning electron microscopy: The relative doping level of the thin films was confirmed by scanning electron microscopy equipped with energy-dispersive X-ray spectroscopy (SEM-EDX). SEM and EDX measurements were performed using JEOL JSM – 5600 LV scanning electron microscope. The instrument is equipped with a tungsten electron source. Electron beams were subjected to an acceleration at a voltage of 15 kV, and the resultant secondary electrons were subsequently collected using a secondary electron (SE) detector. The signals were processed using SmartSEM software. The sample solutions were drop-cast on 1×1 cm glass substrate. The samples were air-dried and solvent was removed to form a thin film. In order to make the surface conductive and prevent surface charging, a 10 nm thin layer of gold is sputtered over the thin films.

X-ray photoelectron spectroscopy: XPS analysis was performed using PHI 5000 VersaProbe II, ULVAC-PHI Inc., USA, equipped with a monochromatic Al K α X-ray (1486.60 eV) excitation source. The surface chemical composition and valence band spectra in the pristine and doped thin films were obtained using XPS. The survey spectra were recorded with an X-ray source having a power of 50 W and pass energy of 187.85 eV. High-resolution spectra were recorded at 46.95 eV pass energy. The C

1s line at 284.80 eV was used as an internal energy reference. The valence band spectra were recorded from -5 to 30 eV. The samples were drop-cast on a glass substrate coated with gold (as a standard) for valence band spectra measurement.

Ultraviolet photoelectron spectroscopy: The highest occupied molecular orbital (HOMO) energy levels were obtained from ultraviolet photoelectron yield spectroscopy (UPS) measurements using Sumitomo Heavy Industry Co. PCR-202 with an excitation source consisting of a He-discharge lamp (21.22 eV). The samples were drop-cast on ITO substrate.

OFET measurement: The device was fabricated on silicon substrate, where the solution (concentration: 2 mg/500 μ L) was spin coated on the SiO₂ dielectric with gold coated source and drain electrode of 30 μ m channel length.

Film preparation for TE measurement: The molecules were dissolved in chloroform with a 50 mg/mL concentration. The substrate was cleaned by ultrasonication with Extran, distilled water, and isopropanol. The devices were fabricated by drop-casting molecules dissolved in chloroform solution on a precleaned glass substrate of dimension 16 \times 4 \times 0.7 mm. It was then dried under the ambient atmosphere. The films were doped with FeCl₃ by immersing them in FeCl₃/nitromethane solution for 30 minutes, followed by rinsing with nitromethane to remove the excess dopant.

Measurement of TE properties: The electrical conductivity of the sample films was measured using the two-probe method with a Keithley 2450 source meter. The α was

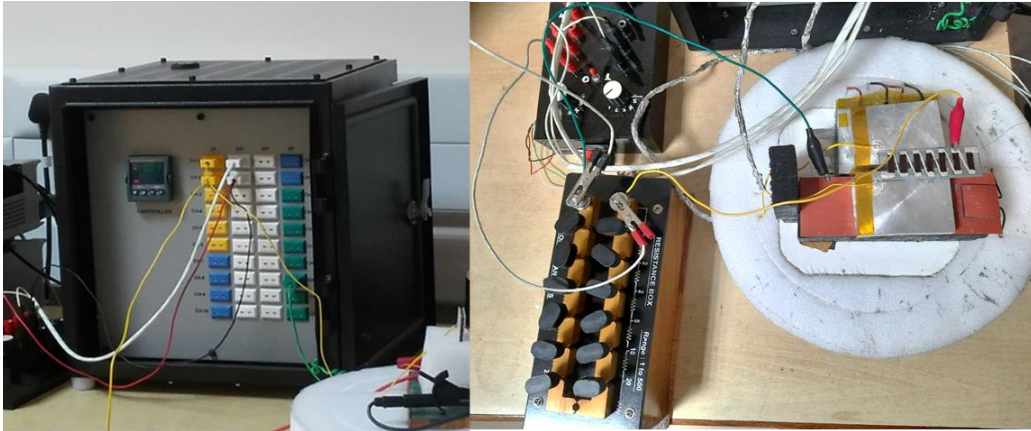


Figure 2.18. Seebeck coefficient measurement setup using a cold junction reference system.

evaluated using a custom-made measurement set up using a cold junction reference system (Tempsens™) and a delta mode system (Keithley™). The setup consisted of a silicon rubber heater (TEMPSENS Instruments Pvt. Ltd.) and a Peltier device (Laird Thermal Systems, Inc.) to maintain controlled stages that could independently function as the hot part and cold part, respectively (**Figure 2.18**). One side of the device was heated, and the other side was cooled using commercial TE modules. The exact temperature of the device terminals was measured using a K-type thermocouple. Upon providing a temperature gradient, the voltage output was measured using a Keithley 2182A nano-voltmeter. The entire setup was thermally insulated to avoid external thermal interference. The Seebeck coefficient of platinum wire was measured and used as the standard.

2.6. References

- [1] H. A. Eivari, Z. Sohbatzadeh, P. Mele, M. H. N. Assadi, *Mater. Today Energy* **2021**, *21*, 100744.

-
- [2] W. Zhao, S. Fan, N. Xiao, D. Liu, Y. Y. Tay, C. Yu, D. Sim, H. H. Hng, Q. Zhang, F. Boey, J. Ma, X. Zhao, H. Zhang, Q. Yan, *Energy Environ. Sci.* **2012**, *5*, 5364.
- [3] R. Kroon, D. A. Mengistie, D. Kiefer, J. Hynynen, J. D. Ryan, L. Yu, C. Müller, *Chem. Soc. Rev.* **2016**, *45*, 6147.
- [4] E. Liu, A. Negm, M.M.R. Howlader, *Mater. Today Energy* **2021**, *20*, 100625.
- [5] D. Beretta, N. Neophytou, J. M. Hodges, M. G. Kanatzidis, D. Narducci, M. M. Gonzalez, M. Beekman, B. Balke, G. Cerretti, W. Tremel, A. Zevalkink, Anna I. Hofmann, C. Müller, B. Dörfling, M. C. Quiles, M. Caironi, *Mater. Sci. Eng. R Rep.* **2019**, *138*, 100501.
- [6] Z. H. Zheng, X. L. Shi, D. W. Ao, W. D. Liu, M. Li, L. Z. Kou, Y. X. Chen, F. Li, M. Wei, G. X. Liang, P. Fan, G. Q. Lu, Z. G. Chen, *Nat. Sustain.* **2023**, *6*, 180.
- [7] M. Wu, K. Yao, D. Li, X. Huang, Y. Liu, L. Wang, E. Song, J. Yu, X. Yu, *Mater. Today Energy* **2021**, *21*, 100786.
- [8] I. Vijitha, N. Jacob, N. Raveendran, C. Vijayakumar, B. Deb, *Mater. Today Energy* **2022**, *31*, 101233.
- [9] C. Liu, X. Yin, S. Wang, C. Gao, L. Wang, *Chem. Eng. J.* **2023**, *451*, 138751.
- [10] H. Shang, H. Gu, F. Ding, Z. Ren, *Appl. Phys. Lett.* **2021**, *118*, 170503.
- [11] J. Cao, J. Zheng, H. Liu, C. K. I. Tan, X. Wang, W. Wang, Q. Zhu, Z. Li, G. Zhang, J. Wu, L. Zhang, J. Xu, A. Suwardi, *Mater. Today Energy* **2022**, *25*, 100964.
- [12] T. Zhu, Y. Wu, S. Li, F. F. Tonni, M. Nomura, M. Zebarjadi, *Mater. Today Phys.* **2023**, *30*, 100942.
- [13] V. Vijayakumar, Y. Zhong, V. Untilova, M. Bahri, L. Herrmann, L. Biniek, N. Leclerc, M. Brinkmann, *Adv. Energy Mater.* **2019**, *9*, 1900266.
- [14] C. K. Mytafides, L. Tzounis, G. Karalis, P. Formanek, A. S. Paipetis, *ACS Appl. Mater. Interfaces* **2021**, *13*, 11151.

-
- [15] T. Cao, X. L. Shi, Z. G. Chen, *Prog. Mater. Sci.* **2023**, *131*, 101003.
- [16] A. H. Sakr, L. Biniek, J. L. Bantignies, D. Maurin, L. Herrmann, N. Leclerc, P. Lévêque, V. Vijayakumar, N. Zimmermann, M. Brinkmann, *Adv. Funct. Mater.* **2017**, *27*, 1700173.
- [17] E. Lim, A. M. Glauddell, R. Miller, M. L. Chabinye, *Adv. Electron. Mater.* **2019**, *5*, 1800915.
- [18] H. Zeng, M. Mohammed, V. Untilova, O. Boyron, N. Berton, P. Limelette, B. Schmaltz, M. Brinkmann, *Adv. Electron. Mater.* **2021**, *7*, 2000880.
- [19] I. Vijitha, N. Raveendran, A. Prabhakaran, Y. T. Puli, C. Vijayakumar, B. Deb, *Chem. Eng. J.* **2021**, *409*, 128294.
- [20] M. P. Gordon, S. A. Gregory, J. P. Wooding, S. Ye, G. M. Su, D. S. Seferos, M. D. Losego, J. J. Urban, S. K. Yee, A. K. Menon, *Appl. Phys. Lett.* **2021**, *118*, 233301.
- [21] S. Wu, W. Xing, M. Zhu, Y. Zou, Y. Sun, W. Xu, D. Zhu, *J. Mater. Chem. C* **2021**, *9*, 4158.
- [22] S. Xu, M. Hong, X. Shi, M. Li, Q. Sun, Q. Chen, M. Dargusch, J. Zou, Z. G. Chen, *Energy Environ. Sci.* **2020**, *13*, 3480.
- [23] J. Wu, Y. Sun, W. B. Pei, L. Huang, W. Xu, Q. Zhang, *Synth. Met.* **2014**, *196*, 173.
- [24] D. Wang, J. Li, K. Yang, Y. Wang, S. Y. Jeong, Z. Chen, Q. Liao, B. Li, H. Y. Woo, X. Deng, X. Guo, *ACS Appl. Mater. Interfaces* **2023**, *15*, 9714.
- [25] J. Duan, J. Ding, D. Wang, X. Zhu, J. Chen, G. Zhu, C. Chen, Y. Yu, H. Liao, Z. Li, C. Di, W. Yue, *Adv. Sci.* **2023**, *10*, 2204872.
- [26] X. Yan, M. Xiong, J. T. Li, S. Zhang, Z. Ahmad, Y. Lu, Z. Y. Wang, Z. F. Yao, J. Y. Wang, X. Gu, T. Lei, *J. Am. Chem. Soc.* **2019**, *141*, 20215.
- [27] E. Selezneva, A. Vercouter, G. Schweicher, V. Lemaur, K. Broch, A. Antidormi, K. Takimiya, V. Coropceanu, J. L. Brédas, C. Melis, J. Cornil, H. Sirringhaus, *Adv. Mater.* **2021**, *33*, 2008708.

-
- [28] F. Zhong, X. Yin, Z. Chen, C. Gao, L. Wang, *ACS Appl. Mater. Interfaces* **2020**, *12*, 26276.
- [29] D. Huang, H. Yao, Y. Cui, Y. Zou, F. Zhang, C. Wang, H. Shen, W. Jin, J. Zhu, Y. Diao, W. Xu, C. A. Di, D. Zhu, *J. Am. Chem. Soc.* **2017**, *139*, 13013.
- [30] D. Yuan, D. Huang, C. Zhang, Y. Zou, C. A. Di, X. Zhu, D. Zhu, *ACS Appl. Mater. Interfaces* **2017**, *9*, 28795.
- [31] H. Kojima, R. Abe, F. Fujiwara, M. Nakagawa, K. Takahashi, D. Kuzuhara, H. Yamada, Y. Yakiyama, H. Sakurai, T. Yamamoto, H. Yakushiji, M. Ikeda, M. Nakamura, *Mater. Chem. Front.* **2018**, *2*, 1276.
- [32] T. Ghosh, S. Nagasawa, N. Raveendran, V. Darshan, A. Saeki, V. C. Nair, *Chem. Asian J.* **2019**, *14*, 963.
- [33] Z. Liang, Y. Zhang, M. Souri, X. Luo, A. M. Boehm, R. Li, Y. Zhang, T. Wang, D. Y. Kim, J. Mei, S. R. Marder, K. R. Graham, *J. Mater. Chem. A* **2018**, *6*, 16495.
- [34] I. H. Jung, C. T. Hong, U. H. Lee, Y. H. Kang, K. S. Jang, S. Y. Cho, *Sci. Rep.* **2017**, *7*, 1.
- [35] B. Li, X. Li, F. Yang, Y. Chen, X. Mao, S. Wan, H. Xin, S. Yan, M. Wang, C. Gao, L. Wang, *ACS Appl. Energy Mater.* **2021**, *4*, 4662.
- [36] M. M. Korobov, Y. V. Pervova, L. N. Sidorov, *Mendeleev Commun.* **1992**, *2*, 41.
- [37] H. Mèndez, G. Heimel, S. Winkler, J. Frisch, A. Opitz, K. Sauer, B. Wegner, M. Oehzelt, C. Röthel, S. Duhm, D. Többens, N. Koch, I. Salzmann, *Nature Comm.* **2015**, *6*, 8560.
- [38] A. D. Scaccabarozzi, A. Basu, F. Aniés, J. Liu, O. Z. Arteaga, R. Warren, Y. Firdaus, M. I. Nugraha, Y. Lin, M. C. Quiles, N. Koch, C. Müller, L. Tsetseris, M. Heeney, T. D. Anthopoulos, *Chem. Rev.* **2022**, *122*, 14420.
- [39] Y. Liu, B. Zhao, J. Liu, Z. Wang, Z. Liang, W. Dong, C. Xu, B. Wang, Z. Fei, Y. Han, *ACS Appl. Polym. Mater.* **2022**, *4*, 3877.

-
- [40] M.V. Russo, G. Polzonetti, A. Furlani, *Synth. Met.* **1991**, 39, 291.
- [41] C. Zhang, J. Ma, F. Han, H. Liu, F. Zhang, C. Fan, J. Liu, X. Li, *J. Mater. Chem. A* **2018**, 6, 17982.
- [42] I. Vijitha, N. Raveendran, S. Poovattil, N. Jacob, C. Vijayakumar, B. Deb, *Macromol. Mater. Eng.* **2022**, 307, 8351.
- [43] J. Tang, J. Ji, R. Chen, Y. Yan, Y. Zhao, Z. Liang, *Adv. Sci.* **2022**, 9, 2103646.
- [44] A. M. Glaudell, J. E. Cochran, S. N. Patel, M. L. Chabinyc, *Adv. Energy Mater.* **2015**, 5, 1401072.
- [45] Y. H. Kang, U.-H. Lee, I. H. Jung, S. C. Yoon, S. Y. Cho, *ACS Appl. Electron. Mater.* **2019**, 1, 1282.
- [46] W. Shi, T. Zhao, J. Xi, D. Wang, Z. Shuai, *J. Am. Chem. Soc.* **2015**, 137, 12929.
- [47] Y. Xuan, X. Liu, S. Desbief, P. Leclère, M. Fahlman, R. Lazzaroni, M. Berggren, J. Cornil, D. Emin, X. Crispin, *Phys. Rev. B* **2010**, 82, 115454.
- [48] F. Zhang, Y. Zang, D. Huang, C. Di, X. Gao, H. Sirringhaus, D. Zhu, *Adv. Funct. Mater.* **2015**, 25, 3004.
- [49] N. Mateeva, H. Niculescu, J. Schlenoff, L. R. Testardi, *J. Appl. Phys.* **1998**, 83, 3111.
- [50] T. L. D. Tam, A. Moudgil, W. J. Teh, Z. M. Wong, A. D. Handoko, S. W. Chien, S. W. Yang, B. S. Yeo, W. L. Leong, J. Xu, *J. Phys. Chem. B* **2022**, 126, 2073.
- [51] Y. Wakatsuki, K. Noda, Y. Wada, T. Toyabe, K. Matsushige, *J. Appl. Phys.* **2011**, 110, 054505.
- [52] G. Zuo, X. Liu, M. Fahlman, M. Kemerink, *Adv. Funct. Mater.* **2018**, 28, 1703280.
- [53] E. J. Dell, B. Capozzi, J. Xia, L. Venkataraman, L. M. Campos, *Nat. Chem.* **2015**, 7, 209.
- [54] K. Harada, M. Sumino, C. Adachi, S. Tanaka, K. Miyazaki, *Appl. Phys. Lett.* **2010**, 96, 253304.

-
- [55] K. Hayashi, T. Shinano, Y. Miyazaki, T. Kajitani, *J. Appl. Phys.* **2011**, *109*, 023712.
- [56] K. Hayashi, T. Shinano, Y. Miyazaki, T. Kajitani, *Phys. Status Solidi C* **2011**, *8*, 592.
- [57] W. L. Xing, J. Chen, Y. Y. Liang, Y. Zou, Y. M. Sun, W. Xu, D. B. Zhu, *RSC Adv.* **2019**, *9*, 31840.
- [58] C. Chen, I. E. Jacobs, C. Jellett, X. Jiao, J. F. Ponder, B. Kang, S. B. Lee, Y. Huang, L. Zhang, M. Statz, Y. Sun, Y. Lin, K. Kang, X. She, Y. Hu, T. Zhang, L. Jiang, *Adv. Electron. Mater.* **2022**, *8*, 2200053.
- [59] Y. Kiyota, T. Kadoya, K. Yamamoto, K. Iijima, T. Higashino, T. Kawamoto, K. Takimiya, T. Mori, *J. Am. Chem. Soc.* **2016**, *138*, 3920.
- [60] T. Kadoya, M. Ashizawa, T. Higashino, T. Kawamoto, S. Kumeta, H. Matsumoto, T. Mori, *Phys. Chem. Chem. Phys.* **2013**, *15*, 17818.
- [61] J. P. Meyer, D. Schlettwein, D. Wöhrle, N. I. Jaeger, *Thin Solid Films* **1995**, *258*, 317.
- [62] A. Barbot, C. Di Bin, B. Lucas, B. Ratier, M. Aldissi, *J. Mater. Sci.* **2013**, *48*, 2785.
- [63] W. L. Xing, S. C. Wu, Y. Y. Liang, Y. M. Sun, Y. Zou, L. Y. Liu, W. Xu, D. B. Zhu, *ACS Appl. Mater. Interfaces* **2020**, *12*, 29540.
- [64] S. E. Yoon, B. Kim, S. Y. Chun, S. Y. Lee, D. Jeon, M. Kim, S. Lee, B. E. Seo, K. S. Choi, F. S. Kim, T. Kim, H. Seo, K. Kwak, J. H. Kim, B. S. Kim, *Adv. Funct. Mater.* **2022**, *8*, 2202929.
- [65] Y. Lee, J. Park, J. Son, H. Y. Woo, J. Kwak, *Adv. Funct. Mater.* **2020**, *31*, 2006900.
- [66] K. Kang, S. Schott, D. Venkateshvaran, K. Broch, G. Schweicher, D. Harkin, C. Jellett, *Mater. Today Phys.* **2019**, *8*, 112.

Enhancing Thermoelectric Efficiency in Benzodithiophene-Thienothiophene Copolymers: The Role of Doping-Induced Charge Transfer

3.1. Abstract

This study explores the influence of doping-induced charge-transfer states and polymer aggregation on the thermoelectric properties of F4TCNQ-doped benzodithiophene-thieno[3,2-b]thiophene-based polymers. We focused on two polymers, PBDTTT:C (P1) and PBDTTT:EFT (P2), employing a set of analytical techniques to understand their structural, electrical, and optical characteristics. Our findings reveal distinct doping behaviors: P1 forms a partial charge transfer (PCT) complex due to lower aggregation, while P2 predominantly establishes an integer charge transfer (ICT) complex attributable to higher aggregation. This distinction results in P2 exhibiting enhanced electrical conductivity and a superior thermoelectric power factor compared to P1. The study highlights the critical roles of charge-transfer mechanisms and aggregation in optimizing the thermoelectric performance of F4TCNQ-doped conjugated polymers, offering valuable insights for developing more efficient thermoelectric materials and advancing energy conversion technologies.

3.2. Introduction

Organic TE materials typically exhibit low intrinsic carrier concentrations, rendering them less conductive.^[1-5] To enhance their electrical conductivity, an essential factor for efficient TE devices, doping is employed.^[6-8] Traditional doping methods have often utilized alkali metals or halides; however, these substances are not ideal for long-term TE applications due to their high reactivity and issues with diffusion into the organic matrix, which can lead to instability and degradation of the material properties.^[9-12] Recognizing this challenge, molecular doping has emerged as a viable and effective alternative. Molecular dopants, such as 2,3,5,6-tetrafluoro-7,7,8,8-tetracyanoquinodimethane (F4TCNQ), offer a more stable and controlled means to increase the charge carrier density in organic semiconductors.^[13-16] F4TCNQ, for example, is well-regarded for its strong electron-accepting properties, making it particularly effective for p-type doping. When introduced into conjugated polymer or small molecule systems, such dopants facilitate a higher level of electrical conductivity while maintaining the structural integrity and functional stability necessary for TE applications.^[17-20]

Significant research has been conducted on the doping of polymers like poly(3-hexylthiophene-2,5-diyl) (P3HT) and poly(2,5-bis(3-alkylthiophen-2-yl)-thieno-[3,2-b]thiophene) (PBTTT) with F4TCNQ.^[21,22] These studies have shed light on the mechanisms of charge transfer, the extent of dopant incorporation, and the resultant changes in electrical conductivity and Seebeck coefficient. For instance, P3HT, when

doped with F4TCNQ, exhibits a marked increase in electrical conductivity due to the formation of charge transfer complexes, which facilitate the movement of charge carriers. Meanwhile, in systems like PBTTT, the doping not only improves electrical conductivity but also affects the material's morphology and crystallinity, which in turn influences the TE performance.

Moreover, recent advancements have focused on optimizing the doping process, such as controlling the dopant concentration and distribution throughout the semiconductor matrix, to achieve a uniform and effective doping level. Researchers are also exploring the synergistic effects of co-doping with multiple types of molecular dopants to further enhance the material's TE properties. The development and study of molecular doping in organic TE materials are crucial for the advancement of flexible, lightweight, and efficient TE devices. By improving the understanding and application of molecular dopants, researchers are paving the way for the next generation of organic TE materials with higher performance and broader applicability.

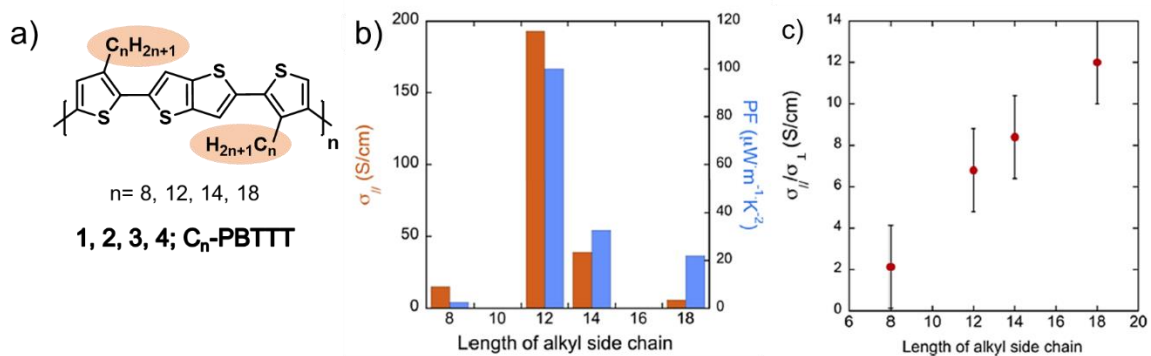


Figure 3.1. a) Molecular structures of **1-4** with varying alkyl chain length, b) Electrical conductivity and power factor along the high-temperature rubbing direction with respect to the alkyl side chain, c) anisotropic conductivity with respect to alkyl side chain. (Adapted from reference 23)

Brinkmann *et al.* investigated the effects of the side chain length and packing in a series of thienothiophene-based polymers with side chains ranging from *n*-octyl to *n*-octyldecyl (**1-4**, **Figure 3.1**). Inserting F4TCNQ into the layers of side chains causes the lattice to expand along the side chains while contracting along the π -stacking direction in all polymers. The degree of lattice expansion decreases as the length of the side chains increases. All the derivatives exhibit complete charge transfer with F4TCNQ. The doping kinetics and level of doping are influenced by both the length of the side chains and how the molecules are packed. The *n*-octyl chain being highly disordered and *n*-octyldecyl chain being highly crystalline hinders the dopant diffusion in the side chain layers, unlike the *n*-dodecyl side chains, which can accommodate a higher proportion of dopants. As a result, the best TE performance was observed for the polymer **3** with an *n*-dodecyl side chain, achieving a PF of $100 \mu\text{Wm}^{-1}\text{K}^{-2}$.^[23]

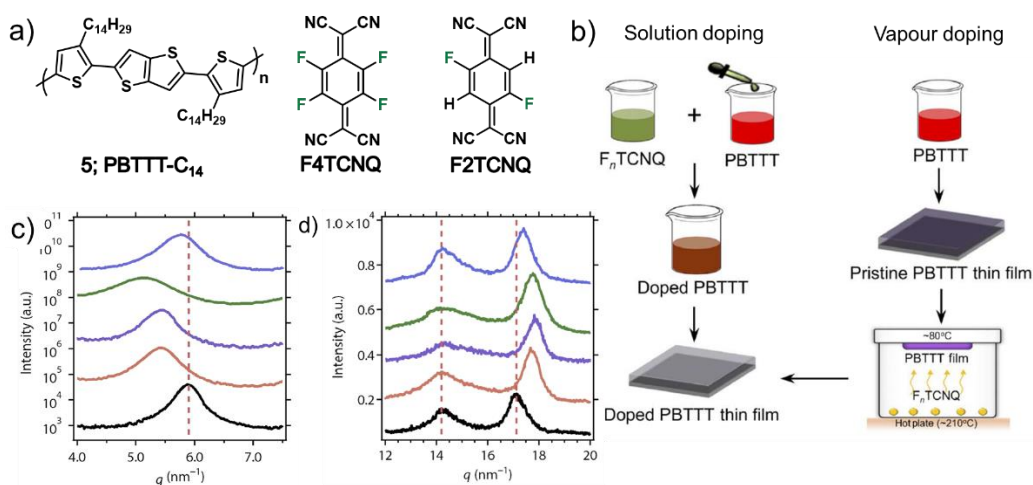


Figure 3.2. Molecular structure of **5**, dopants F2TCNQ and F4TCNQ, b) Representation of solution and vapour doping of **5** with F_nTCNQ, The line-cut profile of c) out-of-plane scattering, d) in-plane scattering. (Pristine film of **5**: black, F4TCNQ solution doping: orange, F4TCNQ vapour doping: purple, F2TCNQ solution doping: green, F2TCNQ vapour doping: blue) (Adapted from reference 24)

The incorporation of dopants is a critical aspect that influences the charge transport properties of the semiconducting polymer. Chabinye *et al.* demonstrated that a semiconducting thin film composed of a thienothiophene-based polymer forms locally π -stacked domains with extended correlation lengths of the conjugated backbones (**5**, **Figure 3.2**). They have incorporated a molecular dopant like F_nTCNQ into the polymer thin film in vapour phase that boosts n and subsequently enhance σ that caused minimal disruption to the local molecular structure. It preserved or even improved the long-range alignment of the conjugated polymer backbone. Hence, with apparently high μ and by precise control over dopant concentration, or opting for a weak molecular dopant, a substantial increase in n without causing a notable decrease in σ could be achieved. The most high-performing sample, have the largest optical coherence length, is a thin film of **5**:F4TCNQ vapour-doped material. This sample demonstrates a high σ of 670 Scm^{-1} , α of $42 \text{ } \mu\text{VK}^{-1}$ and a substantial PF of $120 \text{ } \mu\text{Wm}^{-1}\text{K}^{-2}$. Despite the less favorable charge transfer offset, the introduction of F2TCNQ as a dopant also results in a considerable PF of $70 \text{ } \mu\text{Wm}^{-1}\text{K}^{-2}$. This underscores the potential utility of weak molecular dopants in enhancing TE performance. ^[24]

Quiles *et al.* reported that the thermal conductivity of pure PBTTT films is primarily influenced by the level of crystallinity, and that they have observed a thermal percolation phenomenon at annealing temperatures exceeding $170 \text{ } ^\circ\text{C}$ (**Figure 3.3**). When a relatively small quantity of F4TCNQ dopant is introduced (with an anion content below 1 mol %) into the samples, κ decreases by a factor of two, all by retaining

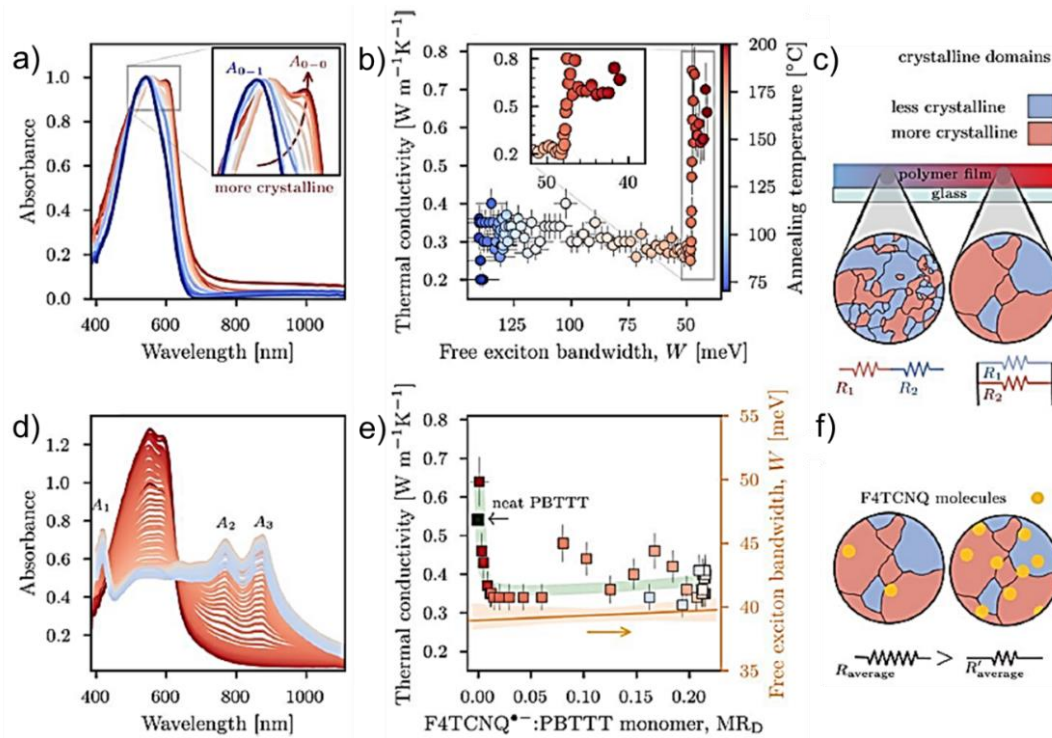


Figure 3.3. a) UV-Vis-NIR absorption spectra of PBTBT with increasing temperature, b) Thermal conductivity v/s free exciton bandwidth, c) Representation of the microstructural changes, d) UV-Vis-NIR absorption spectra of PBTBT with a gradient of doping, e) Thermal conductivity with respect to doping level, f) Representation of the microstructural changes in a doped PBTBT film as a result of varying dedoping temperatures. (Adapted from reference 25)

the crystallinity of the polymer structure. Here, they have used the Wiedemann–Franz law for studying the relationship between σ and κ . The data fit suggests that the lattice contribution of κ of doped polymers ($0.36 \text{ Wm}^{-1}\text{K}^{-1}$) is lower than the undoped polymer. This, again confirms that the inclusion of dopants contributes to a reduction in thermal conductivity. This behavior is analogous to the alloy scattering phenomenon observed in various inorganic systems. These findings indicate that the electronic component's contribution to the total κ remains insignificant until electrical conductivities surpass $\sigma = 6.8 \times 10^3 \text{ Sm}^{-1}$.^[25]

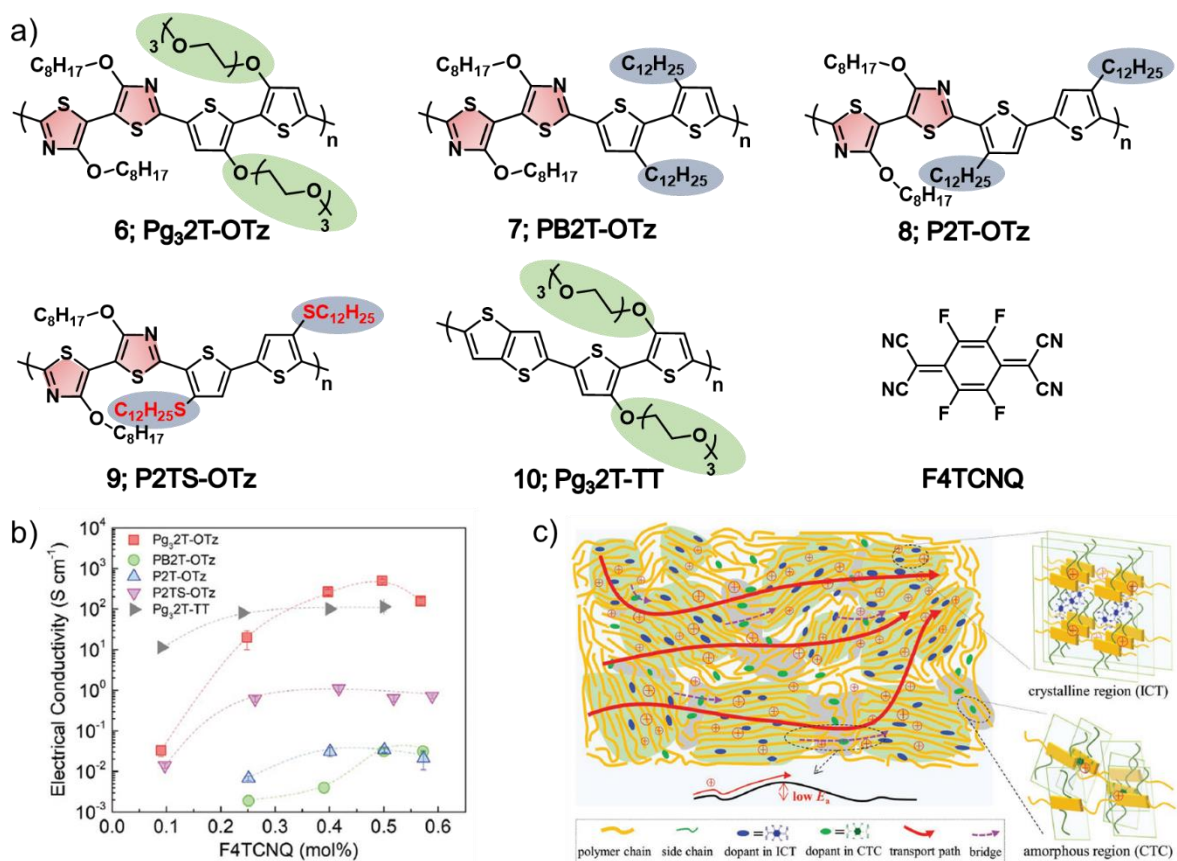


Figure 3.4. a) Chemical structures of polymers 6-10, b) Conductivity plot of polymers with respect to F4TCNQ concentration, c) Representation of dopant (F4TCNQ) intercalation into microstructure of 6. (Adapted from reference 26)

Li *et al.* explored donor-acceptor (D–A) type polymers (6-10, **Figure 3.4**) with varying side chains, such as glycolic, alkoxy, and alkyl, which influence the acceptor strength of the polymers. At a low level of doping with F4TCNQ, a complete charge transfer (ICT) is said to occur. In this scenario, the well-ordered, edge-on orientations of ICT structures effectively counteract the Coulombic interactions, facilitating long-range delocalization of holes within the material. However, at higher doping levels, a network of charge transfer complex states forms in the amorphous regions, connecting

and bridging the crystalline ICT structures. This network enhances efficient charge transport within the polymer, contributing to the overall charge transfer process. Among the polymers studied, the F4TCNQ-doped polymer **10** exhibited high mobility, resulting in a σ of 550 Scm^{-1} . The activation energy or E_a represents the energy barrier associated with charge transport. F4TCNQ-doped **6** polymer thin films show lower E_a values than polymers **9** and **10**. Hence, they propose that CTC states in amorphous regions establish a link between percolation pathways associated with crystalline ICT states, offering a more efficient method for transporting carriers.^[26]

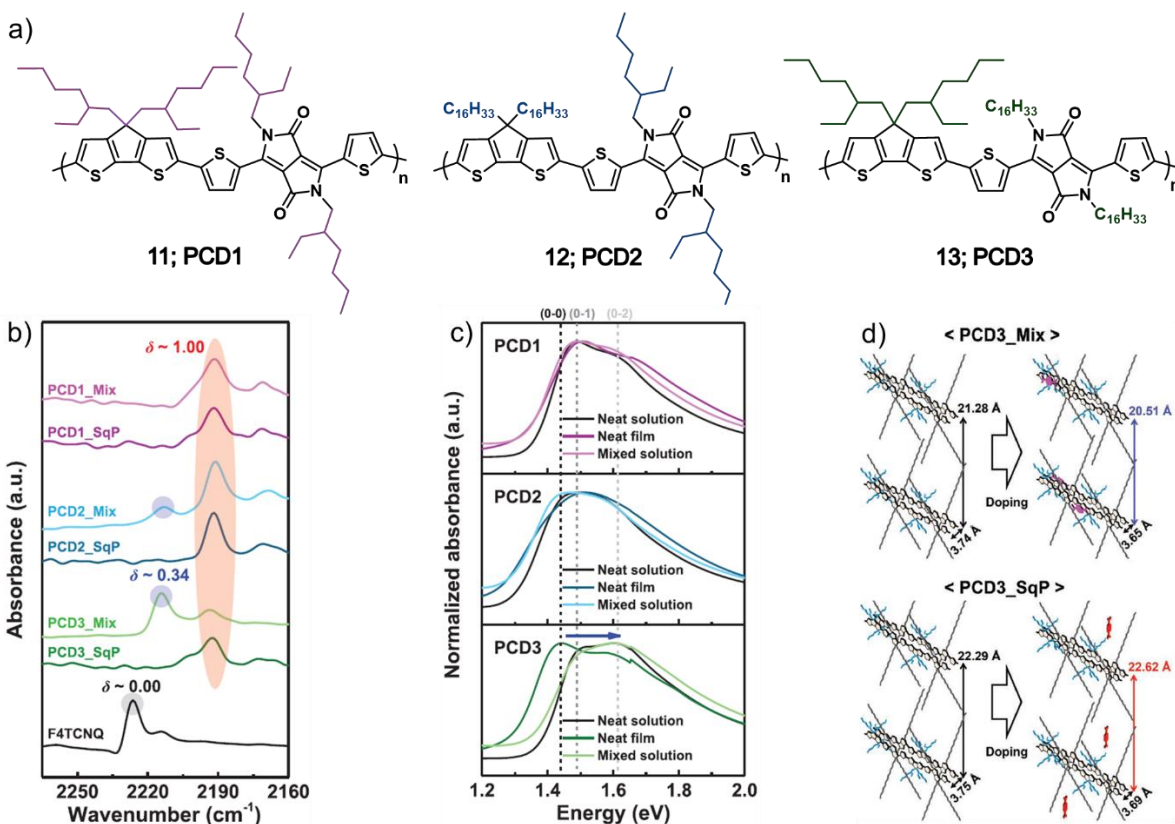


Figure 3.5. a) Molecular structures of **11-13**, b) FTIR absorption spectra of pristine F4TCNQ, F4TCNQ doped polymers, c) UV-Vis-NIR absorption spectra, d) Ordering of polymer stacking of **13**. (Adapted from reference 27)

Suh *et al.* conducted an in-depth study of the doping mechanisms of F4TCNQ-doped polymers with the same D–A backbone but different alkyl side chains (**11-13**, **Figure 3.5**). The various side chain combinations played a crucial role in influencing distinct molecular arrangements, aggregation pattern, and doping characteristics. In a polymer that has lower aggregation, the mixing of solution with the p-dopant leads to the formation of Lewis complexes, which, in turn, reduces the effectiveness of doping and the PF. Sequential processing resulted in comparable doping behaviors and power factors ($9.0\text{--}16.4 \mu\text{Wm}^{-1}\text{K}^{-1}$) among the three donor-acceptor (D-A) polymers. However, when aggregated polymer solutions are mixed, this induces the formation of ion pairs with the dopant (ICT formation), resulting in PFs that are significantly higher, reaching up to $23.7 \mu\text{Wm}^{-1}\text{K}^{-2}$. These findings offer a comprehensive insight into the effective doping of D-A polymers for TE applications in solution-state. These findings underscore the necessity of judicious polymer design strategies when employing the solution-mixing approach.^[27]

Benzodithiophene (BDT)-based polymers have gained significant attention in the fields of organic thin film transistors and solar cells, attributed to their conjugated planar backbone, electron-donating capability, and high stability towards oxidation. These polymers have been reported to exhibit high hole mobility of $0.25 \text{ cm}^2\text{V}^{-1}\text{s}^{-1}$.^[28] However, their TE properties have remained relatively unexplored. Our group has previously investigated the TE properties of a few BDT-TTE polymers by formulating

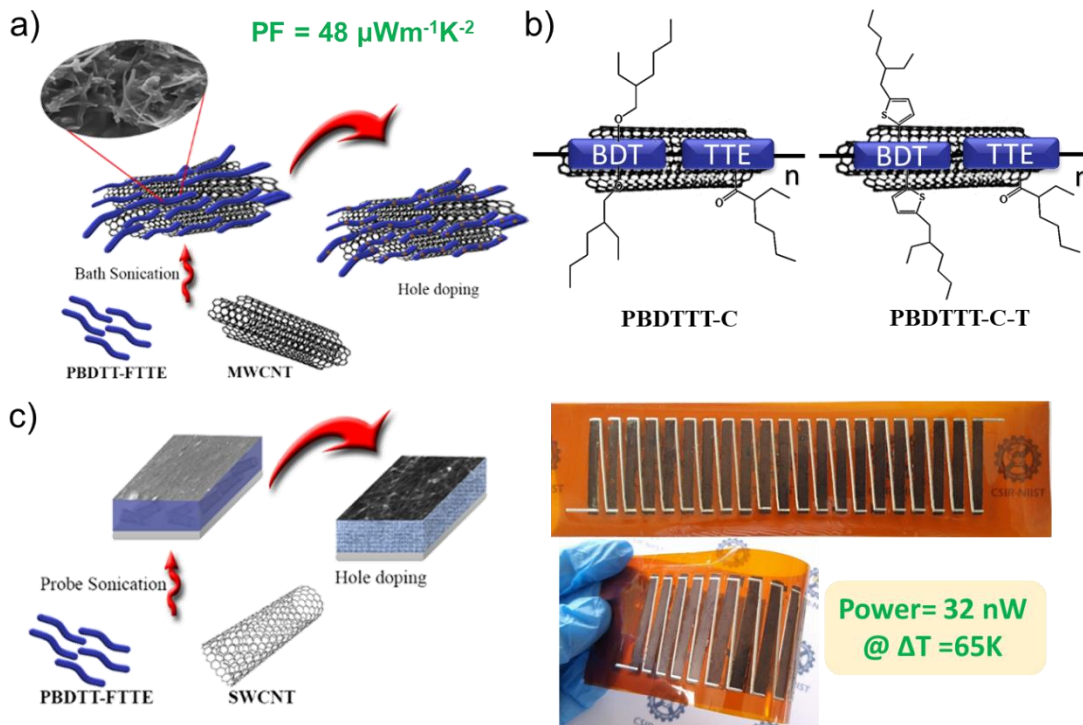


Figure 3.6. a) Representative image and SEM morphology of PBDTT-FTTE:MWCNT composite, b) MWCNT composites of PBDTTT-C and PBDTTT-C-T, c) Preparation of SWCNT:PBDTT-FTTE composite and a flexible TEG developed using 21 legs of the active material. (Adapted from references 29-31)

nanocomposites with carbon nanotubes and doping them with FeCl_3 to study the effects on TE performance and understand the doping mechanism. The TE properties of BDT-thienothiophene (TTE) based conjugated polymer PBDTT-FTTE on composite formation with MWCNT using facile solution based route was studied (**Figure 3.6a**). The as-prepared composites were doped with an oxidating agent like FeCl_3 which enhanced the PF from 1.28 to $48.21 \mu\text{Wm}^{-1}\text{K}^{-2}$. The performance of as-fabricated TEG was demonstrated and an output power of 6.92 nW at $\Delta T = 65 \text{ K}$ was obtained.^[29] Later, the TE properties of two BDT-TTE polymers having differential alkyl side chains

(alkoxy side chain in PBDTTT-C and alkylthiophene side chain in PBDTTT-C-T) were studied (**Figure 3.6b**). The composite containing a polymer with alkylthiophene side chains exhibited a slight elevation in σ after doping with FeCl_3 , while α remained unaltered. Monitoring the electronic structure and density of valence states (DOVS) unveiled the existence of charge-transfer complexes at various coordination sites. Additionally, there were observed shifts in the E_F and VBM, which collectively contribute to the variations observed in the TE response.^[30] Exploration of nanocompositing was extended to quasi 1D structures like SWCNT. We prepared composites of PBDTT-FTTE with SWCNT (**Figure 3.6c**), p-doped with oxidising agent like FeCl_3 and studied the TE properties. The mechanical strength of the polymer has been increased by the presence of SWCNT, leading to robust π - π interfacial interactions. The introduction of SWCNT into the polymer host results in a percolation-like behavior. Additionally, we have computed the ZT value by theoretically determining κ using the DIGIMAT-MF material modeling platform. A maximum ZT (0.044 @ 303 K) was obtained for the doped composite with 55 wt% of SWCNT. A flexible TEG with 21 legs is dispensed through 3D dispenser, yielding an output power of 32.7 nW @ $\Delta T = 65$ K.^[31] TEGs based on these materials typically function at temperatures below 350 °C, offering potential for on-spot sustainable power generation from thermal sources such as hot water from industrial processes, automotive exhaust or even human body heat.

In this chapter, we examined the TE properties of two D-A polymers, PBDTTT:C (**P1**) and PBDTTT:EFT (**P2**), which consist of BDT as the donor and thienothiophene (TT) as the acceptor, doped with F4TCNQ. These polymers differ in their alkyl side chains and acceptor strength. Our findings revealed that the aggregation of polymers upon addition of F4TCNQ varied, leading to the formation of different charge-transfer states. Interestingly, the TE performance of **P2**-F4TCNQ is superior to that of **P1**-F4TCNQ. These results suggest that the development of high-performance organic TE materials can be achieved through rational molecular design of polymers and chemical doping, opening new avenues for further research and potential applications in energy conversion and waste heat recovery.

3.3. Results and discussion

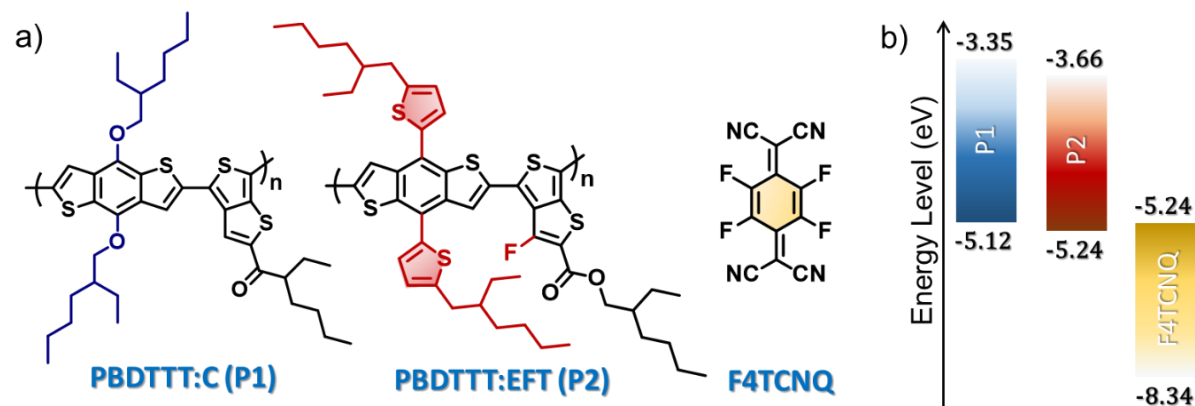


Figure 3.7. a) Molecular structures of benzodithiophene-based polymers (**P1** and **P2**) and dopant (F4TCNQ), b) Energy level diagram of the polymers and dopant.

Figure 3.7a depicts the molecular structures of the polymers, PBDTTT:C (**P1**) and PBDTTT:EFT (**P2**), as well as the dopant F4TCNQ. The chemical structures of these

polymers feature a BDT donor moiety and TT acceptor moiety. In **P1**, an alkoxy side chain was appended to the BDT core, whereas in **P2**, an alkyl thiophene side chain was appended to the BDT core. The energy levels of the highest occupied molecular orbital (HOMO) and the lowest unoccupied molecular orbital (LUMO) were identified for the polymers and dopant (**Figure 3.7b**). For **P1**, the HOMO and LUMO energies were -5.12 eV and -3.35 eV, respectively. In comparison, **P2** exhibited lower energy levels, with a HOMO at -5.24 eV and LUMO at -3.66 eV. This could be attributed to the enhanced π -conjugation in the donor unit, which increases its electron-donating capability, and the improved electron-withdrawing capability of the acceptor unit, resulting from the electron-withdrawing fluorine substitution. Owing to its excellent electron-accepting ability, F4TCNQ is an effective p-type dopant commonly employed in the doping of organic semiconductors. The HOMO and LUMO values of F4TCNQ are -8.3 and -5.2 eV respectively. The deep LUMO is energetically well-matched with many organic semiconductors.^[32,33] It enables efficient injection of positive charges into the organic semiconductor. This process enhanced the conductivity of the host material and improved its p-type doping characteristics.

3.3.1. Doping of the polymers

Chemical doping of the polymers was confirmed by ultraviolet-visible-near infrared (UV-Vis-NIR) spectroscopy. The introduction of dopants, such as F4TCNQ, leads to noticeable changes in the absorption spectra due to alterations in the polymer's electronic structure. These changes can provide insights into the degree of doping and

its impact on the optical and electronic properties of the polymer. **Figure 3.8a** and **3.8b** show the absorption spectra of the pristine polymer films, which reveal the presence of a $\pi-\pi^*$ band at 686 nm for **P1** and 705 nm for **P2**. The redshifted absorption maxima of **P2** can be attributed to the presence of stronger donor and acceptor moieties.

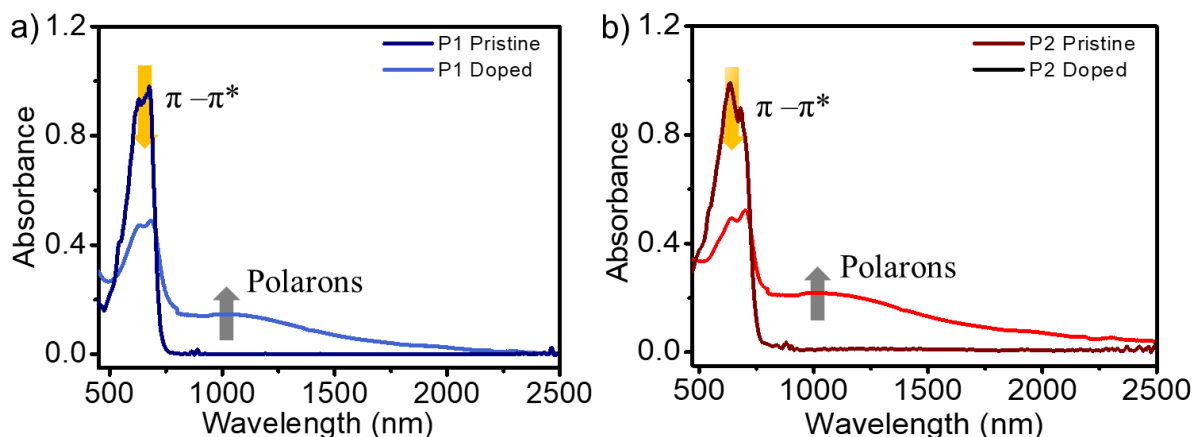


Figure 3.8. UV-Vis-NIR absorption spectra of a) **P1** and b) **P2** films in pristine form and doped with 10 wt% F4TCNQ.

Upon incorporating the dopant F4TCNQ, a strong electron acceptor, bleaching of the $\pi-\pi^*$ absorption of the polymers occurred, and the emergence of new polaronic/bipolaronic absorptions in the NIR region was observed. This evidence supports the occurrence of charge transfer between the polymers and dopant. However, because of the strong overlap between the polaronic/bipolaronic absorption and the F4TCNQ anionic absorption, which is formed as a result of charge transfer, it is challenging to interpret the degree of charge transfer between the polymers and the dopant.

3.3.2. Doping signatures through UPS spectroscopy

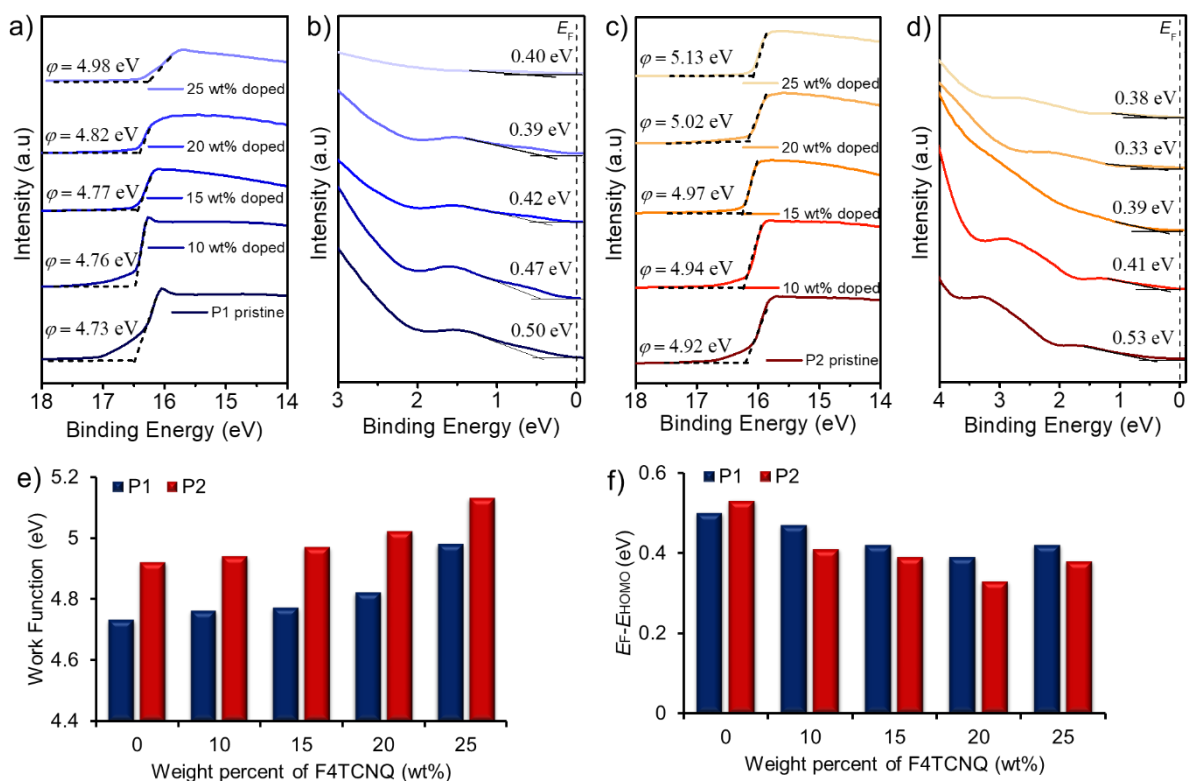


Figure 3.9. Ultraviolet photoelectron spectroscopy (UPS) spectra of a), c) secondary cut-off region, and b), d) low binding energy (BE) regions of **P1** and **P2** respectively, as a function of F4TCNQ weight percentage, e) work function, f) $E_F - E_{HOMO}$ distance plot of **P1** and **P2**.

The chemical doping of the polymers with F4TCNQ was further investigated through the analysis of electronic levels using ultraviolet photoelectron spectroscopy (UPS). **Figure 3.9** displays the work function and $E_F - E_{HOMO}$ distance plot derived from the UPS spectra for both pristine and doped polymer films as a function of F4TCNQ weight percentages (wt%), recorded across the low and high binding energy (BE) regions. The UPS spectra elucidate the relative positioning of the HOMO edge/valence band maximum (VBM) and the work function (ϕ) from the low and high BE regions,

respectively. The HOMO edge was estimated by linear extrapolation of the low BE region, as shown in **Figure 3.9b** and **3.9d**. The Fermi level, denoted as E_F , was calibrated to 0 eV using the Au reference. The distance between E_F and E_{HOMO} was obtained from the tangent of the HOMO curve, which ranged from 0 eV to ~ 3 eV. ϕ is derived from the secondary cut-off region using the relationship, $\text{KE} = h\nu - \phi$, where KE represents the kinetic energy of the ejected electrons and $h\nu$ is the incident energy. Upon incorporating F4TCNQ to the polymers, ϕ shifts to a higher BE region, *i.e.*, from ~ 4.73 eV to ~ 4.98 eV in the case of **P1** and ~ 4.92 eV to ~ 5.13 eV in the case of **P2** (**Figure 3.9e**). This indicates a shift of E_F closer to E_{HOMO} with the addition of F4TCNQ. The characteristic feature of the HOMO peak in the low BE region shifts toward a much lower BE, *i.e.*, $E_F - E_{\text{HOMO}}$ distance shifts from ~ 0.50 eV to ~ 0.39 eV for **P1** and ~ 0.53 eV to ~ 0.33 eV in the case of **P2** (**Figure 3.9f**). This also indicates a shift of E_F towards the HOMO as a result of charge transfer between the polymers and the dopant.

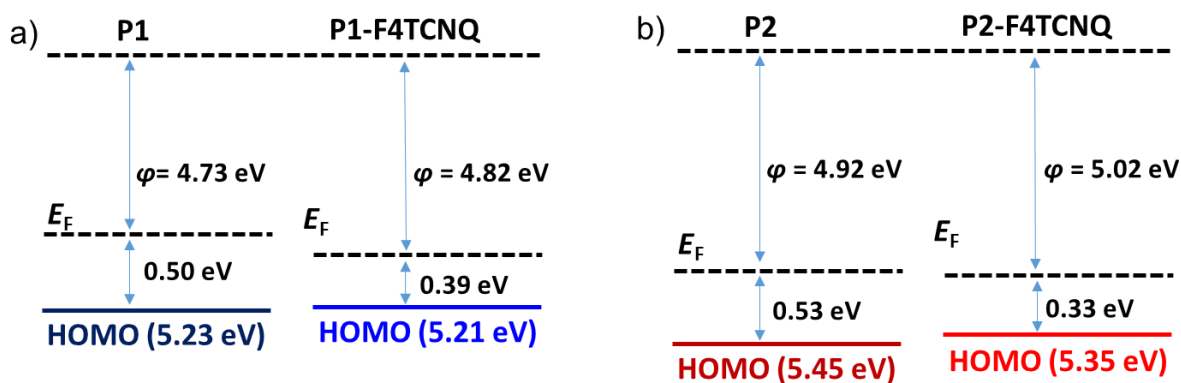


Figure 3.10. Energy band diagrams of a) **P1** and b) **P2** before and after doping with 20 wt% F4TCNQ.

Upon further increasing of F4TCNQ concentration beyond 20 wt%, there is an excessive increase of ionization energy (IE) due to overdoping.^[34] IE is the distance from Vacuum energy level to the HOMO edge or E_{HOMO} , which is calculated as $\text{IE} = \varphi + (E_{\text{HOMO}} - E_{\text{F}})$. This increase in IE was due to the high hole injection barrier at higher dopant concentrations. As a result, the HOMO edge shifts towards higher energy regions beyond 20 wt% of dopant. Hence, a further increase in the dopant concentration results in inferior electrical properties. Therefore, we can consider the optimal doping ratio as approximately 20 wt%. The energy level diagrams before and after doping are shown in **Figure 3.10**.

3.3.3. Thermoelectric properties

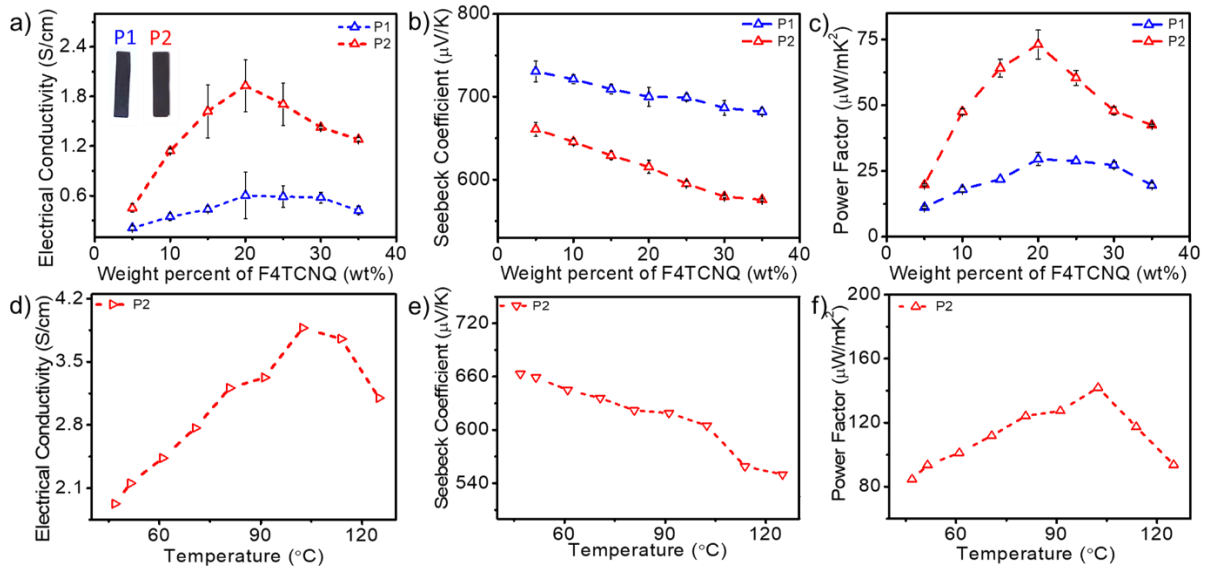


Figure 3.11. a),d) Electrical Conductivity, b),e) Seebeck Coefficient, and c),f) Power Factor of polymers P1 and P2 as functions of the F4TCNQ wt% (measured at 303 K), as a function of varying temperature. Error bars represent the standard deviation from five samples.

The TE properties of **P1** and **P2** were evaluated as a function of increasing wt% F4TCNQ, as shown in **Figure 3.11**. The σ of the pristine polymer films was relatively low, approximately 10^{-5} Scm^{-1} . The addition of F4TCNQ increased σ from 0.21 Scm^{-1} for **P1** and 0.45 Scm^{-1} for **P2** @ 5 wt% dopant to 0.60 Scm^{-1} for **P1** and 1.92 Scm^{-1} for **P2** @ 20 wt% of dopant. Further increasing the dopant concentration to 25 wt% led to a decrease in σ to 0.58 Scm^{-1} for **P1** and 1.70 Scm^{-1} for **P2**, as shown in **Figure 3.11a**. These observations align with the UPS results, where an excessive increase in IE was noted beyond 20 wt% dopant, indicating that the hole concentration was saturated, and any further increase might result in a reduction in σ . Furthermore, increasing the dopant wt% to 25 increases the E_F-E_{HOMO} distance, which further supports the trend of decreasing σ beyond 20 wt% dopant. The positive Seebeck coefficient (α) values confirm the p-type characteristics of the materials. α showed a decreasing trend with increasing F4TCNQ concentration (**Figure 3.11b**), which can be attributed to the inverse relationship between σ and α , in accordance with Mott's relation. The magnitude of α is higher in the case of **P1**, where it decreases from $731 \mu\text{VK}^{-1}$ at 5 wt% dopant to $682 \mu\text{VK}^{-1}$ at 35 wt% dopant. For **P2**, this decrease was from $661 \mu\text{VK}^{-1}$ at 5 wt% of dopant to $576 \mu\text{VK}^{-1}$ at 35 wt% of dopant. The overall PF of the polymer thin films containing 20 wt% of F4TCNQ peaked at $30 \mu\text{Wm}^{-1}\text{K}^{-2}$ ($\mu = 2.10 \times 10^{-1} \text{ cm}^2\text{V}^{-1}\text{s}^{-1}$, $n = 4.57 \times 10^{19} \text{ cm}^{-3}$) for **P1** and $73.10 \mu\text{Wm}^{-1}\text{K}^{-2}$ ($\mu = 4.95 \times 10^{-1} \text{ cm}^2\text{V}^{-1}\text{s}^{-1}$, $n = 6.70 \times 10^{19} \text{ cm}^{-3}$) for **P2** (**Figure 3.11c**). Further, the temperature dependent TE behaviour of **P2** was studied from $30 \text{ }^\circ\text{C}$ to $120 \text{ }^\circ\text{C}$ (**Figure 3.11d-f**). The σ increases upto $104 \text{ }^\circ\text{C}$ which

may due to the thermal energy gained by the charge carriers on increasing temperatures, allowing them to move more freely through the material. Further increase leads to decrease in σ which might be associated with the thermal dedoping behaviour. α exhibits a decrease following the Mott's relation and leads to an optimum PF of $142 \mu\text{Wm}^{-1}\text{K}^{-2}$ @377 K. A noticeable variation in the TE properties can be observed in the two polymer-dopant systems. The PF achieved for **P2** was comparable to that of similar materials reported in the literature. For a comprehensive comparison, the TE performance metrics of other p-type polymers, similar to the **P1** system containing various dopants, are detailed in **Table 3.1** below.

Table 3.1. Comparison of the TE performances of a few p-type polymers reported in the literature with that of the **P2/F4TCNQ** system in the present study.

Polymer	Dopant	σ (S/cm)	α ($\mu\text{V}/\text{K}$)	PF ($\mu\text{W}/\text{mK}^2$)	ZT	Ref
C12-PBTTT	F4TCNQ	193	73	100	–	23
Pg32T-OTz	F4TCNQ	550	–	–	–	26
PCD2	F4TCNQ	3.12	266	23.7	–	27
PBTTT	FeCl ₃ , TFSI	691	25	46.4	–	35
PDFD-T	FeCl ₃	363.0	46.8	79.5	–	36
PCPDTSBT	FeCl ₃	11.9	204.6	49.80	–	37
CDT-BTZ	F4TCNQ	4.4	147.37	9.55	–	38
P3HT	F4TCNQ	160	60	56	–	39
P3HT	F4TCNQ	22	60	8.5	–	40
PQTSC16-TT	NOBF ₄	330	22	–	0.012	41
P2	F4TCNQ	1.92	615	73.10	–	This work

3.3.4. Degree of charge transfer

To understand the differences in the TE properties, it is crucial to investigate the doping behavior of polymers with the dopant. To this end, Fourier transform infrared (FTIR) spectra of the polymer films doped with different weight percentages (wt%) of F4TCNQ were measured. **Figure 3.12** show the C≡N stretching region of the spectra for F4TCNQ-doped **P1** and **P2**, respectively. The cyanide (C≡N) vibrational bands are sensitive to changes in F4TCNQ's charge state, providing an indication of the degree of charge transfer occurring in the molecule.^[42] The red-shift observed in the C≡N band

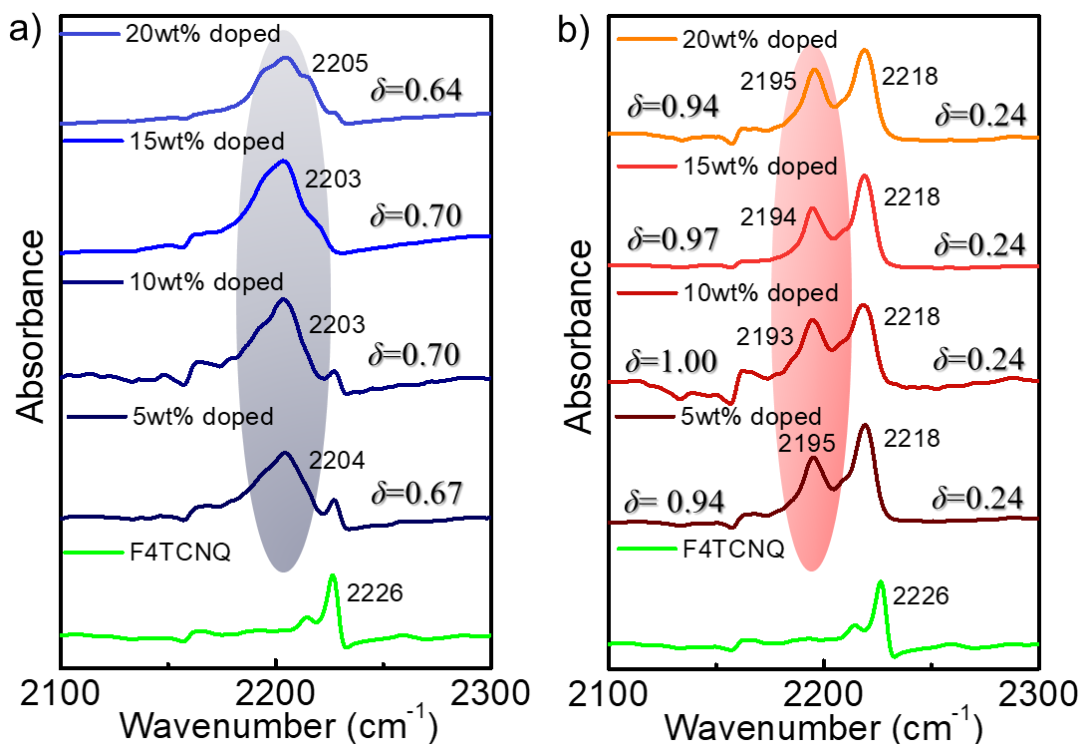


Figure 3.12. FTIR absorption of the C≡N vibrations of a) **P1** and b) **P2**.

(from the neutral state of 2226 cm^{-1}) upon doping is a direct measure of the degree of charge transfer, quantified by the parameter δ .^[42] The degree of charge transfer (δ) between the polymer and the dopant was quantified using the following equation;

$$\delta = \frac{2\Delta\nu}{\nu_0} \left[1 - \frac{\nu_1^2}{\nu_0^2} \right]^{-1} \quad (3.1)$$

Here, ν_0 and ν_1 represent the neutral and ionic frequencies (ionic frequency of F4TCNQ $\approx 2193\text{ cm}^{-1}$), respectively, and $\Delta\nu$ represents the $\text{C}\equiv\text{N}$ shift from the neutral state to the ionized state. A charge transfer amount of δ close to 1.00 corresponds to the formation of fully anionic species of F4TCNQ, indicating complete electron transfer (integer charge transfer or ICT). On the other hand, charge transfer amount of $\delta < 1.00$ corresponds to the formation of partial charge transfer (PCT).^[42,43]

In the case of p-doping, the electron affinity (EA) of the dopant should be higher than the ionization potential (IP) of the polymer ($\text{EA}_D > \text{IP}_P$) for the charge transfer to take place.^[44] This results in the transfer of one electron from the HOMO of the polymer to the LUMO of the dopant, leading to ground-state ICT. Polymers like P3HT and PBTTT are reported to be doped predominantly by an ICT mechanism.^[42,45] The alternate mechanism of PCT formation involves partial hybridization of the frontier molecular orbitals between the polymer and the dopant, resulting in new bonding and anti-bonding orbitals. Many small molecules and oligomers tend to dope predominantly *via* PCT.^[16,26] For example, systems such as quarterthiophene (4T) doped with

F4TCNQ are predominantly doped *via* a PCT mechanism because of their ability to readily form π stacks with the dopant. [16,46-47]

In the case of **P2**, the addition of 5 wt% F4TCNQ resulted in two discrete bands of ν ($\text{C}\equiv\text{N}$), *that is*, 2195 cm^{-1} , $\Delta\nu \approx 31\text{ cm}^{-1}$, 2218 cm^{-1} , and $\Delta\nu_1 \approx 8\text{ cm}^{-1}$. A charge transfer of $\delta \approx 0.94$ and $\delta_2 \approx 0.24$ is said to occur. Upon increasing the wt% of F4TCNQ, an observation similar to that of 5 wt% was obtained. Hence, these results suggest the coexistence of two charge transfer states (ICT and PCT) in **P2** upon doping with F4TCNQ. In contrast, **P1** exhibits a different band. It has only one discrete band ν ($\text{C}\equiv\text{N}$) at $\sim 2204\text{ cm}^{-1}$ which corresponds to a charge transfer of $\delta \approx 0.67$. This strongly suggests that a partial charge transfer mechanism is predominant in the case of **P1**. This partial charge transfer shows that the **P1**-F4TCNQ complexes are formed by orbital hybridization, which is inefficient for generating free charge carriers. In contrast, **P2** exhibited two discrete ν ($\text{C}\equiv\text{N}$) bands of F4TCNQ, wherein free charge carriers were generated through complete charge transfer.

3.3.5. X-ray photoelectron spectroscopy

To further investigate the charge transfer states, X-ray Photoelectron Spectroscopy (XPS) analysis of the pristine and doped thin films was performed. The charge transfer between the polymers and F4TCNQ can be analyzed through the C1s and N1s core-level spectra, as in **Figure 3.13** and **3.14**. The deconvoluted peaks of the C1s core-level spectra suggest the presence of C–C, C–S, C=O, and π – π^* peaks in the pristine polymer

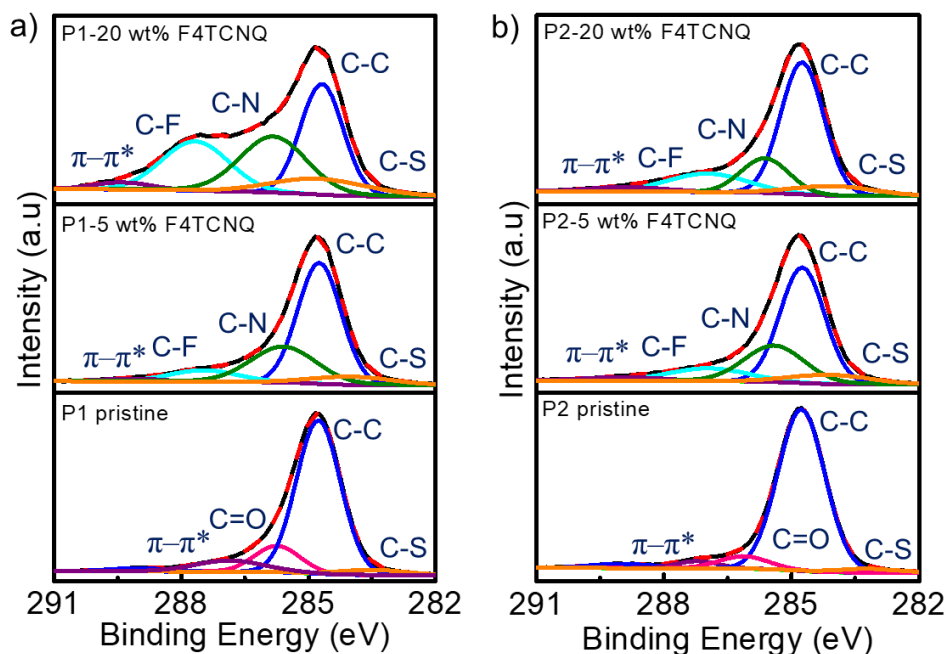


Figure 3.13. C1s XPS core level spectra of a) **P1** and b) **P2** with varying wt% of F4TCNQ.

(**Figure 3.13**). Upon the introduction of 5 wt% F4TCNQ, peaks corresponding to C–C, C–S, C–F, C–N, and π – π^* were present. Upon further increasing the dopant content to 20 wt %, no significant changes in the C–F and C–N peaks are visible in **P2**, whereas there is a considerable change occurring in the case of **P1**. C–F and C–N peaks show an increased intensity at 20 wt% of dopant. The area under a peak in the XPS spectrum corresponds to the number of electrons ejected from that particular orbital. In F4TCNQ, there are carbon atoms bonded to both fluorine (C–F) and nitrogen (C–N). Therefore, we can distinguish the peaks corresponding to C1s electrons from C–F and C–N bonds. When F4TCNQ gains an electron and becomes an anion, the additional electron is primarily delocalized around the conjugated cyano ($C\equiv N$) groups. This increased electron density around the nitrogen atoms can affect the binding energies of the

electrons in the surrounding C–N bonds. Therefore, a higher C–N peak area relative to the C–F peak area in the case of **P2** can be interpreted as a signature of the anionic state in F4TCNQ compared to that of the neutral state in **P1**. Hence, we analyzed the N1s core level spectra for more clarity.

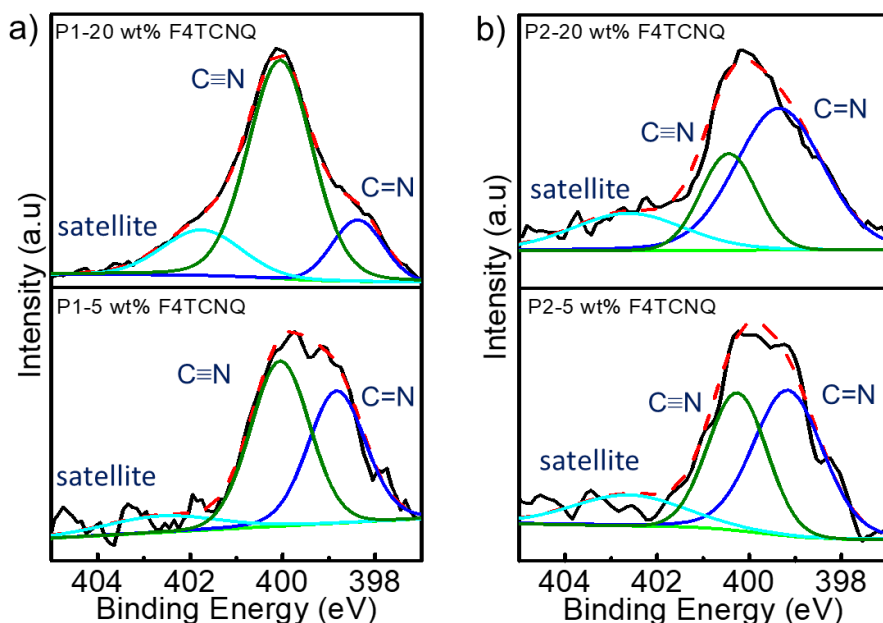


Figure 3.14. N1s XPS core level spectra of a) **P1** and b) **P2** with varying wt% of F4TCNQ.

The N1s core level spectra of the spectral decomposition reveal three peaks (**Figure 3.14**). The deconvoluted peaks correspond to C≡N (neutral), C=N (anionic), and the shake-up satellite peak associated with C=N. Here, at 20 wt% dopant, the contribution of C≡N is higher than that of C=N in the case of **P1**, whereas it is the reverse in the case of **P2**. Hence, partial charge transfer through PCT, which is present in **P1**, was confirmed by the presence of dominant C≡N (neutral state). The relative ratio between the PCT (neutral/anionic) states is more in the case of **P1**-F4TCNQ. However, this ratio

was lower in **P2**-F4TCNQ, where doping proceeded mainly through the ICT mechanism.

The binding energies of O1s and S2p from the XPS core level spectra also reveal the effect of the dopant on the polymers **P1** and **P2** by shifting towards the lower binding energy region **Figure 3.15**. The binding energy shift towards the lower energy range is substantiating proof that E_F shifts closer towards the HOMO. Hence, by correlating this phenomenon with the TE properties, the σ plot shows a higher electrical conductivity in the samples with ICT as the dominant mechanism of charge transfer, *that is*, **P2**, where a complete transfer of one electron ($\delta \approx 1.00$) occurs from the HOMO of **P2** to the LUMO of F4TCNQ. This is reflected by their higher σ compared to **P1**, where only a partial charge transfer of $\delta \approx 0.60$ is said to occur via PCT formation.

To gain insight into the molecular packing of the polymers upon doping with F4TCNQ, grazing incidence small-angle X-ray scattering (GISAXS) and high-resolution transmission electron microscopy (HR-TEM) were performed on the pristine and F4TCNQ doped polymer thin films, as shown in **Figure 3.16** and **3.17**. The interplanar distance was calculated using the reduced fast Fourier transform (FFT) of the HR-TEM images. **P1** shows a decrease in lamellar stacking distance along the in-plane direction from ~ 1.78 nm to ~ 1.76 nm upon doping with F4TCNQ. However, **P2** shows an increased lamellar stacking distance from ~ 2.18 nm to ~ 2.22 nm on doping.

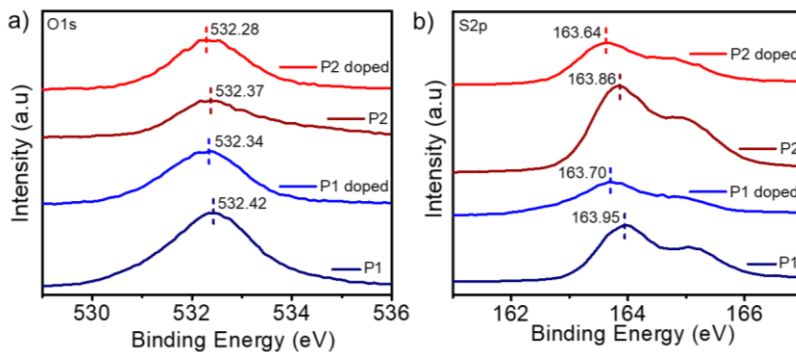


Figure 3.15. a) O1s, b) S2p core level spectra of polymers **P1** and **P2** before and after doping.

3.3.6. Molecular ordering of the polymer thin films

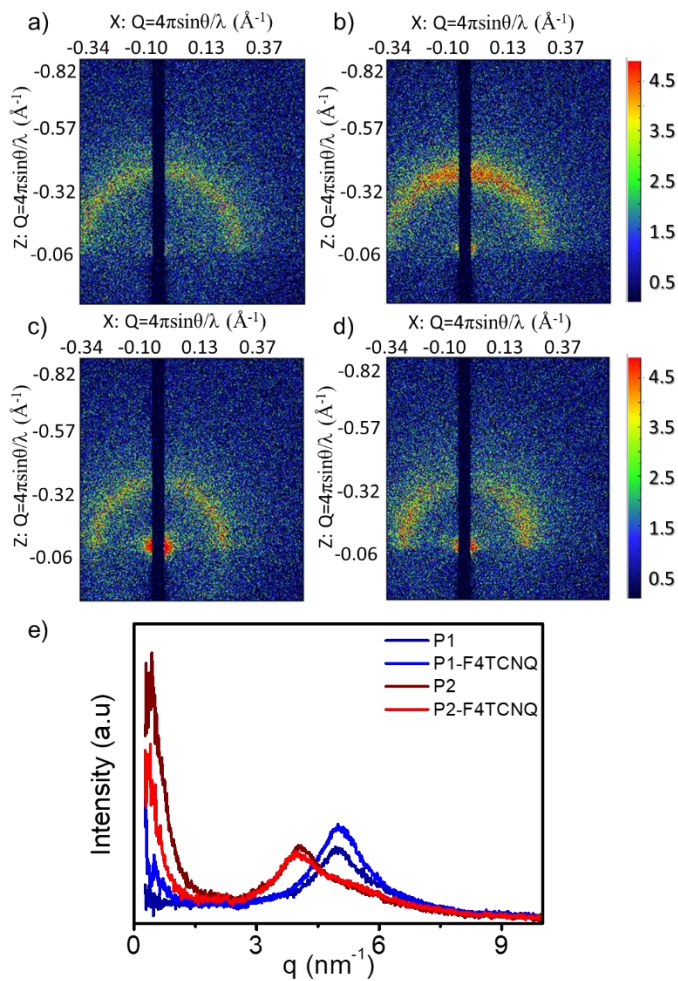


Figure 3.16. 2D GISAXS scattering patterns in the thin-film state of a) **P1** pristine, b) **P1-F4TCNQ**, c) **P2** pristine, d) **P2-F4TCNQ**, e) line-cut profile of **P1** and **P2**.

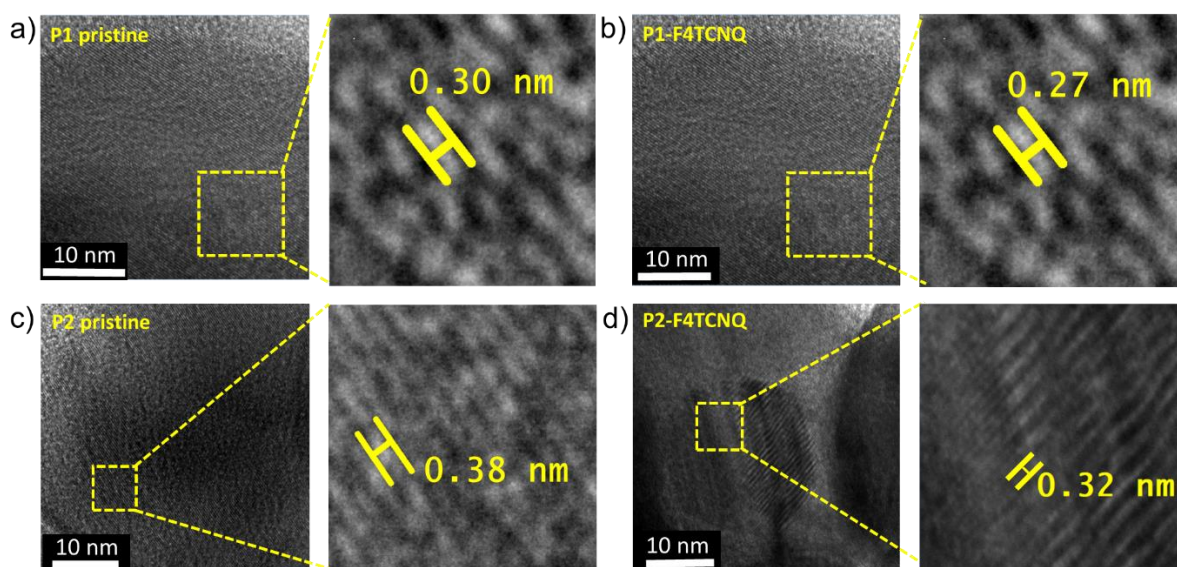


Figure 3.17. High-resolution TEM images of a) **P1** pristine b) **P1-F4TCNQ** c) **P2** pristine d) **P2-F4TCNQ**. A magnified image of the corresponding interlayer spacing is shown on the right.

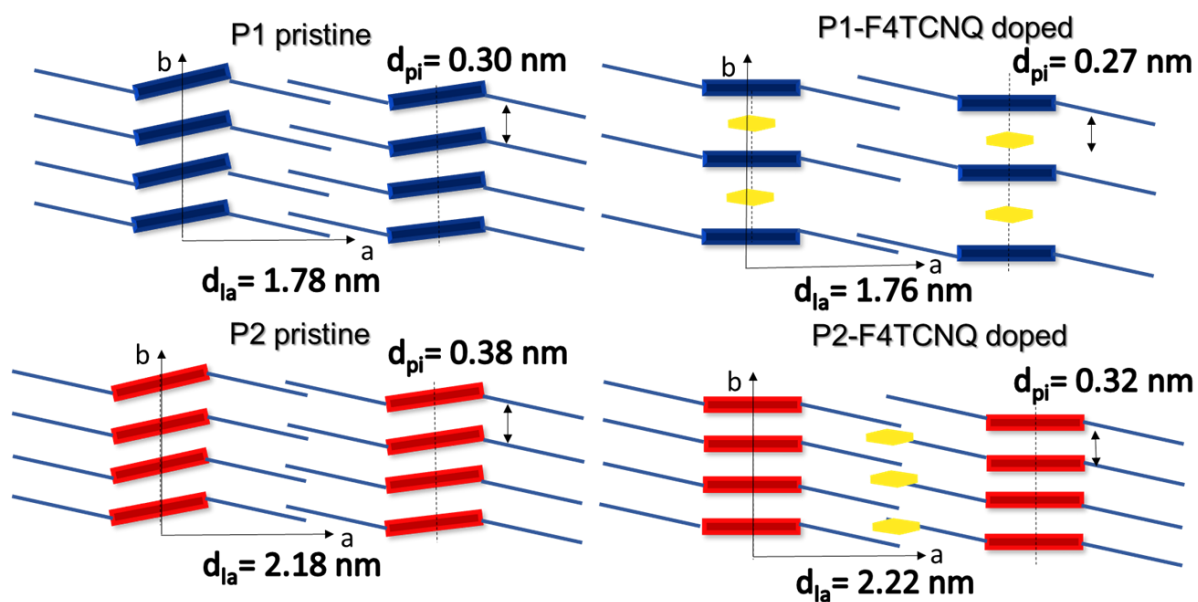


Figure 3.18. Schematic illustration of the structural change in **P1** and **P2** induced by F4TCNQ doping.

From the HR-TEM results, π - π stacking distance of **P1** could be designated as ~ 0.30 nm, which reduces to ~ 0.27 nm on doping with F4TCNQ. This suggests the existence

of alkyl thiophene as the side chain in **P2**, which results in a larger lamellar stacking distance, leading to more dopants intercalating into the side chains. HR-TEM results shows that on doping of **P2**, the π - π stacking distance reduces from ~ 0.38 nm to ~ 0.32 nm. All these polymer rearrangements suggest that the dopants are probably intercalated into the polymer π -stacks in the case of **P1** and in the alkyl side chain or lamellar region in the case of **P2** (**Figure 3.18**). In addition, the decrease in the π spacing in both **P1** and **P2** upon doping was related to a slight reduction in the tilting of the π - π stacking direction upon the addition of the F4TCNQ molecule. This observation is in agreement with the previous report by Stanfield *et al.*^[48] For the formation of the ICT state, the dopant molecules are typically intercalated in the lamellar region, whereas in the case of the PCT states, the dopant molecules are π -stacked with the polymer backbone, creating maximum orbital overlap. Dopant molecules have a preference for occupying the polymer lamellae because it is easier for them to penetrate the lamellae's lower barrier than to disrupt the polymer's π -stacks in order to insert themselves into the more disordered side chains. The placement of dopants within the lamellae, situated at a considerable distance from the polymer backbone, results in ICT. This is because there is insufficient overlap in the wave functions of the donor and acceptor to facilitate PCT formation. In contrast, PCT states only emerge when the dopant F4TCNQ can engage in π -stacking interactions with the conjugated polymer. Hence, the FTIR, XPS, GIXRD, and HR-TEM results confirm the formation of ICT states in **P2** and PCT states in **P1**.

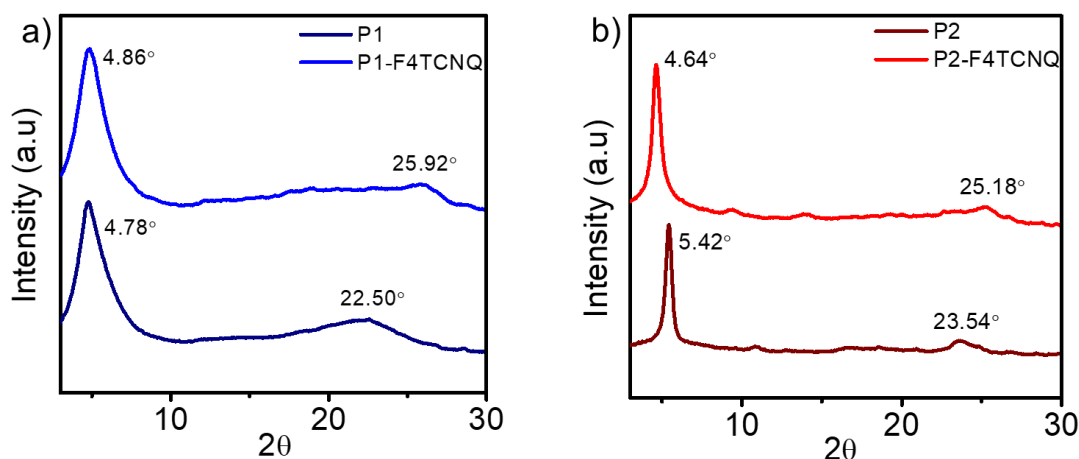


Figure 3.19. Wide-angle X-ray diffraction scattering (WAXS) pattern of a) **P1** and b) **P2** before and after doping with F4TCNQ.

A similar observation in the packing of the polymers was also reflected in the wide-angle X-ray scattering (WAXS) of the polymer thin films (**Figure 3.19**). The variations in the lamellar stacking observed in **P1**, indicating the possibility of PCT, and the enhanced lamellar stacking in **P2**, implying the potential for ICT, can be inferred from their respective d-spacing values. The corresponding d-spacing values before and after doping were compared and tabulated in **Table 3.2** below.

Table 3.2. d-spacing of **P1** and **P2** before and after doping.

Particulars	2θ ($^{\circ}$)	2θ ($^{\circ}$)	d_{100} (nm)	d_{010} (nm)
P1 pristine	4.78	22.50	18.47	3.94
P1-F4TCNQ	4.86	25.92	18.16	3.43
P2 pristine	5.42	23.54	16.29	3.77
P2-F4TCNQ	4.64	25.18	19.08	3.53

3.3.7. Aggregation of the polymers

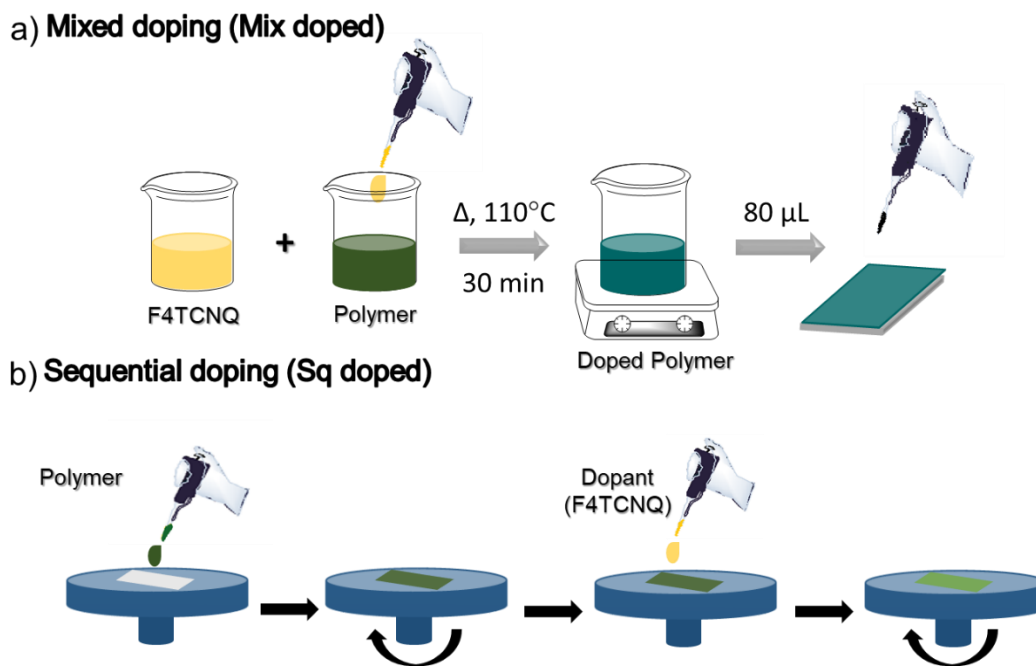


Figure 3.20. Schematic representation of the doping processes a) Mixed doping, b) Sequential doping of P1 and P2 with F4TCNQ dopant.

The doping behavior was found to be notably affected by the extent of polymer aggregation. Mendez *et al.* and Jacobs *et al.* reported the aggregation of P3HT where a highly aggregated state results in the formation of ICT and the solvated state results in formation of PCT where Lewis complexes are formed.^[17,33] P3HT has been utilized as a reference polymer for investigating its response to doping in the solution state. The tendency of the polymer to form aggregates in solution state is a crucial factor that affects the mechanisms, doping efficiencies, kinetics, and polaron delocalization. For instance, when the solution mixing method for doping is adopted, it predominantly occurs within the aggregates of P3HT, resulting in the delocalization of polarons. In

contrast, when P3HT is in a solvated state, a partial charge transfer arises through the formation of a Lewis complex with the p-type dopant F4TCNQ, leading to the localization of polarons, which is insufficient for achieving the high σ which is essential for high performing TE systems.^[48]

In order to study the disparity in the doping mechanism mentioned above, aggregation behaviour in our polymer-F4TCNQ systems were investigated, we doped the polymers **P1** and **P2** with F4TCNQ by two methods, *i.e.*, solution mixing (Mix) and sequential processing (SqP). As depicted in **Figure 3.20**, F4TCNQ was introduced into each polymer through two methods: a) by combining the polymer and F4TCNQ solutions and then followed by drop casting (referred to as "Mix"), or b) by spin coating the F4TCNQ solution onto the as-prepared polymer film (referred to as "SqP").

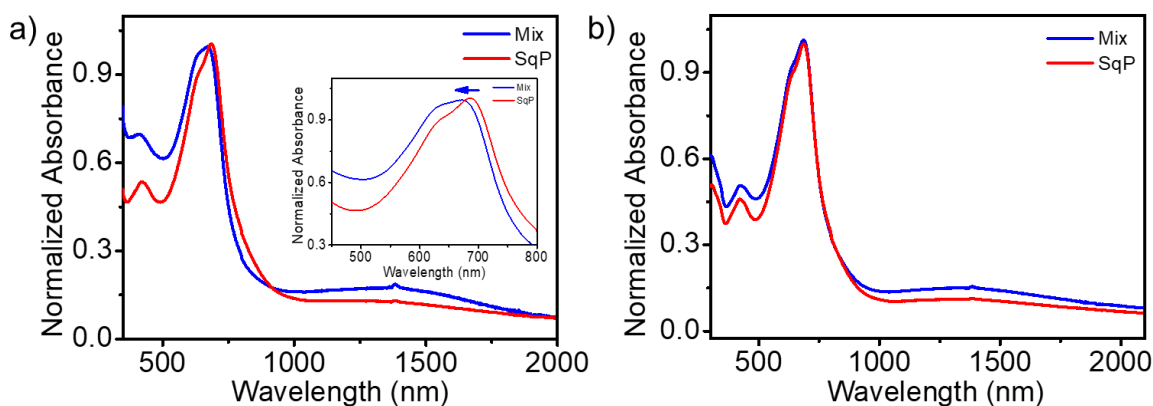


Figure 3.21. UV-Vis-NIR absorption spectra of the polymer-doped F4TCNQ thin films by two methods, that is, solution mixing (Mix) and sequential processing (SqP) of a) **P1** and b) **P2**.

Figure 3.21 shows the UV-Vis-NIR absorption spectra of the polymer-doped F4TCNQ thin films obtained using the above two methods. Here, polymer **P2** aggregated in the solution state; hence, there was no significant change in aggregation

in both the SqP and Mix films. However, **P1** showed blue-shifted absorption in the mixed films compared to the SqP-processed films. Hence, it can be anticipated that aggregation in **P1** occurs during film formation, and this lower aggregation behavior leads to PCT complexes, unlike **P2**, where solution mixing itself induces aggregation that leads to ion-pairs or ICT. In the context of SqP, it has many challenges in achieving both uniform and thermally stable doping within the films simultaneously. This is primarily due to the tendency for dopants to undergo diffusion when subjected to temperature gradients during device operation. To maximize the output power, polymer TE devices typically require thick films (\sim few μm). This thickness is essential for mitigating electrical resistance and minimizing unwanted thermal losses from the substrates, thereby enhancing the device's performance. The solution mixing method hence offers distinct advantages as it enables the creation of TE polymers that are uniformly doped with thermally stable dopants of significant size. Therefore, polymers that tend to form aggregates in solution state are considered advantageous candidates for TE devices.

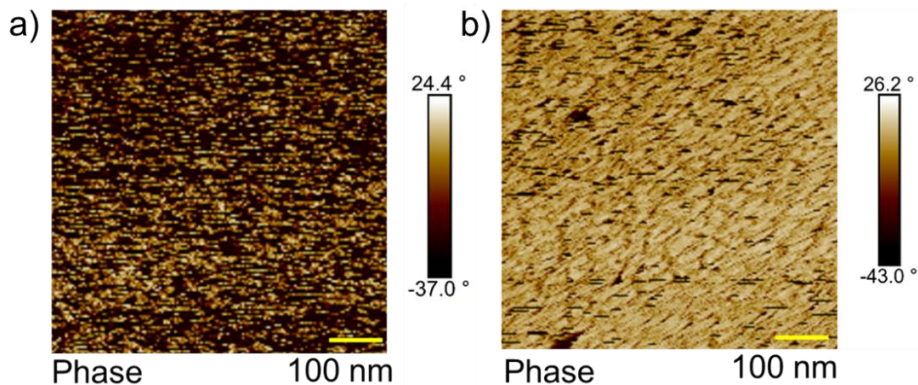


Figure 3.22. AFM phase images of mix-doped thin films of c) **P1**, d) **P2**.

Atomic Force Microscopy (AFM) phase images reveals distinct characteristics in the microstructures of **P1** and **P2** (**Figure 3.22**). **P1** exhibits larger, less interconnected aggregates with a notably sparse network, while **P2** displays smaller aggregates that developed into densely interconnected networks, demonstrating excellent connectivity. In summary, **P1** demonstrates larger, sparsely connected structures, while **P2** showcases smaller, densely interconnected networks.

3.3.8. Current mapping

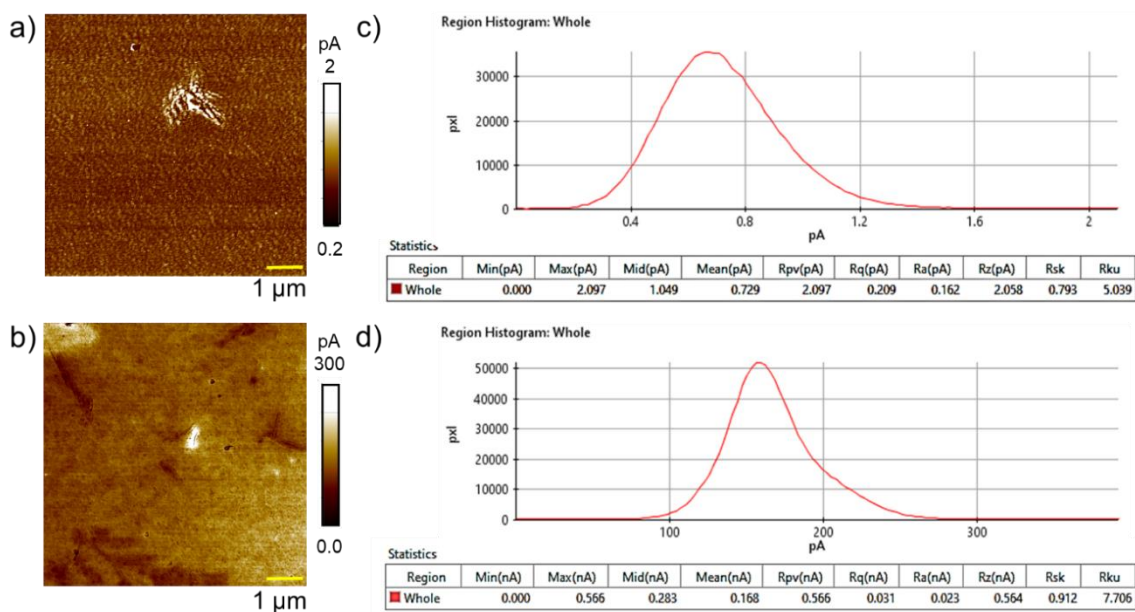


Figure 3.23. Conductivity mapping of a) **P1**, b) **P2**, histogram showing the average current observed in c) **P1-F4TCNQ** d) **P2-F4TCNQ** via c-AFM analysis.

Conductive Atomic Force Microscopy (C-AFM) is a valuable technique for investigating material properties by enabling simultaneous nanoscale measurements of conductivity while obtaining the sample's surface topography.^[49] Current mapping of **P1** and **P2** with 20 wt% F4TCNQ was carried out by c-AFM by spin coating the sample

on a conducting substrate, indium tin oxide (ITO), with one side masked with tape for ground connection. The conducting probe measured the current as a function of the applied voltage (bias voltage= 1 V) to map the local current image. High- and low-conducting domains are clearly visible in the current mapping of both polymers (**Figure 3.23a** and **3.23b**). **P1** exhibited a low current of 0.729 pA, and **P2** exhibited a high current of 168 pA. The corresponding histogram showing the average current is shown in **Figure 3.23c** and **3.23d**. The higher aggregation of polymer **P2** results in the formation of ICT states that lead to higher σ , and the formation of PCT states in **P1** results in lower aggregation and hence lower σ . The better σ (1.92 Scm^{-1}) in **P2** results in a better PF ($73.10 \mu\text{Wm}^{-1}\text{K}^{-2}$) which is in alignment with the current mapping results obtained from c-AFM studies. These results confirm that the existence of ICT states in F4TCNQ-doped **P2** is beneficial for improving its electrical properties. As a result, better TE performance is observed in **P2** with ICT-doped states than in **P1** with a PCT-doped state because it leads to poor σ due to partial charge transfer between the polymer and the dopant.

3.4. Conclusions

In conclusion, our study highlights the critical role of doping-induced charge-transfer states and polymer aggregation in tuning the thermoelectric performance of F4TCNQ-doped conjugated polymers. This work sheds light on the different mechanisms of molecular doping-integer charge transfer (ICT) and partial charge transfer (PCT) complex formation and their direct impact on thermoelectric properties. The more

significant aggregation in **P2** resulted in a predominance of ICT states, leading to a higher electrical conductivity and improved thermoelectric power factor. In contrast, the lesser degree of aggregation in **P1** resulted in the formation of PCT states, with a consequent reduction in the electrical conductivity and thermoelectric performance. This understanding of the relationship between the molecular packing, charge transfer mechanism, and thermoelectric properties provides crucial insights for the development of efficient thermoelectric materials.

3.5. Experimental section

3.5.1. Materials and methods

Materials: The benzodithiophene-based polymers used in the present study were PBDTTT:C ($C_{40}H_{52}O_3S_4$)_n, $M_w > 37,000$, PDI ~ 1.5 – 2.0 , named as **P1**) and PBDTTT:EFT ($(C_{49}H_{57}FO_2S_6)_n$, $M_w > 40,000$, PDI ~ 1.8 – 2.0 , named as **P2**), which were purchased from Ossila Ltd., United Kingdom. 2,3,5,6-Tetrafluoro-7,7,8,8-tetracyanoquinodimethane (F4TCNQ) was purchased from TCI Chemical. Anhydrous 1,2-dichlorobenzene purchased from Sigma Aldrich was used as the solvent. All materials were used without further purification unless otherwise mentioned.

Preparation of polymer-dopant hybrid films: Polymer films were prepared by adding fused thiophene polymers **P1** and **P2** with the dopant F4TCNQ in 1, 2-dichlorobenzene by varying the weight percent of the dopant. The mixture was magnetically stirred for 60 min. An amount of 120 μ L of each solution were drop-casted on a glass substrate

(precleaned with extran, distilled water, and isopropanol, followed by preheating for 15 min at 130 °C) and then dried on a hot plate at 120 °C for 30 min.

Measurements: The details of measurements like profilometry, atomic force microscopy, and x-ray photoelectron spectroscopy are described in the section 2.5.1 of Chapter 2.

Absorption spectroscopy: UV-Visible-NIR spectra were recorded in UV-Vis-NIR spectrophotometer (Agilent Technologies Cary Series). The spectra in the wavelength ranging from 300 to 2500 nm was recorded. The polymer solutions were dissolved in *ortho*-dichlorobenzene and spincoated on quartz substrate.

Infrared spectroscopy: Fourier transform infrared (FT-IR) absorption spectra were recorded on a Perkin Elmer IR Spectrum II instrument. The polymer thin films are coated on glass substrate and then scratched to get the flexible films of polymer-F4TCNQ.

Ultraviolet photoelectron spectroscopy: UPS spectra were obtained with a He lamp providing a resonance line, He-I ($h\nu=21.2$ eV), using a Thermo Fisher Scientific Instruments K-ALPHA + spectrometer, armed with a high-intensity UV source with a photon flux of 1.5×10^{-12} photons/sec. The calibrated spectrum shows Fermi energy level at 0 eV. Valence band/HOMO edge structures are visible from 0-10 eV. The spectrum ends with the secondary electron cut-off region. Work function (φ) can be obtained from $\varphi = h\nu - (E_{cutoff} - E_F)$, where $h\nu$ = energy of the UV photons (21.2 eV for He-I), E_{cutoff} = BE of the electrons at the secondary cutoff, E_F = binding energy of the

electrons at the Fermi edge (~ 0 eV). The polymer solutions were dropcast on $1\text{cm}\times 1\text{cm}$ indium tin oxide (ITO) substrate to form a thin film.

Wide-angle X-ray scattering (WAXS): WAXS measurements were performed using a Xenocs XEUSS Simultaneous WAXS system with Ni-filtered Cu K_α radiation ($\lambda = 1.5405 \text{ \AA}$). The scattering angle (2θ) is expressed as, $D = 2\pi/q$ where $q = 4\pi\sin\theta/\lambda$ and $\lambda =$ wavelength of the x-rays. Fit2D software was used for the data processing. The analysis were obtained using as-casted film samples from the polymer solution.

Grazing incidence small angle X-ray scattering: GISAXS measurements were performed on a Xenocs SAS SAXS system with Cu tube (30 W, 50 kV, 0.6 mA). Xsact and SASfit software were used for data analysis and processing. The polymer solutions were dropcast on $1\text{cm}\times 1\text{cm}$ glass substrate to form a thin film.

Transmission electron microscopy: TEM experiments were performed using a JEOL JEM-F200 microscope at an accelerating voltage of 200 kV with LaB6 cathode. The diffraction pattern of the polymers was obtained using the Fourier transform (FFT) technique in the image processing of HR-TEM using the GATAN digital micrograph 3 software. Samples for TEM were prepared by drop-casting the **P1/P2-F4TCNQ** solution over a carbon-coated copper grid (Tedpella made 400 mesh), which was then left air-dried for 48 h.

Thermoelectric measurements: TE measurements were carried out in a dual mode temperature control system (TEMPSENS Instruments Pvt. Ltd.). The method of measurement is same as described in the section 2.5.1 of Chapter 2.

Conducting-atomic force microscopy: Local current mapping through atomic force microscopy (c-AFM) was performed using a Park NX10. The polymer solutions are spin coated on a conducting substrate ITO, with one side masked with tape for ground connection (**Figure 3.24**). The AFM images are then processed using NanoScope analysis software.

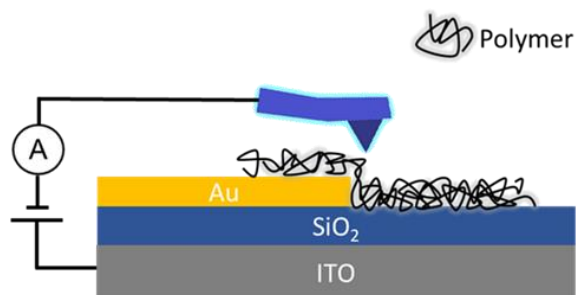


Figure 3.24. Schematic representation of the experimental setup for local current measurements by atomic force microscopy (c-AFM).

3.6. References

- [1] R. Freer, A. V. Powell, *J. Mater. Chem. C* **2020**, 8, 441.
- [2] L. Zhang, X. L. Shi, Y. L. Yang, Z. G. Chen, *Mater. Today* **2021**, 46, 62.
- [3] G. Prunet, F. Pawula, G. Fleury, E. Cloutet, A. J. Robinson, G. Hadziioannou, A. Pakdel, *Mater. Today Phys.* **2021**, 18, 100402.
- [4] I. H. Eryilmaz, Y. F. Chen, G. Mattana, E. Orgiu, *Chem. Commun.* **2023**, 59, 3160.
- [5] Y. Zhao, L. Liu, F. Zhang, C. Di, D. Zhu, *SmartMat.* **2021**, 2, 426.
- [6] L. Deng, Y. Liu, Y. Zhang, S. Wang, *Adv. Funct. Mater.* **2023**, 33, 2210770.
- [7] F. Zhang, C. Di, *Chem. Mater.* **2020**, 32, 2688.
- [8] M. Lindorf, K. A. Mazzio, J. Pflaum, K. Nielsch, W. Brütting, M. Albrecht, *J. Mater. Chem. A* **2020**, 8, 7495.
- [9] B. Russ, A. Glauddell, J. J. Urban, M. L. Chabinyk, R. A. Segalman, *Nat. Rev. Mater.* **2016**, 1, 16050.

-
- [10] Q. Zhang , Y. Sun , W. Xu, D. Zhu, *Adv. Mater.* **2014**, *26*, 6829.
- [11] Y. Chen, Y. Zhao, Z. Liang, *Energy Environ. Sci.* **2015**, *8*, 401-422.
- [12] N. Nandihalli, C. J. Liu, T. Mori, *Nano Energy*, **2020**, *78*, 105186.
- [13] N. Raveendran, T. Ghosh, V. Ignatious, V. Darshan, *Mater. Today Energy* **2023**, *34*, 101296.
- [14] W. Zhao, J. Ding, Y. Zou, C. Di, D. Zhu, *Chem. Soc. Rev.* **2020**, *49*, 7210.
- [15] M. Comin, V. Lemaure, A. Giunchi, D. Beljonne, X. Blase, G. D'Avino, *J. Mater. Chem. C*, **2022**, *10*, 13815.
- [16] R. Kroon, D. Kiefer, D. Stegerer, L. Yu, M. Sommer, C. Müller, *Adv. Funct. Mater.* **2017**, *29*, 1700930.
- [17] H. Mèndez, G. Heimel, S. Winkler, J. Frisch, A. Opitz, K. Sauer, B. Wegner, M. Oehzelt, C. Röthel, S. Duhm, D. Többens, N. Koch, I. Salzmann, *Nat. Commun.* **2015**, *6*, 8560.
- [18] A. H. Sakr, L. Biniek, J. L. Bantignies, D. Maurin, L. Herrmann, N. Leclerc, P. Lévêque, V. Vijayakumar, N. Zimmermann, *Adv. Funct. Mater.* **2017**, *25*, 1700173.
- [19] Y. Zhong, V. Untilova, D. Muller, S. Guchait, C. Kiefer, L. Herrmann, N. Zimmermann, M. Brosset, T. Heiser, M. Brinkmann, *Adv. Funct. Mater.* **2022**, *32*, 2202075.
- [20] O. Z. Arteaga, S. Marina, G. Zuo, K. Xu, B. Dörfling, L. A. Pérez, J. S. Reparaz, J. Martín, M. Kemerink, M. C. Quiles, *Adv. Energy Mater.* **2022**, *12*, 2104076.
- [21] H. Li, M. E. DeCoster, C. Ming, M. Wang, Y. Chen, P. E. Hopkins, L. Chen, H. E. Katz, *Macromolecules* **2019**, *52*, 9804.
- [22] M. Arvind, C. E. Tait, M. Guerrini, J. Krumland, A. M. Valencia, C. Cocchi, A. E. Mansour, N. Koch, S. Barlow, S. R. Marder, J. Behrends, D. Neher, *J. Phys. Chem. B* **2020**, *124*, 7694.
- [23] V. Vijayakumar, E. Zaborova, L. Biniek, H. Zeng, L. Herrmann, A. Carvalho, O. Boyron, N. Leclerc, M. Brinkmann, *ACS Appl. Mater. Interfaces* **2019**, *11*, 4942.

-
- [24] S. N. Patel, A. M. Glauddell, K. A. Peterson, E. M. Thomas, K. A. O'Hara, E. Lim, M. L. Chabinye, *Sci. Adv.* **2017**, *3*, 24.
- [25] O. Z. Arteaga, A. Perevedentsev, S. Marina, J. Martin, J. S. Reparaz, M. C. Quiles, *ACS Energy Lett.* **2020**, *5*, 2972.
- [26] H. Li, Z. Xu, J. Song, H. Chai, L. Wu, L. Chen, *Adv. Funct. Mater.* **2022**, *32*, 2110047.
- [27] E. H. Suh, M. K. Jeong, K. Lee, W. J. Jeong, Y. J. Jeong, I. H. Jung, J. Jang, *Adv. Funct. Mater.* **2022**, *32*, 2207886.
- [28] J. Tang, J. Ji, R. Chen, Y. Yan, Y. Zhao, Z. Liang, *Adv. Sci.* **2022**, *9*, 1.
- [29] V. Ignatious, N. Raveendran, A. Prabhakaran, Y. Tanjore Puli, V. Chakkooth, B. Deb, *Chem. Eng. J.* **2021**, *409*, 128294.
- [30] V. Ignatious, N. Raveendran, S. Poovattil, N. Jacob, V. Chakkooth, B. Deb, *Macromol. Mater. Eng.* **2022**, *307*, 1.
- [31] I. Vijitha, N. Jacob, N. Raveendran, C. Vijayakumar, B. Deb, *Mater. Today Energy* **2023**, *32*, 101233.
- [32] J. Emmy, T. Biskup, Y. Zhang, R. Kroon, S. Barlow, S. R. Marder, C. Mu, *Chem. Mater.* **2022**, *34*, 5673.
- [33] I. E. Jacobs, C. Cendra, T. F. Harrelson, Z. I. Bedolla Valdez, A. M. Faller, A. Salleo, *Mater. Horiz.* **2018**, *5*, 655.
- [34] M. Cui, H. Rui, X. Wu, Z. Sun, W. Qu, W. Qin, S. Yin, X. Wu, Z. Sun, S. Yin, *J. Phys. Chem. Lett.* **2021**, *12*, 8533.
- [35] C. Chen, I. E. Jacobs, C. Jellett, X. Jiao, J. F. Ponder, B. Kang, S. B. Lee, Y. Huang, L. Zhang, M. Statz, Y. Sun, Y. Lin, K. Kang, X. She, Y. Hu, T. Zhang, L. Jiang, *Adv. Electron. Mater.* **2022**, *8*, 2200053.
- [36] S. E. Yoon, B. Kim, S. Y. Chun, S. Y. Lee, D. Jeon, M. Kim, S. Lee, B. E. Seo, K. S. Choi, F. S. Kim, T. Kim, H. Seo, K. Kwak, J. H. Kim, B. S. Kim, *Adv. Funct. Mater.* **2022**, *8*, 2202929.

-
- [37] Y. Lee, J. Park, J. Son, H. Y. Woo, J. Kwak, *Adv. Funct. Mater.* **2020**, *31*, 2006900.
- [38] K. Kang, S. Schott, D. Venkateshvaran, K. Broch, G. Schweicher, D. Harkin, C. Jellett, *Mater. Today Phys.* **2019**, *8*, 112.
- [39] V. Untilova, T. Biskup, L. Biniek, V. Vijayakumar, M. Brinkmann, *Macromolecules* **2020**, *53*, 2441.
- [40] A. H. Sakr, L. Biniek, J. L. Bantignies, D. Maurin, L. Herrmann, N. Leclerc, P. Lévêque, V. Vijayakumar, N. Zimmermann, *Adv. Funct. Mater.* **2017**, *25*, 1700173.
- [41] H. Li, M. E. DeCoster, C. Ming, M. Wang, Y. Chen, P. E. Hopkins, L. Chen, H. E. Katz, *Macromolecules* **2019**, *52*, 9804.
- [42] I. Salzmann, G. Heimel, M. Oehzelt, S. Winkler, N. Koch, *Acc. Chem. Res.* **2016**, *49*, 370.
- [43] B. Neelamraju, K. E. Watts, J. E. Pemberton, E. L. Ratcliff, *J. Phys. Chem. Lett.* **2018**, *9*, 6871.
- [44] D. Kiefer, R. Kroon, A. I. Hofmann, H. Sun, X. Liu, A. Giovannitti, D. Stegerer, A. Cano, J. Hynynen, L. Yu, Y. Zhang, D. Nai, T. F. Harrelson, M. Sommer, A. J. Moulé, M. Kemerink, S. R. Marder, I. McCulloch, M. Fahlman, S. Fabiano, C. Müller, *Nat. Mater.* **2019**, *18*, 149.
- [45] O. Zapata-Arteaga, B. Döring, A. Perevedentsev, J. Martín, J. S. Reparaz, M. Campoy-Quiles, *Macromolecules* **2020**, *53*, 609.
- [46] C. P. Theurer, M. Richter, D. Rana, G. Duva, D. Lepple, A. Hinderhofer, F. Schreiber, P. Tegeder, K. Broch, *J. Phys. Chem. C* **2021**, *125*, 23952.
- [47] L. Fijahi, T. Salzillo, A. Tamayo, M. Bardini, C. Ruzié, C. Quarti, D. Beljonne, S. d'Agostino, Y. H. Geerts, M. M. Torrent, *J. Mater. Chem. C* **2022**, *10*, 7319.
- [48] D. A. Stanfield, Y. Wu, S. H. Tolbert, B. J. Schwartz, *Chem. Mater.* **2021**, *33*, 2343.

-
- [49] D. Mikulik, M. Ricci, G. Tutuncuoglu, F. Matteini, J. Vukajlovic, N. Vulic, E. A. Llado, A. F. Morral, *Nano Energy*, **2017**, *41*, 566.

Chapter 4

Enhanced Thermoelectric Properties of Thiophene Based Small Molecule/SWCNT Composites Through Supramolecular Functionalization

4.1. Abstract

Advances in creating composites of soluble conjugated organic semiconductors with carbon nanotubes have led to notable TE power factors. However, achieving uniform dispersion of single-walled carbon nanotubes (SWCNTs) within the nanocomposites remains challenging. This study focuses on designing thiophene-based organic small molecules and enhancing SWCNT dispersion using a fluorene-terthiophene-based oligomer (OTF). The successful composite formation and debundling of nanotubes were verified using a suite of techniques including UV-Vis-NIR absorption spectroscopy and electron microscopy methods. The resulting composite thin films (1:1 ratio of OTF:SWCNT) demonstrated impressive power factors of up to $124 \mu\text{Wm}^{-1}\text{K}^{-2}$ at 308 K and $215 \mu\text{Wm}^{-1}\text{K}^{-2}$ at 373 K. This work culminates in the development of a flexible TE generator showcasing a significant power output (150 nW at a ΔT of 100 K), thereby underscoring the potential of these nanocomposites in practical TE applications.

4.2. Introduction

The quest for efficient TE materials has recently centered around exploiting the unique properties of carbon nanomaterials known for their excellent electrical conductivity (σ) and structural versatility.^[1,2] Among these, semiconducting carbon nanotubes, particularly single-walled carbon nanotubes (SWCNTs), have garnered attention for their potential to significantly enhance TE performance.^[3-7] The inherent porous structure of these nanotubes is instrumental in achieving an ultra-low thermal conductivity (κ), which is essential for efficient thermoelectric devices.^[8-11] Additionally, a high Seebeck coefficient (α) is obtained through the energy filtering effect at the porous boundaries. This effect selectively allows high-energy charge carriers to pass, reflecting the lower energy ones and thereby improving electrical power generation.^[12-15] Furthermore, the porosity of these materials increases the air volume fraction, leading to a further reduction in κ and an overall boost in TE performance.^[15-19]

Despite the promising properties of SWCNTs, their practical application in thermoelectrics is challenged by issues related to their dispersion in nanocomposites.^[20-21] SWCNTs tend to agglomerate or form bundles due to strong π - π interactions among themselves, hindering their electrical properties by reducing the percolation pathways for charge transport.^[18,22-23] Overcoming this challenge is crucial for fully realizing the potential of SWCNTs in TE applications and beyond. As such, recent efforts have concentrated on improving the dispersion of SWCNTs

within nanocomposites, a critical step for enhancing the electrical conductivity and overall efficiency of TE materials. This introduction sets the stage for discussing the innovative approaches and materials that have been developed to address these challenges, further propelling the field of organic thermoelectrics towards practical and effective energy conversion solutions.

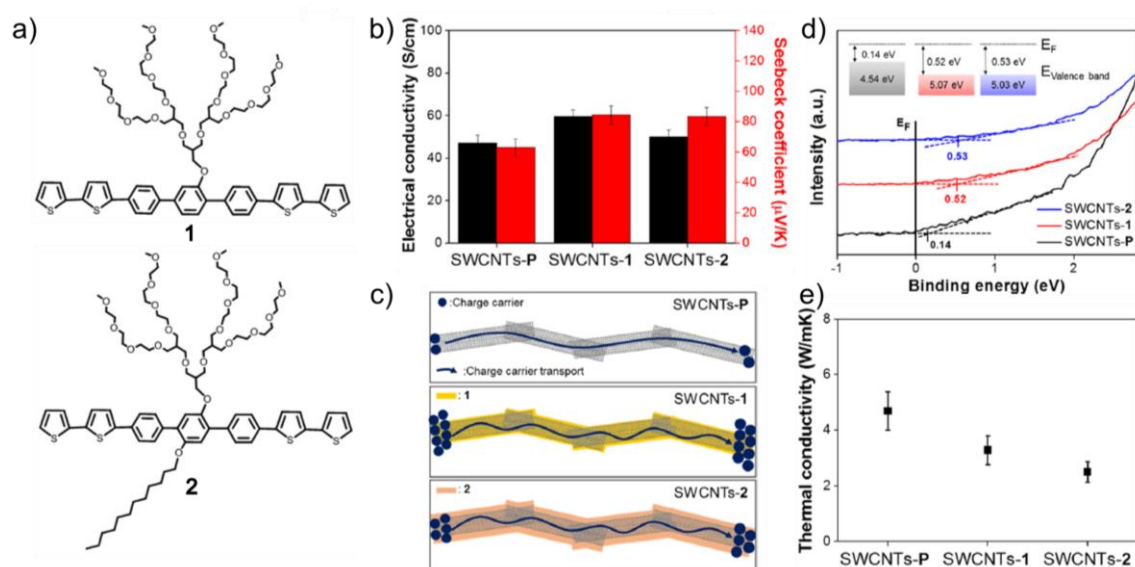


Figure 4.1. a) Chemical structures of **1** and **2**, b) electrical conductivity and Seebeck coefficient of hybrids of **1** and **2**, c) illustration of the charge transfer process, d) UPS spectra indicating the Fermi energy level and valence band region, e) in-plane thermal conductivity plot. (Adapted from reference 24)

The supramolecular functionalization of SWCNTs using bithiophenyl-terphenyl derivatives **1** and **2** was reported by Jang *et al.* (**Figure 4.1**). The aromatic moiety, bis(bithiophenyl)-terphenyl, possesses sufficient π -conjugation length, enabling it to strongly interact with SWCNTs while displaying amphiphilic characteristics. This is achieved by incorporating hydrophilic tri(ethylene oxide) chains which are

hydrophilic in nature. A much deeper HOMO energy level i.e. 5.07 eV (**1**) and 5.03 eV (**2**) than 4.54 eV (SWCNT) appears as an obstacle for the movement of charge carriers. Electrostatic interactions, such as charge transfer interactions, π - π interactions, dipole-dipole interactions between SWCNTs and the organic molecules play a crucial role in increasing the energy gap between the transport (E_{Tr}) and Fermi energy levels (E_F). The charge-transfer interactions lead to a reduction in the bundle diameter of SWCNTs-P, and an increase in the $E_{Tr}-E_F$ value. As a result, the PFs for SWCNTs-**1** and SWCNTs-**2** were 42.63 ± 9.15 and $34.88 \pm 8.22 \mu\text{Wm}^{-1}\text{K}^{-2}$, which is higher compared to pristine SWCNTs. The increased molecular adsorption in **2** enabled it to achieve the lowest κ_L among all. Thermal conductivity analysis shows a noticeable decrease in κ_{total} which effectively contributed to the improved ZT values.^[24]

Alkyl chain engineering of the derivatives similar to **2** were carried out later by the same group (**3-5**, **Figure 4.2**). The derivatives vary in their length of alkyl side chains from hexyl to octadecyl and the composite with the longest alkyl chain (**5**) exhibited a higher performance of $54.1 \pm 6.1 \mu\text{Wm}^{-1}\text{K}^{-2}$ due to the decreased tunneling energy barrier. The AFM histogram distribution profiles showing the length of the hybrids as 318.9 (**3**), 359.9 (**4**), and 483.9 nm (**5**), respectively. Analysis of supramolecular hybrids indicates that an extended alkyl chain length results in the elongation and increased thickness of SWCNT bundles. The longer the

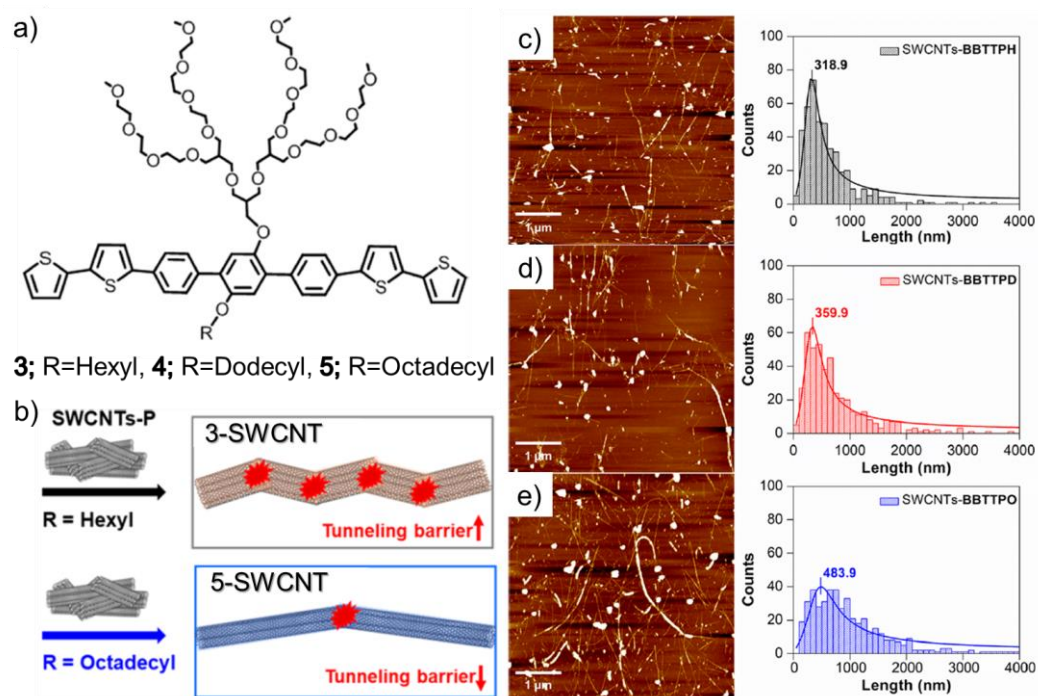


Figure 4.2. a) Molecular structures of **3**, **4**, **5**, b) illustration of the charge transfer showing the tunneling barrier, AFM images with particle length distribution profile of c) **3**, d) **4**, and e) **5**. (Adapted from reference 25)

SWCNT bundles, it has reduced number of junctions for charge carrier transport, leading to the lowest T_1 (temperature of charge carriers crossing over the tunneling barriers) value in **3** and thereby minimizing charge carrier scattering at these junctions.^[25]

The simultaneous modulation of the bandgap and HOMO levels in organic molecules is a strategy to tailor their electronic properties and improve the α , leading to more efficient organic materials. Kim *et al.* reported a few stilbene-based organic small molecules (**6-8**, **Figure 4.3**) that efficiently debundles the SWCNTs. The stilbene derivatives were designed as having no cyano group, one cyano group,

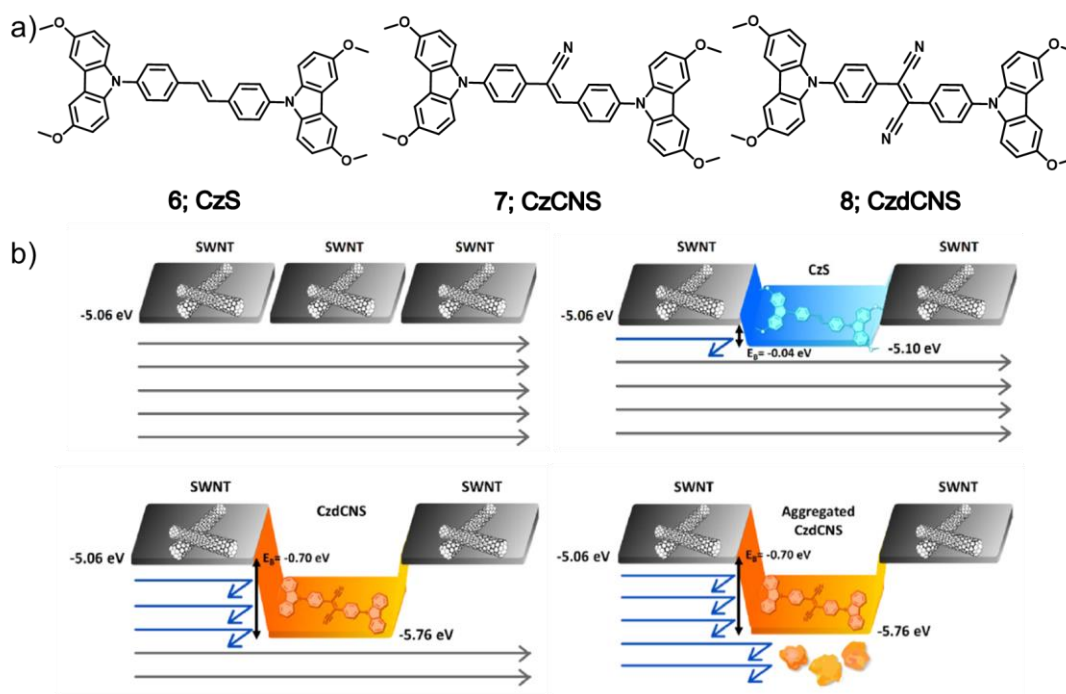


Figure 4.3. a) Chemical structures of **6-8**, b) illustration of the electrical flow and HOMO energy levels. (Adapted from reference 26)

and two cyano groups respectively. The effect of energy levels of the molecules with SWCNTs on their TE performance is analyzed and **6** having a large bandgap and aligned HOMO energy level to that of the SWCNTs showed an enhanced performance of $337.2 \mu\text{Wm}^{-1}\text{K}^{-2}$. The **6**/SWCNT films demonstrated the highest σ compared to the other two hybrids. In contrast, **8**/SWCNT hybrids showed a smaller scattering time (related to carrier mobility) than **6**/SWCNT, which resulted in significant scattering of charge carriers within the **8**/SWCNT hybrids.^[26] Hence, this simple strategy based on energy modulation of molecules gives a promising approach to the development of diverse hybrid materials.

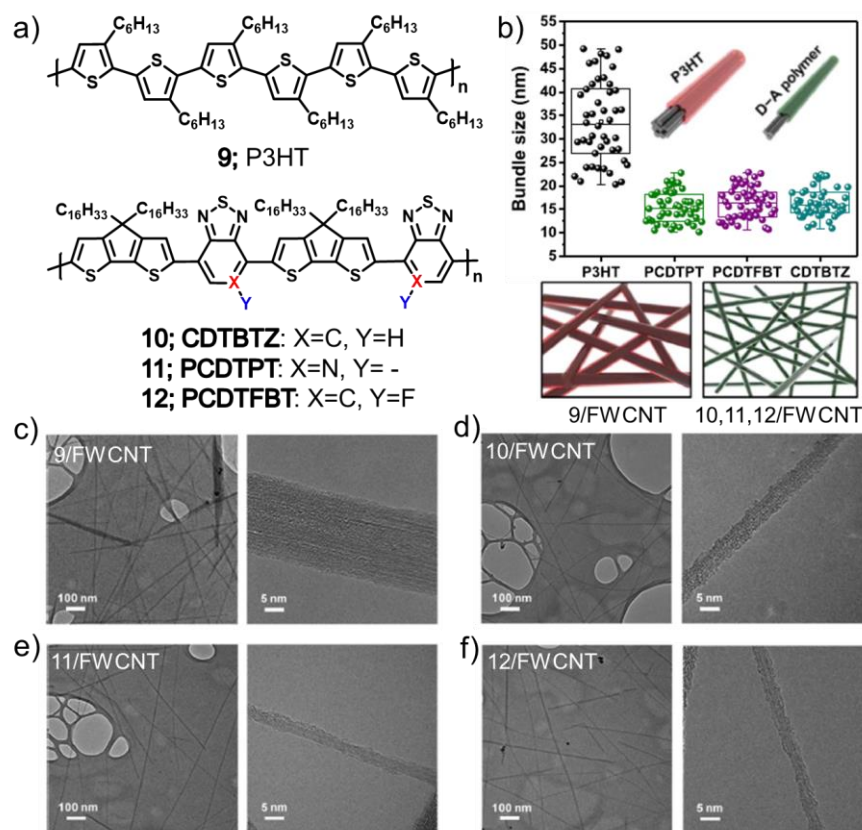


Figure 4.4. a) Chemical structures of **9-12**, b) Distribution of bundle sizes from SEM image, low and high magnification TEM images of c) **9**/FWCNT, d) **10**/FWCNT, e) **11**/FWCNT, and f) **12**/FWCNT. (Adapted from reference 27)

Jung *et al.* developed few donor-acceptor (D-A) polymers (**9-12**, **Figure 4.4**) to disperse and debundle few-walled carbon nanotubes (FWCNTs). Due to its sole presence of hexylthiophene rings, **9** exhibits a relatively limited degree of π -electron delocalization along its backbone. Conversely, the D-A polymers employed in this study exhibit increased backbone planarity due to their substantially elevated torsional potential and enhanced π -electron delocalization. The enhanced planarity of these D-A polymers is also advantageous for their interaction with FWCNTs, as

they can readily adhere to the nanotube surface without necessitating significant conformational alterations. Among all these derivatives, a stronger interaction was obtained in case of **11**/FWCNT composite films with a PF of $459 \mu\text{Wm}^{-1}\text{K}^{-2}$ and a power output (P_O) of 210 nW for 36 legged device prepared with the same as the active material.^[27]

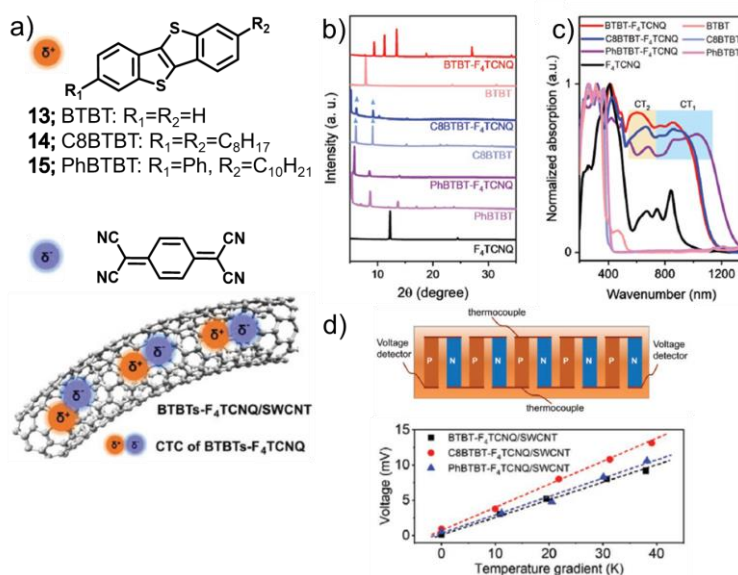


Figure 4.5. a) Structures of **13-15** and dopant F₄TCNQ, b) X-ray diffraction pattern, c) UV-Vis-NIR absorption spectra, d) Illustration of the TE module and open circuit voltage of the TE module. (Adapted from reference 28)

Benzothienobenzothiophene (BTBT) derivatives with varying alkyl chains (**13-15**, **Figure 4.5**) forms charge transfer complexes (CTCs) with electron acceptors like F₄TCNQ. BTBT-F₄TCNQ CTCs are composited with SWCNTs to form both p and n-type TE materials. The **15**-F₄TCNQ/SWCNT composite film exhibits the highest p-type PF of $244.3 \mu\text{Wm}^{-1}\text{K}^{-2}$, attributed to its lower LUMO energy level. This characteristic property enables more effective acceptance of electrons from the

E_F of SWCNT, leading to a higher n in the p-type composite film. On the other hand, the **14**-F4TCNQ/SWCNT composite film achieves the highest n-type power factor of $105.1 \mu\text{Wm}^{-1}\text{K}^{-2}$. This outcome is a result of its moderate n and minimal film defects, contributing to elevated α and σ values in the n-type composite film.^[28]

In this chapter, we have designed and synthesized a semiconducting fluorene-thiophene-based organic small molecule (OTF), which is employed in the development of advanced thermoelectric materials. We have successfully debundled and dispersed pristine SWCNTs using a straightforward solution-based method. This process transforms the aggregated bundles of SWCNTs into individual tubes, facilitating improved interaction with OTF molecules. The resulting OTF:SWCNT composite film demonstrated remarkable thermoelectric performance, with a peak power factor (PF) of $124 \mu\text{Wm}^{-1}\text{K}^{-2}$ at room temperature (308 K) and an even higher PF of $215 \mu\text{Wm}^{-1}\text{K}^{-2}$ at 373 K. Additionally, we constructed a 7-leg flexible TEG from the nanocomposite film. This TEG showcased an impressive maximum output voltage (V_{OC}) of 29.4 mV, a short-circuit current (I_{SC}) of 14.69 μA , and a power output (P_O) of 150 nW at a temperature difference (ΔT) of 100 K. These achievements underscore the potential of the OTF:SWCNT composite in enhancing the performance and applicability of organic thermoelectric devices.

4.3. Results and discussion

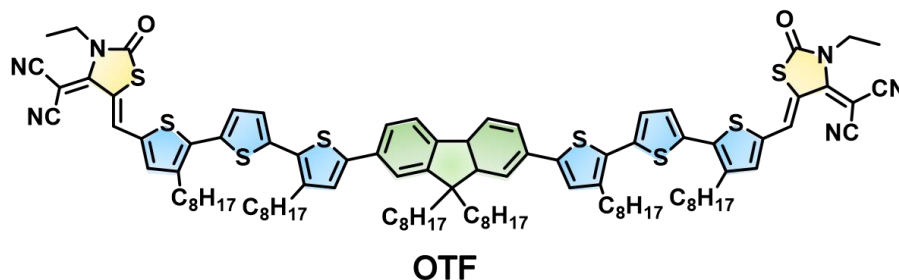
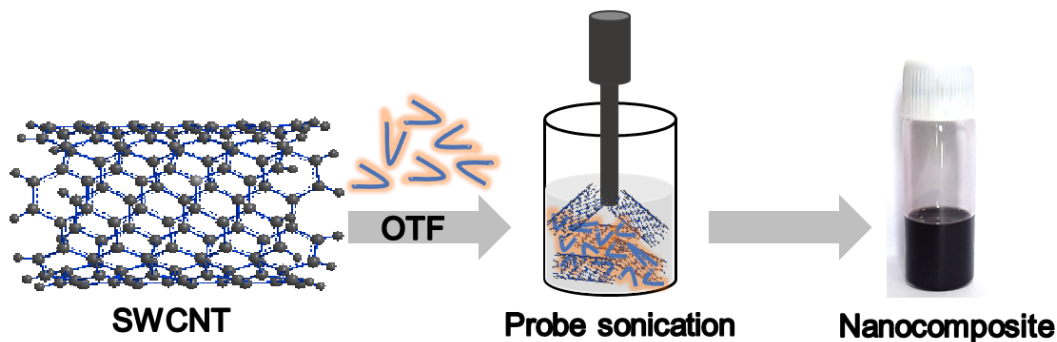


Figure 4.6. Chemical structure of the fluorene-terthiophene derivative under study.

OTF is an acceptor-donor-acceptor (A-D-A) type organic molecule having a fluorene core with an alkyl terthiophene unit as the pi-spacer flanked by 2-(1,1-dicyanomethylene)rhodanine as the acceptor group on both sides. The detailed synthetic scheme of OTF is given in section 4.5.2.



Scheme 4.1. Facile ultrasonication process for the preparation of OTF:SWCNT nanocomposite.

Nanocomposites combining OTF with SWCNT were prepared using a facile ultrasonication process, a technique that ensures thorough mixing and dispersion of the components. This process was varied by adjusting the weight ratio of SWCNT to optimize the thermoelectric properties of the composite. Detailed steps and visual representation of the preparation process can be found in **Scheme 4.1**. The aim was

to achieve an efficient contact between the conjugated molecules of OTF and the surfaces of SWCNTs. This contact is critical as it facilitates rapid electron transport within the composite, a key factor in enhancing the performance of the resulting TE film. The interaction between OTF and SWCNT is particularly beneficial in creating a network that supports efficient charge carrier mobility. The ultrasonication process not only aids in debundling the SWCNTs but also promotes a uniform dispersion of these nanotubes in an ortho-dichlorobenzene suspension. The introduction of OTF to this suspension results in a stable and uniform dispersion of SWCNTs, as illustrated in the photographic images presented in **Scheme 4.1**. The stability of the dispersed SWCNTs in ambient atmosphere is a testament to the effectiveness of the preparation method, ensuring that the nanocomposites remain intact and functional over time.

4.3.1. Photophysical properties

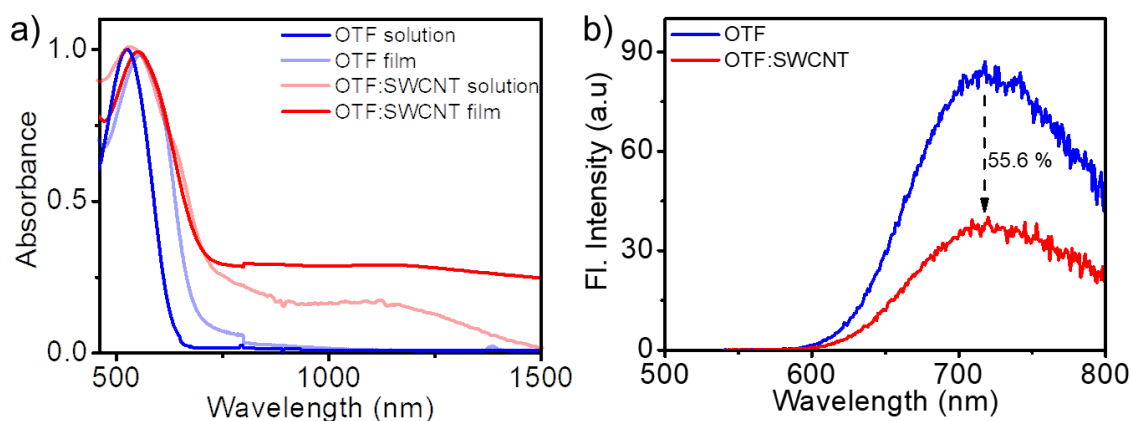


Figure 4.7. a) UV-Vis-NIR absorption spectra, d) PL spectra of pristine OTF, OTF:SWCNT composite.

Figure 4.7a shows the absorption spectra of OTF in solution state which shows a significant absorption centered at 524 nm that corresponds to the π - π^* transition of the conjugated backbone. In the film state, the absorption maximum is redshifted by ~ 33 nm centered at 557 nm and it is also allied with a broadening. This redshift and broadening of the maxima are associated with the aggregation of the molecules in film state. The bandgap of the molecule is obtained as 1.77 eV and that on composite formation decreases to 1.62 eV. On the other hand, OTF did not exhibit much redshifted absorption upon composite formation with SWCNT. This suggests that the intermolecular interaction between OTF and the SWCNT is much stronger and that the molecules adopt a less-coiled conformation when wrapping around with the nanotubes.^[27] The UV-Visible-NIR absorption spectra of the as-prepared composite film is compared to that of the pristine molecule. The interactions between OTF and the SWCNT is studied using fluorescence spectra in solution state as shown in **Figure 4.7b**.

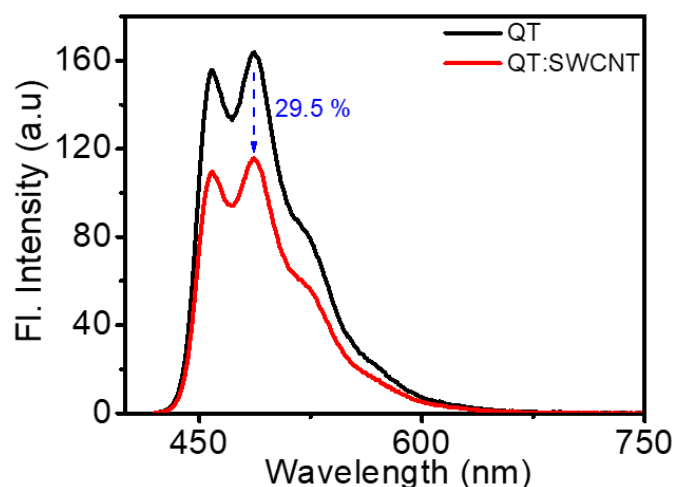


Figure 4.8. PL spectra of pristine α -QT, α -QT:SWCNT composite.

The composite formation is then confirmed by the quenching of the fluorescence of the pristine OTF. The degree of quenching depends on the efficiency of the molecule to interact with the nanotubes. The quenching efficiency is quantified using the equation $QE = (I_0 - I/I_0) \times 100$ where I_0 is the intensity of the pristine molecule and I is the intensity of the composite.^[26-27] For a 1:1 weight ratio of the OTF:SWCNT composite, the QE is $\approx 55.6\%$. The quenching efficiency of OTF is higher compared to other thiophene-based small molecules like α -quarterthiophene (α -QT) where a 1:1 ratio of the composite exhibits a QE of only $\approx 29.5\%$ (**Figure 4.8**). The higher QE of OTF is attributed to the stronger interaction of it with SWCNTs where more number of molecules are wrapped or attached to the surface of the nanotubes through π - π interactions whereas lower QE indicates weaker interaction.

4.3.2. Thermal stability

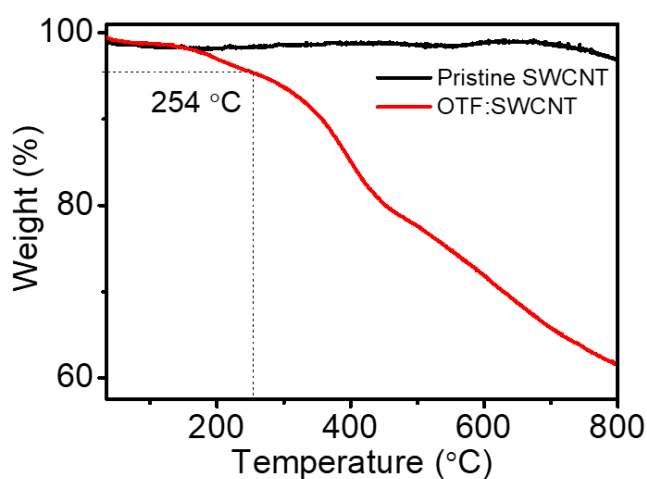


Figure 4.9. Thermogravimetric analysis of pristine SWCNT, OTF:SWCNT composite.

The thermal stability of the samples were characterized using thermogravimetric analysis (TGA). The samples are subjected to a heating rate of 10 °C/min from 30 °C to 800 °C in a nitrogen atmosphere. The temperature at which a material undergoes a 5% weight loss is referred to as the T_5 value. The T_5 value of the OTF:SWCNT composite is 254 °C which suggests that the nanocomposite can be applied for low-grade waste heat harvesting (**Figure 4.9**).

4.3.3. Wide angle X-ray scattering

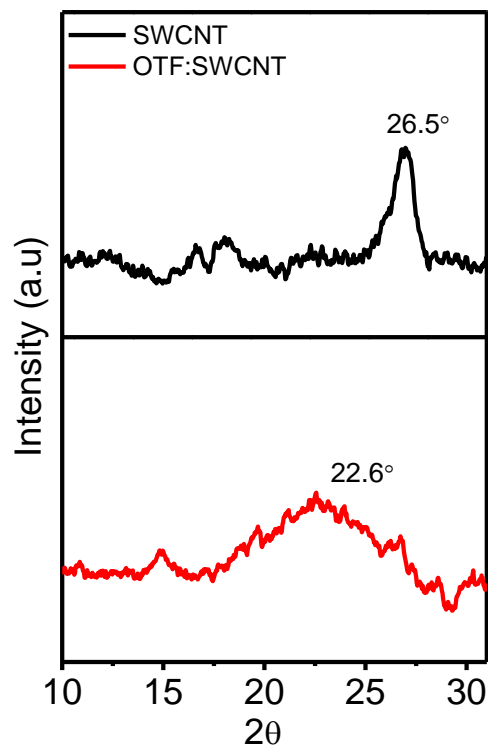


Figure 4.10. Wide angle X-ray diffraction pattern of SWCNT, OTF:SWCNT composite.

The wide-angle X-ray scattering pattern of SWCNT exhibits a diffraction peak at 26.5° which corresponds to the diffraction plane (002) and confirms the highly graphitic structure of the nanotubes (**Figure 4.10**). A wide peak observed at 22.6° in

case of the nanocomposite, indicates a d -spacing of approximately 3.93 Å, that corresponds to the (010) plane and is attributed to the π - π stacking of thiophene rings merged with the graphitic peak of the nanotubes.^[31-32]

4.3.4. Raman spectroscopy

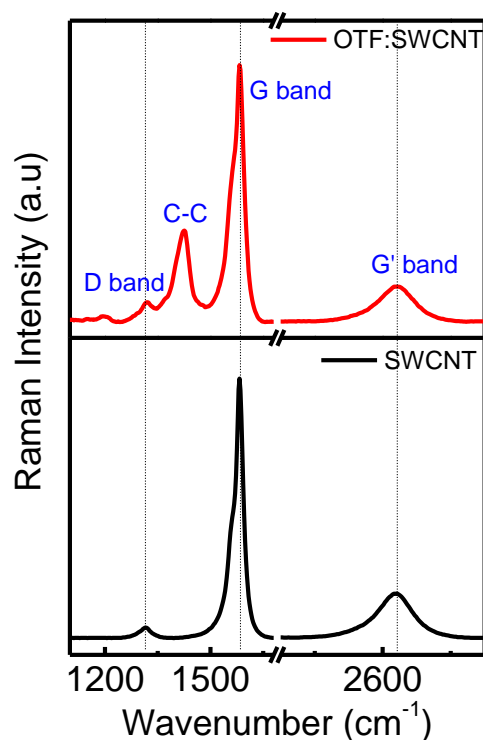


Figure 4.11. Raman spectra of SWCNT, OTF:SWCNT composite.

Raman spectroscopy was used to explore the interfacial interactions of OTF within the composites. **Figure 4.11** shows the Raman spectra of pristine SWCNT and OTF:SWCNT composite. Pristine SWCNT exhibited three characteristic peaks i.e. G band of the sp^2 carbon (1582 cm^{-1}), D band of the sp^3 carbon (1315 cm^{-1}) and a G' band of the graphitic carbon (2619 cm^{-1}). OTF:SWCNT exhibited an additional peak at 1425 cm^{-1} which corresponds to the C-C stretching vibration of the

thiophene ring. Upon formation of the nanocomposite, there is a decrease in the intensity ratio of the G band (I_G) to the D band (I_D) i.e. I_G/I_D . This indicates a reduction in the crystallinity on composite formation. However, the I_D/I_G ratio predicts the defect level within a material and details related to uniformity and smoothness of the film. This ratio slightly increases from 0.03 (pristine SWCNT) to 0.07 (OTF:SWCNT) as indicated in **Table 4.1**. The direct implication is that as when the I_D/I_G ratio increases in the Raman spectra, there is a concurrent rise in the defect density within the film.^[33-34] Here, only a slight increase is observed which may be the contribution from defects or disorder due to the intercalation of the molecules between the nanotube walls.

Table 4.1. I_G/I_D and I_D/I_G ratio of pristine SWCNT, OTF:SWCNT.

	I_G	I_D	I_G/I_D	I_D/I_G
SWCNT	15258	591	25.81	0.03
OTF:SWCNT	15526	1123	13.82	0.07

4.3.5. Microstructural analysis

Analyzing the microstructure of carbon nanotubes entails the investigation of their structural features on a microscopic scale. This process involves studying their size, shape, arrangement, and any defects present within the nanotube structures.^[27] Various techniques are employed to gain insight into these features, providing a detailed understanding of their electronic and TE properties.

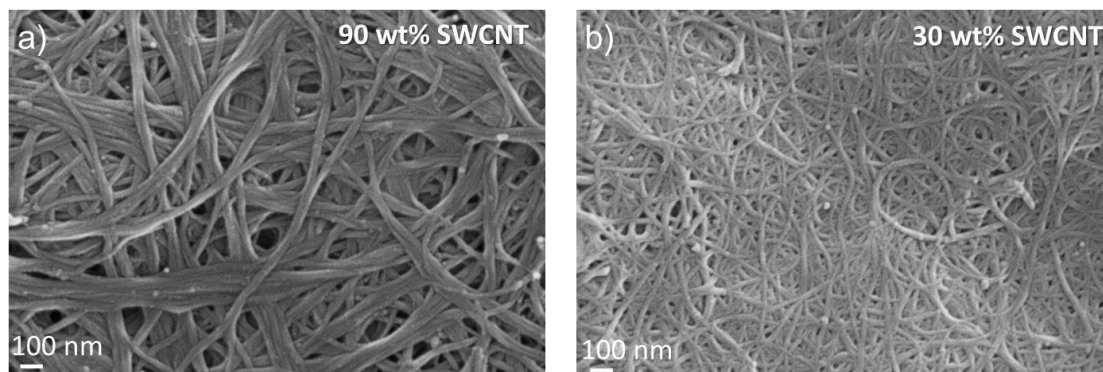


Figure 4.12. SEM images of the drop-cast OTF:SWCNT composite films prepared in a) 10:90, b) 70:30 ratio.

Figure 4.12 shows the microstructural analysis of the composite through scanning electron microscopy (SEM). The SEM images of the nanocomposite film reveals that the nanotubes are intertwined into networks. The molecules wraps around the surface of the nanotubes which creates the interconnecting network between the SWCNTs. A noticeable decrease in the diameter of nanotube bundles becomes apparent with an increase in the content of OTF. Investigation of the microstructure of the materials at a very fine scale was done through TEM analysis.

Figure 4.13 shows the nanoscale morphology of the OTF:SWCNT composite *via* high-resolution transmission electron microscopy (HR-TEM). The HR-TEM images show that the OTF molecules are tightly wrapped along the nanotubes and that it should have dispersed the nanotubes in the solvent medium. The bundle size of the nanotubes are measured and plotted as a histogram to the right of HR-TEM images.

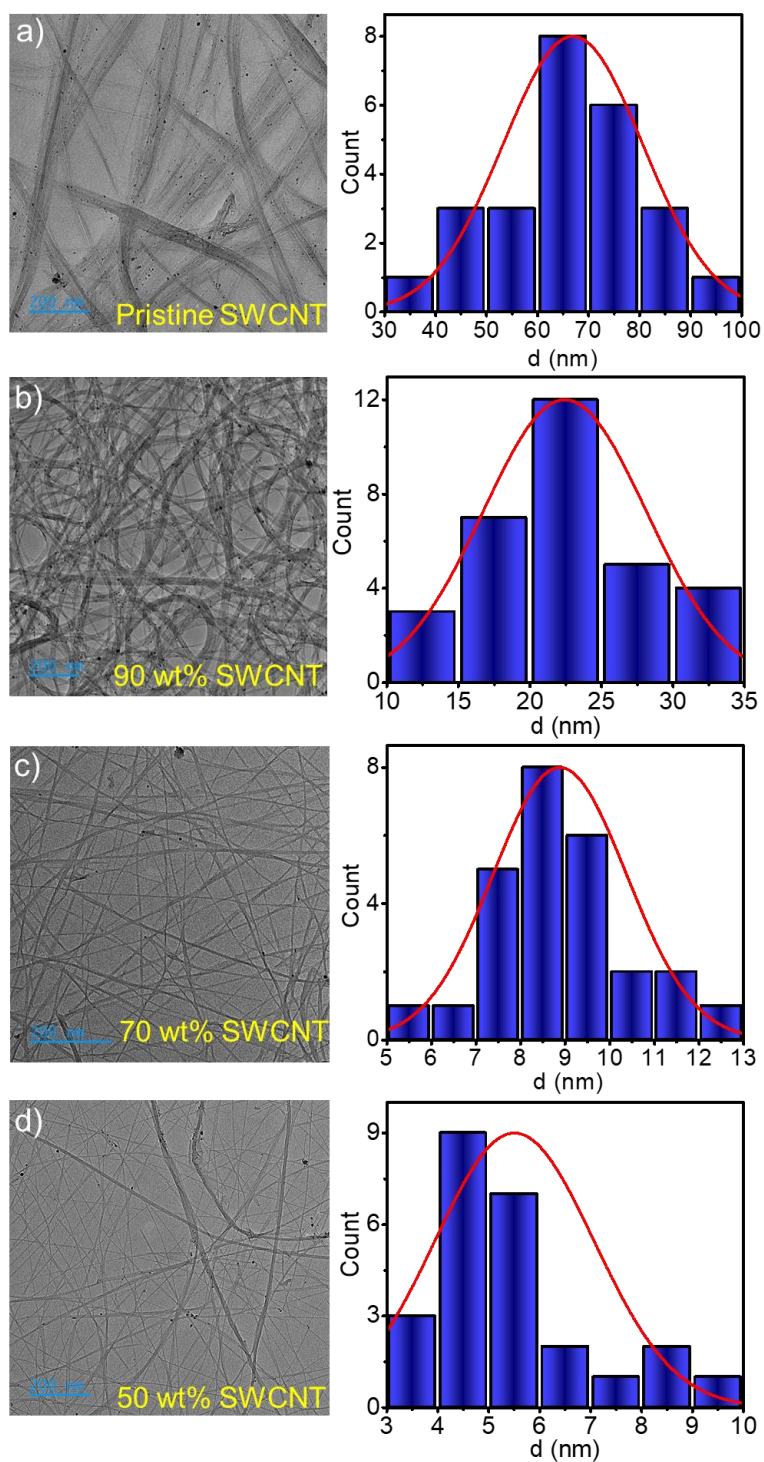


Figure 4.13. a-d) TEM images of SWCNT with varying weight percent of OTF. Corresponding bundle size distributions estimated from TEM images are depicted as histogram in the right.

As observed in the high-magnification images of the pristine SWCNT, thick bundles of diameters 60-70 nm were present predominantly. Upon incorporation of 10 wt% of OTF, the bundle sizes reduced to 20-25 nm. On increasing the content of OTF to 30 wt%, bundle sizes close to 8-9 nm were present in dominance. Further, increasing the OTF content to 50 wt%, bundles sized 4-6 nm were present in large number. This indicates that the incorporation of OTF not only facilitates electron transfer but also efficiently disperse and debundle the carbon nanotubes. Here, a 50 wt% of OTF achieves a complete and efficient debundling that corresponds to the size of an individual nanotube ($\approx 3-4$ nm). The SWCNTs tend to aggregate in solution state due to their strong $\pi-\pi$ interactions between the individual nanotubes. During the ultra-sonication process, the aggregated SWCNTs are de-bundled or split into individual nanotubes. The conjugated molecules attach to the surface of the nanotubes through non-covalent functionalization such that the resultant nanocomposite is stabilized in the solvent. The bundle sizes differ with the varying weight ratio of OTF:SWCNT. This could be attributed to the optimum concentration required to have stronger intermolecular interaction between OTF and the nanotubes. Here, we can infer that a stronger interaction between the nanotubes and OTF is obtained at 1:1 ratio (50 wt%) which leads to the most efficient debundling or formation of much smaller bundles. The smaller bundles would be responsible for better charge transport through more conducting pathways and hence could reflect in a better electrical conductivity. The TEM samples were

dropcasted on TEM grids using very dilute solutions of the composite in order to observe the isolated nanotube bundles. However, for the composite films to be applied in TE devices, dropcasted films from highly concentrated solution of the composite needs to be monitored.

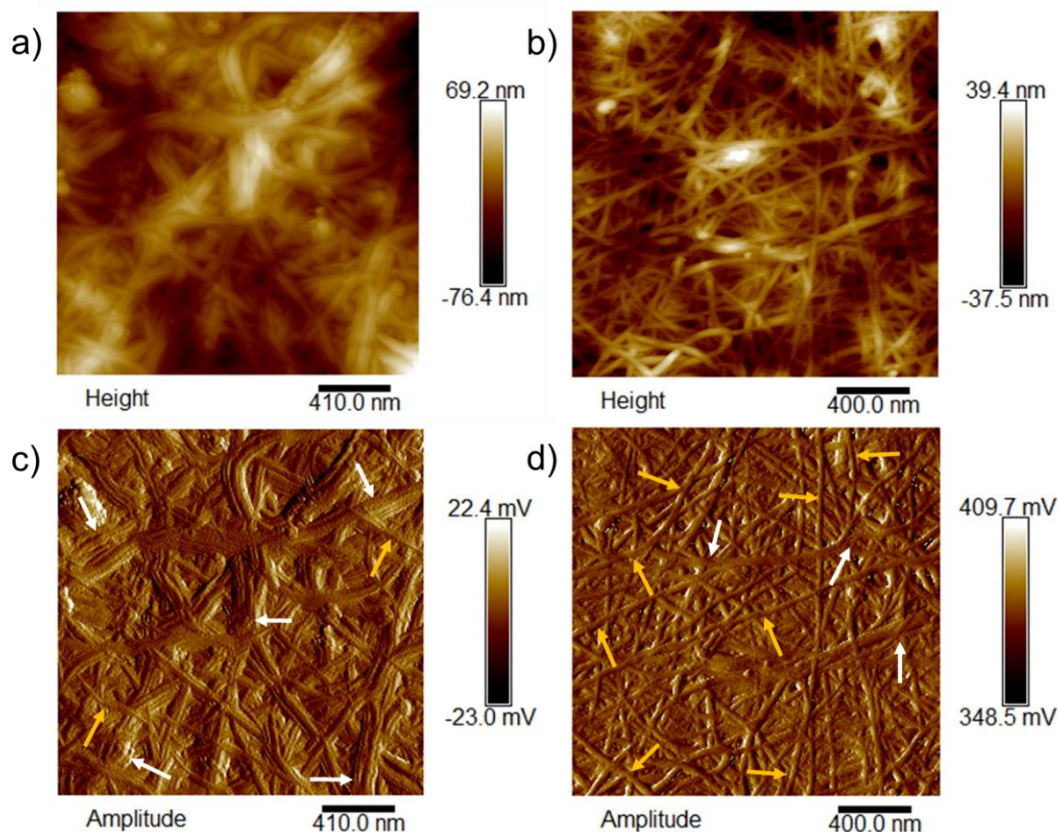


Figure 4.14. AFM images of the a), b) height images and c), d) amplitude images for pristine SWCNT and OTF:SWCNT composite films dropcast on glass substrate.

Figure 4.14 shows the morphology of the highly concentrated solution of the composite analyzed through Atomic Force Microscopy (AFM). The pristine SWCNT shows aggregates or bundled nanotubes in significantly higher number, which is also called as primary particles indicated by the white arrows shown in

AFM amplitude image given in **Figure 4.14c**. These aggregates are called as primary particles of SWCNTs with larger diameter sizes ranging from ≈ 60 -80 nm. The primary particles consists of several number of individual nanotubes and that is seperated in the solvent by OTF molecules using the sonication process. As the molecule is incorporated into the SWCNTs, the primary particles are separated into individual nanotubes as shown by the yellow arrows in **Figure 4.14d**. An abrupt increase in electrical conductivity could be observed due to the presence of more conductive networks or channels. Even with the presence of OTF, there are still presence of aggregates or primary particles that arise as a result of the van der Waals interactions between C–C. The surface roughness (R_a) also decreased from ~ 15.7 nm (pristine SWCNT) to ~ 7.9 nm (OTF:SWCNT). The lower surface roughness indicates more favourable charge transport across the nanotubes. The nanocomposite exhibits a well organized structure with lesser defects. The percolation effect of the nanotubes could be further be elaborated based on the TE performance of the composites.

4.3.6. Thermoelectric properties

Figure 4.15 shows thermoelectric properties of OTF:SWCNT composite with varying the weight ratio (20 to 70 wt%) of the nanotubes. Below 20 wt% SWCNT content, the σ is too low to be measured in the LSR-3 Seebeck measurement system.

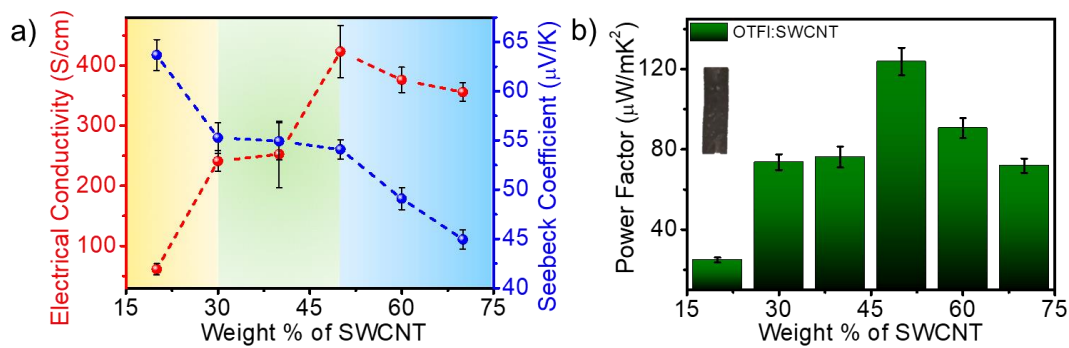


Figure 4.15. a) Electrical conductivity and Seebeck coefficient plot, b) Power factor as a function of the weight % of SWCNT.

The σ and α plot shows different characteristics and based on this, the plot can be divided into three sections. In the first section, the σ increases with the increase in SWCNT content from 20 to 30 wt%. This region may be called as the first percolation-like effect. Here, α shows a sudden decrease from $63 \mu\text{VK}^{-1}$ with the addition of the nanotubes. The sudden decrease in α might be associated with the change in the number or nature of phases within the material system. Further, on increasing the wt% of SWCNT from 30 to 50 wt%, σ increases and reaches the highest value of 425 Scm^{-1} . This region is called the second percolation-like effect. At this ratio, this rapid increase in σ might be resulted from the presence of higher ratio of individual SWCNTs than the SWCNT primary particles. Hence, more pathways are created for charge transport. In this region, α shows an independency with that of the σ trend. At this percolation threshold region, many conductive routes are created with the SWCNTs which results in the rapid increase in σ .

On further increase in SWCNT wt%, σ gets saturated and that the conductivity varies little exhibiting an equilibrium behavior. Hence, the σ slowly increases initially until the first region and then increases drastically reaching the plateau in the second region and then decreases and stays in an equilibrium region. In this region, α decreases and reaches the minimum value of $45 \mu\text{VK}^{-1}$. It is noticeable that α is higher in case of higher wt% of OTF which suggests that for the pristine SWCNT, the α may be much lower than that of the nanocomposite. This may be due to the energy filtering at the interface of the SWCNT and OTF. The PF shows the trend same as that of σ showing an increase upto 50 wt% SWCNT followed by a decrease having a maximum performance @50 wt% SWCNT content i.e. a PF of $124 \mu\text{Wm}^{-1}\text{K}^{-2}$ is obtained. The Hall effect measurement studies suggests that the carrier concentration (n) increases on increase in the CNT content in the first region and then saturates @50 wt% SWCNT as indicated in **Table 4.2**.

This increase in n results in a decreased α with increase in CNT content according to the Mott's relation (**Equation 1.4**) where Seebeck coefficient, Boltzmann constant, absolute temperature, and carrier concentration are represented by α , k_B , T , and n , respectively.^[35-36] According to this relationship, increasing n upon on addition of the nanotubes would improve σ and reduce α . So, as we increase the number of nanotubes, it is essentially increasing the concentration of conductive pathways within the material, leading to improved σ . Simultaneously,

the presence of a greater number of nanotubes helps to mitigate thermal expansion, resulting in a reduction in the α .

Table 4.2. Carrier concentration and mobility of OTF:SWCNT nanocomposite with varying weight % of SWCNT.

	Bulk conc. (cm ⁻³)	Mobility (cm ² /Vs)
20 weight % SWCNT	1.57E20	2.10E-1
50 weight % SWCNT	3.76E21	3.56E-1
70 weight % SWCNT	3.51E21	5.18E-1

4.3.7. Temperature dependent thermoelectric properties

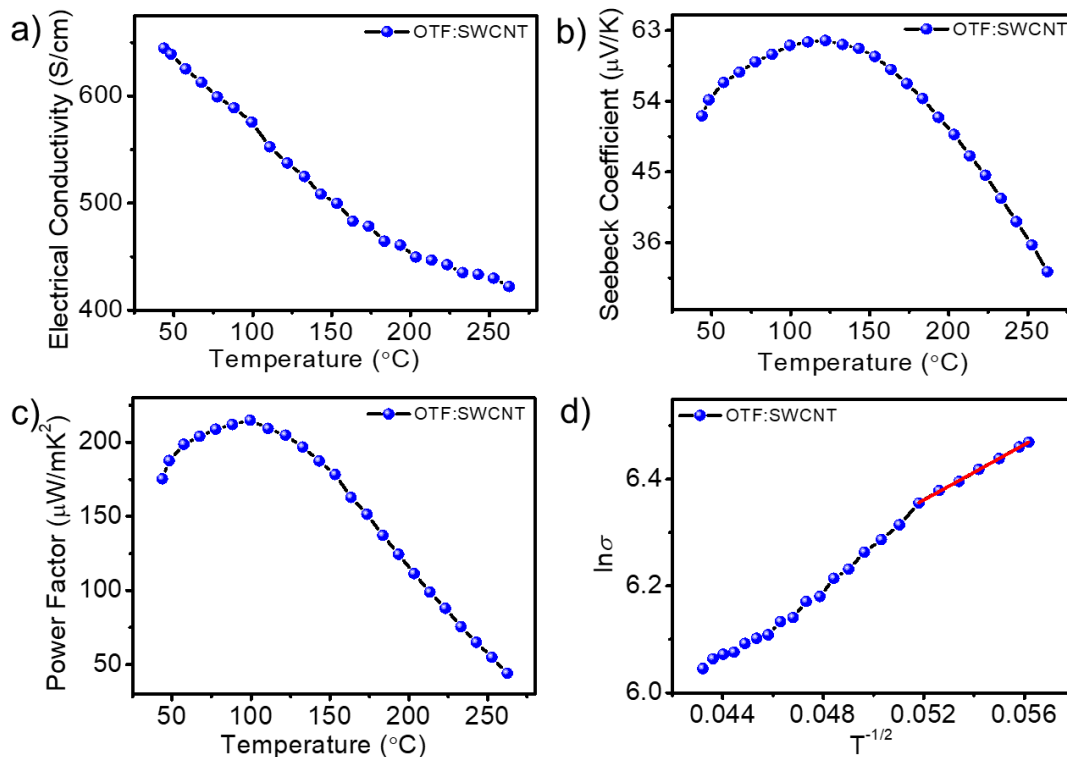


Figure 4.16. a) Electrical conductivity, b) Seebeck coefficient, c) Power factor as a function of temperature, d) $\ln \sigma$ v/s $T^{-1/2}$ plot.

Next, we evaluate the TE properties of the composite on varying the temperature from RT to 250 °C for a 50 wt% OTF:SWCNT sample (**Figure 4.16**). The σ shows a decreasing trend with increase in temperature, which suggests a metal-like behavior of the nanotubes. In metals, both electrical and thermal conduction follows the same mechanism where increase in temperature results in scattering of the conducting electrons by the phonons.^[37] In semiconducting CNTs, including the metal-like behavior, the superiority of the phonon modes governs the thermal conductivity and heat capacity, where the transport is quasi-one-dimensional.^[1,37]

Contrary to this, α exhibits a complex behavior with respect to temperature in case of OTE materials (**Figure 4.16b**). Here, we observe a non-monotonic behavior i.e α first increases with temperature and then decreases. α in SWCNT films is predominantly dictated by the bundles present in the films. Each bundle is conceptualized as a series of laterally aligned parallel circuits composed of semiconducting (s) and metallic (m) SWCNTs.^[38] Unlike σ , α is known to have two contributions; one is the ballistic component that links with the energy dependence near the DOS and another one is the diffusive component that relates to the energy dependence of diffusion coefficient. α is dependent on the ratio of conductance of m/s contribution. The deviation in this ratio may result in an increased α at low temperatures. The increase in α at lower temperatures could have arisen from the diffusive component, specifically a phonon drag effect. This phenomenon may be attributed to the non-uniformity in the diameter of nanotubes, defects due to the

intercalation of OTF, as well as the influence of bundling or deviations from the one-dimensionality of electronic states in SWCNTs.^[38]

Further, the composite film demonstrated a linear relationship between $\ln \sigma$ and $T^{-1/2}$ up to 373 K (**Figure 4.16d**). Hence, the charge transport adheres to the one-dimensional Variable Range Hopping (1D-VRH) model, where $d = 1$. The VRH model focusses the charge transport occurring around the E_F at a constant DOS;

$$\sigma = \sigma_0 \exp\left(-\frac{T_0}{T}\right)^{\frac{1}{d+1}} \quad (4.1)$$

where σ_0 represents the pre-exponential factor, T_0 is the characteristic temperature (inverse relationship to that of hopping), T is the temperature, d stands for hopping exponent (which depends on the dimensionality of the system). In a disordered system like semiconductor:nanotube composite system, a pronounced π - π interfacial interaction is evident between OSC and SWCNT, enabling the carriers to hop from one SWCNT to another through a one-dimensional channel.^[35] This refers to the stacking of π -electron-rich regions in OTF with the π -electron system of the carbon nanotubes. Here, the one-dimensional channel refers to the aligned arrangement of nanotubes, creating a pathway for charge carriers to hop from one nanotube to another. The overall PF of the OTF:SWCNT nanocomposite obtained is $215 \mu\text{Wm}^{-1}\text{K}^{-2}$ at 100 °C. The performance of the as-prepared TEG is compared to that of few reported in literature which is given in **Table 4.3**. The TEG prepared

from the OTF:SWCNT composite material shows good output performance which is close to the benchmark performances in literature.

Table 4.3. Comparison of the TE performances of few nanocomposites reported in the literature with that of the OTF:SWCNT system in the present study.

Compound	Dopant	σ (S/cm)	α ($\mu\text{V/K}$)	PF ($\mu\text{W/mK}^2$)	Ref
Pentacene	F4TCNQ	0.03	280	0.16	39
Pentacene	Iodine	60	40-60	13	40
Pentacene	F4TCNQ	0.43	200	2	41
TPETPA	SWCNT	356.2	123.2	539.8	42
TCzPy	SWCNT	198.4	9.2	113.2	43
CuPc	CN6-CP	0.76	130	1.3	44
CuPc	SWCNT	/	/	70.1	45
C8-BTBT	SWCNT	280	0.29	23.5	46
HAT6	SWCNT	1286	56.45	408.23	47
2	SWCNT	50.02	83.51	34.88	48
This work	SWCNT	850	37.25	124 (308 K) 215 (373 K)	

4.3.8. Energy level estimation

In order to investigate the work function (ϕ) and the distance of E_F from HOMO energy level ($E_{\text{HOMO}} - E_F$) of the composite material, Ultraviolet Photoelectron Spectroscopy (UPS) is carried out as shown in **Figure 4.17**. ϕ is obtained from the secondary cut-off region i.e. observed in the high binding energy (BE) region of the

UPS spectra whereas $E_{\text{HOMO}}-E_{\text{F}}$ distance is obtained from the low binding energy (BE) region of the spectra wherein E_{F} is located at 0 eV. The ϕ of pristine OTF and

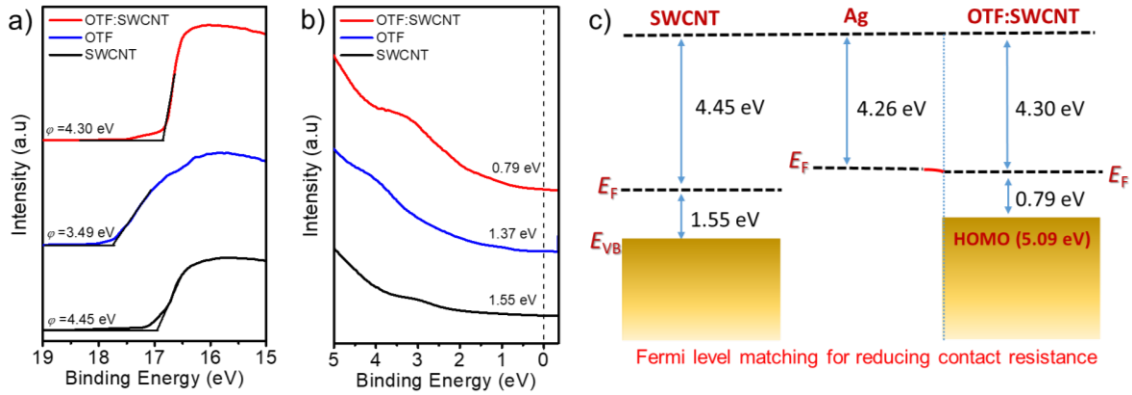


Figure 4.17. UPS spectra of the pristine OTF, SWCNT and OTF:SWCNT composite showing a) Secondary electron cut-off region, b) Low binding energy region and c) Energy level diagram.

SWCNT are 3.49 and 4.45 eV respectively. After composite formation, OTF:SWCNT (1:1) exhibits a ϕ of 4.30 eV. This shows that there is the existence of strong Fermi energy level pinning induced by the presence of OTF. $E_{\text{HOMO}}-E_{\text{F}}$ of pristine OTF and SWCNT are 1.37 and 1.55 eV respectively. On composite formation, this gets much reduced to 0.79 eV which indicates that there is shifting of the E_{F} much closer towards the HOMO energy level. **Figure 4.17c** summarizes the energetics of the pristine molecule, SWCNT and the composite in the form of a band energy diagram. The ϕ of Silver (Ag) which is the interconnects used in the 7-legged p-type TEG is 4.26 eV. The resultant composite material aligns the Fermi much closer towards the E_{F} of the interconnect such that the Schottky energy barrier (ϕ_{B}) between the metal (Ag) and the semiconductor (composite material) is reduced and that it allows free flow of the charge carriers.^[49]

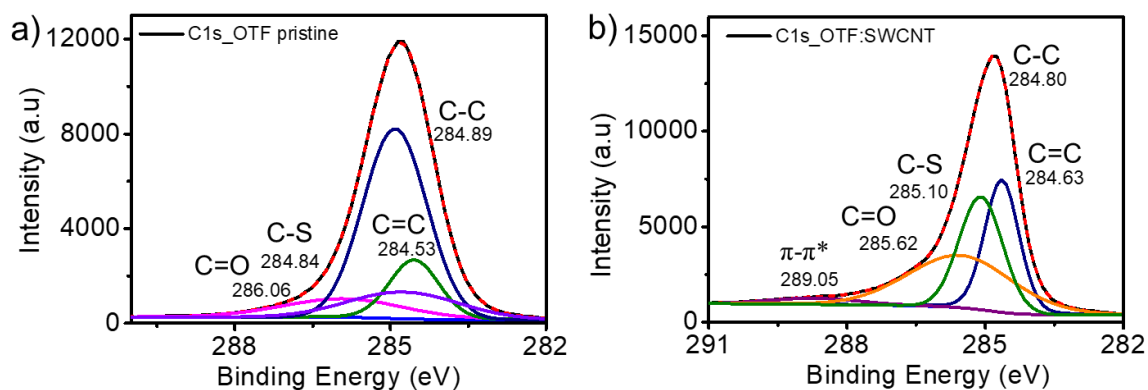


Figure 4.18. High-resolution C1s XPS core level spectra of a) OTF, b) OTF:SWCNT.

This shift in energy of the overall spectrum towards a lower BE is further consistent with the shifts observed in the C1s core level spectra of the X-ray Photoelectron Spectroscopy (XPS) (**Figure 4.18**). The presence of C=O, C=C, C-S, C-C is observed at 286.06, 284.53, 284.84, and 284.89 eV respectively. On composite formation, the corresponding peaks shifts to 285.62, 284.63, 285.10, and 284.80 eV respectively. An additional π - π^* bond is observed in the OTF:SWCNT composite which is designated from the sp^2 C atom of the SWCNTs.

4.3.9. Fabrication of thermoelectric generator

A prototype flexible TEG having 7 p-type legs of the OTF:SWCNT composite is arranged on a polyimide substrate and is fabricated as shown in **Figure 4.19**. Conducting silver ink is used as the interconnects. The method of fabrication of the flexible TEG is explained in detail in section 4.5.1.

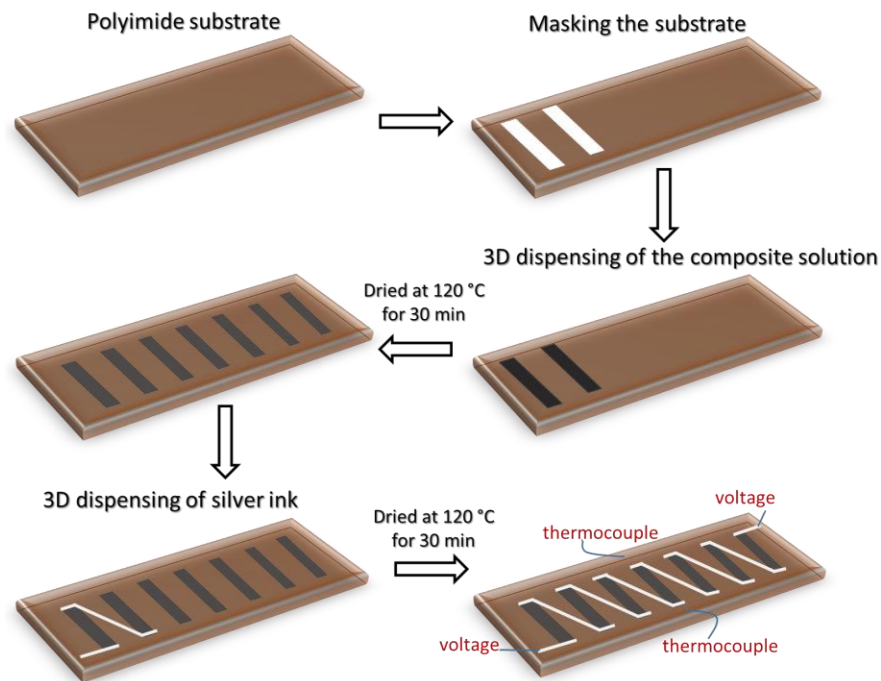


Figure 4.19. Fabrication of the planar TEG consisting of 7 p type legs.

4.3.10. Performance of the TEG

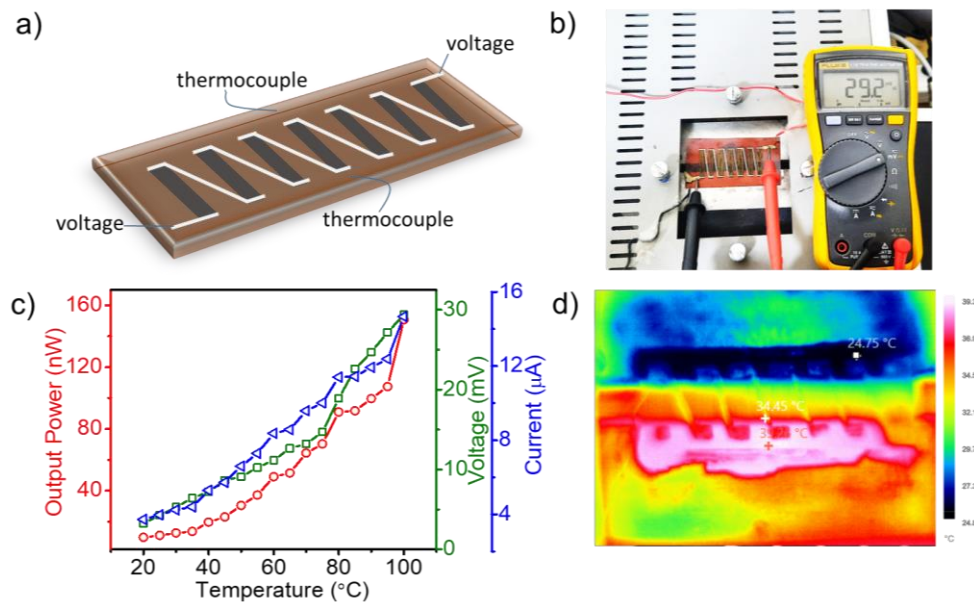


Figure 4.20. a) Schematic representation of 7 leg TEG of the hybrid OTF:SWCNT b) Photograph of the 7-legged flexible TEG c) The output power, output voltage and output current by varying ΔT , d) Thermal image of the temperature distribution.

Figure 4.20a gives the schematic representation of the as-fabricated 7-leg TEG. **Figure 4.20b** shows the photograph of the TEG exhibiting the maximum output voltage when subjected to a ΔT of 100 K. In **Figure 4.20c**, the plot shows the output current, voltage and power of the flexible TEG at different ΔT varying from 20 K to 100 K. The TEG exhibits an output voltage of 29.4 mV and output current of 14.69 μA @ $\Delta T = 100$ K with a load resistance of $\sim 770 \Omega$. A maximum power output (P_O) of 150 nW (@ $\Delta T=100$ K) is obtained.

4.3.11. Flexibility of the TEG

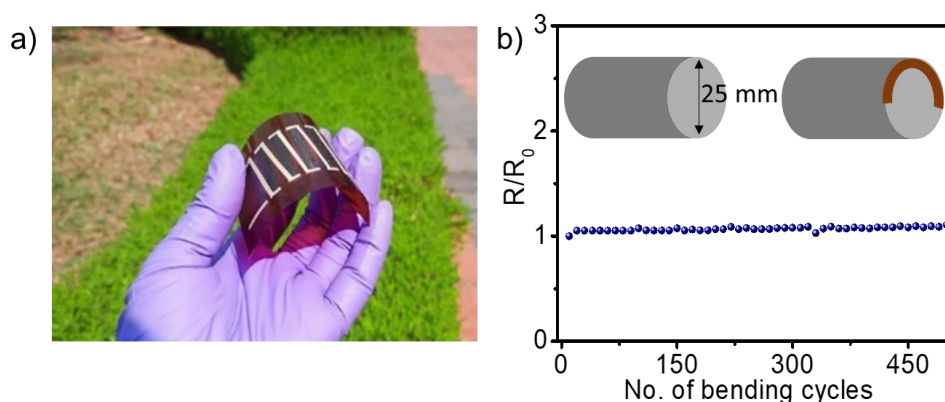


Figure 4.21. a) Photograph of the 7-legged flexible TEG, b) Change in internal resistance of the flexible TEG with respect to the no. of bending cycles (bending diameter= 25 mm).

The flexibility of the TEG is studied by analyzing the change in internal resistance of the device by bending across a cylindrical pipe with a diameter of 25 mm (**Figure 4.21**). The resistance of the TEG before (R_0) and after bending (R) is measured. The change in internal resistance (R/R_0) did not show significant changes up to 500 cycles.

4.4. Conclusions

We have demonstrated a facile solution based method to efficiently disperse and debundle the SWCNT by introducing an thiophene-based organic molecule, OTF. The debundling and dispersion of the nanotubes are confirmed via TEM analyses where individual SWCNTs are majorly formed in a 1:1 ratio of the composite thin film. AFM results also confirm the presence of individual nanotubes that results in better electrical properties. Efficient debundling in combination with enhanced charge transfer between the two components resulted in an enhanced TE performance. The interfacial energy filtering effect between OTF and SWCNT resulted in an enhanced PF of $124 \mu\text{Wm}^{-1}\text{K}^{-2}$ at room temperature (308 K) and $215 \mu\text{Wm}^{-1}\text{K}^{-2}$ at 373 K for a 1:1 ratio of the composite material. A flexible TEG was fabricated with 7 p-type legs of the active material with silver electrodes as the interconnects. The devices showed excellent flexibility and displayed a power output (P_O) of 150 nW (@ $\Delta T=100$ K). The developed composite material exhibited Fermi energy level much closer to that of the electrode such that Schottky energy barrier or ϕ_B is reduced and that results in free flow of the charge carriers. These findings underscore the importance of carefully designed organic molecules and their supramolecular interactions with carbon nanotubes in augmenting TE performance. This research paves the way for further exploration and optimization of organic-inorganic composite materials for efficient and flexible thermoelectric applications.

4.5. Experimental section

4.5.1. Materials and methods

Materials: SWCNT (purity $\geq 89\%$ carbon basis ($\geq 99\%$ as CNT), having a diameter ranging $\sim 3\text{--}4$ nm and length of ~ 10 μm). Anhydrous 1,2-dichlorobenzene purchased from Sigma Aldrich was used as the solvent. The reagents and solvents utilized in the synthesis were procured from Sigma-Aldrich, Alfa Aesar, or TCI. These materials were employed in their as-received form. Synthetic procedures that are sensitive to air and water were carried out in an inert atmosphere. All materials were used without further purification unless otherwise mentioned.

Preparation of the nanocomposite: OTF and SWCNT are dispersed in *o*-DCB at concentration of 5 mg/mL using an ultra sonicator (VCX-750 Vibra-Cell, Sonics and Materials) for 60 min which is kept in an ice bath. The composition was altered by incorporating varying weight percentages (wt%) of SWCNT. The dispersion was then drop-casted onto a glass substrate that has been pre-cleaned sequentially with extran, water, and isopropanol, followed by bath sonication for 15 minutes each. Subsequently, the substrate was pre-heated at 120 °C for 15 minutes and annealed at the same temperature for 30 minutes.

Measurements: The details of materials, measurements, UV-vis absorption spectrophotometer, thermogravimetric analysis (TGA), wide-angle X-ray scattering (WAXS), scanning electron microscopy (SEM), transmission electron microscopy (TEM), atomic force microscopy (AFM), ultraviolet photoelectron spectroscopy

(UPS) and X-ray photoelectron spectroscopy are described in section 3.5.1 of Chapter 3.

Fluorescence spectroscopy: Fluorescence spectra was captured with a SPEX-Fluorolog F112X spectrofluorometer, which was equipped with a 450 W xenon arc lamp. The correction of spectra was carried out using the software provided by the manufacturer.

Hall effect measurement: Mobility and carrier concentration at room temperature were measured in an ECOPIA HMS 3000 system (0.54 T field and 15 mA current) utilizing the Van der Pauw's geometry. The sample solutions were dropcasted onto a 1x1 cm glass substrate to form a film, and the thickness was assessed using a profilometer.

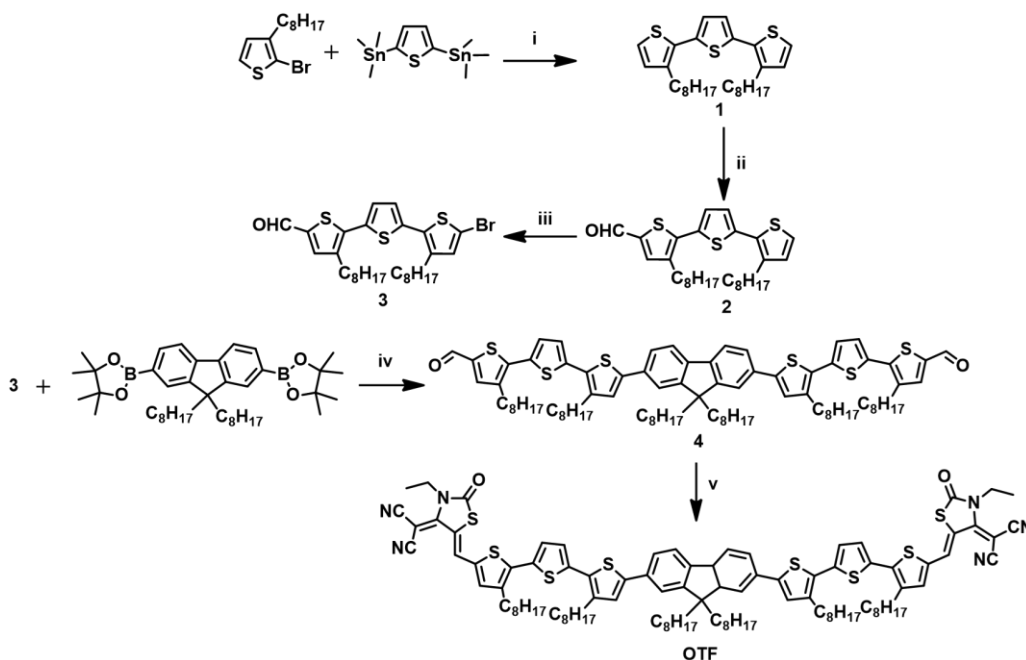
Raman spectroscopy: Raman spectra was measured in a WI-Tec alpha 300R Confocal Raman microscope, having a laser beam of 633 nm excitation wavelength and 7 mW power directed to the sample. Data was evaluated using WI-Tec Project plus v2.1 software package. The sample solution were drop-cast onto a 1x1 cm glass substrate to form a film.

Thermoelectric measurements: The TE properties of the nanocomposite were measured using Linseis LSR-3 thermopower measuring system. Simultaneous measurement of σ and α could be carried out using the system. Each sample was vertically positioned between two electrodes, and a temperature gradient was induced by the lower electrode block, which included a heating coil. The entire

setup was situated within a chamber furnace to ensure insulation and thermal regulation. Two thermocouples in direct contact with the sample's surface were employed to measure the temperature difference between the heated and cooled areas.

Fabrication of flexible TEG and testing: Flexible TEGs were fabricated on a polyimide substrate (DuPont Kapton® HN50) utilizing a formulation composed of OTF:50wt% SWCNT composite. Dispensing was carried out using an automated 3D dispenser needle valve (Nordson EFD 741), and the resulting films were subjected to annealing on a hot plate at 120 °C for a duration of 30 minutes. To interconnect the TE legs, an automated 3D dispenser jet valve (Nordson PICO Pulse) was employed to dispense silver screen ink (Novacentrix Metalon® HPS-FG777). The TEGs were annealed at 120 °C for a duration of 30 min. The evaluation of the fabricated TEG was carried out in a custom-made setup. The setup consists of a heater and a cooler (TEMPSENS Instruments Pvt. Ltd.) in order to maintain the temperatures of the hot and cold side respectively. Exact temperature measurements were carried out using K-type thermocouple. Temperature difference was varied from 10 to 100 K. Keithley 6510 DAQ system was used for measuring the output current and voltage.

4.5.2. Synthesis and characterization



Scheme 4.1. Reagents and conditions: (i) $\text{Pd}_2(\text{dba})_3$, $\text{P}(\text{o-tolyl})_3$, Toluene; (ii) POCl_3 , DMF, 1, 2-dichloroethane; (iii) NBS, AcOH, CHCl_3 (iv) $\text{Pd}(\text{PPh}_3)_4$, THF:H₂O (9:1), K_2CO_3 , 2d; (v) 2-(1,1-dicyanomethylene)rhodanine, dry CHCl_3 , piperidine, 24h.

The synthesis was carried out through a series of stepwise reactions including, palladium catalysed Stille coupling, Vilsmeier–Haack formylation followed by Knoevenagel condensation as shown in **Scheme 4.1**.^[29] The compound was obtained in good yield and characterized using various analytical techniques such as, ^1H NMR, ^{13}C NMR, high-resolution mass spectrometry (HRMS) and FTIR. The compound is soluble in organic solvents like chloroform (CHCl_3), dichloromethane (CH_2Cl_2), 1,2-dichlorobenzene ($\text{C}_6\text{H}_4\text{Cl}_2$) etc.

Synthesis of 3,3-dioctyl-2,2':5',2''-terthiophene (1): A solution of 2,5-bis(tributylstannyl)-thiophene (4 g, 6.04 mmol, 1 eq.), 2-bromo-3-octylthiophene

(3.49 g, 12.68 mmol, 2.1 eq.), Pd₂(dba)₃ (165mg, 0.18 mmol, 3 mol%) and P(o-tolyl)₃ (220 mg, 0.72 mmol, 4 equiv. to Pd catalyst) in dry toluene was refluxed and stirred overnight. The reaction mixture was cool to room temperature and diluted with CH₂Cl₂. The organic layer was washed with water and brine; dried over anhydrous Na₂SO₄ and concentrated in vacuo. The crude compound was purified by flash column chromatography using hexane as the eluent to afford the corresponding product as yellow oil. Yield: 85%. δ_{H} (500 MHz, CDCl₃, *J*/Hz): 7.19 (d, *J* 5, 2H), 7.07 (s, 2H), 6.96 (d, *J* 5, 2H) 2.80 (t, *J* 8, 4H), 1.67 (q, 4H), 1.40-1.27 (m, 20H), 0.89 (t, 6H).

Synthesis of 3,3''-Dioctyl-[2,2':5',2''-terthiophene]-5-carbaldehyde (2): To a solution of 3,3-dioctyl- 2,2':5',2''-terthiophene (**1**) (920 mg, 1.95 mmol, 1 eq.) and N,N-dimethylformamide (0.15 mL, 1.95 mmol, 1 eq.) in 1,2-dichloroethane was slowly added POCl₃ (0.18 mL, 1.95 mmol, 1 eq.) at 0 °C, and stirred for 1 h under argon. Then, the reaction mixture was allowed to heat to 60 °C and stirred overnight. The mixture was cool to 0 °C and neutralized using NaHCO₃ (aq). The organic layer was extracted using CH₂Cl₂ and dried over anhydrous Na₂SO₄ and concentrated in vacuo. The crude compound was purified by column chromatography using the mixture of hexane and CH₂Cl₂ (1:1 v/v) as the eluent to afford the corresponding product as an orange oil. Yield: 80%. δ_{H} (500 MHz, CDCl₃, *J*/Hz): 9.83 (s, 1H), 7.60 (s, 1H), 7.25 (d, *J* 8.5, 1H), 7.23 (d, *J* 8.5, 1H),

7.11 (d, *J* 5.5, 1H), 6.97 (d, *J* 5, 1H), 2.83 (t, *J* 7.75, 2H), 2.82 (t, *J* 8, 2H), 1.72-1.62 (m, 4H), 1.43-1.27 (m, 20H), 0.88-0.86 (m, 6H).

Synthesis of 5''-Bromo-3,3''-dioctyl-[2,2':5',2''-terthiophene]-5-carbaldehyde

(3): To a stirred solution of appropriate 3,3''-dioctyl-[2,2':5',2''-terthiophene]-5-carbaldehyde (**2**) (590 mg, 1.17 mmol, 1 eq.) in chloroform and acetic acid (1:1 v/v), NBS (209 mg, 1.17 mmol, 1 eq.) was added in dark at room temperature for 2 h. The reaction was monitored by TLC to establish completion. The organic layer was extracted with hexane, washed with NaHCO₃ (aq), water and brine; dried over anhydrous Na₂SO₄ and concentrated in vacuo. The crude compound was purified by gravity column chromatography using hexane as the eluent to afford the corresponding product as orange oil. Yield: 98%. δ_{H} (500 MHz, CDCl₃, *J*/Hz): 9.83 (s, 1H), 7.60 (s, 1H), 7.22 (d, *J* 4, 1H), 7.04 (d, *J* 4, 1H), 6.92 (s, 1H), 2.81 (t, *J* 7.75, 2H), 2.71 (t, *J* 7.75, 2H), 1.64 (m, 4H), 1.43-1.26 (m, 20H), 0.87 (m, 6H).

Synthesis of 5'',5''''-(9,9-dioctyl-9H-fluorene-2,7-diyl)bis(3,3''-dioctyl-

[2,2':5',2''-terthiophene]-5-carbaldehyde) (4): To a stirred solution of 2,2'-(9,9-dioctyl-9H-fluorene-2,7-diyl)bis(4,4,5,5-tetramethyl-1,3,2 dioxaborolane) (906 mg, 1.00 mmol, 1.0 equiv.), 3,3''-dioctyl-[2,2':5',2''-terthiophene]-5,5''-dicarbaldehyde (**3**) (621 mg, 2.10 mmol, 2.1 equiv.), 2 M aq.K₂CO₃ (5 mL), Aliquat 336 (1 drop), Pd(PPh₃)₄ (57 mg, 0.05 mmol, 0.05 equiv.), and toluene (8 mL) were added. The crude product was purified using column chromatography (silica gel, hexane). A

pure product was obtained as a brick red solid. Yield: 70%; δ_{H} (500 MHz, CDCl_3 , J/Hz): 8.65 (s, 2H), 7.93 (d, J 8, 2H), 7.73 (d, J 4.4, 4H), 7.63-7.60 (dd, 2H), 7.48 (d, J 1.5, 2H), 2.64-2.60 (m, 8H), 1.59-1.49 (m, 8H), 1.32-1.28 (m, 40H), 0.88-0.86 (m, 18H).

Synthesis of **OTF**: Bisaldehyde (**4**) (373 mg, 0.26 mmol, 1 eq.) and 2-(1,1-dicyanomethylene)rhodanine (514 mg, 2.69 mmol, 10 eq.) was dissolved in a solution of dry CHCl_3 (15 mL) and then three-four drops of piperidine was added and stirred for 48 h under argon at room temperature. The reaction mixture was then diluted with dichloromethane and washed with water and brine. After removal of solvent it was chromatographed on silica gel using CHCl_3 -Hexane (1:1). Yield: 83%. M.P: 167-168 °C. δ_{H} (500 MHz, CDCl_3 , J/Hz): 8.01 (s, 2H), 7.89 (d, J 8, 2H), 7.62-7.60 (dd, 2H), 7.54 (d, J 1.5, 2H), 7.33 (d, J 4, 2H), 7.31 (s, 2H), 7.26 (d, J 3, 2H), 7.19 (d, J 3, 2H), 4.35-4.31 (m, 4H), 2.89-2.83 (m, 8H), 1.78-1.68 (m, 8H), 1.43-1.17 (m, 40H), 0.88-0.87 (m, 12H). δ_{C} (125 MHz, CDCl_3): 165.91, 165.56, 151.82, 143.49, 141.30, 140.96, 140.48, 138.94, 138.67, 133.85, 133.78, 132.74, 129.06, 128.06, 128.09, 126.17, 126.04, 124.65, 120.21, 119.72, 113.45, 113.28, 112.32, 55.59, 55.38, 40.65, 40.40, 31.91, 31.86, 31.80, 30.65, 30.31, 29.96, 29.83, 29.70, 29.57, 29.49, 29.41, 29.32, 29.27, 29.18, 23.74, 22.69, 22.67, 22.59, 14.21, 14.11, 14.06. IR (KBr) ν_{max} : 738, 771, 805, 884, 1120, 1210, 1345, 1368, 1424, 1537, 1593, 1728, 2223, 2842, 2921 cm^{-1} .

4.6. References

- [1] X. Wang, H. Wang, B. Liu, *Polymers*. **2018**, *10*, 1196.
- [2] W. Di Liu, Y. Yu, M. Dargusch, Q. Liu, Z. G. Chen, *Renew. Sustain. Energy Rev.* **2021**, *141*, 110800.
- [3] S. B. Riffat, X. Ma, *Appl. Therm. Eng.* **2003**, *23*, 913.
- [4] M. F. Sanad, A. E. Shalan, S. O. Abdellatif, E. S. A. Serea, M. S. Adly, M. A. Ahsan, *Top. Curr. Chem.* **2020**, *48*, 378.
- [5] R. Kroon, D. A. Mengistie, D. Kiefer, J. Hynynen, J. D. Ryan, L. Yu, C. Müller, *Chem. Soc. Rev.* **2016**, *45*, 6147.
- [6] M. Massetti, F. Jiao, A. J. Ferguson, D. Zhao, K. Wijeratne, A. Würger, J. L. Blackburn, X. Crispin, S. Fabiano, *Chem. Rev.* **2021**, *121*, 12465.
- [7] M. He, F. Qiu, Z. Lin, *Energy Environ. Sci.* **2013**, *6*, 1352.
- [8] B. Kumanek, D. Janas, *J. Mater. Sci.* **2019**, *54*, 7397.
- [9] S. N. Patel, A. M. Glauddell, D. Kiefer, M. L. Chabiny, *ACS Macro Lett.* **2016**, *5*, 268.
- [10] H. Hamasaki, S. Takimoto, K. Hirahara, *Nano Lett.* **2021**, *21*, 3134.
- [11] M. M. Gallego, R. Verdejo, M. Khayet, J. M. O. de Zarate, M. Essalhi, M. A. L. Machado, *Nanoscale Res. Lett.* **2011**, *6*, 1.
- [12] T. Lei, Y. C. Lai, G. Hong, H. Wang, P. Hayoz, R. T. Weitz, C. Chen, H. Dai, Z. Bao, *Small* **2015**, *11*, 2946.
- [13] Y. Bao, Y. Sun, F. Jiao, W. Hu, *Adv. Electron. Mater.* **2023**, *9*, 2201310.
- [14] D. Zhou, H. Zhang, H. Zheng, Z. Xu, H. Xu, H. Guo, P. Li, Y. Tong, B. Hu, L. Chen, *Small* **2022**, *18*, 1.
- [15] J. Li, A. B. Huckleby, M. Zhang, *J. Mater.* **2022**, *8*, 204.
- [16] B. T. McGrail, A. Sehirliglu, E. Pentzer, *Angew. Chemie - Int. Ed.* **2015**, *54*, 1710.
- [17] Q. Zhang, Y. Sun, W. Xu, D. Zhu, *Adv. Mater.* **2014**, *26*, 6829.

-
- [18] L. Deng, Y. Liu, Y. Zhang, S. Wang, P. Gao, *Adv. Funct. Mater.* **2023**, *33*, 1.
- [19] Y. Chen, Y. Zhao, Z. Liang, *Energy Environ. Sci.* **2015**, *8*, 401.
- [20] C. K. Mytafides, L. Tzounis, G. Karalis, P. Formanek, A. S. Paipetis, *ACS Appl. Mater. Interfaces* **2021**, *13*, 11151.
- [21] E. Muchuweni, E. T. Mombeshora, *Appl. Surf. Sci. Adv.* **2023**, *13*, 100379.
- [22] X. Li, Z. Yu, H. Zhou, F. Yang, F. Zhong, X. Mao, B. Li, H. Xin, C. Gao, L. Wang, *ACS Sustain. Chem. Eng.* **2021**, *9*, 1891.
- [23] Q. Yao, Q. Wang, L. Wang, L. Chen, *Energy Environ. Sci.* **2014**, *7*, 3801.
- [24] J. G. Jang, S. Y. Woo, H. Lee, E. Lee, S. H. Kim, J. I. Hong, *ACS Appl. Mater. Interfaces* **2020**, *12*, 51387.
- [25] J. G. Jang, J. Hong, *ACS Appl. Energy Mater.* **2022**, *5*, 13871.
- [26] T. H. Kim, J. I. Hong, *ACS Appl. Mater. Interfaces* **2022**, *14*, 55627.
- [27] J. Jung, E. H. Suh, Y. J. Jeong, H. S. Yang, T. Lee, J. Jang, *ACS Appl. Mater. Interfaces* **2019**, *11*, 47330.
- [28] S. Qin, J. Tan, J. Qin, J. Luo, J. Jin, S. Huang, L. Wang, D. Liu, *Adv. Electron. Mater.* **2021**, *7*, 2100557.
- [29] T. Ghosh, A. Gopal, S. Nagasawa, N. Mohan, A. Saeki, V. C. Nair, *ACS Appl. Mater. Interfaces* **2016**, *8*, 25396.
- [30] I. Vijitha, N. Jacob, N. Raveendran, C. Vijayakumar, B. Deb, *Mater. Today Energy* **2023**, *32*, 101233.
- [31] V. Ignatious, N. Raveendran, A. Prabhakaran, Y. Tanjore Puli, V. Chakkooth, B. Deb, *Chem. Eng. J.* **2021**, *409*, 128294.
- [32] Shaoxin Zhou, J. Xu, Q.-H. Y. S. Chiang, B. Li, H. Du, C. Xu, F. Kang, *Carbon* **2013**, *57*, 452.
- [33] J. Mateos-Gil, L. R. Pérez, M. M. Oliva, G. Katsukis, C. Romero-Nieto, Á. Herranz, D. M. Guldi, N. Martín, *Nanoscale* **2015**, *7*, 1193.

-
- [34] M. R. Muda, M. M. Ramli, S. S. Mat Isa, D. S. C. Halin, L. F. A. Talip, N. S. Mazelan, N. A. M. Anhar, N. A. Danial, *IOP Conf. Ser. Mater. Sci. Eng.* **2017**, *209*, 012030.
- [35] A. M. Glaudell, J. E. Cochran, S. N. Patel, M. L. Chabinyk, *Adv. Energy Mater.* **2014**, *5*, 1401072.
- [36] N. Lu, L. Li, M. Liu, *Phys. Chem. Chem. Phys.* **2016**, *18*, 19503.
- [37] S. Dehghani, M. K. Moravvej-Farshi, M. H. Sheikhi, *Mod. Phys. Lett. B* **2012**, *26*, 1250136.
- [38] D. Hayashi, Y. Nakai, H. Kyakuno, Y. Miyata, K. Yanagi, Y. Maniwa, *Appl. Phys. Express* **2020**, *13*, 015001.
- [39] K. Harada, M. Sumino, C. Adachi, S. Tanaka, K. Miyazaki, *Appl. Phys. Lett.* **2010**, *96*, 253304.
- [40] K. Hayashi, T. Shinano, Y. Miyazaki, T. Kajitani, *J. Appl. Phys.* **2011**, *109*, 023712.
- [41] Y. Jin, S. Nola, K. P. Pipe, M. Shtein, *J. Appl. Phys.* **2013**, *114*, 194303.
- [42] Y. Jeon, J. G. Jang, S. H. Kim, J.-I. Hong, *J. Mater. Chem. C* **2021**, *9*, 8483.
- [43] X. Yin, Y. Peng, J. Luo, X. Zhou, C. Gao, L. Wang, C. Yang, *J. Mater. Chem. A* **2018**, *6*, 8323.
- [44] W. Xing, J. Chen, Y. Liang, Y. Zou, Y. Sun, W. Xu, D. Zhu, *RSC Adv.* **2019**, *9*, 31840.
- [45] Y. Chen, S. Qu, W. Shi, Q. Yao, L. Chen, *Carbon* **2020**, *159*, 471.
- [46] W. Shi, J. Chen, J. Xi, D. Wang, Z. Shuai, *Chem. Mater.* **2014**, *26*, 2669.
- [47] X. X. Li, Z. K. Yu, H. B. Zhou, F. Yang, F. Zhong, X. H. Mao, B. Z. Li, H. Xin, C. M. Gao, L. Wang, *ACS Sustainable Chem. Eng.* **2021**, *9*, 1891.
- [48] J. G. Jang, S. Y. Woo, H. Lee, E. Lee, S. H. Kim, J.-I. Hong, *ACS Appl. Mater. Interfaces* **2020**, *12*, 51387.
- [49] F. Daneshvar, H. Chen, K. Noh, H. J. Sue, *Nanoscale Adv.* **2021**, *3*, 942.

ABSTRACT

Name of the Student: **Ms. Neethi Raveendran**
Faculty of Study: Chemical Sciences
AcSIR academic centre/CSIR Lab: CSIR-National
Institute for Interdisciplinary Science
and Technology (CSIR-NIIST)

Registration No.: 10CC19A39015
Year of Submission: 2024

Name of the Supervisor: Dr. Vijayakumar C.

Title of the thesis: **Thiophene-Based Organic Thermoelectric Materials: Exploring Molecular Design, Doping Techniques and Nanocomposite Formations**

Approximately 67% of primary energy dissipates as thermal energy, highlighting the significance of technologies capable of capturing and converting this waste heat into electricity. Thermoelectric generators (TEGs) are increasingly seen as viable solutions to energy wastage, given their sustainability. As solid-state devices, TEGs convert heat into electricity utilizing the Seebeck effect, thereby promoting efficient waste heat harvesting from a plethora of sources. Organic and hybrid TE research emerged as a distinct sector in thermoelectrics, due to the superior performance of these materials at lower temperatures. In comparison to inorganic TE materials, organic TE materials present several compelling advantages. Organic TE materials also have the potential for scalability and compatibility with printed flexible devices, thereby increasing their utility. These advantages streamline the creation of personal, portable, and flexible TE modules. The **first chapter** provides an overview of organic thermoelectrics, the fundamental concepts involved, discussing the current state-of-the-art materials, and major objectives of the present thesis.

In **chapter 2**, we explore how subtle modifications in the molecular structure impact the TE characteristics of two small molecules, OT1 and OT2. The molecules differ only in their end substitutions with varying acceptor strengths, leading to distinct self-assembled morphologies. Upon doping with FeCl₃, OT2 exhibited better TE performance than OT1. The increased efficiency of doping in OT2 is a result of the weaker acceptor strength in its terminal group. Enhanced charge carrier transport in OT2 was facilitated by a low-lying HOMO energy level and an increased density of states around the HOMO post-doping. Hence, maintaining self-assembly post-doping proved essential for enhancing the electrical properties. These results emphasize the importance of molecular engineering in advancing the development of high-performance thermoelectric materials.

Chapter 3 delves into our examination of the TE properties of two donor-acceptor polymers, PBDTTT:C (P1) and PBDTTT:EFT (P2), doped with F4TCNQ. These polymers consist of benzodithiophene (BDT) as the donor and thienothiophene (TT) as the acceptor, and they exhibit differences in their alkyl side chains. Our investigations revealed diverse charge transfer states arising from variations in polymer aggregation upon the addition of F4TCNQ. This variation prompted further exploration of the polymers' aggregation behavior. Aggregation in the solution state of P2 promotes ion pair formation with F4TCNQ through integer charge transfer (ICT), enhancing doping efficiency, while in P1, the creation of P1-F4TCNQ charge transfer complexes via partial charge transfer results in a non-aggregated state and lower doping efficiency, ultimately leading to superior thermoelectric performance in P2-F4TCNQ, reaching 73.10 $\mu\text{Wm}^{-1}\text{K}^{-2}$.

In **chapter 4**, we focused on the synthesis of a semiconducting thiophene-based organic small molecule (OTF) and its interaction with SWCNT. An efficient solution based method resulted in efficient debundling, paired with the charge transfer between the two components, giving rise to an improved TE performance. The interfacial energy filtering effect between OTF and SWCNT boosted the power factor, achieving 124 $\mu\text{Wm}^{-1}\text{K}^{-2}$ at room temperature and 215 $\mu\text{Wm}^{-1}\text{K}^{-2}$ at 100 °C. A flexible TEG that demonstrated exceptional flexibility, producing a power output of 150 nW (@ $\Delta T=100$ K) was developed using the composite as the active material.

List of Publications Emanating from the Thesis

1. **Neethi Raveendran**, Tanwistha Ghosh, Vijitha Ignatious, Vibhu Darshan, Navin Jacob, Biswapriya Deb,* Chakkooth Vijayakumar,* Thermoelectric properties of self-assembled thiophene derivatives: effect of molecular structure on doping efficiency and Fermi level alignment, *Mater. Today Energy*, **2023**, *34*, 101296.
2. **Neethi Raveendran**, Vijitha Ignatious, Navin Jacob, Ko Ko Shin Thant, Pongsakorn Kanjanaboos, Biswapriya Deb,* Chakkooth Vijayakumar,* Synergy of Integer Charge Transfer and Charge Transfer Complex Yielding Enhanced Thermoelectric Efficiency in Benzodithiophene-Thienothiophene-based Copolymer (*Manuscript under revision- Chem. Eng. J.*).
3. **Neethi Raveendran**, Tanwistha Ghosh, Vijitha Ignatious, Navin Jacob, Dheepika Ramachandran, Biswapriya Deb,* Chakkooth Vijayakumar,* Enhanced thermoelectric properties of SWCNT-thiophene small molecule based nanocomposites through supramolecular functionalization (*Manuscript to be submitted*).

List of Publications not Related to Thesis Work

1. Tanwistha Ghosh, Shinji Nagasawa, **Neethi Raveendran**, Vibhu Darshan, Akinori Saeki, and Vijayakumar C. Nair,* Preferential Face-on and Edge-on Orientation of Thiophene Oligomers by Rational Molecular Design. *Chem. Asian J.* **2019**, *7*, 963.
2. Vijitha Ignatious, **Neethi Raveendran**, Arjun Prabhakaran, Yuvaraj Tanjore Puli, Vijayakumar Chakkooth,* Biswapriya Deb,* MWCNT/Thienothiophene based All-Organic thermoelectric composites: Enhanced performance by realigning of the Fermi level through doping, *Chem. Eng. J.*, **2021**, *409*, 128294.
3. Vijitha Ignatious, **Neethi Raveendran**, Sruthy Poovattil, Navin Jacob, Vijayakumar Chakkooth,* Biswapriya Deb,* Studies on the Doping Mechanism of Conjugated Thienothiophene Polymer/MWCNT Hybrids for Thermoelectric Application, *Macromol. Mater. Eng.* **2022**, *307*, 2100916.
4. Vijitha Ignatious, Navin Jacob, **Neethi Raveendran**, Vijayakumar Chakkooth,* Biswapriya Deb,* Simulation-aided studies on the superior thermoelectric performance of printable PBDTT-FTTE/SWCNT composites, *Mater. Today Energy*, **2023**, *32*, 101233.

5. Ignatious Vijitha, Navin Jacob, **Neethi Raveendran**, Salil N, Chakkooth Vijayakumar*, Biswapriya Deb,* Factors affecting the performance of a flexible organic thermoelectric generator for energy harvesting (*Manuscript under revision-IEEE Trans. Electron Devices*).
6. Navin Jacob, Ignatious Vijitha, **Neethi Raveendran**, Ramachandran Dheepika, Biswapriya Deb,* Chakkooth Vijayakumar,* Enhancing the thermoelectric performance of benzodithiophene-based copolymer and SWCNT composite films via chemical doping and thermal treatment (*Manuscript to be submitted*).
7. Navin Jacob, Ignatious Vijitha, **Neethi Raveendran**, Ramachandran Dheepika, Biswapriya Deb,* Chakkooth Vijayakumar,* An n-type naphthalene diimide based conjugated polymer-carbon nanotube composite for low-grade waste heat harvesting (*Manuscript to be submitted*).
8. Ramachandran Dheepika, Navin Jacob, **Neethi Raveendran**, Biswapriya Deb* and Vijayakumar Chakkooth,* Switchable p to n type Thermoelectric Transport in Single-Walled Carbon Nanotubes by Ionic Liquid Doping (*Manuscript to be submitted*).

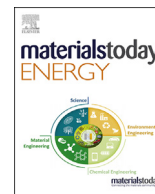
List of Patents

1. Conjugated polymer-carbon nanotube thermoelectric composite film and thermoelectric application thereof, V Chakkooth, B Deb, N Jacob, V Ignatious, **N Raveendran**, S Poovattil, S Kumar, L K Maurya, Y T Puli (*Patent filed in India, Application No. 202311013444*).
2. A n-type thermoelectric composite film and preparation thereof, V Chakkooth, B Deb, N Jacob, V Ignatious, **N Raveendran**, S Kumar, L K Maurya, Y T Puli (*Patent filed in India, Application No. 202311013443*).
3. Semiconducting Organic Small Molecule-Carbon Nanotube Composite for High-Performance Thermoelectric Applications, V Chakkooth, B Deb, **N Raveendran**, N Jacob, T Ghosh. (*Patent to be filed*).

List of Papers/Posters Presented in Conference

1. **Neethi Raveendran**, Tanwistha Ghosh, Biswapriya Deb and Vijayakumar C. Nair,* "Giant Seebeck Coefficient in Thiophene based Semiconducting Oligomers through Doping," International Symposium on New Trends in Applied Chemistry (NTAC '19), Ernakulam, January 2019. (**Poster presentation- *Best Poster Award***).
2. **Neethi Raveendran**, Tanwistha Ghosh, Biswapriya Deb and Vijayakumar C. Nair,* "Waste Heat to Energy: Thiophene based Semiconducting Oligomers for Thermoelectric Applications," 31st Kerala Science Congress (KSC '19), Kollam, February 2019. (**Poster presentation**)
3. **Neethi Raveendran**, Tanwistha Ghosh, Biswapriya Deb, Vijayakumar C. Nair,* Self-Assembly Assisted Tuning of Thermoelectric Power Factor of Thiophene Oligomers, National Conference on Materials Science and Technology (NCMST-2019), Thiruvananthapuram, December 2019. (**Poster presentation- *Best Poster Award***).
4. **Neethi Raveendran**, Tanwistha Ghosh, Biswapriya Deb, Vijayakumar C. Nair,* Tuning Thermoelectric Power Factor of Thiophene Oligomers Induced by Self-Assembly, 14th International Conference on Eco Materials (ICEM 2020), Thiruvananthapuram, February 2020. (**Poster presentation- Selected for *Flash talk***).
5. **Neethi Raveendran**, Biswapriya Deb, Vijayakumar C. Nair,* F4TCNQ Doped Benzodithiophene based p-type Polymer: Unraveling the Doping Mechanism and Thermoelectric Parameters, International Conference on Materials for the Millennium (MatCon 2021), Department of Applied Chemistry, Cochin University of Science and Technology, March 2021 (**Oral Presentation**).
6. **Neethi Raveendran**, Biswapriya Deb, Vijayakumar C. Nair,* F4TCNQ Doped Benzodithiophene based p-type Polymer: Unraveling the Doping Mechanism and Thermoelectric Parameters, RSC-IISER Desktop Seminar with PCCP, May 2021 (**Poster Presentation**).
7. **Neethi Raveendran**, Biswapriya Deb, Vijayakumar C. Nair,* Enhanced Thermoelectric Properties of Benzodithiophene based Donor-Acceptor Polymer by Eliminating Thermal De-doping, National Symposium on Shaping the Energy Future: Challenges and Opportunities (SEFCO 2021), August 2021. (**Poster presentation- *Best Poster Award***).

-
8. **Neethi Raveendran**, Biswapriya Deb, Vijayakumar C. Nair,* Eliminating Thermal de-doping in Benzodithiophene based Polymer for Enhanced Thermoelectric Performance, 22nd RIES-HOKUDAI International Symposium 2021 (RIES 2021), Online mode, December 2021. (**Poster presentation**).
 9. **Neethi Raveendran**, Biswapriya Deb, Vijayakumar C. Nair,* Elimination of Thermal De-doping for Improving Thermoelectric Properties of Benzodithiophene based Donor-Acceptor Polymer, National Conference on Materials Science and Technology (NCMST-2021), Thiruvananthapuram, December 2021. (**Oral presentation**).
 10. **Neethi Raveendran**, Biswapriya Deb, C. Vijayakumar,* Benzodithiophene based Polymer with Low Thermally Induced De-doping for Superior Thermoelectric Performance, International Conference on Chemistry and Applications of Soft Materials (CASM-2022), Thiruvananthapuram, July 2022. (**Poster presentation**).
 11. **Neethi Raveendran**, Biswapriya Deb, C. Vijayakumar,* Enhancement of Thermoelectric Efficiency through the Integration of 'Integer Charge Transfer' and 'Charge Transfer Complex' States in Benzodithiophene-Thienothiophene-Based Polymer, National Conference on New Developments in Polymeric Materials (DPM-2023), Thiruvananthapuram, March 2023. (**Poster presentation**).



Thermoelectric properties of self-assembled thiophene derivatives: effect of molecular structure on doping efficiency and Fermi level alignment



Neethi Raveendran ^{a, b}, Tanwistha Ghosh ^{a, b}, Vijitha Ignatious ^{a, b}, Vibhu Darshan ^{a, b}, Navin Jacob ^{a, b}, Biswapriya Deb ^{a, b, **}, Chakkooth Vijayakumar ^{a, b, *}

^a Photosciences and Photonics Section, Chemical Science and Technology Division, CSIR-National Institute for Interdisciplinary Science and Technology (NIIST), Thiruvananthapuram, 695 019, India

^b Academy of Scientific and Innovative Research (AcSIR), Ghaziabad, 201 002, India

ARTICLE INFO

Article history:

Received 17 January 2023

Received in revised form

20 March 2023

Accepted 25 March 2023

Available online 31 March 2023

Keywords:

Thermoelectric materials

Organic semiconductors

Molecular Engineering

Chemical doping

Self-assembly

ABSTRACT

Organic materials have emerged as promising candidates for thermoelectric (TE) applications, offering distinct advantages over their inorganic counterparts. While polymers have received considerable attention in this context, small organic semiconductors have not been widely explored due to the challenge of obtaining high conducting films. Advancing this field necessitates the development of novel materials and a deeper understanding of their structure-dependent TE properties. The present study reports how slight modifications to the molecular structure affect the TE characteristics of two thiophene-based small molecules (**OT1** and **OT2**), which differ only in their end substitution with varying acceptor strengths. This difference led to distinct morphologies when self-assembled. **OT2** doped with FeCl₃ displayed high electrical conductivity and power factor (52.0 μW/mK²), while **OT1** exhibited significantly lower conductivity and power factor (1.6 μW/mK²) under identical conditions. The weaker acceptor strength of the end group in **OT2** resulted in higher doping efficiency. Improved charge carrier transport in **OT2** was due to a low-lying highest occupied molecular orbital (HOMO) energy level and enhanced density of states around the HOMO after doping. Maintaining its self-assembly after doping was also crucial for better electrical properties. These findings emphasize the importance of molecular engineering in developing high-performance TE materials.

© 2023 Elsevier Ltd. All rights reserved.

1. Introduction

Developing high-performing thermoelectric (TE) materials is crucial for utilizing waste heat to generate electricity and for thermal management devices [1–3]. Converting waste heat into electricity is particularly important because it can provide a sustainable and cost-effective way to generate power while reducing greenhouse gas emissions and increasing energy efficiency. Traditional TE materials based on inorganic compounds such as Bi₂Te₃, PbTe, SiGe, Sb₂Te₃, skutterudites and half-Heusler alloys exhibit high performance [2–4]. However, these materials are either toxic,

scarce, or require complex fabrication techniques and shows peak performance only at high temperatures (above 500 K). However, the abundant waste heat generated by the industrial, commercial and domestic processes are of low-grade (below 500 K). In this context, organic TE materials are potential candidates since they are capable of converting low-grade waste heat into electricity. They have added advantages compared to inorganic TE materials such as low thermal conductivity, facile solution processing, compatibility with printed flexible devices, and good TE properties at room temperature [5–7]. Owing to these benefits, organic TE generators are suitable for portable and wearable electronic devices, biosensors, health monitors and various Internet of things (IoT) devices [8–11].

The TE figure of merit (*ZT*) is a dimensionless metric that characterizes the efficiency of a TE material in converting heat into electrical energy or vice versa. It is calculated by combining the Seebeck coefficient (α), which is a measure of the voltage generated

* Corresponding author.

** Corresponding author.

E-mail addresses: biswapriya.deb@niist.res.in (B. Deb), cviyakumar@niist.res.in (C. Vijayakumar).

per unit temperature difference across the material, with the electrical conductivity (σ), thermal conductivity (κ), and temperature (T) using the equation, $ZT = \alpha^2 \sigma T / \kappa$. The power factor (PF), which is represented by the numerator of the equation ($\alpha^2 \sigma$), can be used to assess the TE property of materials when their thermal conductivity is not known. An ideal TE material should possess high electrical conductivity and low thermal conductivity, which is referred to as the “electron-crystal, phonon-glass” combination [12,13]. Organic semiconductors, due to their low thermal conductivity, fall into the latter category. However, it is challenging to obtain high performance materials due to the mutually restricted TE transport coefficients, i.e., an increase in σ results in a decrease in α , while the electronic contribution to the thermal conductivity (κ_e) increases. As a result, significant efforts have been dedicated to enhancing the σ of organic TE materials through chemical doping, which introduces mobile charge carriers by incorporating molecules that oxidizes or reduces the organic semiconductor by sustaining the α [14,15]. Examples of this include oxidative doping of thiophene polymers and small molecules with ferric chloride, iodine, silver perchlorate, and tetrafluoro tetracyanoquinodimethane [16–21].

Among various organic semiconductors, polymers such as poly (3,4-ethylene dioxythiophene) (PEDOT), polyaniline (PANI), polypyrrole (PPy), and poly (3-hexylthiophene) (P3HT) have exhibited good TE properties [22,23]. The unique feature of these materials is that they can be easily synthesized through solution-based processing techniques, which makes them suitable for large-scale manufacturing. However, the TE performance of organic semiconductors is highly dependent on their structural characteristics. Zhong et al. demonstrated this by showing that the TE parameters of a donor-acceptor type polymer tuned by changing the donor from carbazole to dithienopyrrole [24]. The optimized PF for the carbazole derivative was $10.8 \mu\text{W}/\text{mK}^2$, which was about six times higher than that of the dithienopyrrole derivative ($1.8 \mu\text{W}/\text{mK}^2$). Tang et al. examined the impact of various acceptor units, including benzodithiophenedione (BDD), thieno [3,4-b]thiophene (TT), and diketopyrrolopyrrole (DPP), on a set of semiconducting polymers [25]. They investigated the TE performance in terms of the electron-withdrawing ability of the acceptor units and the highest PF of $105.5 \mu\text{W}/\text{mK}^2$ was observed for BDD-containing polymer doped with FeCl_3 . Yan et al. developed DPP-based polymers, where those containing pyrazine-flanked DPP units showed a higher PF of $57.3 \mu\text{W}/\text{mK}^2$ than the reference polymer containing thiophene-flanked DPP units ($9.3 \mu\text{W}/\text{mK}^2$) [26]. This was attributed to the low-lying lowest unoccupied molecular orbital (LUMO), better electron mobility, and efficient π - π stacking in the former.

Semiconducting organic small molecules are considered to be a favorable choice for TE applications due to their well-defined structures, which can ensure reproducibility and provide a better understanding of structure–property relationships. However, the development and study of small molecule-based TE materials are still in their early stages [27–29]. It has been suggested that careful molecular design is essential for achieving good TE performance in small molecules, as the available pathways for charge transport are limited to intermolecular routes. These intermolecular interactions can be affected by molecular and supramolecular properties, meaning that even small structural differences can result in significant variations in TE performance. Despite these challenges, it is possible to design small organic semiconductors that are suitable for TE applications through the use of molecular engineering. In this context, we have previously reported on the differential self-assembly of two thiophene-based acceptor-donor-acceptor type semiconducting small molecules (**OT1** and **OT2**) in the film state [30], in which the orientation of chromophores during self-assembly was found to be significantly influenced by the

presence of alkyl chains on the rhodanine end groups and thiophene backbone. Herein, we analyze the TE properties of these molecules and their dependence on molecular structure and find a significant correlation between TE performance and structural factors.

2. Results and discussion

The chemical structures of the molecules used in the present study are depicted in Fig. 1a. These molecules consist of a central thienothiophene unit flanked by dioctyl terthiophenes on both sides. The end groups of **OT1** and **OT2** are 2-(1,1-dicyanomethylene) rhodanine and N-octylrhodanine, respectively. 2-(1,1-dicyanomethylene)rhodanine is more electron deficient (strong acceptor) than that of N-octylrhodanine (weak acceptor), as indicated by the red-shifted absorption maxima of **OT1** at 538 nm, compared to the absorption maximum of **OT2** at 506 nm (Fig. 1b). The bandgaps of **OT1** and **OT2** were calculated from the absorption onsets to be 1.71 and 1.74 eV, respectively (Fig. 1c). The highest occupied molecular orbital (HOMO) energy levels were measured in the film state using ultraviolet photoelectron spectroscopy (UPS) and found to be -5.20 eV for **OT1** and -5.51 eV for **OT2** (Fig. 1d–e). Using these HOMO values and the bandgaps obtained from absorption, the LUMO energy levels were deduced as -3.49 and -3.77 eV for **OT1** and **OT2**, respectively (Fig. 1c).

Organic semiconducting molecules typically have low electrical conductivity, which hinders their use in TE applications. Doping these molecules, which alter the distribution of electrons through oxidation or reduction, can improve electrical conductivity without increasing thermal conductivity [31,32]. In this work, the role of doping on the molecules under study was investigated using the *p*-type dopant FeCl_3 , which has been shown to enhance the electronic conductivity and, therefore, the TE characteristics of organic semiconductors [31–33]. FeCl_3 exhibits solution compatibility, strong oxidation capabilities, a lower electron affinity (4.62 eV), and effectiveness at high-loading concentrations [31,34]. To analyze the extent of charge transfer between the molecules and the dopant, ultraviolet–visible–near infrared (UV–vis–NIR) spectra of the sample films with various dopant concentrations were collected (Fig. 2a and b). With an increase in the dopant concentration, the emergence of new peaks were observed in both samples; 708 nm and 1459 nm for **OT1**; 683 nm and 1348 nm for **OT2**. This was associated with a lowering in the intensity of the respective π - π^* absorptions. When FeCl_3 was added to the molecules, the conjugated backbones lost an electron, became positively charged, and formed a complex with dopant anions (FeCl_4^-). The generated positive charge delocalizes over the thiophene rings, resulting in a positive polaron with a charge of $+e$ and a spin of $1/2$. This creates localized electronic states in the semiconductor bandgap [32], as evidenced by the new peaks in the absorption spectra. The ratio of the polaronic absorption band to the neutral absorption band determines the concentration of polarons [31]. This ratio was higher in **OT2** (0.66) than in **OT1** (0.36), indicating a higher doping efficiency and, therefore, a higher potential for better electrical conductivity in **OT2** films.

X-ray photoelectron spectroscopy (XPS) was used for analyzing the elemental composition of both the pristine and doped samples (Fig. S1, #ESI). The presence of Fe2p and Cl2p peaks in the XPS survey spectrum of the doped samples confirms the incorporation of the dopant into the thin films. The concentration of FeCl_3 varied from 0.05 M to 0.30 M, resulting in Fe doping concentrations of 0.5–5.2 wt% in both films. It should be noted that XPS elemental analysis is only valid for the few atomic layers beneath the surface, so some discrepancy with the full thickness of the films may be expected. More precise doping concentration ranges were obtained

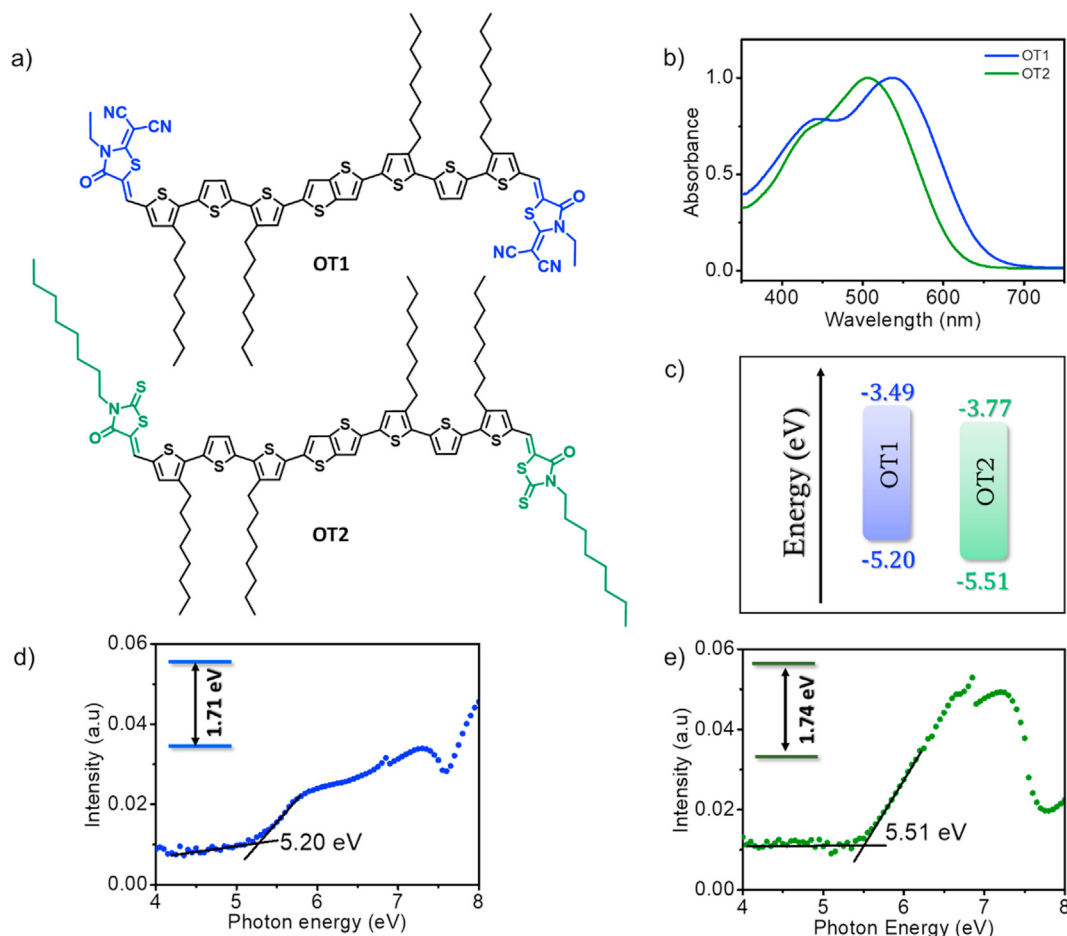


Fig. 1. a) Chemical structures, b) UV–visible absorption spectra in chloroform, and c) energy level diagram of the molecules under study. HOMO energy levels of d) **OT1** and e) **OT2** were obtained from ultraviolet photoelectron spectroscopy (the inset shows the bandgap of the molecules).

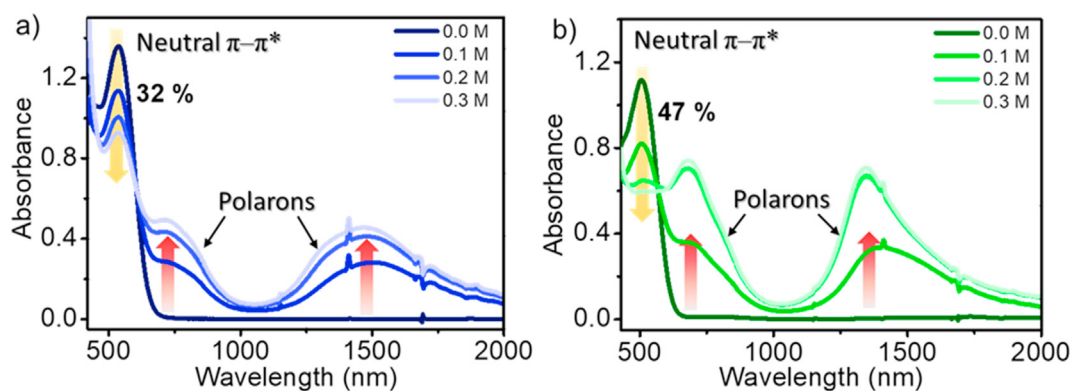


Fig. 2. UV–Vis–NIR absorption spectral changes of a) **OT1** and b) **OT2** with increased doping of FeCl₃ (concentration of FeCl₃ is shown in the inset). The quenching of the neutral $\pi-\pi^*$ absorption and the enhancement in polaronic absorptions upon doping with FeCl₃ are denoted by yellow and red arrows, respectively. (For interpretation of the references to color in this figure legend, the reader is referred to the Web version of this article.)

using scanning electron microscopy (SEM) equipped with energy dispersive X-ray spectroscopy (EDX) on the doped films (**OT1** and **OT2** with 0.10 M dopants; Fig. S2, #ESI), which validated the presence of 2.3–2.4% Fe. The amount of dopant (in weight %) present in each film is given in Table S1, #ESI. Previous research by Liang et al. has shown that the efficiency of p-type doping in an organic semiconductor is influenced by the difference in ionization energy (IE) of the semiconductor and the electron affinity (EA) of

the dopant [31]. A larger difference between these two parameters generally results in higher doping efficiency. In this case, the ionization energy (equivalent to HOMO of organic molecules) of **OT1** and **OT2**, as determined by UPS, was 5.20 and 5.51 eV, respectively (Fig. 1d and e). According to literature reports, the electron affinity of FeCl₃ is 4.62 eV [34]. The difference between the ionization energy of the molecule and the electron affinity of the dopant was 0.58 eV for **OT1** and 0.89 eV for **OT2**, indicating a higher doping

efficiency possibility for **OT2**. This difference should be responsible for the increased concentration of polarons observed in **OT2** [31].

There are several mechanisms possible for the extrinsic doping of organic semiconductors. One of them is the integer charge transfer between semiconductor and the dopant, which requires suitably aligned LUMO of the dopant (or EA) and HOMO of the organic molecule (or IE). This generates negative charge on the dopant and counter charge on the organic molecule [15,31]. Since organic molecules are having a deep HOMO, it never matches with the electron affinity of common oxidizing agents such as FeCl_3 . Such semiconductor/dopant systems follow the charge transfer complex mechanism, through the hybridization of the molecular orbitals of both semiconductor and dopant [35]. Another mechanism is the formation of Lewis acid-base adduct through the interaction between the electron deficient Fe^{3+} ions from the dopant and the electron rich heteroatom on the organic semiconductor. The acid-base adduct formation results in positively charged species or radical cations in the organic semiconductor matrix, which enhances the carrier concentration [36,37]. Matching between the HOMO of the semiconductor and electron affinity of the dopant are not necessary in such systems. In the present case, the formation of Lewis acid-base adduct formation could be the plausible mechanism of doping due to the presence of electron rich and easily oxidizable sulphur atoms on the molecules.

Fig. 3 presents the high-resolution XPS core-level spectra of Fe2p and Cl2p for doped samples. The deconvolution shows that the $\text{Fe}2p_{3/2}$ and $\text{Fe}2p_{1/2}$ peaks for **OT1** are found at binding energies ~ 711.24 and ~ 724.79 eV, respectively (Fig. 3a). On the other hand, the same peaks were observed at ~ 711.35 and ~ 724.56 eV, respectively, for **OT2** (Fig. 3b). This confirms the presence of Fe^{3+} cations in the form of $[\text{FeCl}_4]$ [38]. The presence of characteristic shake-up

satellite peaks for both samples at ~ 715.51 , ~ 729.99 eV for **OT1**, and ~ 715.24 , ~ 727.80 eV for **OT2**, affirms the existence of Fe^{3+} . The $\text{Cl}2p$ core level spectra can be resolved into two peaks corresponding to $\text{Cl}2p_{3/2}$ at ~ 198.30 and ~ 199.97 eV for **OT1** (Fig. 3c) and ~ 198.85 and ~ 200.28 eV for **OT2** (Fig. 3d). The peaks at ~ 198.30 in **OT1** and ~ 198.85 eV in **OT2** denotes the Fe–Cl bonding in FeCl_4 . FeCl_4 formed during the doping acts as a counter ion to the thiophene radical cation. The peak at ~ 199.97 eV for **OT1** is due to ionic chlorine (Cl^-) [38,39]. However, the peaks close to ~ 200.28 eV in **OT2** correspond to C–Cl bonding. The core level spectra showed higher intensity at this binding energy region for **OT2**, which denotes a higher proportion of C–Cl bonding, whereas, in **OT1**, a higher proportion of Fe–Cl bonding is observed. This demonstrates a higher doping level in the case of **OT2**. A similar observation with a higher proportion of C–Cl bonding in PBDB-T was reported by Tang et al. [25,40]. The low intense peaks at ~ 201.89 eV in the former and ~ 201.55 eV in the latter correspond to the $\text{Cl}2p_{1/2}$. Hence, varying acceptor strength leads to different molecule-dopant energetics and results in the disparity of the molecules towards FeCl_3 doping. A weak acceptor in **OT2** would be a less competitor for the p-dopant. In contrast, the strong acceptor in **OT1** can take up the electrons from the donor unit (thiophene backbone), thus hindering the hole transfer process between the FeCl_3 and donor unit leading to lower doping efficiency.

Fig. 4a–c shows the σ , α , and PF of pristine and doped samples. The σ of pristine films was low, in the order of 10^{-4} S/cm (1.1×10^{-4} S/cm for **OT1**; 2.5×10^{-4} S/cm for **OT2**). A significant increase in σ was observed for **OT2** with increasing FeCl_3 concentration, whereas only a moderate increase was observed in **OT1**. A peak σ value of ~ 0.02 S/cm was obtained for **OT2** with 0.20 M dopant. On the other hand, a peak value of only 1.1×10^{-3} S/cm was

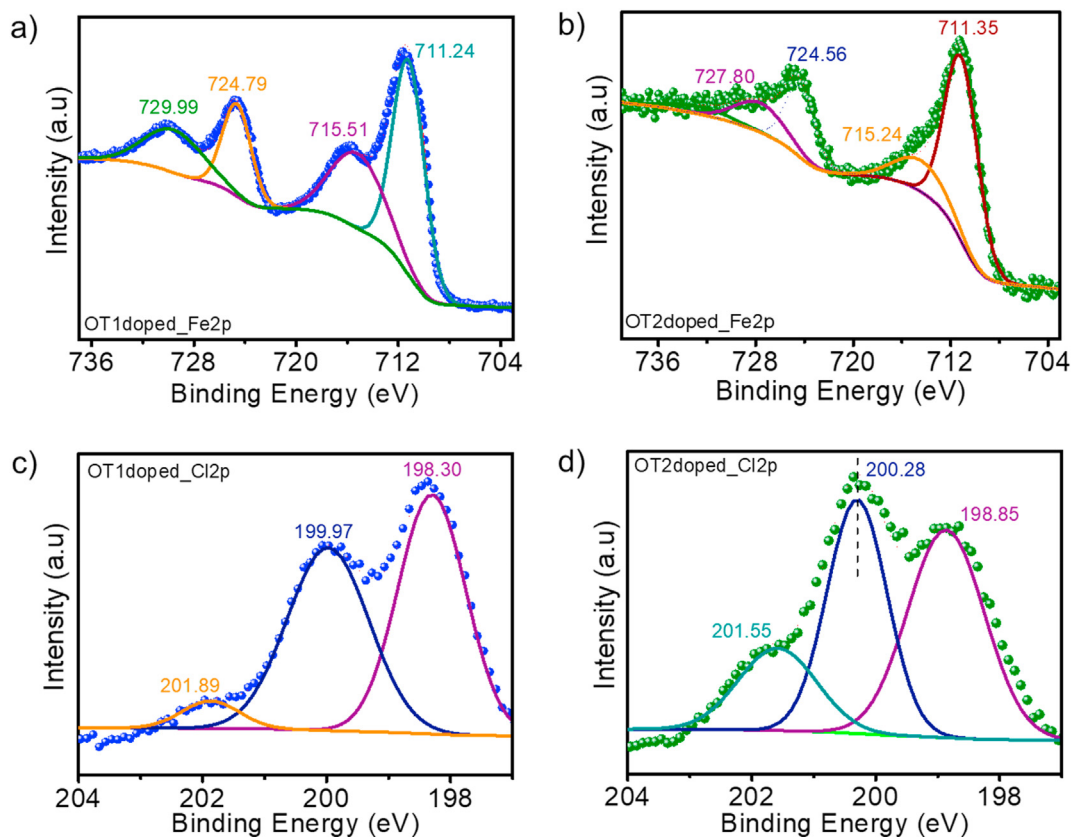


Fig. 3. High-resolution XPS spectra of Fe2p for a) **OT1** and b) **OT2**; Cl2p c) **OT1** and d) **OT2** films doped with 0.10 M FeCl_3 .

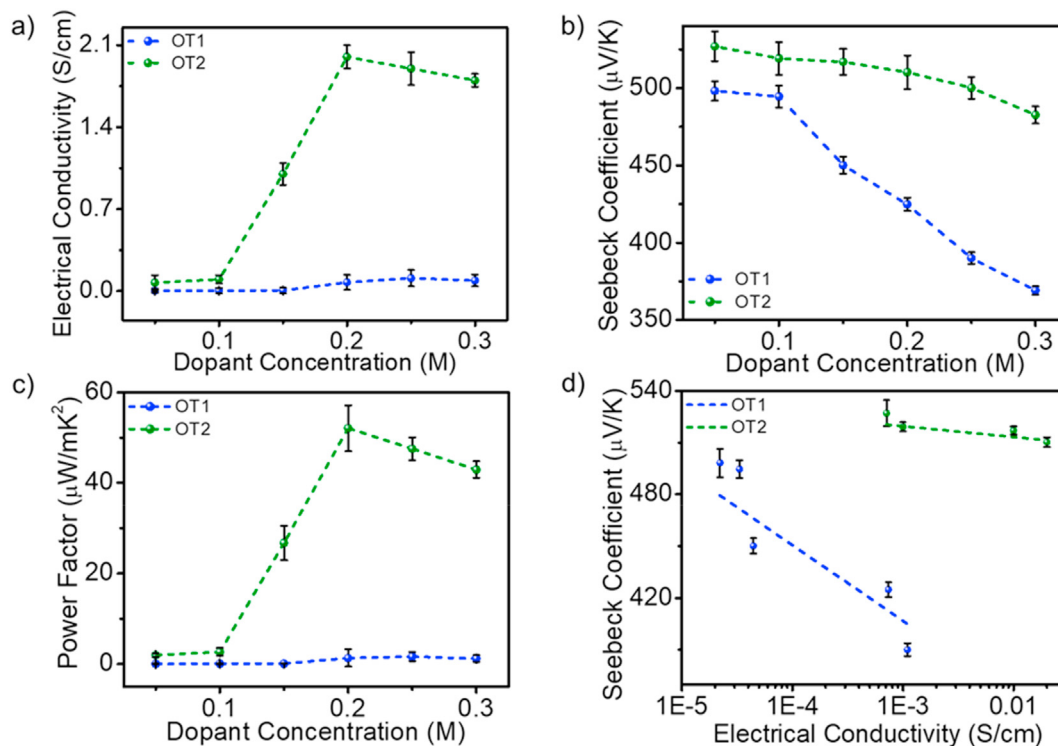


Fig. 4. a) Electrical conductivity, b) Seebeck coefficient, and c) Power Factor of **OT1** and **OT2** with varying doping concentrations of FeCl₃. d) Seebeck coefficient plotted as a function of electrical conductivity ($\ln \sigma$) for **OT1** and **OT2**. The error bars represent the standard deviation of data from five samples.

obtained for **OT1** with 0.25 M dopant. No further increase in σ was observed by increasing FeCl₃ concentration beyond 0.25 M for **OT1** and 0.20 M for **OT2**. Both films showed positive Seebeck values, which confirm the p-type characteristics of the molecules. They showed a decreasing trend with increasing dopant concentration. Mott's relation can explain this inverse relationship between σ and α ,

$$\alpha = \frac{8\pi^2 k_B^2 T}{3eh^2} m^* \left(\frac{\pi}{3n}\right)^{2/3} \quad (1)$$

In this equation, the Seebeck coefficient, Boltzmann constant, absolute temperature, and carrier concentration are represented by α , k_B , T , and n , respectively [41,42]. According to this relationship, increasing n upon doping would improve σ and reduce α . Fig. 4d shows a well-defined linear relationship with a negative gradient between α and $\ln \sigma$, which indicates the trade-off between them with an increase in doping concentration [43]. Similar relationships were previously reported in polymers like poly(3-octylthiophene), poly2,5-bis(3-tetradecylthiophen-2-yl)thieno3,2-bthiophene, and polyaniline [44–46]. As the graph suggests, the trade-off relationship is disproportional for the two derivatives under study, which is highly favorable for **OT2**. In other words, both pristine films possess high α , but the low σ limits their TE performance. When σ was increased by doping with FeCl₃, α of **OT1** decreased drastically, whereas α of **OT2** had been reduced only marginally. As a result, **OT2** exhibited a peak PF of 52.0 $\mu\text{W}/\text{mK}^2$ @ 0.20 M dopant concentration which is about 31 times higher than the peak PF of **OT1** (1.6 $\mu\text{W}/\text{mK}^2$ @ 0.25 M dopant concentration).

The disparity in the TE behavior of the molecules can be correlated to the differences in doping efficiency and polaron formation. Recently, Tam et al. reported that α could be described as the flow of entropy per unit charge across a junction, which can be obtained from a combination of two distinct contributions [47].

$$\alpha = \alpha_{\text{presence}} + \alpha_{\text{transport}} \quad (2)$$

where α_{presence} represents the variation in the entropy of the system due to the introduction of a charge carrier, whereas $\alpha_{\text{transport}}$ is calculated as the net energy transferred in moving a single charge carrier divided by the product of the elementary charge (q) and temperature (T). The contribution of $\alpha_{\text{transport}}$ to the Seebeck coefficient depends on the charge transport mechanism. The α_{presence} can be further decomposed into changes in three individual physical phenomena, such as entropy of mixing (ΔS_{mixing}), spin entropy (ΔS_{spin}), and vibrational entropy ($\Delta S_{\text{vibration}}$) by the introduction of a carrier with a charge of q .

$$\alpha_{\text{presence}} = (\Delta S_{\text{mixing}} + \Delta S_{\text{spin}} + \Delta S_{\text{vibration}}) / q \quad (3)$$

The addition of charge carriers will result in the formation of polarons when the charge carrier is strongly coupled to the lattice vibrations or phonons of the material. Polarons in organic semiconductors can be either localized or delocalized, depending on the strength of the electron-phonon coupling, the size of the polaron, the intrachain/intermolecular distribution of the frontier molecular orbitals, and the temperature of the material. In general, a polaron is considered to be localized when it is confined to a small region of the material, and its wave function has a well-defined shape. On the other hand, a polaron is considered to be delocalized when it is spread out over a large region of the material, and its wave function has a diffuse shape. If a polaron is delocalized, the charge carriers can move more freely through the material without being confined to a small region, making charge transport more effective. If a polaron is delocalized and spans over more atoms, the vibrational modes of the atomic sites that the polaron occupies can become softer, which means that they can vibrate more easily. This can be considered as a “softening” of the lattice; one of the most important

consequences of this softening is the increase of total change in vibrational entropy ($\Delta S_{\text{vibration}}$) for the polaron. This increase in $\Delta S_{\text{vibration}}$ enhances the Seebeck coefficient. Additionally, when the polaron moves between various locations in the system due to the thermal motion of the atoms at these locations, the vibrational energy transferred with the polaron also adds to the Seebeck coefficient as part of $\alpha_{\text{transport}}$. In the present work, higher doping efficiency and polaron formation was observed in **OT2**, as is evident from UV–Vis–NIR absorption and XPS analysis. This translates to an increased α for **OT2** than **OT1**, resulting in an overall increase in PF for the former. The TE parameters obtained for both samples at varying dopant concentrations and their standard deviations are summarized in Tables S2 and S3, #ESI.

Surface morphologies of the pristine and doped films obtained using an atomic force microscope (AFM) are displayed in Fig. 5. AFM image of the pristine molecules shows smooth, terraced-like surfaces for **OT1** and leaf-like intercalating networks for **OT2**. The difference in morphologies is attributed to the differential stacking of the molecules on the substrate [30]. Upon incorporation of the dopant, charge carriers generated in the film, leading to enhancement in σ . However, the intercalation of dopant ions can influence the film structure on a micro and macro scale, which in turn can affect its electrical and TE properties. In this study, significant morphological changes were observed in the films upon intercalation of dopants. In the case of **OT1**, complete destruction of the self-assembled structures and loss of connectivity between the aggregates was observed. However, though there were notable changes in the morphology, the self-assembled structures remained intact and well connected in **OT2** after the addition of the dopant. It should be noted that the size and shape of the self-assembled nanostructures of the molecules have a significant impact on their electrical conductivity and TE performance. Generally, in a polycrystalline film, the grain boundaries can trap the charge carriers, hindering their effective transport. In other words, more the grain boundaries present, the lower the electrical conductivity. The grain size of the nanostructures was calculated from the AFM morphology using the corresponding line-cut profiles (Fig. S3; #ESI). **OT2** consists of larger grains ($\sim 0.791 \mu\text{m}^2$) with fewer grain boundaries, whereas **OT1** has smaller grains

($\sim 0.029 \mu\text{m}^2$) and more grain boundaries. The retention of self-assembled structures, even after doping and the presence of larger grains with fewer grain boundaries in **OT2**, resulted in higher electrical conductivity and better TE performance.

The impact of doping on Fermi level alignment of both samples was analyzed using XPS. Fermi level alignment refers to the adjustment of the Fermi energy (the highest energy level occupied by electrons at absolute zero temperature) at the interface of two materials with different work functions. In the context of organic TE materials, it is important to align the Fermi energy levels of the organic semiconductor with the energy levels of the metal contacts in order to achieve efficient charge transport and maximize the TE performance. When a metal is brought into contact with an organic semiconductor, there is an energy level mismatch between the Fermi levels of the two materials, which can lead to charge carrier injection barriers and reduced electrical conductivity. By adjusting the Fermi energy levels of the organic semiconductors through doping, it is possible to achieve better charge carrier injection and increase the electrical conductivity of the organic semiconductor. This in turn can improve the TE performance of the material by increasing the power factor and reducing the thermal conductivity.

XPS spectra revealed the evolution of the density of states (DOS) distribution near the valence band maximum (VBM) and Fermi level alignment on FeCl_3 doping (Fig. 6). High-purity gold coating on the substrate was used as the energy reference. The VBM position was found by extrapolating the low binding energy edge of the spectrum and its intersection with the internal baseline. The electronic DOS of the semiconductors is related to α and PF through the transport equation,

$$\alpha = \frac{\pi^2}{3} \frac{k_B^2 T}{e} \left(\frac{\partial \ln \mu}{\partial E} + \frac{\partial \ln N}{\partial E} \right)_{E_F} \quad (4)$$

in this equation, the Boltzmann constant, absolute temperature, electron charge, and carrier mobility are represented by k_B , T , e , and μ , respectively. Here, $N(E_f)$ is related to the DOS and its slope at the Fermi level (E_f), which is related to α [48,49]. In the case of the pristine films, the density of states (DOS) is centered on the HOMO levels, which are responsible for charge transport. However, upon

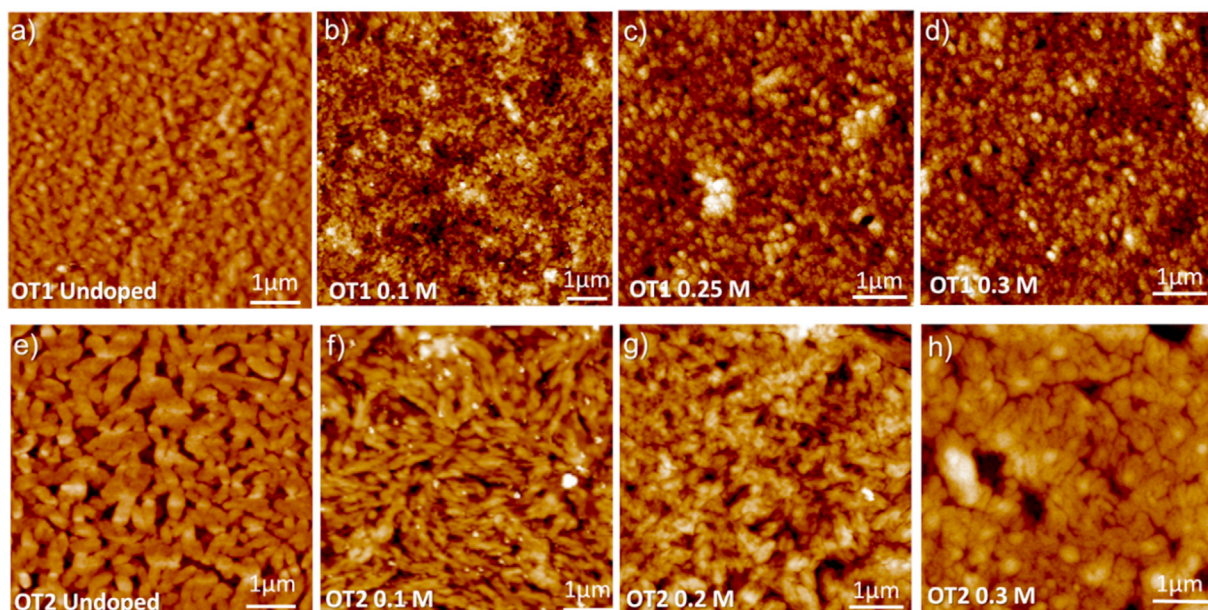


Fig. 5. AFM images of drop-cast a)–d) **OT1** and e)–h) **OT2** with varying FeCl_3 concentration.

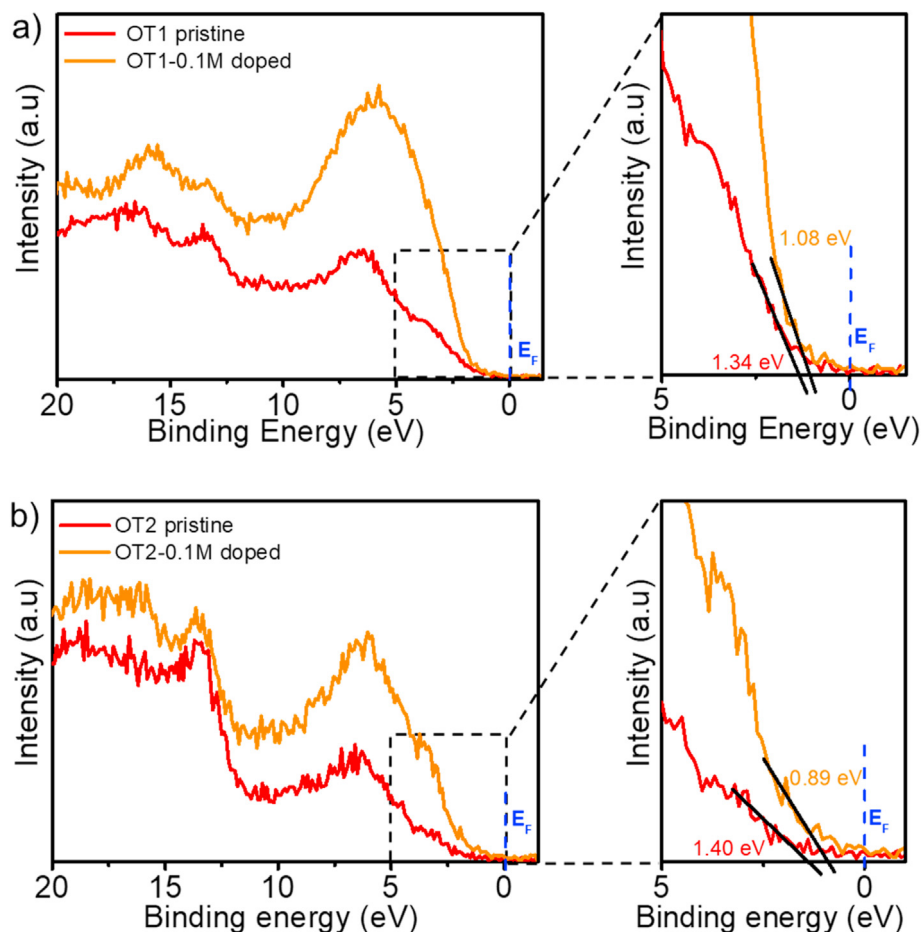


Fig. 6. XPS Valence band spectra of a) **OT1** and b) **OT2** before and after doping. The corresponding zoomed area near the onset of the spectra and Fermi level is shown on the right side.

doping with FeCl_3 , there is a significant increase in the DOS, which is indicative of a higher carrier density. As a result, there is an overall improvement in the electrical conductivity of the material. The increased carrier density initially fills the deep trap states and then shifts the Fermi level closer to the transport level (i.e., HOMO). This proximity of the Fermi level to the HOMO results in a lower activation barrier for charges in the vicinity of the HOMO. When dopants such as FeCl_3 are added to a semiconductor, the Fermi level is pinned at a crossover point between the donor-like states of the organic molecules and the acceptor-like states of the dopant. The E_F-E_{HOMO} of **OT1** and **OT2** before doping were ~ 1.34 and ~ 1.40 eV, respectively. On doping, the HOMO of both molecules moves closer to the reference E_F [19]. Here, the HOMO moves closer to the Fermi level in **OT2** (0.89 eV) than in **OT1** (1.08 eV), considerably increasing the σ of the former. Further, the XPS results suggest that the lower the difference in E_F-E_{HOMO} , the more proportionate the α vs. In σ plot indicating the trade-off relationship between α and σ . Figs. S4 and S5 (#ESI) show the binding energy changes of C1s and S2p of the pristine and doped samples. Compared to the pristine samples, C1s and S2p peaks are shifted slightly towards the lower binding region after doping with FeCl_3 . This binding energy shift towards the lower energy region indicates the overall aligning of E_F towards HOMO [24], which is in agreement with the XPS results.

As observed from the UV–Vis–NIR, UPS, and XPS spectra, higher doping efficiency in **OT2** leads to the HOMO shifting closer toward E_F . Hence, it could be inferred that the α depends strongly on the electron-withdrawing capability of the acceptor units. A higher

doping efficiency could also be achieved by tuning the acceptor strength, resulting in an increased PF. Morphological analysis through AFM proves that retention of the self-assembled structures in post-doped **OT2** also supports the enhancement in σ . Such minimum variations in the molecular structure lead to a remarkable difference in the TE performance of organic semiconductors. The achieved power factor for **OT2** is competitive enough with the similar materials reported in literature. The TE performance of a few p-type organic semiconductors (with or without dopants) comparable to that of **OT2**/ FeCl_3 system are summarized in Table S4 (#ESI).

The study on the TE properties of self-assembled thiophene derivatives reported in this work presents promising opportunities for practical applications and future directions in TE research. The findings demonstrate that small modifications in molecular structure can significantly affect the TE characteristics of organic semiconductors. One potential direction for future research could be the development of new high-performance TE materials based on the findings of this study. By leveraging molecular engineering, researchers could tailor the structure of organic semiconductors to achieve enhanced TE performance. This could lead to the creation of more efficient and cost-effective TE materials for power generation and cooling applications. Another direction could be the optimization of doping strategies for organic semiconductors. The study highlights the importance of achieving high doping efficiency for enhancing electrical conductivity and power factor in TE materials. Researchers could further investigate and develop new

doping techniques to improve the performance of organic TE materials. Additionally, the study emphasizes the significance of maintaining the self-assembled structure of organic semiconductors after doping to achieve enhanced electrical properties. Researchers could explore methods for preserving the morphology and connectivity of organic TE materials post-doping, potentially leading to the development of more stable and reliable TE materials.

3. Conclusions

In conclusion, the TE characteristics of two thiophene-based molecules, **OT1** and **OT2**, were investigated. Both molecules have different acceptor units as their end groups. By combining UV–Vis–NIR, UPS, XPS, SEM, and AFM techniques, we found that **OT2** exhibits higher doping efficiency and a low-lying HOMO, as well as an increased density of states when doped with FeCl₃. These characteristics enhance the charge transport properties of **OT2** and can be correlated with the presence of a weak acceptor. Our results also suggest that the TE properties of these molecules are highly correlated to their molecular packing. Even though the morphology is changed, the self-assembled structure of **OT2** and their connectivity was preserved after doping, which leads to enhanced electrical conductivity. The density of states and valence band spectra analysis revealed the Fermi energy level is aligned with the valence band maximum/HOMO, resulting in an enhancement in electrical conductivity and a decrease in the Seebeck coefficient after doping. Consequently, **OT2** exhibits a power factor of 52.0 $\mu\text{W}/\text{mK}^2$, while **OT1** only shows a power factor of 1.6 $\mu\text{W}/\text{mK}^2$. These findings demonstrate that small structural modifications in organic semiconductors can tune their TE properties to achieve improved performance.

Credit author statement

Neethi Raveendran: Methodology, Data curation, Validation, Formal analysis, Investigation, Writing - Original draft preparation, Visualization; **Tanwistha Ghosh:** Investigation; **Vijitha Ignatious:** Investigation; **Vibhu Darshan:** Investigation; **Navin Jacob:** Investigation; **Biswapriya Deb:** Writing - Reviewing and Editing, Funding acquisition; **Chakkooth Vijayakumar:** Conceptualization, Methodology, Validation, Formal analysis, Data curation, Writing - Reviewing and Editing, Visualization, Supervision, Project administration, Funding acquisition.

Declaration of competing interest

The authors declare that they have no known competing financial interests or personal relationships that could have appeared to influence the work reported in this paper.

Data availability

Data will be made available on request.

Acknowledgment

CV and BD thank the Gas Authority of India Limited (GAIL) for funding. CV thank DST-SERB (CRG/2020/002756) and KSCSTE (KSCSTE/1538/2018-KSYSA-RG) for financial support. NR is grateful to CSIR for the research fellowships. The authors thank Prof. Akinori Saeki, Osaka University, for the UPS analysis, Dr. Saju Pillai, and Mr. Peer Mohamed, CSIR-NIIST, for the XPS analysis.

Appendix. ASupplementary data

Supplementary data to this article can be found online at <https://doi.org/10.1016/j.mtener.2023.101296>.

References

- [1] R. Kroon, D.A. Mengistie, D. Kiefer, J. Hynynen, J.D. Ryan, L. Yu, C. Müller, Thermoelectric plastics: from design to synthesis, processing and structure–property relationships, *Chem. Soc. Rev.* 45 (2016) 6147–6164, <https://doi.org/10.1039/C6CS00149A>.
- [2] E. Liu, A. Negm, M.M.R. Howlader, Thermoelectric generation via tellurene for wearable applications: recent advances, research challenges, and future perspectives, *Mater. Today Energy* 20 (2021), 100625, <https://doi.org/10.1016/j.mtener.2020.100625>.
- [3] D. Beretta, N. Neophytou, J.M. Hodges, M.G. Kanatzidis, D. Narducci, M.M. Gonzalez, M. Beekman, B. Balke, G. Cerretti, W. Tremel, A. Zevalkink, Anna I. Hofmann, C. Müller, B. Döring, M.C. Quiles, M. Caironi, Thermoelectrics: from history, a window to the future, *Mater. Sci. Eng. R Rep.* 138 (2019), 100501, <https://doi.org/10.1016/j.mser.2018.09.001>.
- [4] Z.H. Zheng, X.L. Shi, D.W. Ao, W.D. Liu, M. Li, L.Z. Kou, Y.X. Chen, F. Li, M. Wei, G.X. Liang, P. Fan, G.Q. (Max) Lu, Z.G. Chen, Harvesting waste heat with flexible Bi₂Te₃ thermoelectric thin film, *Nat. Sustain.* 6 (2023) 180–191, <https://doi.org/10.1038/s41893-022-01003-6>.
- [5] M. Wu, K. Yao, D. Li, X. Huang, Y. Liu, L. Wang, E. Song, J. Yu, X. Yu, Self-powered skin electronics for energy harvesting and healthcare monitoring, *Mater. Today Energy* 21 (2021), 100786, <https://doi.org/10.1016/j.mtener.2021.100786>.
- [6] I. Vijitha, N. Jacob, N. Raveendran, C. Vijayakumar, B. Deb, Simulation-aided studies on the superior thermoelectric performance of printable PBDTT-FTTE/SWCNT composites, *Mater. Today Energy* 31 (2022), 101233, <https://doi.org/10.1016/j.mtener.2022.101233>.
- [7] C. Liu, X. Yin, S. Wang, C. Gao, L. Wang, Decoupling of thermoelectric parameters in two-dimensional hyperbranched platinum acetylides, *Chem. Eng. J.* 451 (2023), 138751, <https://doi.org/10.1016/j.cej.2022.138751>.
- [8] H. Shang, H. Gu, F. Ding, Z. Ren, Recent advances in flexible thermoelectrics, *Appl. Phys. Lett.* 118 (2021), 170503, <https://doi.org/10.1063/5.0049451>.
- [9] J. Cao, J. Zheng, H. Liu, C.K.I. Tan, X. Wang, W. Wang, Q. Zhu, Z. Li, G. Zhang, J. Wu, L. Zhang, J. Xu, A. Suwardi, Flexible elemental thermoelectrics with ultra-high power density, *Mater. Today Energy* 25 (2022), 100964, <https://doi.org/10.1016/j.mtener.2022.100964>.
- [10] C.K. Mytafides, L. Tzounis, G. Karalis, P. Formanek, A.S. Paipetis, High-power all-carbon fully printed and wearable SWCNT-based organic thermoelectric generator, *ACS Appl. Mater. Interfaces* 13 (2021) 11151–11165, <https://doi.org/10.1021/acsami.1c00414>.
- [11] T. Cao, X.L. Shi, Z.G. Chen, Advances in the design and assembly of flexible thermoelectric device, *Prog. Mater. Sci.* 131 (2023), 101003, <https://doi.org/10.1016/j.pmatsci.2022.101003>.
- [12] H.A. Eivari, Z. Sohbatazadeh, P. Mele, M.H.N. Assadi, Low thermal conductivity: fundamentals and theoretical aspects in thermoelectric applications, *Mater. Today Energy* 21 (2021), 100744, <https://doi.org/10.1016/j.mtener.2021.100744>.
- [13] W. Zhao, S. Fan, N. Xiao, D. Liu, Y.Y. Tay, C. Yu, D. Sim, H.H. Hng, Q. Zhang, F. Boey, J. Ma, X. Zhao, H. Zhang, Q. Yan, Flexible carbon nanotube papers with improved thermoelectric properties, *Energy Environ. Sci.* 5 (2012) 5364, <https://doi.org/10.1039/C1EE01931G>.
- [14] T. Zhu, Y. Wu, S. Li, F.F. Tonni, M. Nomura, M. Zabarjadi, Enhanced thermoelectric performance of holey silicon thin films using F4TCNQ surface doping, *Mater. Today Phys.* 30 (2023), 100942, <https://doi.org/10.1016/j.mtphys.2022.100942>.
- [15] V. Vijayakumar, Y. Zhong, V. Untilova, M. Bahri, L. Herrmann, L. Biniek, N. Leclerc, M. Brinkmann, Bringing conducting polymers to high order: toward conductivities beyond 105 S/cm and thermoelectric power factors of 2 mW/mK², *Adv. Energy Mater.* 9 (2019), 1900266, <https://doi.org/10.1002/aenm.201900266>.
- [16] A.H. Sakr, L. Biniek, J.L. Bantignies, D. Maurin, L. Herrmann, N. Leclerc, P. Lévêque, V. Vijayakumar, N. Zimmermann, M. Brinkmann, A versatile method to fabricate highly in-plane aligned conducting polymer films with anisotropic charge transport and thermoelectric properties: the key role of alkyl side chain layers on the doping mechanism, *Adv. Funct. Mater.* 27 (2017), 1700173, <https://doi.org/10.1002/adfm.201700173>.
- [17] E. Lim, A.M. Claudell, R. Miller, M.L. Chabinyk, The role of ordering on the thermoelectric properties of blends of regioregular and regiorandom poly(3-hexylthiophene), *Adv. Electron. Mater.* 5 (2019), 1800915, <https://doi.org/10.1002/aelm.201800915>.
- [18] H. Zeng, M. Mohammed, V. Untilova, O. Boyron, N. Berton, P. Limelette, B. Schmaltz, M. Brinkmann, Fabrication of oriented n-type thermoelectric polymers by polarity switching in a DPP-based donor–acceptor copolymer doped with FeCl₃, *Adv. Electron. Mater.* 7 (2021), 2000880, <https://doi.org/10.1002/aelm.202000880>.
- [19] I. Vijitha, N. Raveendran, A. Prabhakaran, Y.T. Puli, C. Vijayakumar, B. Deb, MWCNT/thienothiophene based all-organic thermoelectric composites:

- enhanced performance by realigning of the Fermi level through doping, *Chem. Eng. J.* 409 (2021), 128294, <https://doi.org/10.1016/j.cej.2020.128294>.
- [20] M.P. Gordon, S.A. Gregory, J.P. Wooding, S. Ye, G.M. Su, D.S. Seferos, M.D. Losego, J.J. Urban, S.K. Yee, A.K. Menon, Microstructure and heteroatom dictate the doping mechanism and thermoelectric properties of poly(alkyl-chalcogenophenes), *Appl. Phys. Lett.* 118 (2021), 233301, <https://doi.org/10.1063/5.0052604>.
- [21] S. Wu, W. Xing, M. Zhu, Y. Zou, Y. Sun, W. Xu, D. Zhu, Doped thieno[3,4-b] thiophene-based copolymers for p-type organic thermoelectric materials, *J. Mater. Chem. C* 9 (2021) 4158–4163, <https://doi.org/10.1039/D1TC00211B>.
- [22] S. Xu, M. Hong, X. Shi, M. Li, Q. Sun, Q. Chen, M. Dargusch, J. Zou, Z.G. Chen, Computation-guided design of high-performance flexible thermoelectric modules for sunlight-to-electricity conversion, *Energy Environ. Sci.* 13 (2020) 3480, <https://doi.org/10.1039/D0EE01895C>.
- [23] J. Wu, Y. Sun, W.B. Pei, L. Huang, W. Xu, Q. Zhang, Polypyrrole nanotube film for flexible thermoelectric application, *Synth. Met.* 196 (2014) 173–177, <https://doi.org/10.1016/j.synthmet.2014.08.001>.
- [24] F. Zhong, X. Yin, Z. Chen, C. Gao, L. Wang, Significantly reduced thermal-activation energy for hole transport via simple donor engineering: understanding the role of molecular parameters for thermoelectric behaviors, *ACS Appl. Mater. Interfaces* 12 (2020) 26276–26285, <https://doi.org/10.1021/acsami.0c05771>.
- [25] J. Tang, J. Ji, R. Chen, Y. Yan, Y. Zhao, Z. Liang, Achieving efficient p-type organic thermoelectrics by modulation of acceptor unit in photovoltaic π -conjugated copolymers, *Adv. Sci.* 9 (2022), 2103646, <https://doi.org/10.1002/adv.202103646>.
- [26] X. Yan, M. Xiong, J.T. Li, S. Zhang, Z. Ahmad, Y. Lu, Z.Y. Wang, Z.F. Yao, J.Y. Wang, X. Gu, T. Lei, Pyrazine-flanked diketopyrrolopyrrole (DPP): a new polymer building block for high-performance n-type organic thermoelectrics, *J. Am. Chem. Soc.* 141 (2019) 20215–20221, <https://doi.org/10.1021/jacs.9b10107>.
- [27] D. Huang, H. Yao, Y. Cui, Y. Zou, F. Zhang, C. Wang, H. Shen, W. Jin, J. Zhu, Y. Diao, W. Xu, C.A. Di, D. Zhu, Conjugated-backbone effect of organic small molecules for n-type thermoelectric materials with ZT over 0.2, *J. Am. Chem. Soc.* 139 (2017) 13013–13023, <https://doi.org/10.1021/jacs.7b05344>.
- [28] D. Yuan, D. Huang, C. Zhang, Y. Zou, C.A. Di, X. Zhu, D. Zhu, Efficient solution-processed n-type small-molecule thermoelectric materials achieved by precisely regulating energy level of organic dopants, *ACS Appl. Mater. Interfaces* 9 (2017) 28795–28801, <https://doi.org/10.1021/acsami.7b07282>.
- [29] H. Kojima, R. Abe, F. Fujiwara, M. Nakagawa, K. Takahashi, D. Kuzuhara, H. Yamada, Y. Yakiyama, H. Sakurai, T. Yamamoto, H. Yakushiji, M. Ikeda, M. Nakamura, Universality of the giant Seebeck effect in organic small molecules, *Mater. Chem. Front.* 2 (2018) 1276–1283, <https://doi.org/10.1039/C7QM00596B>.
- [30] T. Ghosh, S. Nagasawa, N. Raveendran, V. Darshan, A. Saeki, V.C. Nair, Preferential face-on and edge-on orientation of thiophene oligomers by rational molecular design, *Chem. Asian J.* 14 (2019) 963–967, <https://doi.org/10.1002/asia.201900024>.
- [31] Z. Liang, Y. Zhang, M. Souri, X. Luo, A.M. Boehm, R. Li, Y. Zhang, T. Wang, D.Y. Kim, J. Mei, S.R. Marder, K.R. Graham, Influence of dopant size and electron affinity on the electrical conductivity and thermoelectric properties of a series of conjugated polymers, *J. Mater. Chem. A* 6 (2018) 16495–16505, <https://doi.org/10.1039/C8TA05922E>.
- [32] I.H. Jung, C.T. Hong, U.H. Lee, Y.H. Kang, K.S. Jang, S.Y. Cho, High thermoelectric power factor of a diketopyrrolopyrrole-based low bandgap polymer via finely tuned doping engineering, *Sci. Rep.* 7 (2017) 1, <https://doi.org/10.1038/srep44704>.
- [33] B. Li, X. Li, F. Yang, Y. Chen, X. Mao, S. Wan, H. Xin, S. Yan, M. Wang, C. Gao, L. Wang, Enhanced thermoelectric performance of a donor–acceptor-based two-dimensional conjugated polymer with high crystallinity, *ACS Appl. Energy Mater.* 4 (2021) 4662–4667, <https://doi.org/10.1021/acsaem.1c00274>.
- [34] M.M. Korobov, Y.V. Pervova, L.N. Sidorov, Electron affinity of iron(III)chloride, *Mendeleev Commun.* 2 (1992) 41–42, <https://doi.org/10.1070/MC1992v002n02ABEH000119>.
- [35] H. Méndez, G. Heimel, S. Winkler, J. Frisch, A. Opitz, K. Sauer, B. Wegner, M. Oehzelt, C. Röthel, S. Duhm, D. Töbrens, N. Koch, I. Salzmänn, Charge-transfer crystallites as molecular electrical dopants, *Nat. Commun.* 6 (2015) 8560, <https://doi.org/10.1038/ncomms9560>.
- [36] A.D. Scaccabarozzi, A. Basu, F. Aniés, J. Liu, O.Z. Arteaga, R. Warren, Y. Firdaus, M.I. Nugraha, Y. Lin, M.C. Quiles, N. Koch, C. Müller, L. Tsetseris, M. Heeney, T.D. Anthopoulos, Doping approaches for organic semiconductors, *Chem. Rev.* 122 (2022) 14420–14492, <https://doi.org/10.1021/acs.chemrev.1c00581>.
- [37] Y. Liu, B. Zhao, J. Liu, Z. Wang, Z. Liang, W. Dong, C. Xu, B. Wang, Z. Fei, Y. Han, Extending the p-doping of polymers to an air stable Lewis Acid–Base adduct by increasing the acidity of the dopant, *ACS Appl. Polym. Mater.* 4 (2022) 3877–3884, <https://doi.org/10.1021/acscapm.2c00342>.
- [38] M.V. Russo, G. Polzonetti, A. Furlani, XPS and IR investigations of FeCl₃-doped polyphenylacetylene: the solvent effect, *Synth. Met.* 39 (1991) 291–301, [https://doi.org/10.1016/0379-6779\(91\)91755-Y](https://doi.org/10.1016/0379-6779(91)91755-Y).
- [39] C. Zhang, J. Ma, F. Han, H. Liu, F. Zhang, C. Fan, J. Liu, X. Li, Strong anchoring effect of ferric chloride-graphite intercalation compounds (FeCl₃-GICs) with tailored epoxy groups for high-capacity and stable lithium storage, *J. Mater. Chem. A* 6 (2018) 17982–17993, <https://doi.org/10.1039/C8TA06670A>.
- [40] I. Vijitha, N. Raveendran, S. Poovattil, N. Jacob, C. Vijayakumar, B. Deb, Studies on the doping mechanism of conjugated thienothiophene polymer/MWCNT hybrids for thermoelectric application, *Macromol. Mater. Eng.* 307 (2022) 8351–8358, <https://doi.org/10.1002/mame.202100916>, 2100916.
- [41] A.M. Glaudell, J.E. Cochran, S.N. Patel, M.L. Chabiny, Impact of the doping method on conductivity and thermopower in semiconducting polythiophenes, *Adv. Energy Mater.* 5 (2015), 1401072, <https://doi.org/10.1002/aenm.201401072>.
- [42] Y.H. Kang, U.-H. Lee, I.H. Jung, S.C. Yoon, S.Y. Cho, Enhanced thermoelectric performance of conjugated polymer/CNT nanocomposites by modulating the potential barrier difference between conjugated polymer and CNT, *ACS Appl. Electron. Mater.* 1 (2019) 1282–1289, <https://doi.org/10.1021/acsaem.9b00224>.
- [43] W. Shi, T. Zhao, J. Xi, D. Wang, Z. Shuai, Unravelling doping effects on PEDOT at the molecular level: from geometry to thermoelectric transport properties, *J. Am. Chem. Soc.* 137 (2015) 12929–12938, <https://doi.org/10.1021/jacs.5b06584>.
- [44] Y. Xuan, X. Liu, S. Desbief, P. Leclère, M. Fahlman, R. Lazzaroni, M. Berggren, J. Cornil, D. Emin, X. Crispin, Thermoelectric properties of conducting polymers: the case of poly(3-hexylthiophene), *Phys. Rev. B* 82 (2010), 115454, <https://doi.org/10.1103/PhysRevB.82.115454>.
- [45] F. Zhang, Y. Zang, D. Huang, C. Di, X. Gao, H. Sirringhaus, D. Zhu, Modulated Thermoelectric properties of organic semiconductors using field-effect transistors, *Adv. Funct. Mater.* 25 (2015) 3004–3012, <https://doi.org/10.1002/adfm.201404397>.
- [46] N. Mateeva, H. Niculescu, J. Schlenoff, L.R. Testardi, Correlation of Seebeck coefficient and electric conductivity in polyaniline and polypyrrole, *J. Appl. Phys.* 83 (1998) 3111–3117, <https://doi.org/10.1063/1.367119>.
- [47] T.L.D. Tam, A. Moudgil, W.J. Teh, Z.M. Wong, A.D. Handoko, S.W. Chien, S.W. Yang, B.S. Yeo, W.L. Leong, J. Xu, Polaron delocalization dependence of the conductivity and the Seebeck coefficient in doped conjugated polymers, *J. Phys. Chem. B* 126 (2022) 2073–2085, <https://doi.org/10.1021/acs.jpcc.2c00303>.
- [48] G. Zuo, X. Liu, M. Fahlman, M. Kemerink, High Seebeck coefficient in mixtures of conjugated polymers, *Adv. Funct. Mater.* 28 (2018), 1703280, <https://doi.org/10.1002/adfm.201703280>.
- [49] E.J. Dell, B. Capozzi, J. Xia, L. Venkataraman, L.M. Campos, Molecular length dictates the nature of charge carriers in single-molecule junctions of oxidized oligothiophenes, *Nat. Chem.* 7 (2015) 209–214, <https://doi.org/10.1038/nchem.2160>.